Transactions of the ASME

Journal of Fluids Engineering

Published Quarterly by The American Society of Mechanical Engineers

VOLUME 104 • NUMBER 1 • MARCH 1982

H. Tsukamoto
Associate Professor,
Department of Mechanical Engineering,
Kyushu Institute of Technology,
Kitakyushu, Japan

H. Ohashi
Professor,
Faculty of Engineering,
University of Tokyo,
Tokyo, Japan

Transient Characteristics of a Centrifugal Pump During Starting Period

A theoretical and experimental study has been made on the transient characteristics of a centrifugal pump during its rapid acceleration from standstill to final speed. Instantaneous rotatinal speed, flow-rate, and total pressure rise are measured for various start-up schemes. Theoretical calculations for the prediction of transient characteristics are developed and compared with the corresponding experimental results. As the results of this study, it becomes clear that the impulsive pressure and the lag in circulation formation around impeller vanes play predominant roles for the difference between dynamic and quasi-steady characteristics of turbopump during its starting period.

Introduction

Performance of a pump is usually expressed by curves, which describe the relation of total pressure rise, efficiency, and driving power to flow-rate at a constant rotational speed. By introducing nondimensional parameters such as flow coefficient ϕ and total pressure rise coefficient ψ, the relation between flow-rate and total pressure rise at any rotational speed can be reduced into a unique relation between ϕ and ψ independent of rotational speed. This relation expresses the performance of a pump under steady and cavitation-free operating condition in the most general form, and is called hereafter steady-state characteristics.

Numerous studies have been done on the steady-state characteristics of turbopumps. At present we have almost reached a point where steady-state characteristics can be predicted by available data with sufficient accuracy.

On the contrary, little is known about the characteristics when turbopumps operate under unsteady conditions. In this case rotational speed and/or flow-rate of a pump changes with time according to the nature of the unsteadiness. The characteristics of a pump under such unsteady conditions have usually been thought to follow along its steady-state characteristics curves [1]. This assumption is called hereafter quasi-steady change. In the case of low frequency or slow change of operational condition, such assumption is obviously acceptable.

When the changing rate of the operational point exceeds a certain limit, however, the pump cannot respond quickly enough to follow along its steady-state characteristics curves, thus resulting in a considerable change in the actual characteristics curve. One typical example of such unsteady operation is surging. The flow-rate of a surging pump oscillates periodically, while the fluctuation of rotational speed is negligible small. One of the authors has idealized this case and studied the dynamic relationship between ϕ and ψ when the flow-rate changes sinusoidally around its mean value at a constant rotational speed [2]. This study has revealed the nature of the frequency response of the total pressure rise (pumping action) to the fluctuating flow-rate and has shown how the dynamic characteristics deviate from the ones at steady-state as the fluctuation frequency increases.

Another interesting example of unsteady operation is found during the starting period of a pump. The rotational speed is accelerated rapidly from standstill to its final speed, while flow-rate and total pressure rise are boosted accordingly. From the viewpoint of theoretical treatment, this case offers far more difficulty than the previous case, because both rotational speed and flow-rate are variable and also because the linearization of the problem is fundamentally impossible.

Fang [3], and Miyashiro and Takada [4] discussed the axial hydraulic thrust caused by the starting of a pump. Their interests are, however, not in the deviation of the characteristics from quasi-steady change, but purely in thrust problems. Studies on transient characteristics during start-up have not been reported to data except the one by the present authors [5], in which the deviation of characteristics from quasi-steady change was pointed out, but no clear explanation was given for the observed phenomena.

The aim of this study is to try to explain the nature of pumping action during starting transients. In order to find the critical acceleration rate beyond which the assumption of quasi-steady change becomes unacceptable, the tests are conducted up to very rapid acceleration rate, which hardly occurs in practice. Such extreme test conditions result in clear difference between dynamic and quasi-steady change and help understand the mechanism of transient phenomena. Another aim is to establish the method by which the transient characteristics of turbopump during starting period can be predicted theoretically. The present analysis is limited to the case of cavitation-free, incompressible, and inviscid flow.
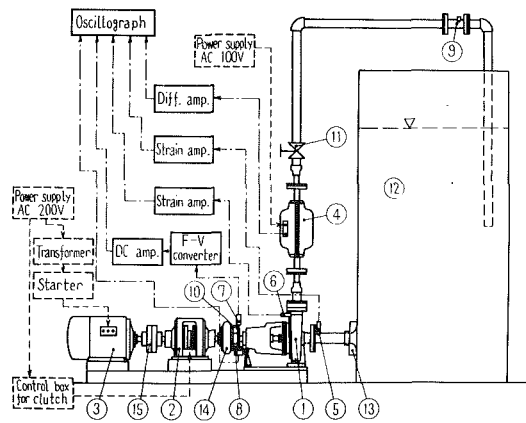
1. Test pump
2. Electro-magnetic clutch
3. Motor
4. Electro-magnetic flowmeter
5. Transducer for suction pressure
6. Transducer for discharge pressure
7. Electro-magnetic pickup
8. Photo-sensor
9. Turbine flowmeter
10. Gear for pulse generation
11. Discharge valve
12. reservoir
13. Bell mouth
14. Rubber flexible coupling
15. Coupling

Fig. 1 Schematic view of test setup and instrumentation system

Table 1 Specifications of test pump

Suction diameter		50 mm
Discharge diameter		40 mm
Rating:	Flow-rate	0.2 m³/min
	Total head rise	30 m
	Rotational speed	2950 rpm
Impeller:	Outer Diameter	166 mm
	Outer passage width	4.2 mm
	Outlet vane angle	26 deg
	Number of vanes	5

Experiment

Test Equipment and Method. A single stage, volute type centrifugal pump is used for the experiment and its principal specifications are summarised in Table 1. The arrangement of test setup and instrumentation system is illustrated schematically in Fig. 1.

The inlet pipe from the reservoir to the suction flange of the pump is 250 mm in length and 50 mm in inner diameter. The inner diameter of the discharge line is 40 mm except for the part of the electro-magnetic flowmeter where the inner diameter measures 25 mm. From the standpoint of inertia resistance, the length of the discharge line is equivalent to 4.5 m.

The test pump is driven by a 2-pole 7.5 kW induction motor through an electro-magnetic clutch, which connects or disconnects both shafts depending on the exciting current on the magnet coil.

To achieve the desired acceleration rate of the rotational speed, various methods are adopted. The highest acceleration can be obtained by the activation of the electro-magnetic clutch, which connects the pump shaft in standstill with the motor in idling. The acceleration rate can be adjusted to some extent by controlling the exciting current to the magnet coil, in other words, by limiting the maximum transmission torque of the clutch.

Slow acceleration is obtained by the usual starting method of the induction motor. The magnetic clutch is kept in the connected position and the motor accelerates the pump directly by its starting torque. The acceleration rate in this case can be adjusted by selecting either the delta or star connection and by controlling the line voltage to the motor.

The flow-rate is measured by an electro-magnetic flowmeter installed in the discharge line. Although DC excitation of the magnet is advantageous to measuring the rapidly changing flow-rate, we have adopted 50 Hz AC excitation mainly to avoid severe drift problems encountered in the DC excited flowmeter. The turbine flowmeter installed on the discharge line is used to measure the final flow-rate after the starting transient, and is used also for the calibration of the electo-magnetic flowmeter.

The suction and discharge pressure are measured by semi-conductor type pressure transducers, which are installed directly on the pressure taps in order to prevent the decrease of natural frequency in the pressure measurement system.

The rotational speed of the pump shaft is detected by the pulse signals (60 pulses a revolution), which are fed to a frequency-analogue converter for the recording. Besides this the output of the photosensor is amplified and recorded directly on the oscillograph. This serves to find out the exact moment when the pump begins to rotate, and also to detect the angular displacement of the shaft in the period immediately after starting.

In order to avoid cavitation during the starting transient, special precautions have been taken. Water is supplied to the suction port from a large reservoir with a water level of 1 m above the pump center through a short inlet pipe.

Before starting each test, the pump and piping loop are completely filled with water. The discharge valve is so adjusted that the final flow-rate coincides with the desired value. The valve setting is not changed during the starting period.

Presentation of Data. The first step involves measuring the steady-state performances at various rotational speed. The results are reduced to a non-dimensional characteristics curve, which is independent of the rotational speed. This steady-state characteristics curve is used as a standard, to which all measured transient characteristics are referred for comparison.

Starting tests have been conducted for various combinations of the two parameters, i.e. discharge valve setting and acceleration rate of rotational speed N_i. Since final flow-rate Q_f after starting is determined by the valve setting only, the opening degree of the valve is expressed indirectly by the ratio of Q_f to the rating flow-rate Q_r (0.2 m³/min). Acceleration rate dN_i/dt is not constant for the entire starting period. It is, therefore, difficult to express this complicated acceleration history by a simple parameter. In this study, we introduce a nominal acceleration time T_{na}, which is defined as the acceleration time of the pump shaft from standstill to 63.2 percent of its final rotational speed N_f.

From the data recorded on the oscillograph, instantaneous flow-rate $Q_i(t)$, total pressure difference between discharge and suction port $P_i(t)$, and rotational speed $N_i(t)$ are read out as the function of time t after the start.

Now, we will consider the total pressure rise achieved by the pump, $P(t)$, during the starting period. In the case of unsteady flow-rate, it is necessary to differentiate the total pressure rise of the pump, $P(t)$, from the indicated total pressure difference between the suction port and the discharge of the pump, $P_i(t)$. The total pressure difference is, of course, generated mainly by the pumping action itself. However, it is also affected by the inertia of the water contained in the pump casing. Hence, the true total pressure rise $P(t)$ is obtained by subtracting the apparent static pressure difference $p_c(t)$ due to the inertia from the indicated total pressure difference $P_i(t)$, as the following equation shows:

$$P(t) = P_i(t) - p_c(t)$$
$$= P_i(t) + (\rho L_{eq}/A_0)\{d Q_i(t)/dt\} \qquad (1)$$

where the pump is represented by a straight pipe with cross sectional area A_0 and length L_{eq}.
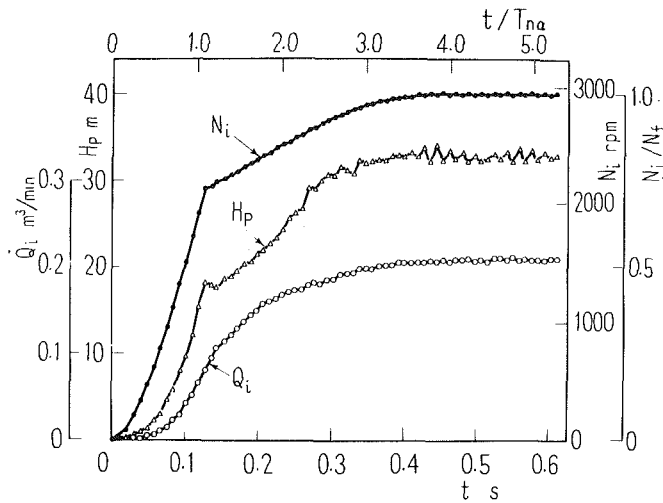
Fig. 2 Time histories of N_i, Q_i and H_p for Case 1. Uncertainty: N_i/N_f ± 3.0 percent, Q_i/Q_f ± 3.5 percent, $H_p/H_p(\infty)$ ± 3.5 percent (10:1 odds).

There are several methods to estimate the equivalent pipe length L_{eq} of a turbopump [6]. In the present study, the passage area $A(s)$ of the pump is estimated by use of drawings, and the equivalent pipe length is calculated by the equation

$$L_{eq} = \int_{s=0}^{L} \{A_0/A(s)\} ds \qquad (2)$$

where s is the distance measured from the suction port, and L is the total path length.

The instantaneous flow coefficient ϕ_i and the instantaneous total pressure rise coefficient ψ_i are defined as follows:

$$\left.\begin{array}{l} \phi_i(t) = Q_i(t)/\{\pi\, d_2 b_2 u_2(t)\} \\[2mm] \psi_i(t) = P(t)/\{\rho\, u_2(t)^2/2\} \end{array}\right\} \qquad (3)$$

where d_2 and b_2 the outer diameter and passage width of the impeller, respectively, and $u_2(t) = \pi d_2 N_i(t)$ is the instantaneous peripherial speed of the impeller.

Test Results. All of the test data are processed as explained above. Due to limited space available in this paper, results will be shown only for two representative cases listed in Tabe. 2.

Figure 2 shows a sample of the time histories of the rotational speed N_i, flow-rate Q_i and total head rise $H_p = P/(\rho g)$ during starting transient for Case 1 in which the pump is started with the highest attainable acceleration rate by clutch-on starting method. As seen from the figure, the flow-rate as well as the total head rise increases as rotational speed increases, and they finally approach the steady-state values. In this test, flow-rate reaches the steady-state value immediately after rotational speed reaches the final value. This is due to the small inertia effect of the water contained in the piping of the relatively short test loop.

Time histories of ϕ_i, ψ_i, and N_i in Case 1 are shown in Fig. 3. Flow coefficient ϕ_i starts from zero and approaches its final value ϕ_f, while total pressure rise coefficient ψ_i starts from very large value and approaches its final level ψ_f.

Figure 4(a) and (b) indicate the locus along which the coordinates of ϕ_i and ψ_i move during the starting transient for Case 1 and 2, respectively. The time sequence is written on the locus as a parameter and the point corresponding to the nominal acceleration time is marked by a large circle. These loci represent the characteristics curves during the starting period and should be compared with the steady-state characteristics drawn by dash line. As can be seen clearly from these figures, the deviation of transient characteristics is essential.

Table 2   List of test condition

Case No.	N_f[rpm]	T_{na}[s]	Q_f/Q_r	Starting method
1	2950	0.12	1.04	clutch-on
2	2932	0.68	1.03	direct
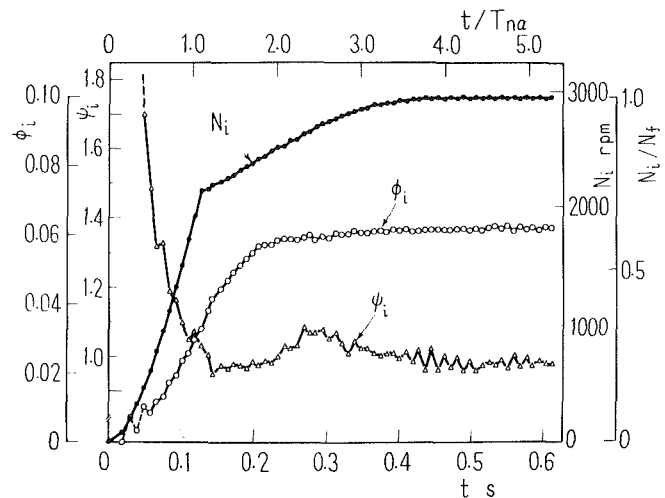
Fig. 3   Time histories of N_i, ϕ_i and ψ_i for Case 1. Uncertainty: N_i/N_f ± 3.0 percent, ϕ_i/ϕ_f ± 5.5 percent, ψ_i/ψ_f ± 5.5 percent (10:1 odds).

Here we classify these starting transients into four stages, i.e. A, B, C, and D as indicated in Fig. 4(a). At the very beginning of the starting period, stage A, the total pressure rise coefficient ψ_i is greater than the quasi-steady value ψ_s at the same instantaneous flow coefficient ϕ_i. This tendency is mainly caused by the effect of the impulsive pressure difference between the inlet and exit ports of the impeller as supported by the numerical calculations described in the analysis. In addition to this effect, boundary layers are still very thin, and the whole flow behaves like the potential flow without separation and losses. Therefore, it also leads to a greater value for ψ_i than the steady-state value ψ_s.

The next stage B appears near the point of $t = T_{na}$ only in the case of the clutch-on start. In this stage the tendency of decreasing ψ_i is suspended once and ψ_i shows even slight increases. This is attributed to the sudden change in the acceleration rate $d\,N_i/dt$ near the instant of $t = T_{na}$ in the case of clutch-on start.

In stage C, ψ_i is always smaller than ψ_s. This reason might be attributed largely to the lag in circulation growth around the impeller vanes. As presented later this lag can be fundamentally calculated by the potential flow theory.

In the last acceleration stage D, ψ_i exceeds ψ_s again. Since this stage is still in an acceleration period, the boundary layers are kept thin and are yet resistive to separation. This can be the reason of the above overshoot of ψ_i compared to the quasi-steady value.

Analysis

Modeling of Flow. The aim of this analysis is to establish calculating method for the time histories of the flow-rate and total pressure rise when the increase of the rotational speed is given as a function of time. Among many assumptions necessary for the analysis, it is first assumed that the transient characteristics of a pump can be determined by solving the unsteady flow on a representative stream surface, i.e., mean stream surface.

In a centrifugal impeller, which is our main concern, the impeller blades on the stream surface constitute a rotating circular cascade. As is well known, the unsteady flow analysis of *rotating circular cascade requires impractical mathematical*
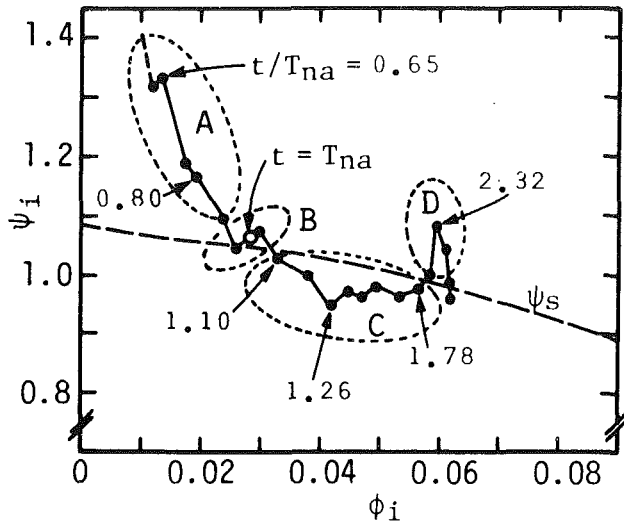
(a) Case 1
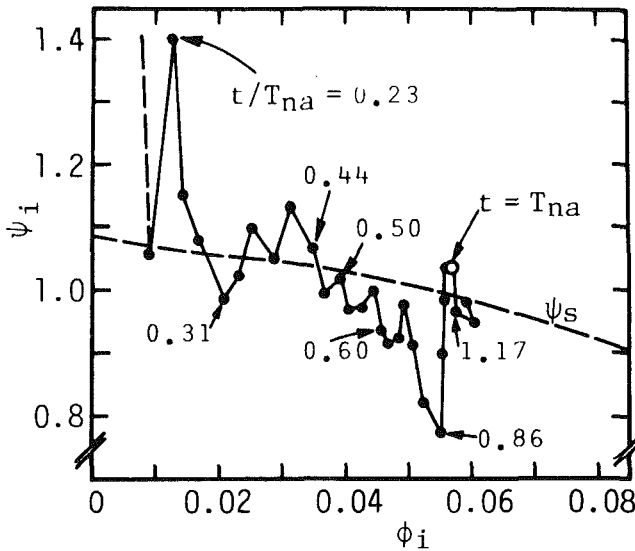
(b) Case 2

Fig. 4 Dynamic characteristics curve during starting period. Uncertainty: $\phi_i/\phi_f \pm 5.5$ percent (10:1 odds).

complexity and these circumstances lead to the second assumption that the characteristics of a rotating circular cascade is approximately replaced by those of an equivalent linear cascade, whose geometries are obtained by conformal transformation of original cascade, as shown in Fig. 5. In the following sections, therefore, unsteady flow analysis is made only for two-dimensional linear cascade.

The pressure rise of guide vane or diffuser, which follows the impeller, is assumed simply to be quasi-steady. Therefore, the total pressure rise per a stage of a pump can be determined as the sum of the increase in both static and dynamic pressure at the outlet edge of the rotor.

It is assumed also that flow is incompressible, cavitation-free and invisicid, and inlet flow to the impeller has no pre-rotation and is axisymmetric.

Inlet Flow Condition. In the present analysis the unsteady relative inlet flow W_1 is obtained as the vector sum of the axial velocity $V_a(t)$ and the peripheral speed $V_r(t)$. Therefore, it is instantaneously uniform in the region preceding the cascade, and varies only with respect to time t, $W_1(t)$. This is "in phase" inlet unsteadiness.
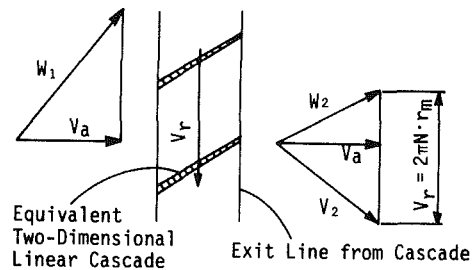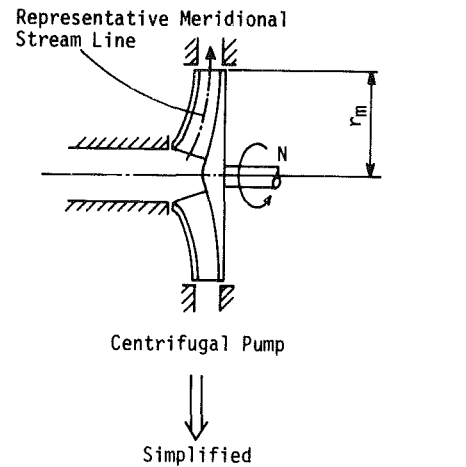
Fig. 5 Flow model in a centrifugal pump
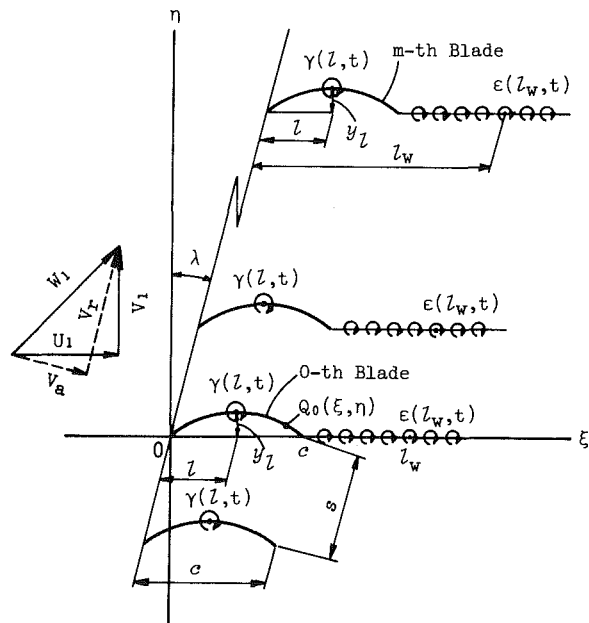
Fig. 6 Model of an airfoil cascade

The flow around the moving cascade will be discussed with respect to the relative coordinate system ξ, η fixed to the cascade, as shown in Fig. 6. Relative inlet velocity W_1 is then divided into $\xi-$ and $\eta-$ components, U_1 and V_1, respectively, and they are expressed by

$$\left.\begin{array}{l} U_1 = V_r\sin\lambda + V_a\cos\lambda \\ V_1 = V_r\cos\lambda - V_a\sin\lambda \end{array}\right\} \tag{4}$$

Vorticity Distribution. The configuration of the cascade used in the present theory is shown in Fig. 6. It is a staggered

cascade of thin airfoil with a chord length c, stagger angle λ, spacing s, and camber distribution y_l. Since only in phase unsteadiness is considered, each airfoil can be represented by an identical bound vortex sheet $\gamma(l, t)$. According to the change in circulation, each airfoil sheds vortices into downstream and they form a vortex sheet of strength $\epsilon(l_w, t)$. This vortex sheet is assumed to be convected parallel to the chord line of the airfoil with instantaneous velocity $U_1(t)$. The shed vortex sheet from the zeroth blade extends in the present approximation on ξ-axis from $\xi = c$ to $\xi = c + \int_0^t U_1(\tau)d\tau$. All other vortex sheets have the same extention.

The boundary condition on airfoil requires that the total induced velocity normal to the blade surface should be zero. This condition is expressed by the following integral equation for unknown vorticity $\gamma(l, t)$, in which the velocity induced by shed vortices is rewritten in the manner similar to reference [7]:

$$V_1(t) + \int_0^c \gamma(l,t)\{g(\xi,\eta,l) - g(\xi,\eta,c)\}dl + \int_0^t \Gamma_c(t_1)$$

$$\times \left\{\frac{d}{dt_1}g\left(\xi,\eta,c + \int_{t_1}^t U_1(\tau)d\tau\right)\right\}dt_1 - (dy_l/d\xi)\left[U_1(t)\right.$$

$$+ \int_0^c \gamma(l,t)\{f(\xi,\eta,l) - f(\xi,\eta,c)\}dl + \int_0^t \Gamma_c(t_1)$$

$$\times \left\{\frac{d}{dt_1}f\left(\xi,\eta,c + \int_{t_1}^t U_1(\tau)d\tau\right)\right\}dt_1\right] = 0 \qquad (5)$$

where, $f(\xi,\eta,l) = -\{e^{i\lambda}K(\bar\Lambda) + e^{-i\lambda}K(\Lambda)\}/(4\pi s)$,

$\qquad g(\xi,\eta,l) = -i\{e^{i\lambda}K(\bar\Lambda) - e^{-i\lambda}K(\Lambda)\}/(4\pi s)$,

$\qquad K(\Lambda) = \pi\cot(\pi\Lambda)$,

$$\Lambda = \begin{cases} -i\,e^{-i\lambda}\{\xi - l - i(\eta - y_l)\}/s & (0 \leqq l \leqq c) \\ -i\,e^{-i\lambda}(\xi - l - i\eta)/s & (l \geqq c) \end{cases}$$

$$\bar\Lambda = \begin{cases} i\,e^{i\lambda}\{\xi - l + i(\eta - y_l)\}/s & (0 \leqq l \leqq c) \\ i\,e^{i\lambda}(\xi - l + i\eta)/s & (l \geqq c) \end{cases}$$

and $\Gamma_c(t_1) = \int_0^c \gamma(l,t_1)dl \qquad (6)$

In order to eliminate the errors associated with the numerical calculations of equation (5), the integration with respect to time t_1 is directly carried out by assuming $\Gamma_c(t_1)$ to be linear for a small interval Δt. For example, the third term of left side of equation (5) is then expressed as

$$\sum_{i=0}^{M-1}\{\Gamma_c(t_i) + \Gamma_c(t_{i+1})\}\left\{g\left(\xi,\eta,c + \int_{t_{i+1}}^t U_1(\tau)d\tau\right)\right.$$

$$\left. - g\left(\xi,\eta,c + \int_{t_i}^t U_1(\tau)d\tau\right)\right\}/2$$

where, $t_i < t_1 < t_{i+1}$, $\Delta t = t_{i+1} - t_i$, $t_0 = 0$, $t_M = t$, and $\Gamma_c(t_i)$ is known except for $\Gamma_c(t_M) = \Gamma_c(t)$.

For the numerical calculation with respect to space l by use of trapezoidal rule, a transformation to new independent variable θ and Θ is made

$l = (c/2)(1 - \cos\theta)$, $\qquad (0 \leqq \theta \leqq \pi)$

$\xi = (c/2)(1 - \cos\Theta)$, $\qquad (0 \leqq \Theta \leqq \pi$

Then bound vortices can be specified at $(n + 1)$ points

$\theta = (k - 1)\pi/n \qquad (k = 1,2, \ldots \ldots, n+1)$

The value of γ for $k = n + 1$, that is at the trailing edge, is
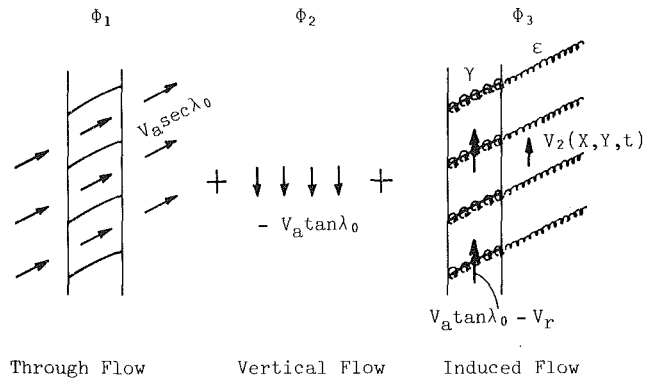
Fig. 7 Construction of flow field
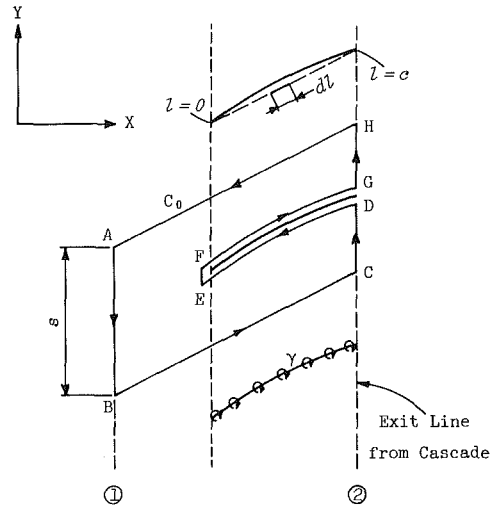
Fig. 8 Control surface for considering pressure rise through cascade

unnecessary since in the integration it is always multiplied by $\sin\theta = 0$. The n values of γ can be determined so as to satisfy equation (5) at n points only, and these points are chosen so as to be allocated midway between the points at which bound vortices are specified.

$$\Theta = (2k - 1)\pi/2n \qquad (k = 1,2, \ldots \ldots, n)$$

In this manner, equation (5) yields n simultaneous equation for the n unknowns, $\gamma(l, t)$.

Pressure Rise. For a given peripheral speed of the rotor cascade V_r, the static pressure difference between inlet and outlet of rotor can be calculated by the following unsteady Bernoulli's equation with respect to the moving relative system [8]

$$(\partial\Phi/\partial t) + W^2/2 - V_r^2/2 + p/\rho = F(t) \qquad (7)$$

where $\partial\Phi/\partial t$: time rate of change of velocity potential of absolute velocity at fixed station in the relative system, W: relative velocity, p: static pressure, ρ: density, $F(t)$: arbitrary function to fit initial condition.

To calculate the impulsive pressure term $\rho(\partial\Phi/\partial t)$ in equation (7), the flow field represented by Φ is here divided into three basic parts, Φ_1, Φ_2, and Φ_3, as shown in Fig. 7. The Φ_1 represents the through flow in which the circulation around airfoil does not change, Φ_2 the vertical translatory flow of which velocity is $-V_a \tan\lambda_0$ (λ_0: zero-lift angle), and Φ_3 the flow induced by vortices on airfoils as well as in wakes. As can be seen easily, the flow represented by ($\Phi_1 + \Phi_2$) is not concerned with the change in circulation around airfoils of cascade. Therefore, the contribution of Φ_1 and Φ_2 to the impulsive pressure term can be omitted from our interest.

The effect of Φ_3 on the impulsive pressure term is calculated

using the control surface shown in Fig. 8, where the line integration of complex potential $w_3 = \Phi_3 + i \cdot \Psi_3$ along a closed curve C becomes

$$i \cdot s(\bar{\Phi}_{3_2} - \bar{\Phi}_{3_1}) + Z_D \Gamma_c(t) - \int_0^c Z_l \gamma(l,t) dl$$

$$+ \int_B^C Y \, d\Psi_3 + \int_H^A Y \, d\Psi_3 = 0$$

where $Z_D = c(\cos \lambda + i \cdot \sin \lambda)$, $Z_l = l(\cos \lambda + i \cdot \sin \lambda)$, and $\bar{\Phi}_3$ means velocity potential defined by

$$\bar{\Phi}_3(X,t) = \int_Y^{Y+s} \Phi_3(X,Y,t) \, dY/s$$

The consideration of the imaginary part in the above equation gives the following impulsive pressure difference between inlet and outlet of rotor cascade:

$$\rho\{ (\partial \Phi/\partial t)_1 - (\partial \Phi/\partial t)_2 \}$$

$$= (\rho \sin \lambda/s) \cdot \frac{d}{dt} \left\{ c\Gamma_c(t) - \int_0^c l\gamma(l,t) dl \right\}$$

Using the above equation and equation (7) after introducing the mean induced velocity on outlet edge of rotor, $\bar{v}_2(t) = \Gamma_c(t)/s$, we obtain the increase of static pressure at the outlet edge of rotor as follow:

$$p_2 - p_1 = \{ \rho \Gamma_c(t)/(2s) \} [2V_r(t) - \{ \Gamma_c(t)/s \}]$$

$$+ (\rho \sin \lambda/s) \cdot \frac{d}{dt} \left\{ c\Gamma_c(t) - \int_0^c l\gamma(l,t) dl \right\} \quad (8)$$

Since our analysis is limited to the case in which inlet flow to rotor has no prerotation, the increase of dynamic pressure at the outlet is given by

$$\Delta p_d = \rho \bar{v}_2(t)^2/2 = (\rho/2)\{ \Gamma_c(t)/s \}^2 \quad (9)$$

Thus total pressure rise per a stage of a pump, $P(t)$, is given as the sum of equation (8) and equation (9), and becomes

$$\psi_i(t) = P(t)/\{ (\rho/2)V_r^2 \}$$

$$= \{ 2\Gamma_c(t) \}/\{ s \, V_r(t) \} + (2 \, \rho \sin \lambda/s)$$

$$\times \frac{d}{dt} \left\{ c\Gamma_c(t) - \int_0^c l\gamma(l,t) dl \right\}/V_r(t)^2 \quad (10)$$

Numerical Calculation. Before going into the numerical calculations, the equation for determining the instantaneous flow-rate $Q_i(t)$ must be derived. The piping is supposed to be filled with water before each starting. Assuming that the pump delivers no elevation head, the total pressure rise generated by pumping, $P(t)$, balances with the pressure loss in the piping system, $p_l(t)$, and the apparent pressure difference $p_c(t)$ caused by the inertia of the water contained in the pipe:

$$P(t) - p_l(t) + p_c(t) = 0$$

that is,

$$(\rho l_{eq}/A_0)\{ dQ_i(t)/dt \} + (\rho \zeta/2)\{ Q_i(t)/A_0 \}^2 = P(t)$$

or,

$$\rho l_{eq}\{ dV_a(t)/dt \} + (\rho \zeta/2)V_a(t)^2 = P(t) \quad (11)$$

where, A_0: nominal flow area, l_{eq}: equivalent pipe length referred to area A_0, and ζ: pressure loss coefficient which is determined by using equation (11) at the final operating condition.

$$\zeta = \psi_f/\phi_f^2 \quad (12)$$

Table 3 shows the input data in the calculation of transient

characteristics. As a start-up condition, the instantaneous rotational speed $N_i(t)$ is assumed to follow

$$N_i(t) = N_f\{ 1 - \exp(-t/T_{na}) \} \quad (13)$$

where the final speed N_f and nominal acceleration time T_{na} are the given parameters.

The numerical procedure is presented in Fig. 9. Starting from $t = 0$, equation (11) is computed to obtain V_a as a function of t by application of Euler's method [9], which is explicit and requires no additional starting values. Under the unsteady inlet condition expressed by equation (4) the circulation Γ_c is subsequently computed by the method mentioned previously. Finally total pressure rise by pumping is determined by equation (10). This procedure is repeated step by step in time till the steady-state condition is satisfied.

Table 3   Input data in the numerical calculations

Number of rotor vanes	N_R
Equivalent two-dimensional linear cascade:	
Solidity	σ
Stagger angle	λ
Pipe line:	
Nondimensional equivalent pipe length	$l_{eq}^*(= l_{eq}/r_m)$
Pump starting condition:	
Final flow coefficient	ϕ_f
Final total pressure rise coefficient	ψ_f
Final rotational speed	N_f
Nominal acceleration time	T_{na}

Similarity Rule. Let us compare the transient phenomena in pumping systems with geometrically similar pump and pipings. Once we fix the following seven parameters, that is, the representative length of the pump, r_m, total length of the piping, l_{eq}, density and viscosity coefficient of the fluid, ρ and μ, final rotational speed, N_f, final flow-rate, Q_f, and nominal acceleration time, T_{na}; a unique experimental condition can be established, under which a specific transient phenomenon takes place.

According to the theory of dimensional analysis, the above seven physical quantities can be reduced to four independent non-dimensional parameters, i.e., normalized piping length l_{eq}/r_m, Reynolds number $N_f d^2/(\mu/\rho)$, normalized flow-rate $Q_f/(N_f d^3) \propto Q_f/Q_r$ and a newly introduced dimensionless number $N_f T_{na}$. The latter two parameters can be controlled in the experiment by adjusting the opening of delivery valve and the acceleration rate of rotational speed. The influence of Reynolds number on transient characteristics is omitted from the present study.

$N_f T_{na}$ is the most important parameter for the transient characteristics of a rotating impeller. As can be easily proved, $N_f T_{na}$ is proportional to the total number of revolutions necessary to accelerate the impeller from standstill up to final speed N_f. When $N_f T_{na}$ is small, the transient ends up with relatively small angular displacement of the impeller.

As a simple analogy we consider the lift response of an airfoil to a gust with ramped zone. From unsteady airfoil theory [10] it is obvious that the shorter the extent of the ramped zone relative to the airfoil chord, the larger the effect of unsteadiness, and thus the more the deviation of transient lift from the quasi-steady one.

An analogous conclusion can be also reduced to an accelerating impeller when we read $N_f T_{na}$ for relative extent of the ramped zone. Smaller $N_f T_{na}$ means, in this case, a stronger unsteadiness and a larger deviation of the transient characteristics from the quasi-steady ones.

Comparison Between Theory and Experiment

Figure 10 indicates the calculated and measured loci, along

START

Input data ———— Table 3

ζ ———— Eq. (12)
$l_{eq}/c \leftarrow l_{eq}^* N_R / (2\pi\sigma)$

$m \leftarrow 1$

$t(1) \leftarrow 0,\ V_r(1) \leftarrow 0,\ V_a(1) \leftarrow 0$
$\Gamma_c(1) \leftarrow 0,\ \phi_i(1) \leftarrow 0,\ \psi_i(1) \leftarrow 0$ — Initial condition

$m \leftarrow m + 1$

$t(m) \leftarrow t(m-1) + \Delta t$

$N_i(m)$ ———— Eq. (13)

$V_r(m)/c \leftarrow N_R\, N_i(m)/\sigma$

$V_a(m)$ ———— Eq. (11): Euler's method (Ref. [9])

$U_1(m),\ V_1(m)$ ———— Eq. (4)

$\gamma(l,t)$ ———— Eq. (5)

$\Gamma_c(m)$ ———— Eq. (6)

$\psi_i(m)$ ———— Eq. (10)

$\phi_i(m) \leftarrow V_a(m)/V_r(m)$

NO — $D \leq \delta$ — YES

$D = |\Gamma_c(m)/\Gamma_c(m-1)| - 1$
δ: Small value

STOP

END
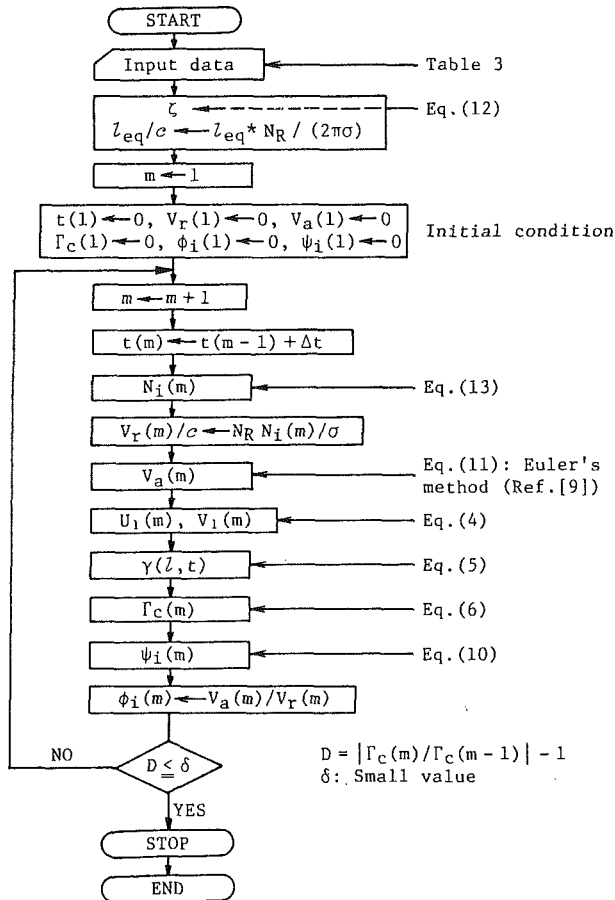
Fig. 9 Calculating procedure

which the coordinates of ϕ_i and ψ_i move during starting transient for Case 1 and 2. Time sequence as well as the point corresponding to nominal acceleration time T_{na} are written in these figures in the same manner as in Fig. 4. The measured steady-state characteristics curve and the calculated one by use of singularity method [11] are indicated by a dot-dash-line and a two-dot-dash-line, respectively.

Calculated total pressure rise coefficient ψ_i is here split into two parts, as shown in Fig. 10. One is the part contributed by the relative and absolute velocity difference between inlet and outlet of rotor, which is expressed by the first term in the right side of equation (10). This part of pressure rise cannot exceed quasi-steady value ψ_s but approaches ψ_s asymptotically. This is due to the fact that the circulation around airfoil cannot respond to the rapid change in the circumferential condition, i.e., the lag in the circulation formation.

The other is the part contributed by the impulsive pressure difference between inlet and outlet of rotor, which is expressed by the second term in the right side of equation (10). This part of pressure rise is remarkable in the first half of the starting period, but decreases with time and approaches zero asymptotically.

As seen clearly from these figures, the dynamic relationship between ϕ_i and ψ_i is determined by these two unsteady effects, i.e., the lag of circulation growth and the impulsive pressure difference. They have, however, an inverse tendency of deviation from a quasi-steady change.

At the very beginning of the start, stage A in Fig. 4(a), ψ_i is greater than ψ_s since the impulsive pressure difference is greater than the lag of circulation formation as seen clearly in these figures. Conversely, the lag of circulation formation plays a predominant role in stage C where ψ_i is smaller than ψ_s. In the calculated result for Case 1, stage C was not seen.
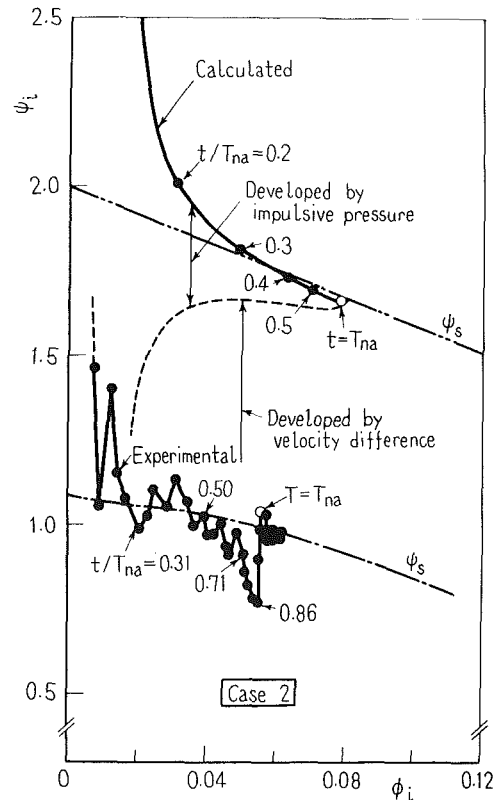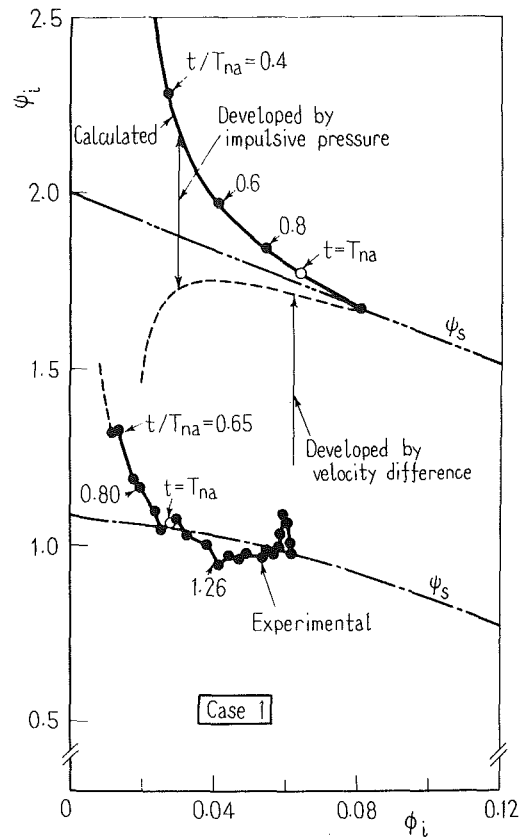
Fig. 10 Comparison between experimental and calculated dynamic characteristics curves during starting period. Experimental uncertainty: ϕ_i/ϕ_f ±5.5 percent, ψ_i/ψ_f ±5.5 percent (10:1 odds).

Fig. 11 Comparison between experimental and calculated time histories of ψ_i^* and ψ_i^* for Case 1. Experimental uncertainty: ψ_i^* ±5.5 percent, ψ_i^* ±5.5 percent (10:1 odds).

This is due to the overestimation of axial velocity which causes the overestimation of the impulsive pressure difference.

In the experimental results, another feature, i.e., stage D in Fig. 4(a), is found in the last half of acceleration. In this period, ψ_i becomes greater than ψ_s again. The primary reason seems to be the lag of boundary layer growth around the impeller vanes which is not considered in the present theory.

From the comparison between Fig. 10(a) and (b), it is also found that the effect of unsteadiness on the pump characteristics decreases with increased T_{na} so that the period on the quasi-steady characteristics curve becomes longer.

Figure 11 shows the time histories of $\phi_i^* = \phi_i/\phi_f$ and $\psi_i^* = \psi_i/\psi_f$ for Case 1. The calculated ϕ_i^* approaches the final value more quickly than the measured one, since the calculated pressure rise is greater than the measured one and this results leads to a faster acceleration of the water contained in the pipe line.

Since the analysis was conducted on the basis of inviscid flow, i.e. 100 percent efficiency, the quantitative agreement between theory and experiment is poor. However, the calculated results agree qualitatively with the measured ones and offer a basis of explaining transient characteristics during the starting period.

Conclusion

The performance of a centrifugal pump during the rapid acceleration of the rotational speed was studied experimentally and theoretically. When the pump is started quickly, the dynamic relationship between flow coefficient and total pressure rise coefficient does not always coincide with the one obtained for a steady-state operation.

The results of the numerical calculations were compared with the experiments and the following conclusions were found:

(1) At the very beginning of the start, the total pressure rise coefficient tends to become larger than the quasi-steady value. The impulsive pressure difference is the primary reason of this characteristics.

(2) There is the period in which the total pressure rise coefficient tends to be smaller than the quasi-steady value. This is due to the lag of circulation growth around the impeller vanes.

In addition to the above results, nondimensional parameter $N_f T_{na}$ was introduced as the parameter which is determinant for the transient characteristics of a pump during the starting period.

References

1 Knapp, R. T., "Complete Characteristics of Centrifugal Pumps and Their Use in the Prediction of Transient Behavior," ASME *Transactions*, Vol. 59, Nov. 1937, pp. 683–689.

2 Ohashi, H., "Analytical and Experimental Study of Dynamic Characteristics of Turbopumps," NASA TN D-4298, Apr. 1968.

3 Fang, K. S., "Axial Thrust in Vertical Turbine Pumps," *Agricultural Engineering*, Vol. 46, No. 3, Mar. 1965, pp. 140–143.

4 Miyashiro, H., and Takada, K., "Axial Hydraulic Thrust Caused by Pump Starting," ASME *Journal of Basic Engineering*, Vol. 94, No. 3, Sept. 1973, pp. 629–635.

5 Daigo, H., and Ohashi, H., "Experimental Study on Transient Characteristics of a Centrifugal Pump during Rapid Acceleration of Rotational Speed," *Proceedings of the Second International JSME Symposium, Fluid Machinery and Fluidics*, Tokyo, Vol. 2, Sept. 1972, pp. 175–182.

6 Anderson, D. A., Blade, R. J., and Stevans, W., "Response of a Radial-Bladed Centrifugal Pump to Sinusoidal Disturbances for Noncavitating Flow," NASA TN D-6556, Dec. 1971.

7 Whitehead, D. S., "Force and Moment Coefficient for Vibration Aerofoils in Cascade," Aeronautical Research Council, Report and Memoranda, No. 3254, Feb. 1960.

8 Milne-Thomson, L. M., *Theoretical Hydrodynamics*, 5th ed., Macmillan, 1968, p. 89.

9 Lambert, J. D., *Computational Methods in Ordinary Differential Equation*, Wiley, 1973, pp. 114–116.

10 Bisplinghoff, R. L., Ashley, H., and Halfman, R. L., *Aeroelasticity*, Addison-Wesley, 1955, pp. 281–283.

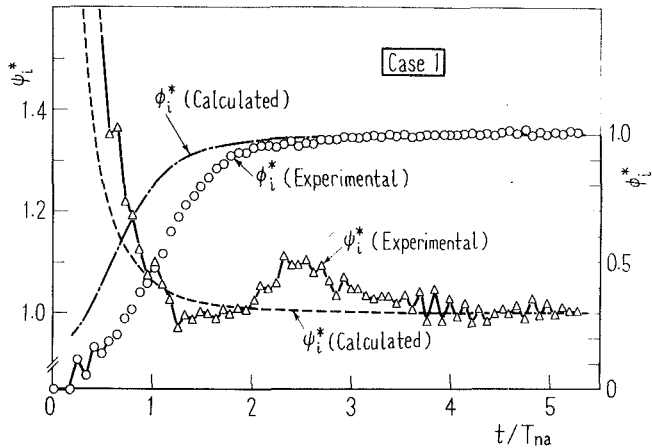11 Schlichting, H., "Durchführung der Rechnung für das Gitter," VDI-Forsch. -h. 447, 1955.

Fig. 11 Comparison between experimental and calculated time histories of $\psi_i{}^*$ and $\psi_i{}^*$ for Case 1. Experimental uncertainty: $\psi_i{}^* \pm 5.5$ percent, $\psi_i{}^* \pm 5.5$ percent (10:1 odds).

This is due to the overestimation of axial velocity which causes the overestimation of the impulsive pressure difference.

In the experimental results, another feature, i.e., stage D in Fig. 4(a), is found in the last half of acceleration. In this period, ψ_i becomes greater than ψ_s again. The primary reason seems to be the lag of boundary layer growth around the impeller vanes which is not considered in the present theory.

From the comparison between Fig. 10(a) and (b), it is also found that the effect of unsteadiness on the pump characteristics decreases with increased T_{na} so that the period on the quasi-steady characteristics curve becomes longer.

Figure 11 shows the time histories of $\phi_i{}^* = \phi_i/\phi_f$ and $\psi_i{}^* = \psi_i/\psi_f$ for Case 1. The calculated $\phi_i{}^*$ approaches the final value more quickly than the measured one, since the calculated pressure rise is greater than the measured one and this results leads to a faster acceleration of the water contained in the pipe line.

Since the analysis was conducted on the basis of inviscid flow, i.e. 100 percent efficiency, the quantitative agreement between theory and experiment is poor. However, the calculated results agree qualitatively with the measured ones and offer a basis of explaining transient characteristics during the starting period.

Conclusion

The performance of a centrifugal pump during the rapid

acceleration of the rotational speed was studied experimentally and theoretically. When the pump is started quickly, the dynamic relationship between flow coefficient and total pressure rise coefficient does not always coincide with the one obtained for a steady-state operation.

The results of the numerical calculations were compared with the experiments and the following conclusions were found:

(1) At the very beginning of the start, the total pressure rise coefficient tends to become larger than the quasi-steady value. The impulsive pressure difference is the primary reason of this characteristics.

(2) There is the period in which the total pressure rise coefficient tends to be smaller than the quasi-steady value. This is due to the lag of circulation growth around the impeller vanes.

In addition to the above results, nondimensional parameter $N_f T_{na}$ was introduced as the parameter which is determinant for the transient characteristics of a pump during the starting period.

References

1 Knapp, R. T., "Complete Characteristics of Centrifugal Pumps and Their Use in the Prediction of Transient Behavior," ASME *Transactions*, Vol. 59, Nov. 1937, pp. 683–689.

2 Ohashi, H., "Analytical and Experimental Study of Dynamic Characteristics of Turbopumps," NASA TN D-4298, Apr. 1968.

3 Fang, K. S., "Axial Thrust in Vertical Turbine Pumps," *Agricultural Engineering*, Vol. 46, No. 3, Mar. 1965, pp. 140–143.

4 Miyashiro, H., and Takada, K., "Axial Hydraulic Thrust Caused by Pump Starting," ASME *Journal of Basic Engineering*, Vol. 94, No. 3, Sept. 1973, pp. 629–635.

5 Daigo, H., and Ohashi, H., "Experimental Study on Transient Characteristics of a Centrifugal Pump during Rapid Acceleration of Rotational Speed," *Proceedings of the Second International JSME Symposium, Fluid Machinery and Fluidics*, Tokyo, Vol. 2, Sept. 1972, pp. 175–182.

6 Anderson, D. A., Blade, R. J., and Stevans, W., "Response of a Radial-Bladed Centrifugal Pump to Sinusoidal Disturbances for Noncavitating Flow," NASA TN D-6556, Dec. 1971.

7 Whitehead, D. S., "Force and Moment Coefficient for Vibration Aerofoils in Cascade," Aeronautical Research Council, Report and Memoranda, No. 3254, Feb. 1960.

8 Milne-Thomson, L. M., *Theoretical Hydrodynamics*, 5th ed., Macmillan, 1968, p. 89.

9 Lambert, J. D., *Computational Methods in Ordinary Differential Equation*, Wiley, 1973, pp. 114–116.

10 Bisplinghoff, R. L., Ashley, H., and Halfman, R. L., *Aeroelasticity*, Addison-Wesley, 1955, pp. 281–283.

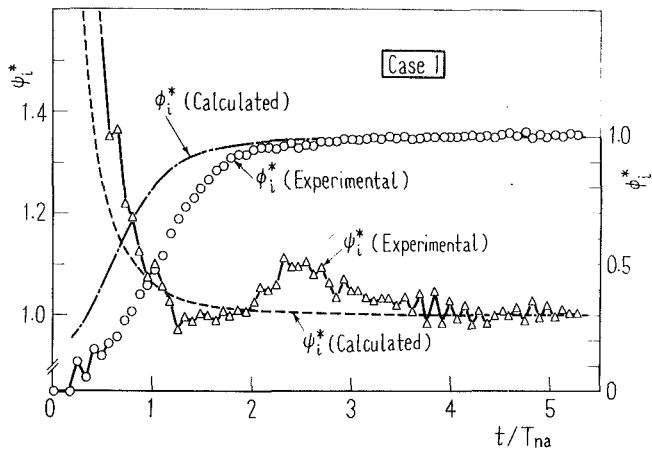11 Schlichting, H., "Durchführung der Rechnung für das Gitter," VDI-Forsch. -h. 447, 1955.

──── DISCUSSION ────

R. E. Henderson [1]

The authors are to be commended for addressing the very significant and practical problem of the transient operating characteristics of a centrifugal pump. The experimental approach to this problem and the measured transient operating characteristics which are presented will serve as a guide to other investigations concerned with this problem.

The major question raised by this paper is the application of an unsteady, two-dimensional linear cascade analysis to model the flow in a centrifugal pump rotor. The assumption that the unsteady flow can be represented by a mean stream surface is valid, as is the conformal transformation of this surface of a circular cascade into a linear cascade. This

[1] Associate Director, Garfield Thomas Water Tunnel; Professor of Mechanical Engineering, Applied Research Laboratory, State College, Pa. 16801.

transformation provides an equivalent axial-flow rotor. Once the linear has been obtained, the authors follow the usual linear cascade unsteady flow analysis based on an irrotational, thin airfoil model. In such an analysis, the inlet disturbance flow is assumed to be irrotational and the unsteady circulation generated on the blades and shed into the blade wakes are related in a manner (Kevin's theorem) which assures that the flow through the cascade remains irrotational.

The most fundamental difference between a centrifugal-flow and axial-flow rotor is the existence of vorticity in the relative flow in a centrifugal-flow rotor. This vorticity is generated because the radius of the stream surface changes through the rotor and makes the flow relative to the rotor rotational. It is this relative vorticity which results in the familiar slip-factor in centrifugal turbomachines.

The fundamental question is then the application of an

irrotational flow analysis to the solution of a rotational flow. While the approach used by the authors is valid for a stationary radial cascade, since no relative vorticity is generated, it is not valid for a rotation radial cascade.

Author's Closure

The authors express their gratitude to Prof. R. E. Henderson for his valuable discussion. They agree with Professor Henderson's comment that an irrotational relative flow is not valid for a rotating circular cascade.

The unsteady flow in a rotating circular cascade should be treated on a real physical plane itself without any transformation into a linear cascade, since the pressure calculated directly from the transformed flow field does not always agree with the pressure in a rotating circular cascade.

However, the unsteady flow analysis in a rotating circular cascade requires an impractical mathematical complexity as is well known. In order to avoid this complexity, therefore, the authors have partly applied the calculating method for a linear cascade into a rotating circular cascade.

The problem in this process lies in no consideration of the displacement flow which constructs a part of the irrotational absolute flow field after the conformal transformation of a rotating circular cascade into a linear cascade. The displacement flow affects on the velocity at outlet of rotor, and also the time rate of change in velocity potential of the displacement flow contributes to impulsive pressure. It is suspected that the above two effects introduce the errors in the analysis, though it is difficult to estimate them quantitatively. Therefore, the authors hope that the calculated results in the present study should be compared with the experimental ones considering the above approximation.

R. P. Dring

Manager, Gas Turbine Technology,
United Technologies Research Center,
East Hartford, Conn. 06108

Sizing Criteria for Laser Anemometry Particles

Introduction

It is the objective of this paper to provide the experimentalist using laser anemometry with some guidance in the form of a single dimensionless parameter describing the relationship between tracking particle size and measurement error due to particle lag. It has historically been necessary to examine a variety of particle sizes and densities in order to demonstrate that they are accurately tracking the flow. An extensive body of analytical and experimental studies of this kind are available in the literature [1, 2]. A very thorough and concise review of this matter is provided by Durst et al. [3]. In the present approach, however, the effects of particle size and density, fluid viscosity and density, and the characteristic length dimension of the flow under examination can all be accounted for in a single dimensionless parameter, the Stokes number [4]. In an effort to demonstrate the generality of this approach, solutions of the equation describing particle motion in a fluid are presented which will allow the experimentalist to estimate a priori what particle size is required to achieve a desired level of accuracy. Examples are provided in the form of several sample flow situations.

Discussion

A number of relatively unrestrictive assumptions are made to simplify the analysis. These are 1) that the particles are rigid spheres with a density much greater than that of the fluid; 2) that the effects of the virtual mass of the fluid and the Magnus force (due to particle spin) are negligible; 3) that in the local region of interest the fluid density is uniform; and 4) that there is no interaction between particles. These assumptions are discussed in greater detail in references [3, 5, 6, and 7]. As a result of these assumptions, the only external forces on the particle that are accounted for in the present analysis are the frictional and pressure drag. The added assumption of Stokes' theory for these drag forces is also made here. The assumption of Stokes drag is valid here since one is usually only interested in particles that follow the flow closely and hence have low relative particle Reynolds numbers and low relative particle Mach numbers. Since the Stokes' prediction for drag is less than actual drag, the estimates here are slightly conservative as to how small a particle must be to follow a particular flow accurately. Under these conditions the nondimensionalized vector equation of motion for a particle in a moving fluid is as follows (see [5]).

$$X'' = (U - X')/St \qquad (1)$$

Solutions of this equation are presented in the following for four sample flow situations: 1) two-dimensional flow over an

$$S_t = \left(\frac{\rho_p U_1 D_p^2}{18 \mu b} \right)$$
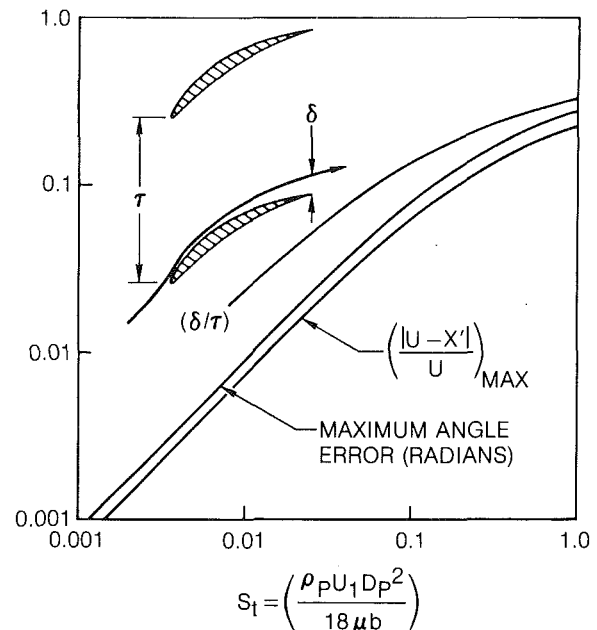
Fig. 1 Particle response to flow over a compressor cascade airfoil

axial compressor cascade airfoil, 2) a one-dimensional step (shock) deceleration, 3) a one-dimensional exponential acceleration, and (4) a sinusoidal oscillation.

As in reference [5], the fluid flow over the compressor cascade airfoil is based on the analysis of Caspar et al., [8]. The cascade has a pitch to chord ratio of 1.0 and 25 deg of turning. The order of equation (1) effectively changes from two to one as the Stokes number becomes small. For this reason the Runge-Kutta integrator of reference [5] becomes unstable for small Stokes number. This difficulty is eliminated in the present work by using an implicit integrator based on successive substitution. The results of the integration of equation (1) are shown in Fig. 1. The maximum local speed error ($|U - X'| U$), the maximum local angle error and the region swept clean by particles hitting the airfoil (δ/τ) are shown as functions of the Stokes number based on the upstream fluid velocity (U_1) and the airfoil axial chord (b). At a Stokes number of 0.1 the maximum speed error is 6 percent, the maximum angle error is 4.6 deg, and 14 percent of the airfoil pitch is swept clean of particles at the trailing edge plane. At a Stokes number of 0.01 these numbers drop to 0.7 percent, 0.5 deg, and 2.3 percent, respectively. Similar calculations were carried out for a turbine inlet guide vane and they have been presented in reference [5]. It was concluded there also that for accurate particle tracking the Stokes
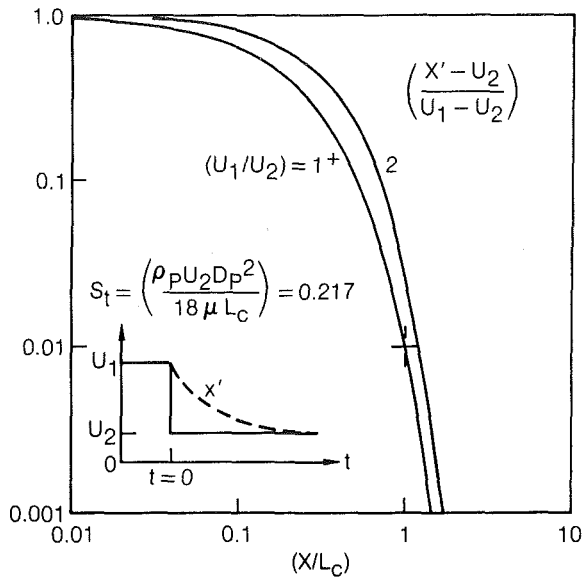
Fig. 2 Particle response to a step deceleration

Fig. 3 Particle response to an exponential acceleration
$U = U_1 + (U_2 - U_1) \cdot (1 - exp(-t/T_c))$

number must be less than 0.01. It was also pointed out in reference [5] that compressibility effects (density variations) do not significantly alter these results.

For a flow of air (at standard conditions) at an upstream velocity (U_1) of 300 m/s over a cascade airfoil with a 3 cm axial chord (b) and particles such as oil (with a specific gravity near 1) a Stokes number of 0.01 requires a particle diameter of 0.6 μm.

The case of a step deceleration is similar to the flow downstream of a normal shock. There is no natural length scale so the characteristic dimension (L_c) is chosen as the distance required to obtain 99 percent recovery for the case of a small deceleration, $(U_1/U_2) = 1^+$. The Stokes number based on this distance and U_2 is 0.217. From this one can calculate the 99 percent recovery distance as a function of particle size. Figure 2 illustrates the speed recovery as a function of distance (X/L_c) and fluid velocity ratio (U_1/U_2). Note that the recovery distance increases with velocity ratio. For a velocity ratio of 2 the 99 percent recovery distance is 22 percent greater than for a velocity ratio of 1^+.

For a flow of air at a velocity (U_2) of 300 m/s, particles having a specific gravity of 1, and a desired 99 percent recovery distance of 1 mm, a particle diameter of 0.5 μm is required for a (U_1/U_2) of 1^+.

The solution for an exponential acceleration from U_1 to U_2 is shown in Fig. 3. The Stokes number for this case is based on the exponential rise time (T_c). The maximum speed error (as a fraction of $U_2 - U_1$) is independent of the velocity ratio (U_1/U_2). The location at which this maximum occurs (X_m), however, does depend of the velocity ratio. For small Stokes numbers (<0.01) the maximum speed error is equal to the Stokes number, and the dimensionless location at which it occurs is equal to St $ln(1/St)$.

An accelerating air flow with a rise time of 1 ms and par-
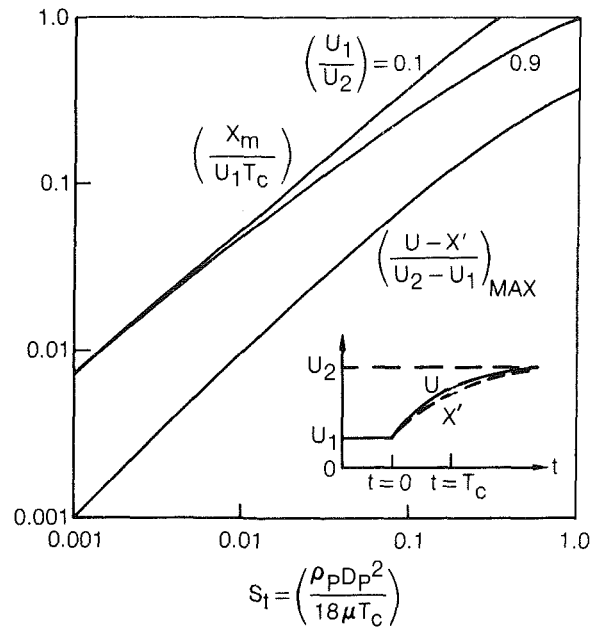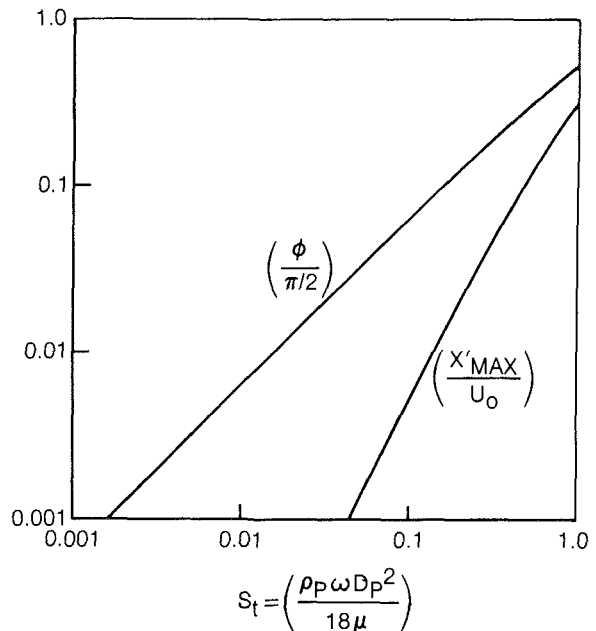
Fig. 4 Particle response to a sinusoidal oscillation $U = U_o \sin \omega t$

ticles with a specific gravity of 1 requires particle diameters less than 1.8 μm in order to have a maximum speed error less than 1 percent (or St = 0.01).

Finally, the solution for a sinusoidally oscillating flow is shown in Fig. 4 in terms of particle motion amplitude and phase lag (ϕ) as a function of Stokes number based on the

---

Nomenclature

b = airfoil axial chord
D_p = particle diameter
L_c = characteristic length dimension
St = Stokes number, $(\rho U_c D_p^2)/(18\mu L_c)$
t = time
T_c = characteristic time

U = fluid velocity vector
U_c = characteristic speed
U_o = fluid oscillation speed amplitude
X = particle position vector
X' = particle velocity vector
X'' = particle acceleration vector

δ = defined in Fig. 1
ρ = particle density
τ = compressor airfoil cascade pitch
ω = angular speed
ϕ = particle phase lag
μ = absolute viscosity

angular velocity of the oscillation (ω, as in reference [6]). For a Stokes number of 0.14 the particle speed amplitude is 1 percent less than that of the fluid and it has a phase lag of 8 deg. This solution is an extension of that of reference [6].

For an air flow and particles having a specific gravity of 1, the particle size must be less than 0.9 μm to follow a 10 kHz oscillation with 1 percent speed accuracy (St = 0.14).

The underlying assumption in this analysis has been that of Stokes drag. As a check on the accuracy of this assumption for any particular solution the following procedure is recommended: 1) Assume Stokes drag is valid. 2) Perform the particle motion calculation to determine the maximum velocity lag encountered by the particles. 3) Using this maximum lag, check the validity of the Stokes drag assumptions.

Summary

It has been demonstrated in the foregoing pages that fully nondimensional solutions can be obtained describing the trajectories of laser anemometry particles and that these solutions depend on a single dimensionless parameter, the Stokes number. Four sample solutions have been presented to demonstrate this dependence. A similar solution for the case of particles in a free-vortex swirling flow is already available in reference [9]. Comparisons between measured particle trajectories and trajectories computed using this approach are presented in reference [5]. It was intended that these parametric solutions would give guidance in determining the particle size required to provide the desired level of accuracy

in various laser anemometry applications. These solutions and others can, through the Stokes number, be applied to flows of arbitrary length dimension, velocity, particle or fluid density, and viscosity.

Although the approximations employed in the analysis may not be entirely adequate from the point of view of accurately determining particle size under all flow situations, they should be quite adequate for the present application, that is, in determining laser anemometry measurement error as a function of tracking particle size.

References

1 *Proceedings of the First International Workshop on Laser Velocimetry*, 1972.

2 *Proceedings of the Second International Workshop on Laser Velocimetry*, 1974.

3 Durst, F., Melling, A., and Whitelaw, J. H., *Principles and Practice of Laser Doppler Anemometry*, Academic Press, 1976 (Chapter 10).

4 Duckworth, R. A., "A Review of Research in the United Kingdom in the Field of Multiple Flows of Solids and Gases," *Flow of Solid Particles in Gases*, AGARD-AG-222, Oct. 1976, pp. 33-45.

5 Dring, R. P., Caspar, J. R., and Suo, M., "Particle Trajectories in Turbine Cascades," *AIAA Journal of Energy*, Vol. 3, No. 3, May-June 1979, pp. 161-166.

6 Melling, A., and Whitelaw, J. H., "Seeding of Gas Flows for Laser Anemometry," *DISA Information*, No. 15, Oct. 1973, pp. 5-14.

7 Haertig, J., "Introductory Lecture on Particle Behavior," *Proceedings of the ISL/AGARD Workshop on Laser Anemometry*, May 5-7, 1976.

8 Caspar, J. R., Hobbs, D. E., and Davis, R. L., "Calculation of Two-Dimensional Potential Cascade Flow Using Finite Area Methods," *AIAA Journal*, Vol. 18, No. 1, Jan. 1980, pp. 103-109.

9 Dring, R. P., and Suo, M., "Particle Trajectories in Swirling Flows," *AIAA Journal of Energy*, Vol. 2, No. 4, July-Aug. 1978, pp. 232-237.

F. Bario

Société METRAFLU,
69130 Ecully, France

G. Charnay

K. D. Papailiou

Laboratoire de Mécanique des Fluides,
69130 Ecully, France

An Experiment Concerning the Confluence of a Wake and a Boundary Layer

Measurements have been performed at low speed in the confluent region of a two dimensional wake and turbulent boundary layer. A tandem symmetrical arrangement was used, placed in a variable pressure gradient wind tunnel. Pressure and turbulent quantities were measured and current semi-empirical laws were examined in the light of the experimental results.

Introduction

High-lift devices play a significant role in aircraft engineering. Slotted flaps and leading edge slats are now present in most aircraft. In the turbomachinery field, tandem or slotted blades are also used in some special applications. Calculation and design of such devices are based mainly on inviscid calculations (see for instance the bibliography of [1]). Viscous considerations have been made either on the basis of simple boundary layer calculations or tests results. In many devices, however, interactions between wakes and boundary layers are frequent and sometimes optimum configurations are obtained with a strong interaction [1]. Hence, it is necessary to use viscous flow calculation methods which take into account the interaction between two viscous layers and more particularly between a wake and a boundary layer. Such theoretical prediction methods have made their appearance recently. The interaction approach of Bradshaw [2], successfully used for duct flows, has been developed by Morel and Torda [3] to free flows with velocity extremum (jets and wakes). Perrier et al. [4] used Jeandel and Mathieu's [5] development based on the Nee-Kovasznay's hypothesis for the calculation of wake and boundary layer interactions. The calculations compare favorably with experimental results. Integral methods have been also used by Stevens, Goradia, and Braden [6] for multi-component airfoils viscous flow calculations. Again, these calculations compare favorably with experimental results.

The experimental results available to validate theoretical predictions are scarce in this domain and they mainly concern the mean velocity field. Bradshaw and Gee [7] made measurements in turbulent wall jets on a blown flap in an adverse pressure gradient. Monnerie and Lovat [8] made an experimental study of boundary layer control by blowing at the knee of a flap. They measured the mean velocity field and the Reynolds stresses in the jet-boundary layer mixing zone. Railly et al. [9] measured the mean velocity field around a tandem airfoil cascade. Ljungström [10] measured the mean

velocity field on the suction side of a three component wing (slat and flap) for different incidence angles and wing configurations. Moore [11] studied experimentally the development of the interaction between the wake of a cylinder and a boundary layer developing on a flat plate in an adverse pressure gradient. Loudet [1] gave experimental results about the influence of the incidence angle on the viscous interaction in a tandem cascade configuration (mean velocity measurements).

The interaction region investigated here is that resulting from the wake created by a symmetrical airfoil and the boundary layer developing on the surface of a trailing, longitudinally displaced airfoil. The arrangement is placed in the variable wall-geometry tunnel of our laboratory. Thus the interaction develops under a positive pressure gradient which results in the boundary layer separation near the trailing edge of the second airfoil.

It was the intention of the present work to provide experimental results in the confluent region of a wake and a boundary layer in order to investigate the turbulence behavior in this region and at the same time to provide experimental support for the corresponding calculation methods.

With the recommendations of reference [1], the choice of the relative position of the two airfoils has been made so that the interaction gives a favorable effect on the boundary layer of the second airfoil. A visualization without the first airfoil has proved the importance of this airfoil on the behavior of the boundary layer on the suction side of the second airfoil, the separation point moving forward when the first airfoil was removed. This improved performance is of secondary importance in the design of the present experiment; the primary motivation is to document, and to better understand, the interaction of turbulent shear flows.

Description of the Experimental Apparatus

The low speed variable pressure-gradient wind tunnel of our laboratory possesses at the inlet dust filters and screens. The test section is 1.8 m wide and 2.5 m long. It has a flat upper wall and a variable shape porous lower wall. The
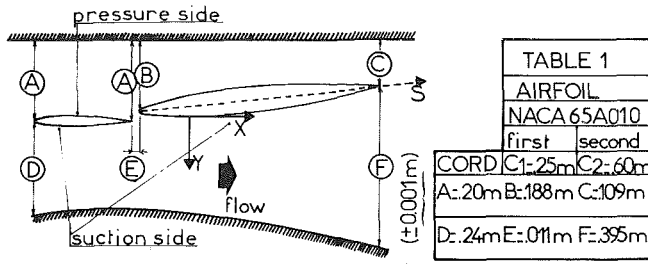
Fig. 1 Tandem airfoil arrangement

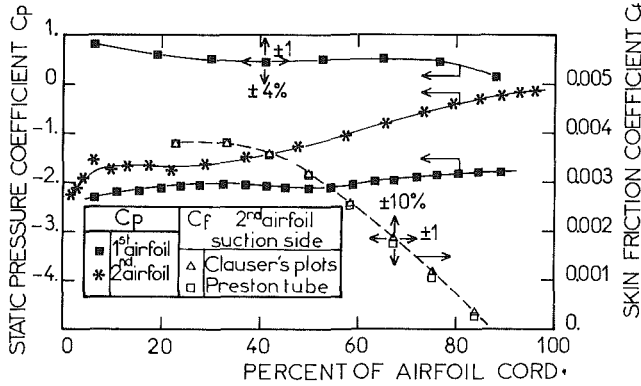**Fig. 2 Wall static pressure and skin friction coefficients**

principal blower delivers up to 18 m³/s which corresponds a speed of about 30 m/s in the throat of the test section. Suction is applied in all four walls before, in, and after the test section to prevent wall boundary layer separation. The blower used for boundary layer suction delivers 4 m³/s at 16,000 N/m².

The tandem airfoil arrangement used in this experiment is presented in Fig. 1. The principal dimensions are given in Table 1. Two NACA 65 A 010 symmetrical airfoils were used. They were fixed with jacks and piano-wires on the upper wall. The second airfoil was placed at a 7 deg incidence with respect to the oncoming stream. The lower wall was shaped in such a way that the longitudinal pressure distribution imposed on the second airfoil led to boundary layer separation very close to its trailing edge. Two-dimensional flow has been achieved

using test section walls boundary layer suction, the large width of the wind tunnel being a favorable factor.

The wall static pressure on the airfoil surface was measured by static pressure taps; these data are presented in Fig. 2. The total and static pressure distributions were measured by a special probe which was made in such a way that the static pressure holes were located in the same plane as the total pressure one. Consequently, no correction for hole position was necessary. The skin friction coefficient was measured by a Preston tube of a .002 m diameter.

The turbulent quantities were measured by means of DISA 55 P 51 x wire probe connected to two DISA 55 M01 anemometers. Analog signal processing was performed. The mean velocity, normal and shear stresses, third and fourth moments of the normal velocity fluctuation component were simultaneously measured. The measurements were taken at the stations registered in Table 2. They were realized in a direction perpendicular to the airfoil wall.

Presentation of the Experimental Results

Two-dimensional flow was achieved by boundary layer suction. Smoke and lamp-black visualizations helped the suction adjustment. Mean velocity distributions measured at different lateral positions and near the trailing edge of the second airfoil showed that the mean longitudinal velocity profile in the boundary layer, in the wake, and in the outer flow remained unchanged for a lateral distance between 0.60 m and 1.20 m measured from the side wall. Outside of this interval, the flow is affected by the presence of the first airfoil supports and by the lateral wall boundary layers. Good two-dimensionality is indicated by the momentum balance applied to the boundary layer up to the station $S/C_2 = 0.83$. The following analysis adapted from [12], is presented to establish the integral equation which will be used to evaluate the two-dimensionality of the flow field. The momentum equation integrated from $y = 0$ to $y = \delta$ is

$$\frac{\tau_w}{\rho} + \frac{1}{\rho} \int_0^\delta \frac{d\Delta P_{t\delta}}{dx} dy = \frac{d}{dx}(U_\delta^2 \delta_2) + U_\delta \delta_1 \frac{dU_\delta}{dx} \qquad (1)$$

where $\Delta P_{t\delta}$ is the difference between the free stream stagnation pressure P_{to} and the stagnation pressure at $y = \delta$, $P_{t\delta}$. Note that the $d(\Delta P_t \delta)/dx$ term is introduced in response to the decrease in the stagnation pressure along the line of the

——— Nomenclature ———

C_f = wall friction coefficient
C_P = pressure coefficient
C_2 = cord of the second airfoil
H_{12} = form factor δ_1/δ_2
P_{st} = static pressure
P_{st1} = static pressure at the leading edge of the first airfoil
P_{to} = free stream total pressure
Q_1 = dynamic pressure at the leading edge of the first airfoil
S = location of the measurement stations on the cord of the second airfoil
U = mean velocity
U_c = Velocity deficit; $U_\delta - U_m$ for the inner half wake; $U_o - U_m$ for the outer half wake
U_m = minimum velocity in the wake

U_o = free stream velocity (outside of the wake)
U_{out} = velocity at the edge of the half wake: U_δ or U_o
U_δ = velocity at the edge of the wall layer
U_T = friction velocity
u = instantaneous velocity fluctuation in the longitudinal direction (x)
v = instantaneous velocity fluctuation in the transversal direction (y)
x or X = direction parallel to the airfoil wall
y or Y = direction perpendicular to the airfoil wall or the distance from the wall

δ = wall layer thickness
δ_1 = wall layer displacement thickness
$\delta_1 = \int_0^\delta (1 - U/U_\delta) dy$
δ_2 = wall layer momentum thickness
$\delta_2 = \int_0^\delta (1 - U/U_\delta) U/U_\delta dy$
$\Delta P_{t\delta}$ = difference between the free stream total pressure and the total pressure at $y = \delta$
ν = kinematic viscosity
ρ = density
τ_w = wall shear stress

Superscripts

$(\bar{\ })$ = average
$(\hat{\ })$ = $[(\ )^2]^{1/2}$

Table 2

S/C$_2$(±0.01)	0.12	0.24	0.33	0.42	0.50	0.58	0.67	0.75	0.83	0.92	1.00
LHS		0	0.226	0.401	0.548	0.656	0.726	0.767	0.786		
RHS		0	0.236	0.415	0.512	0.665	0.855	1.050	1.026		
S (10³m ±5%)	3	5.5	7	8	8.5	11	13	17	24	31	48.5
YUm	20.5	22.	23.	24.	26.5	30.	33.5	38.	46.	54.	64.
1-Um/Uo (±0.004)	0.182	0.139	0.118	0.109	0.118	0.120	0.135	0.155	0.155	0.153	0.159
1-Um/Uδ	0.199	0.142	0.134	0.129	0.127	0.119	0.119	0.120	0.095	0.081	0.043

merged boundary layers between the two airfoils and is a result of the integration of the pressure term of the momentum equation if we consider the following expression.

$$\frac{dP_{st}}{dx} = \frac{dP_{st\delta}}{dx} = \frac{dP_{t\delta}}{dx} - \rho U_\delta \frac{dU_\delta}{dx}$$

$$= \frac{d(P_{to} - \Delta P_{t\delta})}{dx} - \rho U_\delta \frac{dU_\delta}{dx} = - \frac{d(\Delta P_{t\delta})}{dx} - \rho U_\delta \frac{dU_\delta}{dx}$$

As in [12] this equation is normalized and integrated with respect to S from $S_o/C_2 = 0.24$ to $S/C_2 = 0.83$.

$$\int_{S_o}^{S}\left(\frac{U_T}{U_\delta}\right)^2 d\left(\frac{S}{\delta_{2So}}\right) = \frac{U_\delta^2 \delta_2}{(U_\delta^2 \delta_2)_{So}} - 1 + \frac{1}{2}\int_{S_o}^{S}\frac{\delta_1}{\delta_{2So}} d\left(\frac{U_\delta^2}{U_{\delta o}^2}\right)$$

$$- \int_{S_o}^{S}\frac{\delta}{\rho(U_\delta^2\delta_2)_{So}}\left(\int_{o}^{S(S)}\frac{d\Delta P_{t\delta}}{ds} dy\right) ds \qquad (2)$$

The left and right-hand sides of this equation (LHS and RHS) are presented in Table 2. Particularly good agreement is obtained before mixing starts ($S/C_2 = 0.50$); a maximum difference of 25 percent between LHS and RHS is obtained at the station prior to the separation of the boundary layer. This difference is of the same order of magnitude of those presented in reference [12] for a set of boundary layer experiments. This seems to confirm that the flow is satisfactorily two-dimensional.

The wall static pressure distribution on the second airfoil is presented in Fig. 2 in the form of a static pressure coefficient defined as

$$C_P(S) = (P_{st}(S) - P_{stl})/Q_1 \qquad (3)$$

where P_{st} is the local static pressure, and P_{stl}, Q_1 are the static and dynamic pressures upstream of the leading edge of the first airfoil.

The first airfoil is subjected to a negligible pressure gradient (Fig. 2). The velocity peak on the suction side of the second airfoil is very near to the leading edge. Downstream of this peak, the flow is strongly decelerated up to $S/C_2 = 0.10$. Then, there is a region of nearly constant pressure (up to about $S/C_2 \simeq 0.3$) followed by a zone in which the pressure coefficient increases up to the trailing edge.

The evolution of the mean velocity field (presented in Fig. 3) shows that, initially, the two viscous layers are apart, separated by a constant velocity region up to $S/C_2 = 0.50$. Downstream of this point, the disappearance of the constant velocity region indicates that mixing of the two shear layers is taking place. The velocity distributions $U_o(S)$ (outside of the two viscous layers) and $U_\delta(S)$ (at the edge of the boundary layer) are presented in Fig. 4. In the mixing region, the work of the shearing stresses results in a decrease of the total pressure. The magnitude of this decrease may be taken to characterize the importance of the mixing of the two layers. This is presented in Fig. 4. The evolution of the wake mean velocity-field is given in Fig. 3. The relative depth of the external half wake, $1 - U_m/U_o$ (U_m being the minimum velocity in the wake) is decreasing up to the point $S/C_2 = 0.42$ and increasing thereafter and up to the station $S/C_2 = 0.75$ (Table 2). This behavior is associated with the
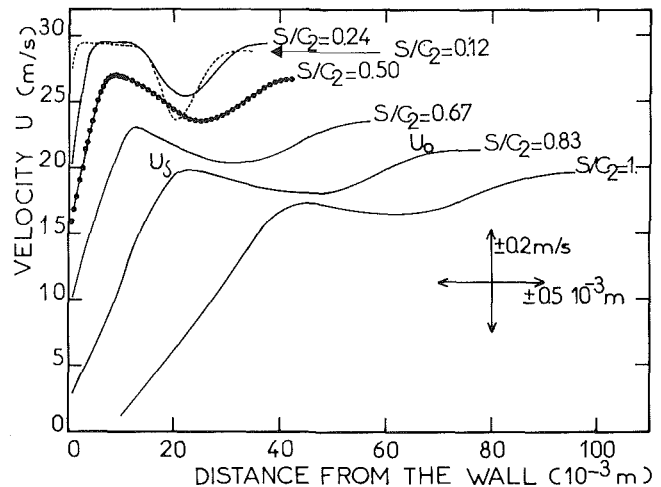
Fig. 3 The mean velocity field. (Note: Experimental points are shown only for one velocity profile. Scatter and density were the same for all the other velocity distributions.)
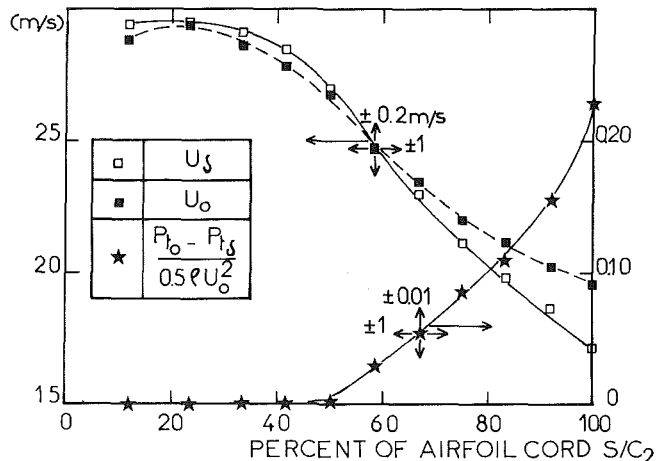
Fig. 4 Evolutions of the mean velocities at the edge of the boundary layer and outside of the wake

imposed external pressure distribution [13]. Flow separation appears near the trailing edge of the second airfoil. The separation line, as indicated by flow visualization, is located at the position $S/C_2 = 0.88$ and is laterally quite straight. After the trailing edge of the second airfoil, the first airfoil wake is still visible although nearly absorbed by the wake of the second airfoil.

The skin friction coefficients deduced from the Clauser's method and measured with a Preston tube are presented in Fig. 2.

The velocity fluctuations $\tilde{u}$ and $\tilde{v}$, presented in Fig. 5(a) and Fig. 5(b), have similar evolution. $\tilde{u}$ is always greater than $\tilde{v}$ as it is observed in isolated wake and boundary layer measurements. In the wake, the center of the kinetic energy producton is more clearly distinguishable for the u fluctuation component than for the v one. For instance, the longitudinal

Fig. 5 a)The velocity fluctuation $\tilde{u}$; b) the velocity fluctuation $\tilde{v}$

Fig. 6   The correlation factor $R_{uv} = \overline{uv}/\tilde{u}\tilde{v}$

Fig. 7   The law of the wall

velocity fluctuation $\tilde{u}$ distribution presents two distinct maxima, which is not the case for the normal velocity fluctuation $\tilde{v}$. This fact is consistent with the concept that the energy transfer is taking place from the mean velocity field to the longitudinal fluctuation u and that it is redistributed through the pressure field in the normal and transverse directions. The magnitude of the fluctuations in the region between the wake and the boundary layer is of the same order of that of the external flow at the first measuring station. After this station, this magnitude increases comparatively in the region between the boundary layer and the wake, probably because of the simultaneous contribution of the wake and the boundary layer.

The velocity scale, $U_c = U_{out} - U_m$ (where U_{out} is the velocity outside the half-wake, (U_o or U_δ) and U_m is the mimimum velocity of the wake) is introduced in the presentation of the wake measurements. The evolution in the longitudinal direction of the maximum value of the quantity $\tilde{u}/U_c$ is increasing with decreasing U_c/U_o up to the station $S/C_2 = 0.50$ (see Figs. 3 and 5) as it is generally observed [15, 16] in wakes with positive or zero pressure gradient. The inner half wake presents a different evolution because of the interaction with the boundary layer which introduces a strong decrease of the deficit velocity $U_\delta - U_m$.

The shear stress evolution is presented in Fig. 6 in the form of the correlation factor $\overline{uv}/\tilde{u}\tilde{v}$.

Discussion of the Results – The Mean Velocity Field

Introductory Remark: Uncertainty Estimates Considerations. The uncertainties of length, velocity or pressure measurements are estimated easily with the use of instruments specifications. These are: $\pm$ .0005 m $\pm$ .005 m for y and S measurements respectively, $\pm$ 0.2 m/s for velocity measurements and 1 percent (relative value) of the local value for the pressure measurements. The determinations of skin friction coefficient, normal stresses, and shear stress uncertainty estimates are more difficult. Considering the skin friction coefficient measurement techniques, a generally accepted ten percent error has been used. It is difficult to estimate the systematic uncertainties of $\tilde{u}$, $\tilde{v}$, $\overline{uv}$ measurements because of the complex process of calibration of the X-wire probe. Nevertheless, we think that the uncertainty estimates noted on the figures give a good idea of the measurement error. The relative uncertainty estimates are given in percentage of the local value and are noted with the symbol % on the uncertainty band of the figures.
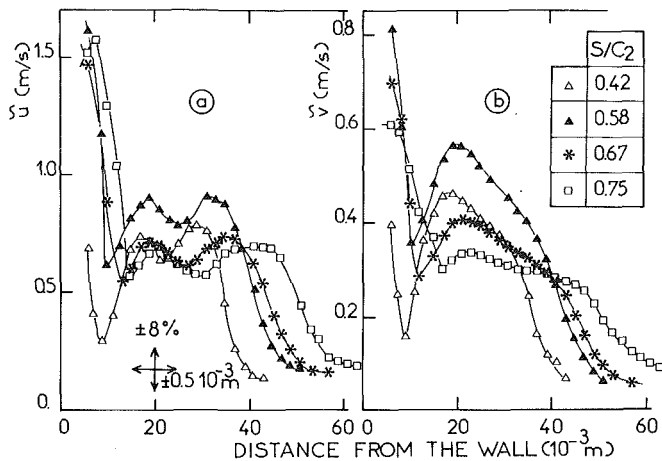
The measured velocity profiles were plotted in the usual semi-logarithmic form. It was found that a semi-logarithmic region existed up to the station prior to separation. Typical
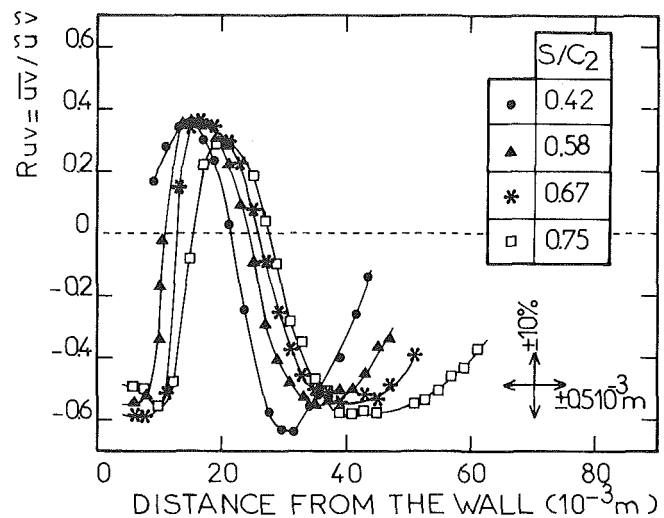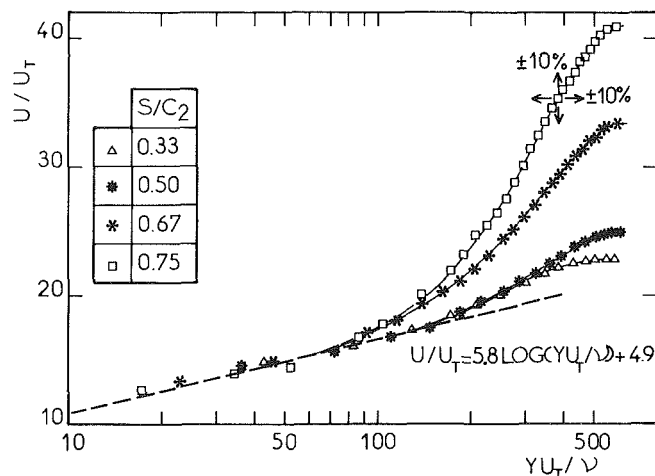
velocity profiles are presented in Fig. 7. A value for the skin friction coefficient was calculated from Clauser's plots, using the velocity U_δ, outside the boundary layer as defined previously. The skin friction coefficient calculated in this way is presented in Fig. 2, along with the one coming from the Preston tube measurements. Agreement of the two values is observed even inside the mixing region. The skin friction coefficient goes to zero (extrapolated value) at the station where separation was visualized.

We would like to draw attention concerning the conditions at the stations prior to the mixing. It seems that at these stations, transition from laminar to turbulent flow is not completed. In fact the skin friction coefficient value calculated by means of the usual Ludwieg and Tillman correlation

$$C_f = 0.246 \ 10^{-0.678} \ H_{12}(U_\delta\delta_2/\nu)^{-0.268}$$

is lower than the measured value. Some preliminary theoretical calculations confirmed this fact. Theoretical considerations based on reference [17] show, however, that we are not very far from fully turbulent flow. The wall shear stress measured with the Preston tube is calculated from the relation developed in [14]. This relation uses the hypothesis of a universal log-law in the wall region of the boundary layer.

However, the major and significant point is that two independent methods (Preston-tube and Clauser's plot) yield the same values for the wall shear stress. It is obvious, from the Clauser's plot method, that a logarithmic region exists in the wall region of the shear layer (the experimental points
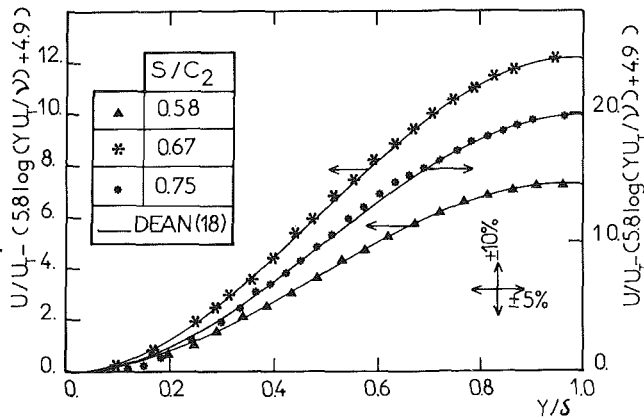
Fig. 8 The law of the wake
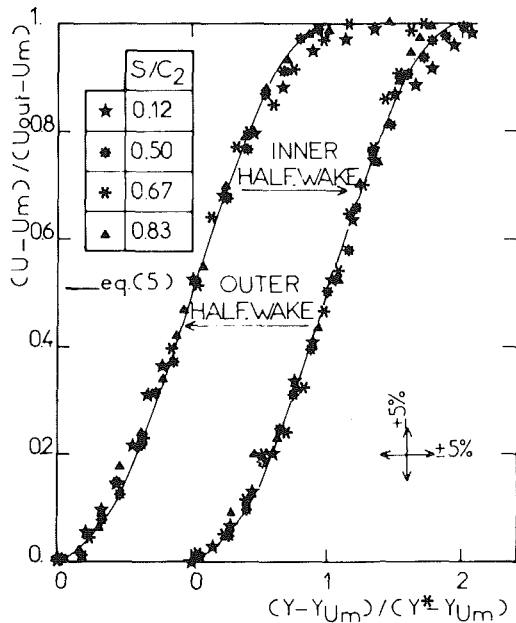
Fig. 9 The velocity distribution of the wake
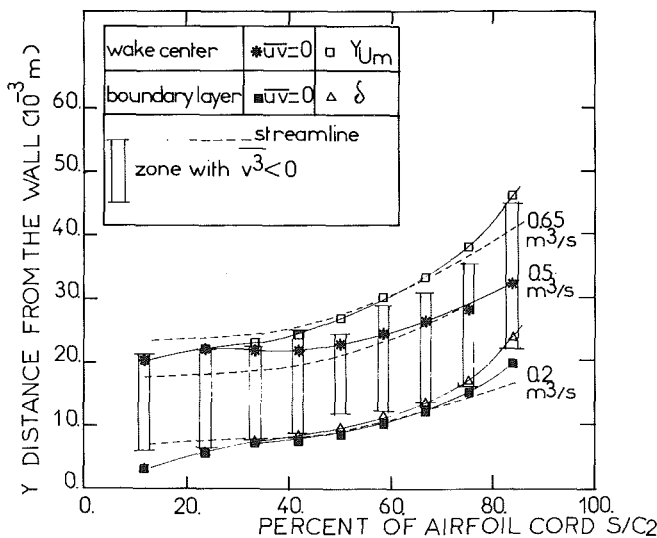
Fig. 10 The loci of zero shear $\overline{uv}$ and zero velocity gradient $\delta U/\delta y$ for the boundary layer and wake

correct and second, that a log-law region exists near the wall, indicating the turbulent behavior of the boundary layer.

The law of the wake as given by Dean [18] was used to represent the outer region of the boundary layer and some results are presented in Fig. 8. It can be seen that the law of the wake is well satisfied in all stations inside the mixing region.

Having successfully represented the boundary layer region by means of the usual velocity profile representation, the same procedure was attempted with the wake. It was evident that the two half-wakes should be represented separately. The analytical form of the representation was the usual one, viz.

$$(U - U_m)/(U_{out} - U_m) = F\,[(y - y_{U_m})/(y^* - y_{U_m})] \qquad (4)$$

where y_{U_m} is the ordinate of the point of the minimum velocity of the wake.

y^* is the ordinate of the point of velocity 0.5 $(U_m + U_{out})$.
The corresponding velocity profiles are presented in Fig. 9 and as it can be seen, it is possible to use a single algebraic formula such as

$$(U - U_m)/(U_{out} - U_m)$$
$$= (1 - \cos\left(\frac{\pi}{2}\,(y - y_{U_m})/(y^* - y_{U_m})\right))/2 \qquad (5)$$

to describe the velocity profiles with relatively good accuracy.

Discussion of the Results – The Fluctuation Velocity Field

Figure 10 presents the locus of zero velocity gradient $\delta U/\delta y$ as well as the locus of zero shear stress in the boundary layer and in the wake. As have already been reported for wall jets by Bradshaw [7] and Mathieu [19], and by Kacker and Whitelaw [20] for a wall wake, the position of zero shear stress $\overline{uv}$ does not coincide with the one where $\delta U/\delta y$ is zero. In this respect, Mathieu, in 1971 [19], pointed out the physical unreality of hypotheses such as those of Boussinesq and Prandtl. He also suggested that this phenomenon could be due to the memory of the turbulent structures and to the effects of the transport phenomena. For Beguier [22], the role of "big turbulent structures" is predominant. In fact, it is not possible to speak of a memory effect for "small turbulent structures" which are rapidly suppressed by viscosity.

We have drawn the streamlines in Fig. 10. The importance of the advection process on the difference existing in the location of the zero shear stress and the zero velocity gradient can be qualitatively explained.

Considering that structures are transported on the average along streamlines, we can remark that for the 0.65 m^3/s streamline, such a structure travels successively in a region in which the mean velocity gradient is positive (outer half wake) and in a region in which the mean velocity gradient is negative (inner half wake). Because of the memory effect, such a structure conserves its identity for a certain distance after it penetrates in the region of the inner half wake, transporting with it the turbulent properties generated in the region of the outer wake. Consequently, in a limited region of the inner half wake and in spite of the negative velocity gradient the total shear stress $\overline{uv}$ remains negative.

We can also consider the transverse transport of a turbulent eddy by the fluctuation kinematic velocity field (also called diffusional transport [21]). The transport of the kinetic energy and the transport of the shear stress $\overline{uv}$ are generally assumed in the same direction; for instance, a positive energy flux $\overline{vu^2}$ which implies a transport in the positive direction v_+ of a turbulent eddy could be associated with a negative shear stress-flux $\overline{uv^2}$ is the shear stress transported $\overline{uv}$ is negative, or with a positive $\overline{uv^2}$ if the shear stress $\overline{uv}$ is positive. In the region between the point of zero shear stress $\overline{uv}$ and the point

being located on a straight line in a U/U_δ versus log $(Y U_\delta/\nu)$ plot). Figure 7 shows the log-law, the wall shear stress used, being that obtained from the Clauser's plot method. So, it seems, first, that the measurements with the Preston tube are

of the minimum velocity, the negative quantity $\overline{v^3}$ implies a transport towards the wall. So a turbulent eddy with negative $\overline{uv}$, convected by the mean velocity field in the inner half wake could be convected by the fluctuation velocity field towards the wall. The evolution of the correlation factor $R_{uv} = \overline{uv} / \tilde{u} \, \tilde{v}$ is presented in Fig. 6. The maximum of $|R_{uv}|$ is 0.60 in the wall region and in the outer half wake. This value is greater than the usual value of 0.45 obtained in fully developed turbulent flows in wind tunnels. Comparison between several such results ([16-20]) obtained in wind tunnels seems to suggest that the maximum value of the correlation is affected by the value of the Reynolds number and that $|R_{uv}|$ may reach values of 0.7 in low Reynolds number flows. The maximum value of $|R_{uv}|$ decreases with increasing Reynolds number down to 0.30 (atmospheric boundary layers). In our experiment, the Reynolds number calculated on the airfoil cord was 1,200,000; this is a relatively low Reynolds number. The high value of the maximum of $|R_{uv}|$ is also in accordance with the suggestion of the presence of turbulent "big structures." Relatively well ordered "big structures" can give higher contributions at this maximum value.

Concluding Remarks

An experiment has been presented in this paper of a strong viscous interaction between a wake produced by a symmetrical airfoil and a turbulent boundary layer. The interaction took place in an adverse pressure gradient leading the boundary layer up to separation.

In view of the scarceness of experimental results of this type, much care was taken to ensure two-dimensional conditions and produce as much information as possible concerning the turbulent quantities and their behavior.

The measurements show that:

• It is possible to separate the flow in three viscous regions : the wall boundary layer, the internal, and the external half wake.

• The "law of the wall" and the "law of the wake" provide valid descriptions of the observed velocity field in the adverse pressure gradient region between the two airfoils.

• The position of zero shear stress does not coincide with the position of zero velocity gradient. This fact is now well known and has been observed in several experiments.

In our experiment the role of the longitudinal and normal advection is particularly in evidence. The analysis of the experimental results using existing theoretical models seems to confirm the viability of an integral approach such as the one developed in reference [6].

Acknowledgments

References

1 Loudet, C., "Contribution theorique et experimentale a l'etude des grilles d'aubes en tandem a forte deflexion et a forte charge," These Institut von Karman, Belgique, 1971.

2 Bradshaw, P., Dean, R. B., and McEligot, D. M., "Calculation of Interacting Turbulent Shear Layers: Duct flow," ASME JOURNAL OF FLUIDS ENGINEERING, June 1973, pp. 214-220.

3 Morel, T., and Torda, T. P., "Calculation of Free Turbulent Mixing by Interaction Approach," AIAA Paper 73-649, 6th Fluid and Plasma Dynamics conference, Palm Springs, California, July 1973.

4 Perrier, P., and Lavenant, M., "Progress Report on Mechanical Flaps," AGARD Conference Proceedings, No. 143 V/Stol Aerodynamics, 1974.

5 Jeandel, D., and Mathieu, J., "Methode de calcul de la couche limite turbulente utilisant une equation d'evolution du coefficient de Boussinesq," Journal de Mecanique, Vol. 12, No. 4, 1973.

6 Stevens, W. A., Goradia, S. H., and Braden J. A., "Mathematical Model for Two-Dimensional Multi-Component Airfoils in Viscous Flow," NACA CR 1843, 1971.

7 Bradshaw, P., Gee, M. T., and Gee, B. A., "Turbulent Wall Jets With and Without an External Stream," Reports and Memoranda No. 3252, 1960; also ARC 22-008.

8 Monnerie, B., and Lovat, G., "Etude theorique et experimentale du soufflage de couche limite a la charniere d'un volet hypersustentateur," AGARD Conference Proceedings, No. 143, V/STOL Aerodynamics, 1974.

9 Railly, J. W., Deeb, S. D., and Moore M. J., "Wake Boundary Layer Interaction in Tandem Cascades," Thermodynamics and Fluid Mechanics Convention Proceedings 1969-1970, Vol. 184, Part 3G(III) paper 36, University of Glasgow, 23-25 March, Institution of Mechanical Engineers, United Kingdom.

10 Ljungstrom, B. L. G., "Boundary Layer Studies on a Two-Dimensional High Lift Wing" Rapport AU-862, Aeronautical Research Institute of Sweden, 1972.

11 Moore, M. J., "The Theory of Design of Slotted Blade Cascades and Their Evaluation," Ph.D. thesis, University of Birmingham, 1965.

12 Kline, S. J., Morkovin, M. V., Sovran, G., and Cockrell, D. J., (eds.), "Computation of Turbulent Boundary Layers," 1968 AFOSR-IFP-Stanford Conference, Vol. 2, Thermosciences Division, Department of Mech. Engng., Stanford Univ., Calif., 1968.

13 Hill, P. G., Schaub, U. W., and Senoo, Y., "Turbulent Wakes in Pressure Gradients," ASME Journal of Applied Mechanics, Dec. 1963, p. 518.

14 Mathieu, J., Alcaraz, E., and Guillermet, G., "Mesures de frottement a la paroi a l'aide de tubes de PRESTON et d'une balance," Compte rendu a l'Academie des Sciences Paris, t. 266, serie A, 1968.

15 Chevray, R., and Kovasznay, L. S. G., "Turbulence Measurements in the wake of a Thin Flat Plate," AIAA Journal, Vol. 7, No. 8, 1969, pp. 1641-1643.

16 Fayet, J., Garem, J. H., and Tsen, L. F., "Tensions de Reynolds dans un sillage dissymetrique d'un profil en ecoulement decelere," Contrat DRME No. 71-349/1, CEAT Poitiers, 1972.

17 Dhawan, S., and Narasimha, R., "Some Properties of Boundary Layer Flow During the Transition From Laminar to Turbulent Motion," Journal of Fluid Mechanics, Vol. 3, 1958, pp. 418-436.

18 Dean, R. B., "A Single Formula for the Complete Velocity Profile in a Turbulent Boundary Layer," ASME JOURNAL OF FLUIDS ENGINEERING, Vol. 98, No. 4, Dec. 1976, pp. 723-727.

19 Mathieu, J., "Remarks on Turbulent Flows With Free Stream Boundaries," Von Karman Inst., LS 36, 1971.

20 Kacker, S. C., and Whitelaw, J. H., "The Turbulent Characteristics of a Two-Dimensional Wall Jet and Wall Wake Flow," ASME Journal of Applied Mechanics, Vol. 38, No. 1, Mar. 1971.

21 Hanjalic, K., and Launder, B. E., "Fully Development Asymmetric Flow in a Plane Channel," Journal of Fluid Mechanics, Vol. 51, Part 2, pp. 301-335.

22 Beguier, C., "Ecoulements dissymetriques en regime turbulent," Compte Rendu a l'Academie des Sciences, Paris, t. 260, May 1965, p. 5460-5463.

of the minimum velocity, the negative quantity $\overline{v^3}$ implies a transport towards the wall. So a turbulent eddy with negative $\overline{uv}$, convected by the mean velocity field in the inner half wake could be convected by the fluctuation velocity field towards the wall. The evolution of the correlation factor $R_{uv} = \overline{uv}/\ \tilde{u}\ \tilde{v}$ is presented in Fig. 6. The maximum of $|R_{uv}|$ is 0.60 in the wall region and in the outer half wake. This value is greater than the usual value of 0.45 obtained in fully developed turbulent flows in wind tunnels. Comparison between several such results ([16-20]) obtained in wind tunnels seems to suggest that the maximum value of the correlation is affected by the value of the Reynolds number and that $|R_{uv}|$ may reach values of 0.7 in low Reynolds number flows. The maximum value of $|R_{uv}|$ decreases with increasing Reynolds number down to 0.30 (atmospheric boundary layers). In our experiment, the Reynolds number calculated on the airfoil cord was 1,200,000; this is a relatively low Reynolds number. The high value of the maximum of $|R_{uv}|$ is also in accordance with the suggestion of the presence of turbulent "big structures." Relatively well ordered "big structures" can give higher contributions at this maximum value.

Concluding Remarks

An experiment has been presented in this paper of a strong viscous interaction between a wake produced by a symmetrical airfoil and a turbulent boundary layer. The interaction took place in an adverse pressure gradient leading the boundary layer up to separation.

In view of the scarceness of experimental results of this type, much care was taken to ensure two-dimensional conditions and produce as much information as possible concerning the turbulent quantities and their behavior.
The measurements show that:
• It is possible to separate the flow in three viscous regions : the wall boundary layer, the internal, and the external half wake.
• The "law of the wall" and the "law of the wake" provide valid descriptions of the observed velocity field in the adverse pressure gradient region between the two airfoils.
• The position of zero shear stress does not coincide with the position of zero velocity gradient. This fact is now well known and has been observed in several experiments.

In our experiment the role of the longitudinal and normal advection is particularly in evidence. The analysis of the experimental results using existing theoretical models seems to confirm the viability of an integral approach such as the one developed in reference [6].

Acknowledgments

References

1 Loudet, C., "Contribution theorique et experimentale a l'etude des grilles d'aubes en tandem a forte deflexion et a forte charge," These Institut von Karman, Belgique, 1971.
2 Bradshaw, P., Dean, R. B., and McEligot, D. M., "Calculation of Interacting Turbulent Shear Layers: Duct flow," ASME JOURNAL OF FLUIDS ENGINEERING, June 1973, pp. 214-220.
3 Morel, T., and Torda, T. P., "Calculation of Free Turbulent Mixing by Interaction Approach," AIAA Paper 73-649, 6th Fluid and Plasma Dynamics conference, Palm Springs, California, July 1973.
4 Perrier, P., and Lavenant, M., "Progress Report on Mechanical Flaps," AGARD Conference Proceedings, No. 143 V/Stol Aerodynamics, 1974.
5 Jeandel, D., and Mathieu, J., "Methode de calcul de la couche limite turbulente utilisant une equation d'evolution du coefficient de Boussinesq," Journal de Mecanique, Vol. 12, No. 4, 1973.
6 Stevens, W. A., Goradia, S. H., and Braden J. A., "Mathematical Model for Two-Dimensional Multi-Component Airfoils in Viscous Flow," NACA CR 1843, 1971.
7 Bradshaw, P., Gee, M. T., and Gee, B. A., "Turbulent Wall Jets With and Without an External Stream," Reports and Memoranda No. 3252, 1960; also ARC 22-008.
8 Monnerie, B., and Lovat, G., "Etude theorique et experimentale du soufflage de couche limite a la charniere d'un volet hypersustentateur," AGARD Conference Proceedings, No. 143, V/STOL Aerodynamics, 1974.
9 Railly, J. W., Deeb, S. D., and Moore M. J., "Wake Boundary Layer Interaction in Tandem Cascades," Thermodynamics and Fluid Mechanics Convention Proceedings 1969-1970, Vol. 184, Part 3G(III) paper 36, University of Glasgow, 23-25 March, Institution of Mechanical Engineers, United Kingdom.
10 Ljungstrom, B. L. G., "Boundary Layer Studies on a Two-Dimensional High Lift Wing" Rapport AU-862, Aeronautical Research Institute of Sweden, 1972.
11 Moore, M. J., "The Theory of Design of Slotted Blade Cascades and Their Evaluation," Ph.D. thesis, University of Birmingham, 1965.
12 Kline, S. J., Morkovin, M. V., Sovran, G., and Cockrell, D. J., (eds.), "Computation of Turbulent Boundary Layers," 1968 AFOSR-IFP-Stanford Conference, Vol. 2, Thermosciences Division, Department of Mech. Engng., Stanford Univ., Calif., 1968.
13 Hill, P. G., Schaub, U. W., and Senoo, Y., "Turbulent Wakes in Pressure Gradients," ASME Journal of Applied Mechanics, Dec. 1963, p. 518.
14 Mathieu, J., Alcaraz, E., and Guillermet, G., "Mesures de frottement a la paroi a l'aide de tubes de PRESTON et d'une balance," Compte rendu a l'Academie des Sciences Paris, t. 266, serie A, 1968.
15 Chevray, R., and Kovasznay, L. S. G., "Turbulence Measurements in the wake of a Thin Flat Plate," AIAA Journal, Vol. 7, No. 8, 1969, pp. 1641-1643.
16 Fayet, J., Garem, J. H., and Tsen, L. F., "Tensions de Reynolds dans un sillage dissymetrique d'un profil en ecoulement decelere," Contrat DRME No. 71-349/1, CEAT Poitiers, 1972.
17 Dhawan, S., and Narasimha, R., "Some Properties of Boundary Layer Flow During the Transition From Laminar to Turbulent Motion," Journal of Fluid Mechanics, Vol. 3, 1958, pp. 418-436.
18 Dean, R. B., "A Single Formula for the Complete Velocity Profile in a Turbulent Boundary Layer," ASME JOURNAL OF FLUIDS ENGINEERING, Vol. 98, No. 4, Dec. 1976, pp. 723-727.
19 Mathieu, J., "Remarks on Turbulent Flows With Free Stream Boundaries," Von Karman Inst., LS 36, 1971.
20 Kacker, S. C., and Whitelaw, J. H., "The Turbulent Characteristics of a Two-Dimensional Wall Jet and Wall Wake Flow," ASME Journal of Applied Mechanics, Vol. 38, No. 1, Mar. 1971.
21 Hanjalic, K., and Launder, B. E., "Fully Development Asymmetric Flow in a Plane Channel," Journal of Fluid Mechanics, Vol. 51, Part 2, pp. 301-335.
22 Beguier, C., "Ecoulements dissymetriques en regime turbulent," Compte Rendu a l'Academie des Sciences, Paris, t. 260, May 1965, p. 5460-5463.

——————— D I S C U S S I O N ———————————————————

J. Andreopoulos [1]

The authors have been looking at a very useful and important problem of fluids engineering, namely: the interaction between 'an aerofoil wake and a boundary layer developing over a rather flat surface of a second aerofoil. The flow field is quite complicated since an accelerating flow, the wake, interacts with a decelarating flow, the boundary layer, under the influence of an adverse pressure gradient. This picture with so many parameters involved at the same time is quite common in real life. However, if all these parameters are

[1] Universität Karlsruhe, Karlsruhe, Germany.

varied at the same time it is difficult to see their isolated effect on the results. Usually the strategy in attacking such complicated problems is to split the experiment in more than one by varying one only parameter at a time. In the present case there is a lack of experimental information on the interaction between a symmetrical wake with a flat plate boundary layer in zero pressure gradient. The authors are not blaimed for not having looked at that; on the contrary are encouraged to do so. Despite this weak critism which may be considered as difference in opinion, the results of their investigation are quite interesting. Their first observation that the separation point on the second aerofoil moves downstream with the presence of the first ties up with other observations too. The

authors postulated successfully the use of velocity and length scales in the form of equation (4) to collapse their mean profiles. However, it is doubtful to say that similar scales can be applied to scale turbulence quantities.

The authors pointed out the well known fallacy of the eddy viscocity concept which is present almost in all asymmetrical and sometimes in symmetrical flows. Before saying that there is a physical unreality or invoking theories to explain such old behaviour, it is always useful to look at the full form of production terms of turbulent kinetic energy, $\overline{q^2}$, $(\overline{q^2} = \overline{u^2} + \overline{v^2} + \overline{w^2})$ as it appears in the transport equation of q^2. The reason being that even in 2-dimension flows the thin shear layer approximation may not be everywhere valid because some main terms can be extremely small. The full production term is

$$\overline{uv}\frac{\partial U}{\partial y} + (\overline{u^2} - \overline{v^2})\frac{\partial U}{\partial x} + \overline{uv}\frac{\partial V}{\partial y}$$

with the last part being negligible. It was found in [23] for example, where a symmetrical and an asymmetrical wake have been investigated, that the second part of the production term is not negligible, since $\partial U/\partial x$ is significant, and the negative production has been moderated but not vanished. The same feature is evident in the present flow configuration at the regions where the flow is accelerated as in the first half of the second aerofoil (Fig. 3) since always is $\overline{u^2} > \overline{v^2}$. Over the second half, however, the flow is clearly decelerated and the negative production is increased absolutely; in other words a bigger amount of turbulent kinetic energy returns to the mean flow.

The authors found the skin friction coefficient C_f by using Clauser charts and replacing the external velocity U_e' with $U\delta$. What are the arguments which allow them to use Clauser's method? Is it true to say that

$$\frac{U_T}{U_\delta} = \sqrt{\frac{C_f}{2}} \tag{5}$$

is valid? The fact that plots of U/U_δ versus log $(yU\delta/v)$ show a straight line is an important result but does not support the existense of equation (5). Consequently the agreement with Preston tube results is odd.

One important parameter which characterizes the wake is the friction velocity U_T and the momentum thickness of the boundary layer at the trailing edge of the first aerofoil (see [12]). The interaction process is controlled by the big eddies at the trailing edge basically because the "boundary layer eddies," if we could descriminate them, start to grow later in time. It is expected that at the early stages of the interaction

the big eddies coming from either side of the first aerofoil control the time sharing process in a manner described in [23] and only at the late stages when the "boundary layer" eddies are bigger, are participating in the time sharing. In that sense it can be argued that the external half wake is not affected by the presence of the boundary layer and some of the present results support that idea.

The authors are attemping to explain the high values of the correlation coefficient Ruv in terms of big structures which are present at low Reynolds number effects. In a recent work described in [24] and [25] has been found that Ruv varies with the Reynolds number but never exceeds the value of 0.48 at a Reynolds number based on momentum thickness of 791. As the authors have pointed out the uncertainties in measuring Ruv are higher than in other turbulence quantities and they have noted a 10 percent possible error. I think it is not redundant to say that an error of only 1 deg in setting the X-wire angles can cause a 8.5 percent error in Ruv.

Additional References

23 Andreopoulos, J. and Bradshaw, P., "Measurements of Interacting Turbulent Shear Layers in the Near Wake of a Flat Plate," *J. F. M*, Vol. 100, 1980, pp. 639–668.

24 Murlis, J., Tsai, H. M., and Bradshaw, P. "The Structure of Turbulent Boundary Layers at Low Reynolds Numbers," 1980, Submitted to *J. Fluid Mech.*

25 Murlis, J., Ph.D thesis, Imperial College, London University, 1975.

Authors' Closure

The authors are grateful to Dr. Andreopoulos for his interesting comments on their work. Dr. Andreopoulos has brought out in his discussion the complexity of this phenomenon often encountered in fluids engineering.

We agree with him on the point concerning the strategy of attacking such a problem. The production term $\overline{uv}\partial U/\partial y + (\overline{u^2} - \overline{v^2})\partial U/\partial x$ has been calculated. It has been found to be always positive except in a part of the wake where the negative production was found to be very low in absolute.

The Preston tube gives the value of the wall shear stress by means of measurement of total and static pressures in the wall region. The friction velocity is calculated with the relation $u_T = \sqrt{\tau/\rho}$ and the friction coefficient with the formulation (5). The Clauser method uses only the hypothesis of a log-law near the wall. If we define the friction coefficent as $C_f = \tau/\frac{1}{2}\rho U_\delta^2$, the linear part of the curve U/U_δ versus log (yU_δ/v), can be fit by a straight line with C_f as parameter; so the two values of the friction coefficient can be compared as they are calculated with the same formulation.

R. C. Johnson, Jr.
Mobil Research & Development Corp.,
Dallas, Tex.

G. E. Ramey
Associate Professor,
Department of Civil Engineering,
Auburn University,
Auburn, Ala. 36849

D. S. O'Hagan
Design Engineer,
Figg and Mueller,
Tallahasse, Fla. 32301

Wind Induced Forces on Trees

Introduction

When Hurricane Frederic struck the central U.S. Gulf Coast on September 12, 1979, $2.3 billion in damage resulted making Frederic the most costly hurricane in U.S. history. There were many types of damage; however, the most widespread was that associated with forests.

Accurate recording of Hurricane Frederic's windspeeds was accomplished at National Weather Service (NWS) and other weather stations along the Gulf Coast [1]. A post-hurricane damage survey thoroughly documented tree and other damages in these same regions. The purpose of this study is to investigate the correlation of tree damage with the known recorded windspeeds and to develop methods of predicting maximum windspeeds based on observed damage in future windstorms. This study is part of a larger research project to determine maximum windspeeds, windspeed contours, and wind loadings on structures associated with tornadic windstorms. Included are both field damage documentation and laboratory wind tunnel testing. It is expected that the results contained herein will give engineers a basis for a more complete understanding of windfields in cyclonic storms where no meterological data exist as is often the case for tornadoes.

Wind Tunnel Experimentation

Because of their great variation in shape, permeability and material properties, trees have been the subject of limited aerodynamic research. Field experimentation on mature rooted specimens has not occurred due to the physical complexity of the problem and the inconvenience of predicting windstorms and traveling to the test site whenever a storm is expected. Consequently, wind tunnel studies are undertaken to obtain the desired information.

Attempting to minimize windthrow damage in British forests, A. I. Fraser reported a series of experiments [2] that were designed to determine the relationship between wind-

speed and the horizontal wind induced force or drag exerted on a tree. Four species of cut, mature trees were tested in the 24-ft wind tunnel at the Royal Aircraft Establishment in Fornborough. The resulting drag was expressed, by Fraser, as a function of wind velocity in a relationship that included the tree weight. The relationship is of little value for windstorms in the U.S. since it was formulated for species atypical to the area and was expressed in terms of the tree weight, a parameter not easily measured in the field.

Mayhead's 1973 investigation [3] of tree drag took a more classical fluid mechanics approach. Using the same experimental facilities as Fraser, Mayhead related the wind force on a tree to the wind velocity by means of drag coefficients as expressed by

$$C = P/qA \tag{1}$$

where $q = 1/2 \, \rho v^2$. In these expressions, q is the dynamic wind pressure, v is the windspeed, ρ is the air density, P is the wind force, and A is the projected frontal area of the tree canopy in still air. Results of his research indicated a reduction of the drag coefficient with increased windspeed and a large variation in drag coefficients both between and within a species. Mayhead attributed this variation to wide morphological variations and poor experimental data reduction technique in approximating projected frontal areas, A, by the equation,

$$A = bh/2 \tag{2}$$

where b and h are the tree canopy diameter and height, respectively, in still air. The error resulting from this approximation, however, is not viewed as being of primary significance since the pines which presented the most problems in area determination showed the highest degree of uniformity in drag coefficients. Rather, it is felt that blockage was the primary experimental technique leading to error since the trees were between 19 and 28 ft tall and they were subjected to winds in a 24-ft dia wind tunnel.

Test Program. The wind tunnel studies conducted at Auburn University were designed to measure both the
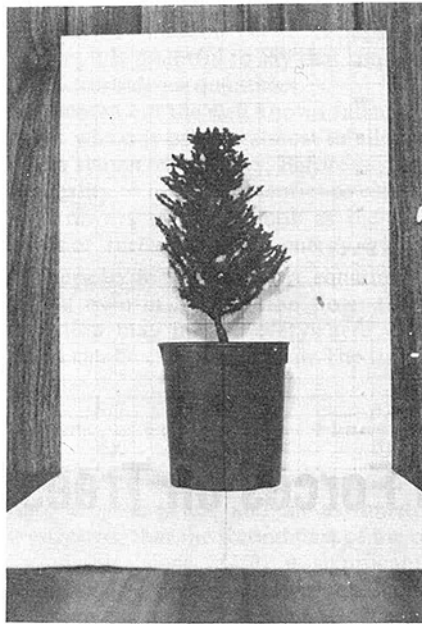
Fig. 1(a)
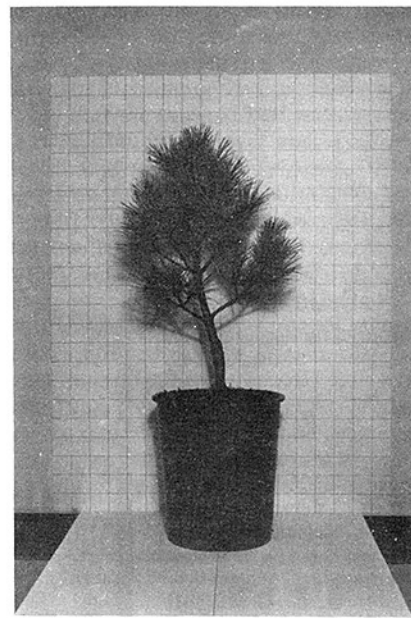
Fig. 1(b)

horizontal (drag) force and the pitching moment experienced using a pyramidal balance. Three species of live dwarf conifers were used to reproduce rooted specimen response and to duplicate crown similarities to the trees most often destroyed by winds in the southeastern United States. The slender bole and symmetric crown of the dwarf white pine (*pinus strobus*) naturally appeared to approximate the full-sized white pines' appearance as well as that of slash and loblolly pines with somewhat spherical crowns and high solidities. Two of this species were tested. The trunk length and somewhat cylindrical crowns of lower solidity slash and loblolly pines were approximated by two cryptomeria (*cryptomeria japonica*). The crown shapes of this species were approximately symmetric with respect to horizontal and vertical axes with a crown height to width ratio of approximately 1.5. One dwarf Alberta spruce (*picea glavea*) was included in the testing program to observe the effect of shape asymmetry with respect to the horizontal axis on the location of the center of pressure. All specimens included in the testing program were approximately vertically axisymmetric to reduce torsional forces on the boles. Figure 1 is a photograph of the three species of dwarf conifers tested.

Using photographs of the untested specimens in still air, the projected frontal canopy surface areas were determined by both planimetric methods and Mayhead's approximation (equation 2). The latter method underestimated the planimetric area by a maximum of 7 percent. Hence for reasons of convenience and conservatism, equation (2) was

Fig. 1(c)

Fig. 1 Dwarf conifers

―――――― Nomenclature ――――――――

A = projected frontal area of tree canopy in still air
b = canopy diameter in still air
C = wind pressure coefficients
D = tree bole diameter at failure
$\bar{D}$ = average tree bole diameter between failure and canopy base
H = height of tree bole exposed to wind above failure in still air

h = height of tree canopy in still air
M_b = wind induced bending moment at location of tree failure
M_u = ultimate moment capacity of tree at failure section
m = constant giving the location of the canopy wind pressure force, measured as a decimal fraction of the canopy height from the canopy base
P = wind force on tree

p = wind pressure force
q = dynamic wind pressure
R = modulus of rupture
S = tree section modulus at failure section
v = windspeed
ρ = air density

Subscripts

B = tree bole
C = tree canopy

used in any calculations requiring the projected frontal surface area for windspeed analysis of field documented tree damage.

Test Procedure. The test section of the tunnel used in this study has throat measurements of 48 in. (122 cm) wide × 36 in. (91 cm) high × 60 in. (152 cm) long and has a boundary layer thickness of approximatley 1 1/2 in. (38 mm) at the specimen location. Within the central portion of the tunnel (i.e. not in the boundary layer), an extremely flat velocity profile is produced. At any point, the dynamic pressure does not deviate from the mean by more than 0.1 percent. The experimental procedure consisted of fitting each specimen in a pyramidal balance and subjecting it to increasing windspeeds in the wind tunnel. At various intervals the windspeed was allowed to stabilize and data were automatically recorded and reduced. From pressure transducer readings, the dynamic pressure, q, of the moving air was recorded and translated into air velocity based on the kinetic energy of the moving air. Strain gage load cells recorded the drag force, P, on the specimen and the wind pressure coefficient, C, was found from equation (1). The area, A, in that equation is the original undeformed projected area of the tree. Hence the calculated wind pressure coefficient should be applied to undeformed areas in wind loading applications.

Additionally, the pitching moment caused by the drag force about the pyramidal balance's resolving center was measured by load cells at the base of the balance. From the readings, the center of pressure of the drag force was calculated. This center of pressure evaluation yields correct values for the actual pressure distribution acting on the deformed tree projected area. However, for convenience, the center of pressure location is reported in terms of the undeformed tree canopy height since this is the parameter that is most easily measured or estimated in field applications.

All specimens were tested at three different angles of orientation to the moving air. After randomly labeling and testing one position as a reference, each specimen was turned 45 and 90 deg from this position and tested as well. For each species' 45 and 90 deg orientations, to avoid the possible destruction of the specimens, windspeeds were limited to a maximum of 80 fps (24.4 mps). However, for the final 0 deg (reference) orientation the full capacity of the subsonic wind tunnel was utilized to produce a maximum windspeed of about 130 fps (39.6 mps). The photograph of the cryptomeria in Fig. 2 was taken at this maximum windspeed.

Test Results. The results of this investigation are presented in Figs. 3–8. Figures 3 and 4 are plots of the wind pressure coefficients of the various species versus the applied windspeed. Examination of Fig. 3 reveals the differences in the responses of the dwarf white pines tested. For the windspeeds where trees fail, the differences between the specimens' wind pressure coefficients are substantial. At high windspeeds, both specimens appear to be approaching constant values of C, with the average for the two specimens being 0.5. Examination of Fig. 4 reveals that both specimens of cryptomeria showed a high degree of uniformity in their wind pressure coefficients both between the orientation angles and between the specimens themselves. Both these specimens have coefficients similar to the dwarf white pine specimen 2, especially at the higher windspeeds. The estimated coefficient C at high windspeeds for this species is 0.3. The wind pressure coefficients of the dwarf Alberta spruce, also plotted in Fig. 4, are strikingly similar to those of the dwarf white pine specimen 1 at higher windspeeds.

The calculated centers of pressure were nondimensionalized with respect to the canopy height to produce the canopy height parameter, m, (decimal fraction of canopy height locating the resultant drag force). Figures 5 and 6 are plots of
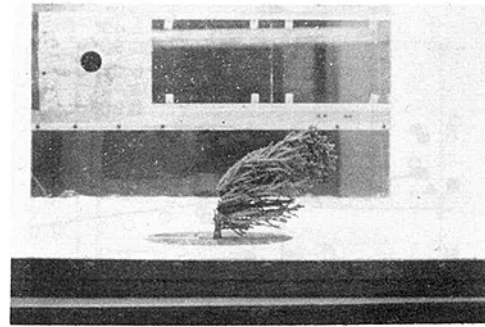
Fig. 2 Cryptomeria in 130 fps wind
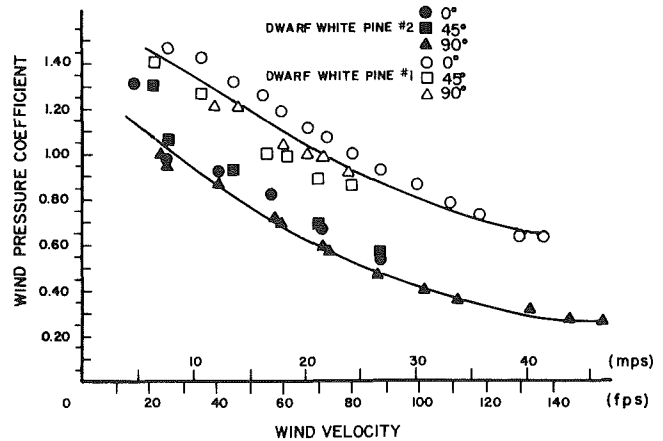
Fig. 3 White pine wind pressure coefficients
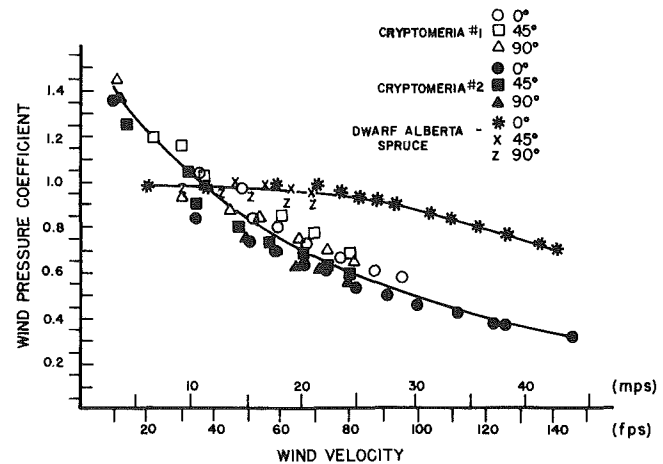
Fig. 4 Cryptomeria and Alberta spruce wind pressure coefficients

the canopy height parameter versus windspeed for the dwarf white pine and cryptomeria species, respectively. Above 60 fps (18.3 mps) this parameter is between 0.37 and 0.50. Being based on the canopy height in still air, the decrease of this parameter is expected since the drag force height decreases as the tree bends in the severe winds. Thus the value of 0.50 appears reasonable for species that are symmetric about horizontal and vertical axes. Figure 6 also includes the canopy height parameters at which drag forces on the dwarf Alberta spruce acted. Being vertically axisymmetric with an isosceles shape, the dwarf Alberta spruce 0.35 value is also reasonable.

Plots of wind pressure coefficient versus Reynolds number for the species tested are presented in Figs. 7 and 8. Both of these figures indicate decreasing values of C with increasing Reynolds number over the range tested. Unfortunately, maximum windspeed capabilities of the wind tunnel were
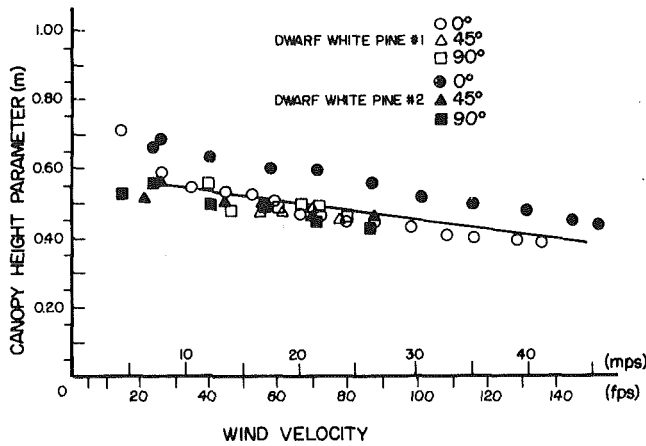
Fig. 5 Vertical location of wind force resultant for white pine
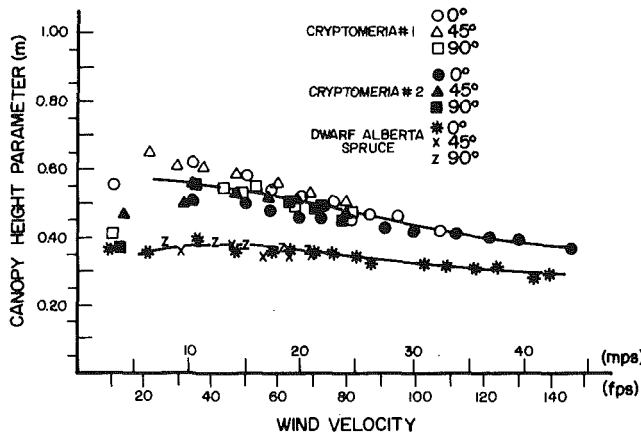
Fig. 6 Vertical location of wind force resultant for cryptomeria and Alberta spruce

Fig. 7 Wind pressure coefficients versus Reynolds number of white pine

Fig. 8 Wind pressure coefficients versus Reynolds number for cryptomeria and Alberta spruce

reached before escaping the critical flow region. Hence, the value of C at high windspeeds and Reynolds number can only be estimated at the values cited in the paragraphs above.

Errors. Uncertainty sources in the variables plotted in Figs. 3–8 are of two types—random and fixed. Dynamic pressures, measured with pressure transducers; drag force, measured with strain gage load cells; and the tree dimensional data, measured from photographs were used to reduce the data. The source of error in measuring dynamic pressures and drag forces was primarily random since the wind tunnel is frequently calibrated. Based on these regular calibrations and day-to-day repeatability of data, the drag force and dynamic pressure are accurate to within ±0.1 percent. The error in the reference area was a fixed error which was introduced during the photography and planimeter operations. This fixed error was estimated to be ±1 percent. A fixed error was also introduced in the measurement of the specimen dimensions (bole height to foliage and maximum width and height of the foliage). These measurements were carefully taken with a vernier caliper from a photograph of the specimen in still air. It is estimated that the error in each of these measurements was ±0.01 in.

Based on the above measurement accuracies, the resulting uncertainty in wind pressure coefficients was found to be ±0.007. Uncertainty in wind velocity was again primarily random. The source of this error was small, long period variations of the air speed in the test section of the tunnel. Velocities were calculated based on the kinetic energy of the moving air and are accurate to within ±0.1 percent. Based on uncertainty calculations, Reynolds number and the canopy
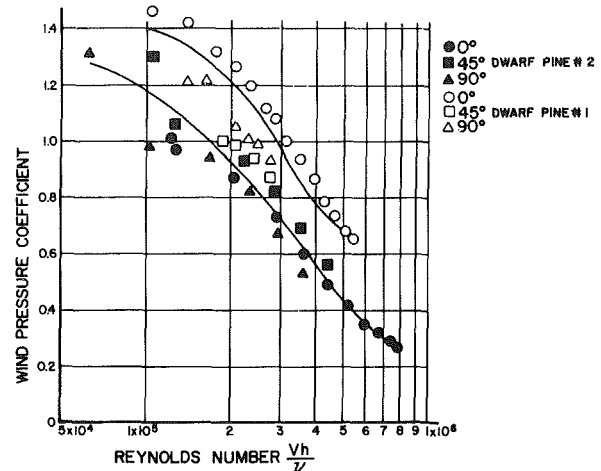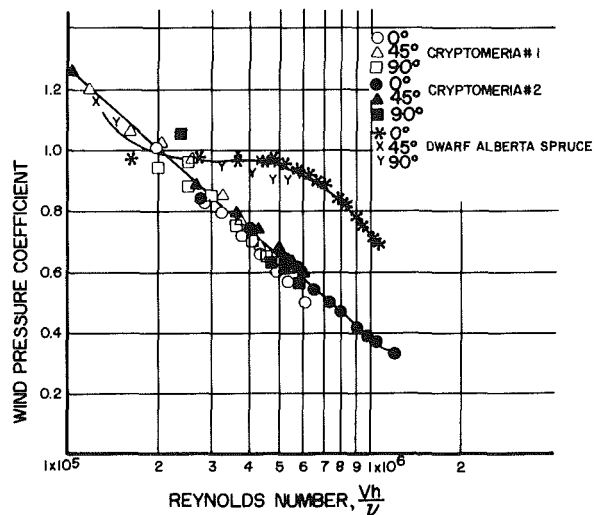
height parameter are accurate to within ±0.2 percent and ±0.5 percent, respectively.

Tree Windspeed Analysis

Using the experimental data in a windspeed analysis requires that simplifying assumptions be made in the idealization of tree failures. These assumptions are:

1 Trees are analyzed as isolated, vertical cantilever beams fixed at ground level and failing in the height of the bole. Uprooting to any degree will be neglected.

2 A uniform wind pressure distribution is assumed to act along the height of the tree above the failure point.

3 Wind pressure coefficients for tree canopies will be taken from the dwarf tree wind tunnel results. For tree canopies with high solidities, wind pressure coefficients will be assumed to be those of the dwarf white pine. For canopies with low solidities, wind pressure coefficients will be assumed to be those of the cryptomeria. Wind pressure coefficients for the bole will be assumed to approximate those of a thin smooth cylinder (1.2) even though the bark roughness and high windspeeds would both increase these coefficients. (Note, wind forces on the bole are minor relative to those on the canopy.)

4 Wind pressure force resultants on the crown will be assumed to act at the center of pressure of the projected frontal area in still air.

5 The bark thickness is assumed to be 10 percent of the total bole diameter.

The statically applied uniform wind load p applied to the tree in Fig. 9 produces a wind force on the bole equal to

$$P_B = p\bar{D}H \qquad (3)$$

where $\bar{D}$ and H are the average diameter and height of the tree bole, respectively. Approximating the projected frontal area of the canopy as given by equation (2), the wind force on the canopy is given by

$$P_C = pbh/2 \qquad (4)$$

The applied bending moment at the point of failure is

$$M_b = \tfrac{1}{2}[p\bar{D}H^2 + pbh(H+mh)] \qquad (5)$$

where m is a fraction of the canopy height which locates the canopy wind pressure resultant force. The ultimate bending capacity of the tree is described by

$$M_u = RS = \pi RD^3/32 \qquad (6)$$

where R is the modulus of rupture, and D and S are the diameter and section modulus at the failure location, respectively. For purposes of this analysis, tree failure is assumed to occur upon attainment of the ultimate moment capacity of the bole. Hence, equating equations (5) and (6) and substituting the relation between wind pressure and windspeed

$$p = 0.00256\, v^2 C \qquad (7)$$

yields

$$v = 8.76\sqrt{\dfrac{RD^3}{C_B\bar{D}H^2 + C_C bh(H+mh)}}\ \text{mph} \qquad (8)$$

$$(1\ \text{mph} = 1.61\ \text{km/h})$$

for R in psf and D, $\bar{D}$, H, b, h in feet. In equation (8), C_B and C_C are the wind pressure coefficients for the bole and canopy, respectively. Examination of this equation reveals that the calculation of tree failure windspeeds is an iterative procedure since for a given tree the canopy wind pressure coefficient is a function of windspeed.

Coniferous trees are slender, flexible structures whose dynamic response is important under the turbulent periodic gusts of a hurricane. The dynamic analysis of a tree is complicated by the many parameters inherent in "natural" structures. Neglecting the bias caused by surrounding trees on the sway period and employing a single degree of freedom model, the dynamic amplification factor can be found as a ratio of the period of the time varying load, t, to the natural period, T, of the tree.

Sugden [4] experimentally determined the sway of red pines (*pinus resinosa*) and white pines to be a function of the ratio of diameter at breast height to total height as indicated in Fig. 10. The loblolly pines documented during the post hurricane storm survey had an average ratio of diameter to height of 0.21 which by Sugden's curve gives an approximate sway period of 2.5 s for these trees.

The periodic gustiness of hurricane winds is very difficult to measure. Gust recorder charts depicting Hurricane Frederic's winds could not be used to determine the gust period because the time scale was too small to differentiate distinct peaks in the recorder readings. During Cyclone Gervaise on June 2, 1975, a record of the storm's gusts was made on an expanded time scale [5] and is reproduced in part in Fig. 11. Examination of this figure reveals that the cyclonic winds have gust periods between 2.5 and 3 s. Thus, if one assumed an isosceles triangular wind gust with a ratio of load period to natural period of 1, this results in an amplification factor of approximately 1.4 [6]. Consequently wind-induced bending moments are also amplified by a factor of 1.4 which modifies equation (8) to
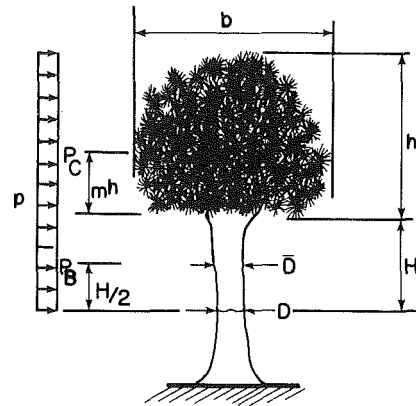
Fig. 9 Idealized tree
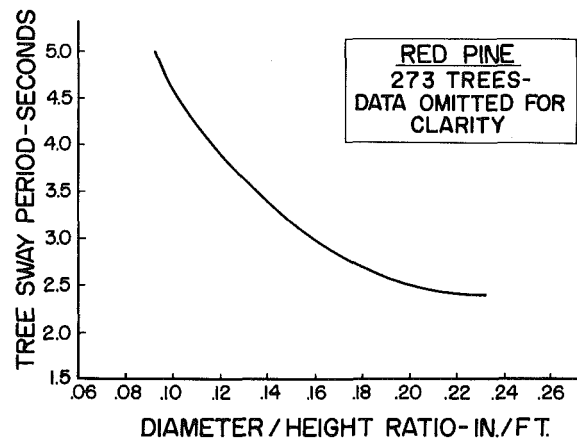
Fig. 10 Tree sway period

$$v = 7.40\sqrt{\dfrac{RD^3}{C_B\bar{D}H^2 + C_C bh(H+mh)}}\ \text{mph} \qquad (9)$$

Documented Tree Failure Windspeeds

Included in the damage documentation following Hurricane Frederic were several loblolly pines in the area of Mobile County, Alabama. These trees were selected for detailed documentation because of their bole failures and wind susceptible locations. The trees were located on the windward periphery of either a low density forest or suburb. These locations were selected to minimize the effect of surrounding trees and missile damage. The modulus of rupture, R for the loblolly pines was assumed to be 7980 psi [7]. Values of m were obtained by examining the shape of the tree canopy while the canopy wind pressure coefficients were taken from the data shown in Figs. 3 and 7.

Results for four documented trees which satisfied the location requirements are given in Table 1. As can be seen in that table, some of the analytically estimated windspeeds are higher than NWS recordings and some lower. This is as one would expect and indicates the analyses are not strongly biased on the conservative or unconservative side. Additionally, it is indicative of the statistical nature of predicting windspeeds from post-mortem damage analyses.

While the lowerbound estimates of windspeed as calculated and shown in Table 1 are felt to be in good agreement with recorded windspeeds, it should be noted that several uncertainties have not been included in the analysis. As indicated earlier, the wind tunnel velocity profile was essentially uniform and the dwarf tree specimens were therefore subjected to a much more uniform pressure distribution than the
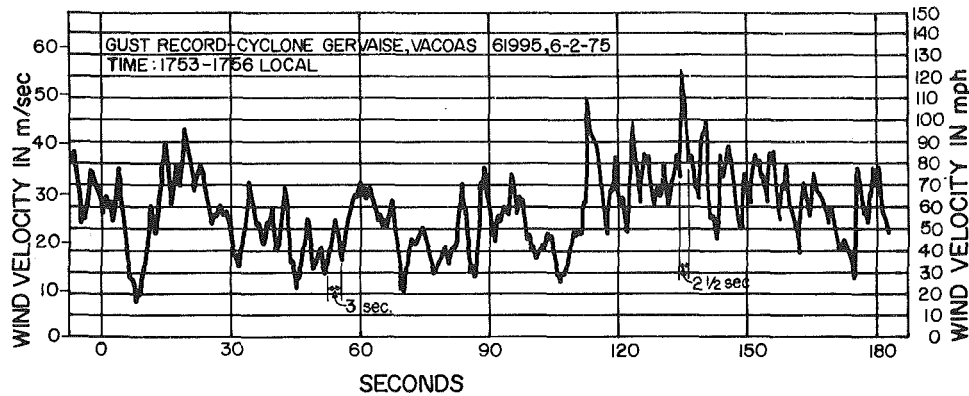
Fig. 11 Gust record—Cyclone Gervaise

Table 1 Calculated failure windspeeds for loblolly pines

| Tree Location | Tree Parameters | | | | | | | Calculated Windspeed (mph) |
	D (ft)	$\bar{D}$ (ft)	H (ft)	h (ft)	b (ft)	m	C_c	
Mobile, AL*	0.9	0.8	10	28	23.5	0.5	0.5	75
Mobile, AL**	1.0	1.0	27	17	13	0.4	0.5	129
Mobile, AL**	1.1	1.0	20	26	23	0.5	0.5	92
Theodore, AL***	1.0	1.0	6.5	31.5	18	0.5	0.5	100

* 8 miles southwest of Mobile where gusts of 92 mph were recorded
** 5 miles west of NWS station recording 97 mph gusts
*** Center of Theodore where maximum windspeed exceeded 110 mph
(1 mph = 1.61 km/h, 1 ft = 0.305 m)

loblolly pines which were located in the natural boundary layer of Hurricane Frederic. The detailed characteristics of the boundary layer in the vicinity of the loblolly pines are unknown, and hence a precise quantification of the effect of the natural boundary layer on the estimated failure windspeeds is not possible. A rather simplistic approach one could take in attempting to evaluate the effect of the natural boundary layer would be to consider the variation of effective velocity pressure with height and exposure. The loblolly pines were located in relatively open and flat coastal terrain where an average power-law exponent of approximately 1/7 is generally appropriate. For the heights of interest this variation would result in a ten to fifteen percent difference between the wind velocities at the top and bottom of the tree canopies. This velocity gradient would tend to raise the location of the center of pressure above that obtained in the wind tunnel test results where there was a uniform velocity profile. This in turn would lower the estimated failure windspeed. However, tree branches are flexible and tend to bend back into the tree in a windfield. The degree of bending increases as windspeed increases resulting in a decreasing frontal area and in general a lowering of the center of pressure. For the loblolly pines, inclusion of this effect would tend to lower the location of the center of pressure and increase the estimated failure windspeed. The net resultant effect of raising of the center of pressure due to the natural boundary layer and its lowering due to the tree bending is unknown. Additionally, it should be noted that the flexibilities of the individual tree branches would also tend to lengthen the period of gust loading on the tree bole, and this in turn would tend to reduce the dynamic amplification factor. Including this effect would result in higher calculated windspeeds for failures.

Summary of Results

Detailed engineering knowledge of windstorms is necessary

for development of probabalistic models for windfields and for design criteria for building codes. Many windstorms do extensive damage to forest areas in rural locations. In order to make use of the obtainable data from these storms, wind tunnel tests were conducted on three species of dwarf trees to determine the wind pressure coefficients. These coefficients and the location of the resultant wind force were plotted versus windspeed. For the dwarf trees and windspeeds included in the testing program, it appears that the flow is in the critical range. Results of the laboratory experimentation were applied to actual damaged trees observed near NWS stations in Hurricane Frederic. Correlations between predicted windspeeds and observed values are good. These results should allow for a more complete understanding of windfields of other cyclonic windstorms where no meteorological data exist.

Acknowledgment

References

1 Hebert, P. J., "Atlantic Hurricane Season of 1979," *Final Report*, National Hurricane Center, National Weather Service, NOAA, Miami, 1980.

2 Fraser, A. I., "Wind Tunnel and Other Related Studies on Coniferous Trees and Tree Crops," *Scottish Forestry*, Vol. 18, No. 2, 1964, pp. 84–92.

3 Mayhead, G. J., "Drag Coefficients for British Forest Trees Derived from Wind Tunnel Studies," *Agricultural Meteorology*, Vol. 12, 1973, pp. 123–130.

4 Sugden, M. J., "Tree Sway Periods—A Possible New Parameter for Crown Classification and Stand Competition," *Forestry Chronicle*, Vol. 138, Sept. 1962, pp. 336–344.

5 Padya, B. M., "Spatial Variability and Gustiness of Cyclonic Winds: Gervaise, Mauritius, February 1975," *Australian Meteorological Magazine*, Vol. 23, No. 3, Sept. 1975, pp. 61–69.

6 Biggs, J. M., *Introduction to Structural Dynamics*, McGraw-Hill, 1964.

7 Biblis, E. J., "Tensile Properties of Loblolly Pine Growth Zones," *Wood and Fiber*, Vol. 1, 1969, pp. 18–28.

Manlio Bertelà

Research Engineer.

Fabio Gori

Assistant Professor.

Università di Firenze,
Facoltà di Ingegneria,
Fisica Tecnica,
50139 Florence, Italy

Laminar Flow in a Cylindrical Container With a Rotating Cover

Unsteady and steady flow in a cylindrical chamber with a rotating cover has been studied for two Reynolds numbers and three aspect ratio values. The structure of the velocity and pressure fields in the apparatus is described. Primary and secondary volumetric flow rates and torque coefficients are also calculated for all six cases solved.

1 Introduction

The flow of a Newtonian fluid in a cylindrical container when its rotating cover provides the motion is not completely known. The authors who have dealt with this theme, [1-6], have restricted their analyses to chamber aspect ratios, λ, less than [2-4] or equal to [1, 5, 6] 1. The present authors know of no work where this geometry with λ > 1 has been investigated; moreover λ = 1, the highest value considered, has been associated with rather small Reynolds numbers, Re, even in the most recent solutions of this problem [5, 6].

This paper makes an effort to widen both λ and Re ranges. The increase in the first parameter gradually transforms the nature of the geometry and as a consequence the pattern of the flow; in the elongated version the apparatus deserves attention because of several technical applications (fluid machinery, heat exchangers with a rotating fluid, chemical mixers, etc.).

A cylindrical container is filled with a Newtonian, incompressible, isothermal fluid and its cover is imagined to be driven to steady rotation in a time $\Delta t \rightarrow 0$. This movement induces both a rotational flow round the chamber axis and a secondary one in the *rz* plane (Fig. 1).

This study was conducted by solving numerically the full
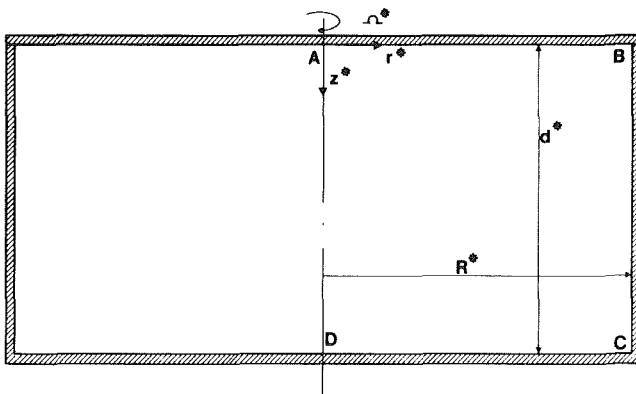
Fig. 1   The sketch of the apparatus

Navier-Stokes equations; its purpose is to describe the features of the steady and unsteady flow in the chamber and the influence of Re and λ on the structure of the velocity and pressure fields. Several quantities of technical interest were calculated too: 1) the torque coefficient, 2) the primary and 3) the secondary flow rates. Solutions to the Navier-Stokes partial differential equations were obtained for Re = 100, 1000 and λ = 0.5, 1, 2. Three further solutions were specially computed in order to make comparisons with experimental, theoretical, and numerical data available in the literature.

2   The Problem and the Method of Solution

The physical system investigated (Fig. 1) is referred to a cylindrical frame; laminar flow is assumed. By virtue of the supposed axial symmetry, the dimensionless continuity and Navier-Stokes equations for a Newtonian, incompressible fluid must be written as follows (in conservative form).

$$\frac{1}{r}\frac{\partial}{\partial r}(ru) + \frac{\partial w}{\partial z} = 0$$

$$\frac{\partial u}{\partial t} + \frac{1}{r}\frac{\partial}{\partial r}(ruu) + \frac{\partial}{\partial z}(wu) - \frac{v^2}{r}$$

$$= -\frac{\partial p}{\partial r} + \frac{1}{Re}\left[\frac{\partial^2 u}{\partial z^2} - \frac{\partial^2 w}{\partial r \partial z}\right]$$

$$\frac{\partial v}{\partial t} + \frac{1}{r}\frac{\partial}{\partial r}(ruv) + \frac{\partial}{\partial z}(wv) + \frac{uv}{r}$$

$$= \frac{1}{Re}\left\{\frac{\partial^2 v}{\partial z^2} + \frac{\partial}{\partial r}\left[\frac{1}{r}\frac{\partial}{\partial r}(rv)\right]\right\} \tag{1}$$

$$\frac{\partial w}{\partial t} + \frac{1}{r}\frac{\partial}{\partial r}(ruw) + \frac{\partial}{\partial z}(ww)$$

$$= -\frac{\partial p}{\partial z}$$

$$+ \frac{1}{Re}\left[\frac{\partial^2 w}{\partial r^2} + \frac{1}{r}\frac{\partial w}{\partial r} - \frac{1}{r}\frac{\partial^2}{\partial r \partial z}(ru)\right].$$

In these equations dimensionless quantities are defined (a star

denotes a dimensional quantity) by the chamber radius, R^*, and the cover angular speed, Ω^*.

$$u = \frac{u^*}{\Omega^* R^*}; \quad v = \frac{v^*}{\Omega^* R^*}; \quad w = \frac{w^*}{\Omega^* R^*}; \quad p = \frac{p^*}{\rho^*(\Omega^* R^*)^2};$$

$$\mathrm{Re} = \frac{\Omega^* R^{*2}}{\nu^*}; \quad \lambda = \frac{d^*}{R^*};$$

ρ^* and ν^* are the density and kinematic viscosity of the fluid; d^* is the distance between the cylinder bases. The dimensionless spatial coordinates and time are defined as follows:

$$r = \frac{r^*}{R^*}; \quad z = \frac{z^*}{R^*}; \quad t = \Omega^* t^*.$$

Boundary conditions are now given for the dimensionless radial, azimuthal, axial velocity components, $u(r,z,t)$, $v(r,z,t)$, $w(r,z,t)$, and the pressure $p(r,z,t)$:

$$u = v = w = p = 0$$

for $t < 0$; for $t \geq 0$

$u = w = 0$ on solid walls;

$v = 0$ on stationary solid walls;

Fig. 2 Comparisons between theoretical, numerical, and experimental steady $v(z)/r$ profiles

$v = r$ on the rotating cover;

$$u = v = \frac{\partial w}{\partial r} = 0 \text{ on the container axis.}$$

The modified pressure p is obtained as in [7] by the solution of the following Neumann problem.

$$\begin{cases} \nabla^2 p = -\nabla \cdot [(\mathbf{v} \cdot \nabla)\mathbf{v}] \\[2mm] \frac{\partial p}{\partial n} = G(r,z); \end{cases}$$

$\mathbf{v}$ and n are respectively the velocity vector and the normal direction to the boundary; $G(r,z)$ indicates all p boundary conditions which are now specified.

$$\frac{\partial p}{\partial z} = -\frac{1}{\mathrm{Re}} \cdot \frac{1}{r} \cdot \frac{\partial^2(ru)}{\partial r \partial z} \text{ on AB and DC (Fig. 1);}$$

$$\frac{\partial p}{\partial r} = -\frac{1}{\mathrm{Re}} \cdot \frac{\partial^2 w}{\partial r \partial z} \text{ on BC;}$$

$$\frac{\partial p}{\partial r} = 0 \text{ on AD.}$$

A Fourier series expansion was used for the solution of this problem according to [7]; the Navier-Stokes equations were numerically treated by the M.A.C. method and steady solutions were approached as the limit of an evolution in time for $t \to \infty$. Details for both procedures are given in [7, 8 (p. 194–201),9].

The cases solved are now listed: Re = 100 and $\lambda = 0.5$; 1; 2; Re = 138 and $\lambda = 0.2$; Re = 900 and $\lambda = 0.5$; Re = 1000 and $\lambda = 0.5$; 1; 2; Re = 1296 and $\lambda = 0.33$.

The basic mesh dimensions were $\Delta r = \Delta z = 0.05$ and results are generally given for them. As will be seen later, such sizes yield a good agreement with data from other papers for Re = 100. So calculations were repeated with the halved mesh only for Re = 1000, $\lambda = 0.5$ and Re = 1000, $\lambda = 2$, and compared with the corresponding previous ones; they showed that the degree of convergence given by the basic mesh is satisfactory everywhere in the field of flow. See, for example, Figs. 6 and 7, where some halved mesh solutions are added. The largest departures were found to be not greater than 6 percent both for the time-dependent and steady velocity profiles and are located along the chamber axis and the side wall.

The time steps chosen, Δt, were slightly smaller than the limits which meet the stability condition $\Delta t < \frac{1}{8}$. Re. Δr^2 given in [7]. The halving of the time step with the basic mesh has
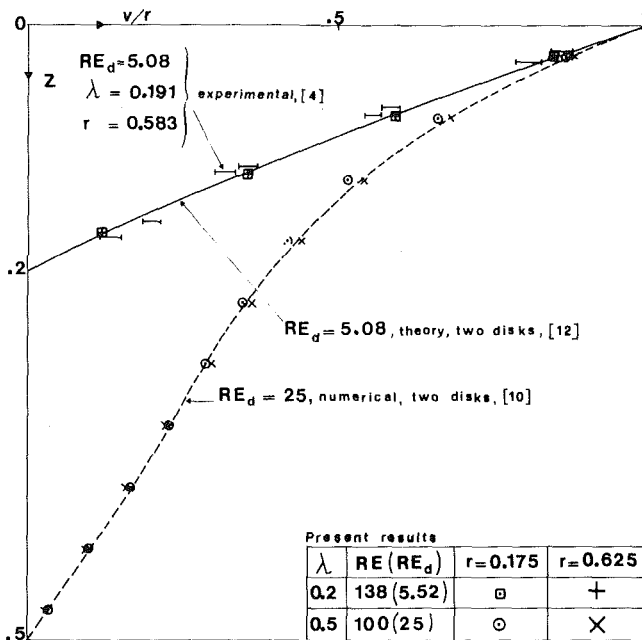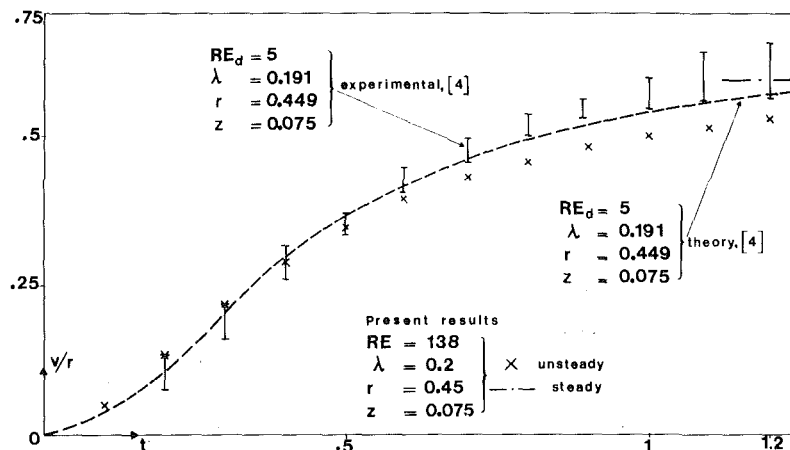

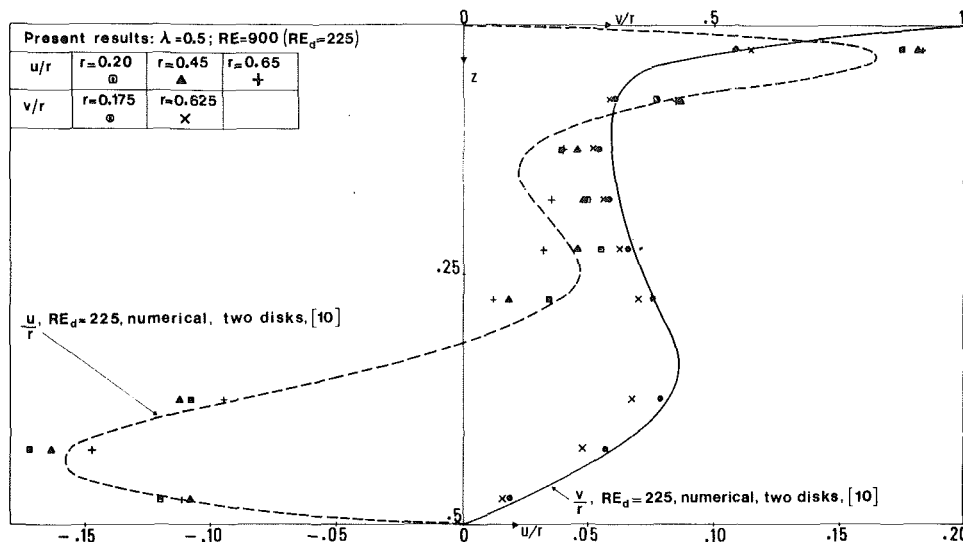Fig. 3 Comparisons between theoretical, numerical, and experimental unsteady $v(t)/r$ profiles

Fig. 4 Comparisons for u/r and v/r steady numerical results

precisely no effect on results; this was proved in cases Re = 1000, $\lambda = 0.5$, and Re = 1000, $\lambda = 2$.

An indication as to the incidence of artificial viscosity on numerical solutions in this paper was obtained by the evaluation of its coefficients which are proportional to Δr^2, Δz^2, Δt^2. Since in all cases they were estimated to be very small as compared with the dimensionless physical viscosity $1/\text{Re}$ [9], it is believed that solutions are not invalidated by numerical diffusion; thus consistency is preserved even for Re = 1000.

3 Some Comparisons With Available Data

Results from the case Re = 138, $\lambda = 0.2$, compared with the steady and unsteady experimental data in [4], in which the same geometry is studied as in this work, make it possible to test the reliability of this numerical scheme.

It must first of all be noticed that in [4, 10 and 11] (results from these references are cited in this paper) the distance d^* is used to define the Reynolds number. Therefore

$$\text{Re}_d = \text{Re} \cdot \lambda^2.$$

Bien and Penner [4] made their measurements in a chamber with $\lambda = 0.191$. A grid for the flow field with this value of λ would have required very small mesh sizes; thus $\lambda = 0.2$ was assumed here in order to simplify the grid adjustment to the field dimensions. The aforementioned authors gave information for steady azimuthal velocity profiles at $\text{Re}_d = 5.08$ (Re = 139); unsteady ones were instead measured at $\text{Re}_d = 5$ (Re = 137). To avoid repeating calculations twice, the solution in this paper was computed for the average value Re = 138. Some points from it, as well as steady experimental data from [4] are set out in Fig. 2. The agreement is fairly good. The grid used does not allow one to calculate any value for $r = 0.583$; however, the $r = 0.575$ and $r = 0.625$ $v(z)$ contiguous profiles are practically coincident; therefore points of the latter curve were marked on the figure as an interpolation for $r = 0.583$. Unsteady data are set out in Fig. 3. The numerical data transferred to the figure derive from an adequate interpolation and are therefore comparable with experimental results. For small enough dimensionless time, values from this work are within the scattering of experimental results. Instead, 7 percent departures are revealed for $0.65 < t < 1.2$ The agreement seems to improve going towards the steady conditions, as suggested by the present value.

The case Re = 100, $\lambda = 1$ was numerically solved by Pao [6] for the same geometry as above. Many corresponding profiles

Table 1   Times to reach steady flow versus Re and λ

Re \ λ	0.5	1	2
100	15	20	52.5
1000	67.5	90	195

from that paper and this were compared and the agreement was always found to be excellent. Results in [6] were obtained by a very different approach, as use was made of steady motion equations.

The data available in the literature did not enable us to make other comparisons for a finite cylindrical container besides those given above.

As a premise to what is following, let us recall that the apparatuses in this paper and in [4] can be considered as made of two finite disks surrounded by a cylindrical shroud. The solutions for Re = 138, $\lambda = 0.2$, and Re = 100, $\lambda = 0.5$ outlined by points in Fig. 2 reveal the presence of a broad region of the fluid field (approximately $0.15 < r < 0.65$) where v/r profiles as functions of z are almost independent of r. The figure shows a full overlapping for $\lambda = 0.2$ and a noticeable closeness for $\lambda = 0.5$ between the $r = 0.175$ and the $r = 0.625$ v/r sequences of marks. This has suggested comparisons with numerical results by Lance and Rogers [10] for two infinite disks, one of which is stationary. By the use of similarity solutions they transform the full Navier-Stokes equations into a system of ordinary, nonlinear, differential equations which are then treated by the Runge-Kutta method. The von Karman [12] similarity assumption states that v/r does not depend on r for two infinite disks. Data from [10] for $\text{Re}_d = 25$ and from this work for Re = 100, $\lambda = 0.5$ are seen to be in agreement in Fig. 2. However, some discrepancies are found when u/r and v/r profiles for Re = 900, $\lambda = 0.5$, $0.15 < r < 0.65$, and the corresponding data in [10] for $\text{Re}_d = 225$ are drawn on the same sheet (Fig. 4). In the borderline case of a simply diffusive steady transport of momentum either the presence or the absence of the shroud would make no difference as regards the shape of v/r profiles. This explains why the shroud has a small effect inside the aforesaid radial limits when Re is small enough, since the azimuthal momentum transport is almost entirely diffusive. When a large contribution to this transport is supplied by advection (Re = 1000), the finite geometry makes all velocity components very sensitive functions of r.

The applied numerical method ensures a fairly good agreement with the experimental results; the continuity
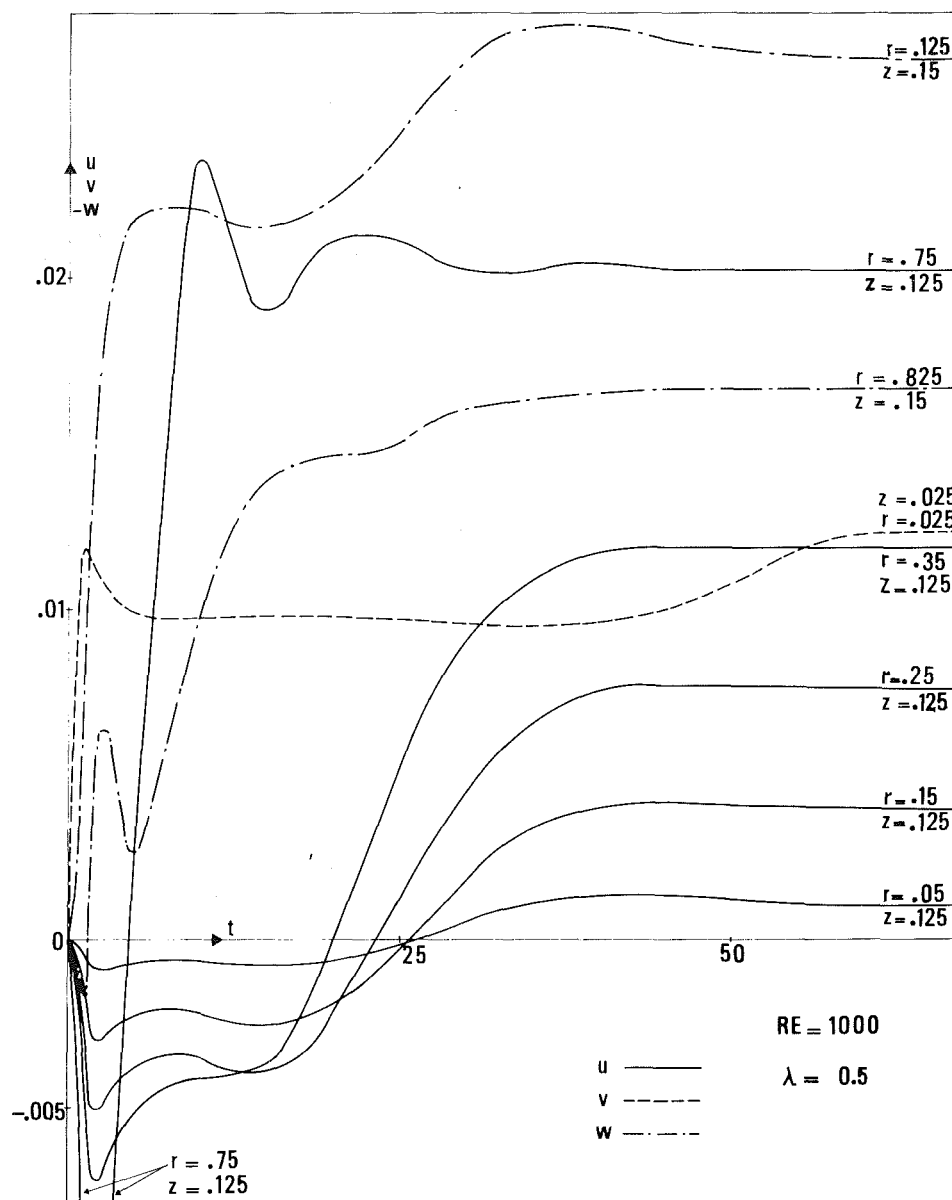
Fig. 5 Examples of u(t), v(t), w(t) behavior at some mesh points whose coordinates are quoted at the figure right edge

equation is met by u and w local values with a high degree of accuracy (10^{-12} at worst). Numerical diffusion acts only weakly upon solutions whose degree of convergence is estimated to be good with reference to the halved mesh size calculations. The M.A.C. method supplies an $O(\Delta r^2; \Delta z^2; \Delta t^2)$ accuracy for each discrete analogue to differential terms in the Navier-Stokes equations. Boundary conditions either are satisfied exactly or their accuracy is $O(\Delta r^2; \Delta z^2)$. Thus we believe that the results in this paper are a good approximation to exact solutions to the differential equations of motion.

4 Results and Discussion

Unsteady Flow. Plots of $u(t)$, $v(t)$, $w(t)$ for many points in every field of flow computed have shown how steady local conditions are approached and what influence is exerted by Re and λ.

Some features are common to the three velocity components. A general effect of an increasing Re at a constant λ is to lengthen the time needed to reach steady local values; the same effect is noted for an increase in λ at a constant Re (see

Table 1). The curves $u(t)$, $v(t)$, $w(t)$ may have different shapes even for contiguous grid points; sometimes they are spatially mutable in a quite sudden way. Thus in a flow region where a certain shape of behavior in time of a component largely prevails, some isolated inner mesh points may be found for which that component exhibits a different course.

For Re = 100 the steady local values are generally reached in a very simple way whatever the chamber height; $u(t)$, $v(t)$, $w(t)$ are very often monotonic increasing or decreasing functions according to whether their final values are positive or negative. For a few points these functions display no more than either one maximum or minimum which are more likely to occur near the upper portions of the chamber walls than elsewhere. As they were never found near the vessel bottom for all λ, it is inferred that the increased distance from the rotating disk affects time functions in such a way as to smooth down the extreme values. An influence of λ was observed, but it did not seem to lend itself to generalization. If the same functions are compared for the same coordinates in flow fields with different λ's, no recurrent behavior or well-defined trends can be detected. For Re = 1000, particularly when $\lambda = 0.5$, 1, $u(t)$, $v(t)$, $w(t)$ have a much more complicated
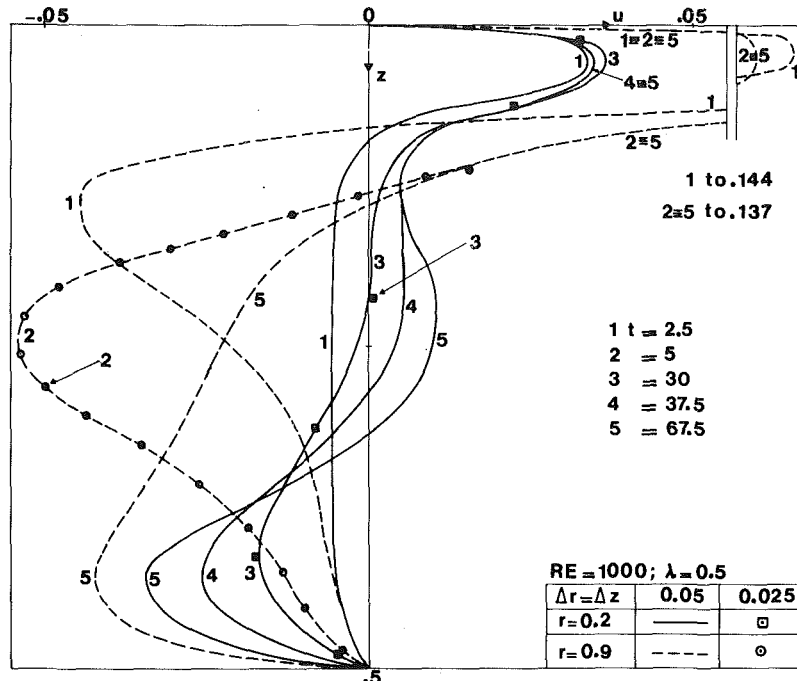
Fig. 6 Evolution in time of two $u(z)$ profiles at $r = 0.20$ (solid lines) and $r = 0.90$ (dashed lines). Labels indicate the time at which profiles have the configuration drawn.
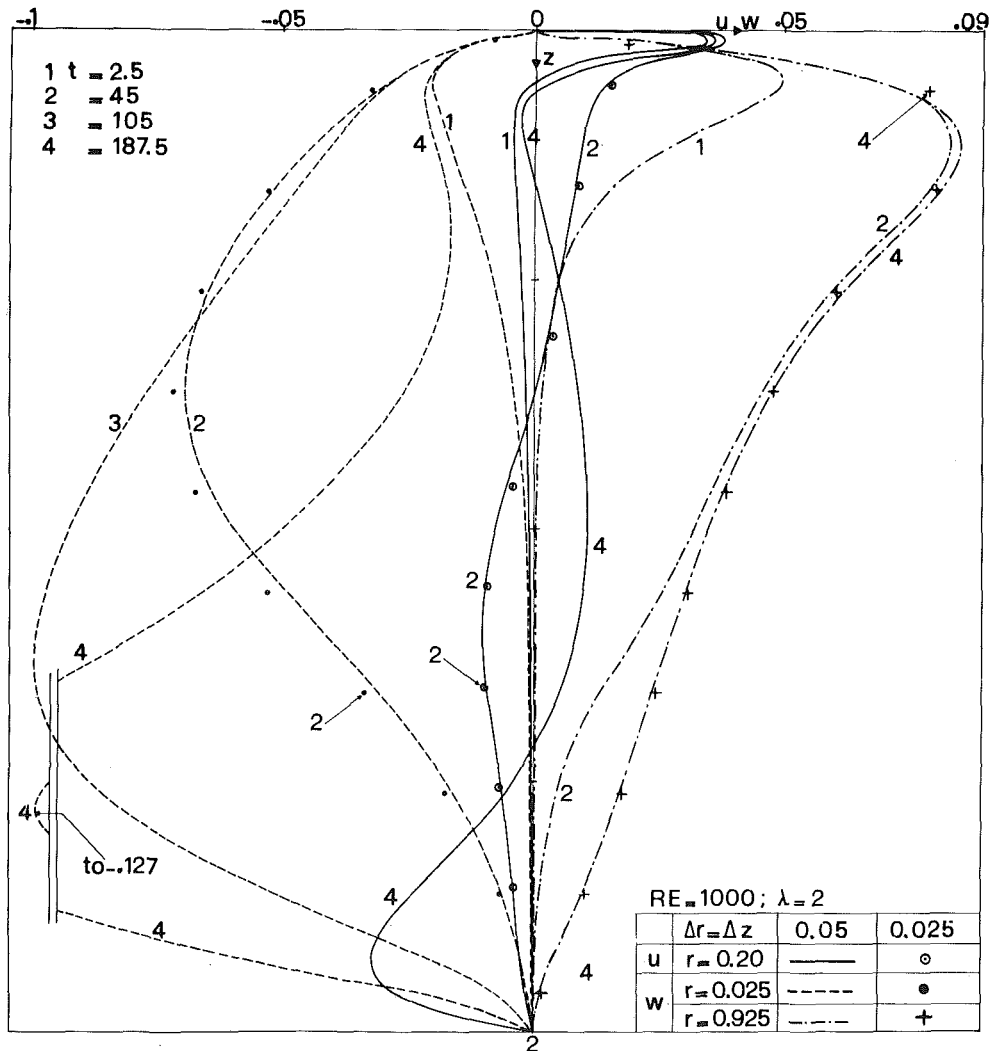
Fig. 7 Evolution in time of one $u(z)$ ($r = 0.20$, solid lines) and two $w(z)$ ($r = 0.025$, dashed lines and $r = 0.925$, dot-dashed lines) profiles
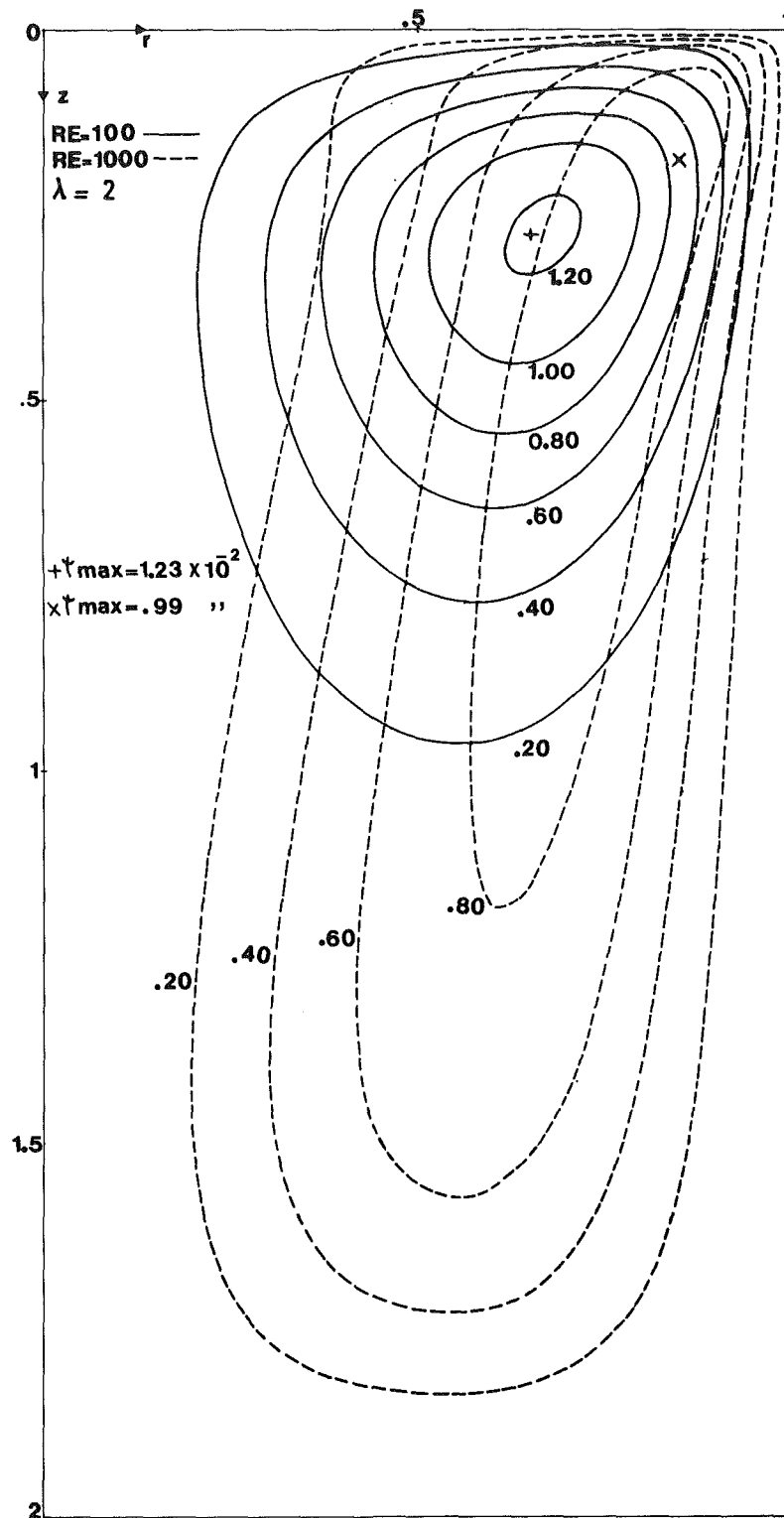
Fig. 8 Streamlines for the flow in the $\lambda = 2$ container

structure than for Re = 100. For most of the mesh points they attain steady values after repeated oscillations which sometimes cause the functions to change in sign. As the waves were almost faithfully reproduced by calculations with the halved mesh, they are probably real, not numerical distortions. The effect of the λ change is clearly observed. If points at equal r and z are considered, the growth of this parameter yields more or less apparent modifications which may include the increase in the wavelength, the amplitude diminution of

oscillations (roughly speaking, as they are never regular) and their reduction in number, particularly for $\lambda = 2$. The same effects on $u(t)$, $v(t)$, $w(t)$ are induced by a growing z for fixed λ and r, with some differences: Positions of the wave crests and troughs are shifted towards higher values of t, their heights are attenuated, and some of them may vanish. Time functions are monotonic for many, but not all, points near the bottom plate.

Some peculiarities were noted for the v velocity component.
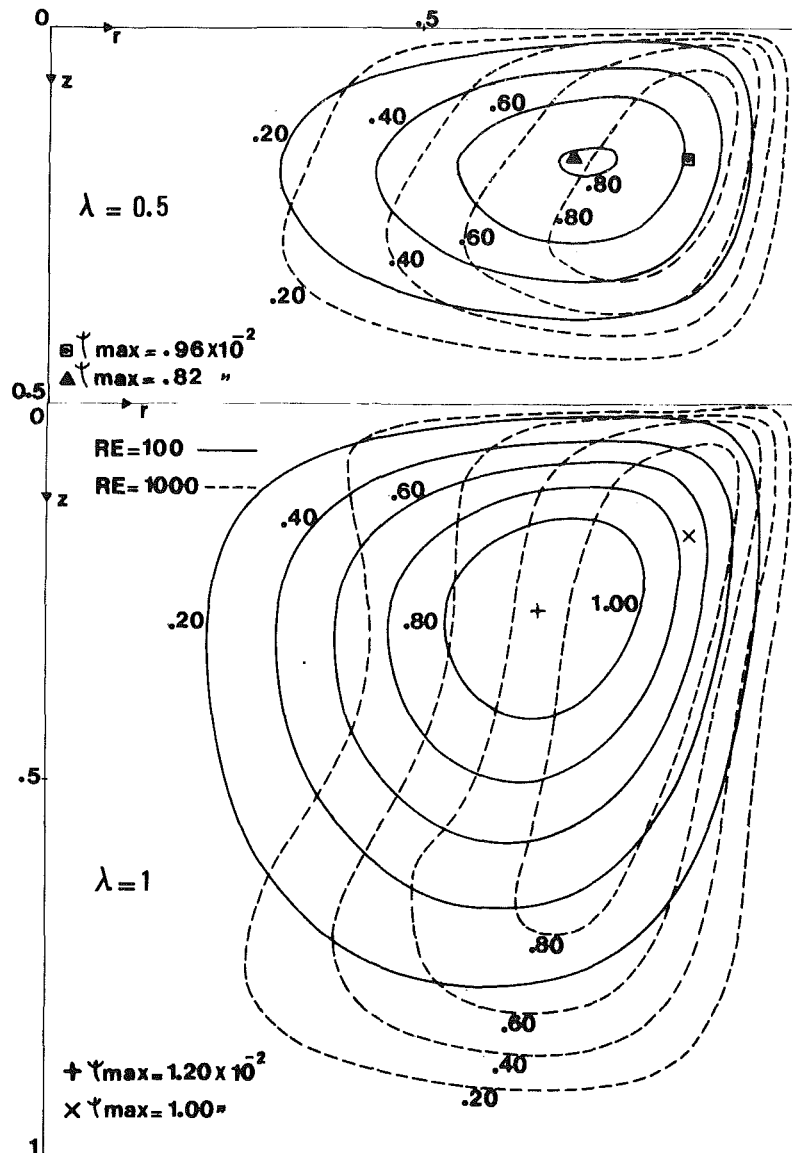
Fig. 9 Streamlines for the flow in the $\lambda = 0.5$ and $\lambda = 1$ containers

The $v(t)$ for all mesh points inside the left half of the upper rotational boundary layer always exhibits a maximum for Re = 100 and $\lambda = 1$, 2. When Re = 1000 and $\lambda = 2$, $v(t)$ curves do not show oscillations for many mesh points far enough from the rotating disk; there, $v(t)$ curves have only one maximum.

Several examples of evolution in time of the local velocity components are plotted in Fig. 5; the $u(t)$ curve for $r = 0.75$, $z = 0.125$ is cut by the lower edge of the figure. Figure 6 shows how time progressively modifies the shape of two $u(z)$ profiles for the case Re = 1000, $\lambda = 0.5$. In order to reduce the extension of figures, here and elsewhere, those plots with very prominent maxima and/or minima were cut; their ordinates were quoted whereas the values of their spatial coordinates, r or z, were not altered and are readable in the figures. This procedure was used in Fig. 6 for No. 1, 2, 5 dashed curves.

The evolution in time of one $u(z)$ and two $w(z)$ profiles for the case Re = 1000, $\lambda = 2$ is set out in Fig. 7. The radial boundary layer at the rotating disk is settled early (see solid lines) and there the u curve undergoes only minor modifications after a very short time from the beginning of the motion. Near the bottom base of the vessel the steady configuration is approached slowly. This also holds for the $w(z)$ profile close to the chamber axis (dashed lines) which

presents its minimum not far from the bottom base; the process of accelerating the upward stream takes all the time of the spin-up. This is not the case for the $w(z)$ profile near the side wall (dot-dashed lines). A survey of the figure gives the idea of a slow, fatiguing, progressive propagation of the recirculating motion towards the deep regions of the chamber.

Dimensionless times at which computations were stopped are quoted in Table 1. After these times steady conditions were deemed to exist everywhere, as azimuthal viscous and inertia forces were seen to be locally equal (consider equation (1) for steady conditions and [9]) throughout the flow field.

The stream due to the v component only is called primary flow. Its evolution in time is very fast for points inside the upper rotational boundary layer; the slowest development occurs near the bottom end of the chamber axis. So spin-up times are functions of r and z.

The combined action of u and w components generates the so-called secondary flow. Its evolution was followed by observing the modifications of the stream function surfaces, $|\psi(r,z,t)|$, which always showed only one maximum except for Re = 1000, $\lambda = 2$, $25 < t < 53$; in this time interval two maxima coexist. The suspicion of a disagreement with what can be seen in Fig. 5 of [3] arose. In that figure two maxima of $|\psi(r,z)|$, or two flow cores, are drawn in the field of flow for

Table 2 Several quantities versus Re and λ

λ	0.5		1		2	
Re	100	1000	100	1000	100	1000
P	$.792 \times 10^{-1}$	$.713 \times 10^{-1}$	$.951 \times 10^{-1}$	$.102$	$.101$	$.145$
S	$.513 \times 10^{-1}$	$.602 \times 10^{-1}$	$.756 \times 10^{-1}$	$.627 \times 10^{-1}$	$.772 \times 10^{-1}$	$.622 \times 10^{-1}$
C_m	$.338$	$.592 \times 10^{-1}$	$.343$	$.611 \times 10^{-1}$	$.343$	$.625 \times 10^{-1}$

the steady condition of a case (Re = 1296, λ = 0.33 according to definitions in the present paper) whose parameters are only slightly different from Re = 1000, λ = 0.5. So that case was checked and two flow cores were never found during the entire evolution of the fluid motion.

Some words about the transport of the angular momentum tangential component seem useful. Distributions of tangential viscous and inertia force were followed during the development of the flow. For Re = 100, spin-up from rest is essentially driven by viscosity and then it is of a diffusive type for all λ. When Re = 1000, inertia forces largely contribute to the angular momentum transport, particularly for the smaller values of λ; a mixed diffusive and convective character is ascribed to it. But there is evidence that the increase in λ at this Re tends to stress the diffusion phenomena.

Steady Flow. No figure relative to the steady flow was included in the text for the sake of brevity. Figures are however available. The pattern of the steady flow is described.

Azimuthal velocities become comparatively smaller and smaller near the bottom plate for Re = 100 and an increasing λ. For λ = 2 the fluid particles in the bottom half of the container have negligible v components. This is why the transport of angular momentum is almost only diffusive and the constraint of the boundary conditions prevents this quantity from penetrating the container deeply. Passing to Re = 1000, rotational boundary layers at the cover become thinner and, as for Re = 100, they are very weakly affected by the value of λ. The smaller it is, the greater the v values are near the lower disk. There, they are now important in all cases. A conspicuous contribution to the transport of angular momentum is given by advection and the secondary flow is capable of conveying this quantity down to the bottom of the vessel.

Effects of Re and λ on the velocity components of the secondary flow were clearly pointed out. Well developed radial boundary layer are present at both end plates of the container for Re = 100 and λ = 0.5, 1, but not for λ = 2; in the latter case u velocities are vanishingly small near the bottom base where instead radial boundary layers are found for Re = 1000; for this value of Re they appear to be reinforced at both end plates of the shorter containers. The influence of λ is weakly felt by $u(z)$ curves near the rotating disk; instead its increase attenuates radial boundary layers at the bottom plate.

As Re rises, the axial boundary layer along the side wall of the chamber becomes thinner, and the descending stream, whatever λ may be, is quickened. The position of the minima of $w(z)$ profiles near the chamber axis (one of such profiles is shown in Fig. 7) are shifted z-wise in passing from Re = 100 to Re = 1000, for which value they are located near the bottom plate. Thus the core of the ascending stream is more quickly accelerated to its maximum speed for Re = 1000 than for Re = 100. This maximum speed is not greatly influenced by the change of Re at λ = 0.5; the same cannot be said for λ = 1, where the maximum ascending speed for Re = 100 is never reached at Re = 1000, nor for the λ = 2 container, in which a considerable increase in velocity takes place. The variation of λ from 0.5 to 1 causes a growth of both maxima and minima for all $w(z)$ lines; this effect is less apparent, or even op-

posite, for some profiles in passing from λ = 1 to λ = 2. For this increase at Re = 100 the w component almost ceases to exist at the chamber bottom. There, the w negative values rise with λ at Re = 1000 while positive ones attenuate.

Many $w(r)$ plots were drawn and analyzed. They showed that, regardless of the value of λ, when Re = 1000, there is a restricted region of the flow core where the ascending stream is faster than the surrounding fluid near the bottom plate, but becomes slower travelling towards the cover. From the observation of the shapes of $w(r)$ profiles in proximity to $r = 1$, it is deduced that the increase of λ reinforces the flow in the axial boundary layer for both values of Re. As the intersection points between $w(r)$ profiles and the abscissa (w is negative for a small r and positive for a great one) are shifted right by the rise of this quantity, a broadening of the ascending stream is caused for any value of λ.

Figures 8 and 9 show the pattern of the secondary flow for the six cases computed. Streamlines for λ = 0.5 were drawn at the top of Fig. 9. For Re = 100 equally labelled streamlines run over much more restricted regions of the motion field than for Re = 1000, particularly when λ = 2. It is confirmed that the rise in λ progressively enlarges the areas where all velocity components are very small or tending to extinction if Re is kept within the viscous range. When Re = 1000 the secondary flow is not so sluggish at the chamber bottom, and there radial boundary layers can then develop.

5 Some Remarks on Several Computed Quantities

Three quantities have been calculated to characterize the operation of the apparatus and are quoted in Table 2 in terms of Re and λ.

Primary volumetric flow rate is defined as

$$\frac{P^*}{\Omega^* R^{*3}} 8 = P = \int_0^\lambda \int_0^1 v \, dr \, dz.$$

It is an indication of the effectiveness of the disk in driving the fluid into rotational motion. The chamber volume expansion causes P to increase for a fixed Re. One must note that for λ = 0.5 P decreases in passing from Re = 100 to Re = 1000; the contrary is true for λ = 1, 2. When Re is raised in a shallow vessel, the diminution of the rotating disk driving effect overcomes the increasing importance of advection in redistributing angular momentum and P decreases. The contrary happens when λ ≥ 1.

Secondary volumetric flow rate is defined as

$$\frac{S^*}{\Omega^* R^{*3}} = S = 2\pi r_1 \int_0^{z_1} u \, dz$$

if use is made of the radial velocity component; r_1 and z_1 are the coordinates of the toroidal vortex center. S is the well-known indication of the pumping effect of the rotating disk. It is not very sensitive to Re and λ changes within the ranges here investigated.

Torque coefficient is calculated by the following expression:

$$\frac{C_m^*}{\frac{1}{2}\rho^* \Omega^{*2} R^{*5}} = C_m = \frac{4\pi}{Re} \int_0^1 \left| \frac{\partial v}{\partial z} \right|_{z=0} \bullet r^2 \bullet dr.$$

C_m is not substantially varied by a change in λ if Re = 100,

and only weakly so if Re = 1000. But it is strongly decreased by the rise in Re for any value of λ. The pumping effect increases with λ for Re = 100; the best S is found for a small Re and a large λ, but its cost in terms of C_m is not the least. From this viewpoint the condition Re = 1000, λ = 1 is centainly the most advantageous (consider the C_m/S ratio). If one wanted to reinforce P, the best condition would be Re = 1000, λ = 2, with which the least C_m/P and S/P ratios are also connected; the smallest S for the unitary P would be driven into circulation.

$C_m = 0.31$ is calculated in [6] for Re = 100; λ = 1. This value must be doubled if one wants C_m for a disk rotating in the mid-height position of a container with λ = 2. The first value agrees fairly well with the corresponding datum in Table 2 if it is remembered that C_m in [7] is said to be under-estimated. The second value makes it possible to compare C_m values for Re = 100 and two different positions of the rotating disk in the same λ = 2 container. It is $C_m = 0.62$ for the disk in the central position versus $C_m = 0.34$ (Table 2) when it is at the top end of the chamber.

6 Conclusion

It was found that all aspects of this case of spin-up from rest are influenced by both Re and λ parameters. Somewhat different evolutions of the unsteady flow were observed for Re = 100 and Re = 1000. In the first case the transport of angular momentum is essentially diffusive; in the second case a redistribution of this quantity is operated by the centrifugal action of the rotating disk and its transport appears to have a mixed diffusive and convective character.

An increase of λ at Re = 1000 tends to stress the viscous behavior.

Steady solutions for v show that the rotational flow is brisk in the whole chamber only for small values of λ. When this is raised, most of the fluid cannot acquire a large amount of angular momentum whatever the Re number is. The rotating disk is not capable of supporting an active rotational flow at a great distance; almost motionless regions exist there, which extend more and more with an increasing λ.

The same can be said for the secondary flow if Re = 100. When the chamber is elongated, the pumping effect of the rotating disk is less and less capable of activating a secondary

circulation in such a way that u and w magnitudes can be of the same order near to and far from the cover. The case λ = 2 is significant. There is instead only a slight unbalance between top and bottom u and w steady values for Re = 1000 and any value of λ in the investigated range.

The calculation of P, S, C_m has thrown light on how several integral effects and their modifications are linked to the geometry and operating conditions of the apparatus; a criterion for the use of these effects is thus immediately at our disposal.

References

1 Grohne, D., "Über di laminare Strömung in einer kreiszylindrischen Dose mit rotierendem Deckel," *Nachr. Akad. Wiss. Gottingen*, Vol. 12, 1955, pp. 263–281.

2 Daily, J. W., and Nece, R. E., "Chamber Dimensions Effects on Induced Flow and Frictional Resistance of Enclosed Rotating Disks," ASME *Journal of Basic Engineering*, 1960, pp. 217–232.

3 Dorfman, L. A., and Romanenko, Yu.B., "Flow of Viscous Fluid in a Cylindrical Vessel With a Rotating Cover," *Izv. Acad. Nauk. SSSR, Ser. Mek. Zhidk. Gaza*, Vol. 1, 1966, pp. 63–69.

4 Blen, F., and Penner, S. S., "Velocity Profiles in Steady and Unsteady Rotating Flows for a Finite Cylindrical Geometry," *Phys. Fluids*, Vol. 13, 1970, pp. 1665–1671.

5 Tomlan, P. F., and Hudson, J. L., "Flow Near an Enclosed Rotating Disk: Analysis," *Chem. Eng. Sci.*, Vol. 26, 1971, pp. 1591–1600.

6 Pao, H. P., "Numerical Solution of the Navier-Stokes Equations for Flows in the Disk Cylinder System," *Phys. Fluids*, Vol. 15, 1972, pp. 4–11.

7 Williams, G. P., "Numerical Integration of the Three Dimensional Navier-Stokes Equations for Incompressible Flow," *Journal of Fluid Mechanics*, Vol. 37, 1969, pp. 727–750.

8 Roache, P., *Computational Fluid Dynamics*, Hermosa Publishers, 1972.

9 Bertelà, M., "Effect of the Chamber Depth on Steady and Unsteady Flow of a Rotating Fluid in A Finite Cylindrical Container - I," *Comp. and Fluids*, Vol. 7, 1979, pp. 231–246.

10 Lance, G. N., and Rogers, M. H., "The Axially Symmetric Flow of a Viscous Fluid Between Two Infinite Rotating Disks," *Proc. Roy. Soc.*, Vol. A266, 1962, pp. 109–121.

11 Mellor, G. L., Chapple, P. J., and Stokes, V. K., "On the Flow Between a Rotating and a Stationary Disk," *Journal of Fluid Mechanics*, Vol. 31, 1968, pp. 95–112.

12 von Karman, T., "Laminare Reibung an einer rotierenden Scheibe," *Z. Angew. Math. Mech.*, Vol. 1, 1921, pp. 244–252.

Discharge Jet Interaction With Multiple Port Diffusers

F. Y. Sorrell

Professor.

B. W. Smith

Graduate Research Assistant.

Department of Mechanical and Aerospace
Engineering,
N.C. State University,
Raleigh, N.C.   27650

A model for the flow dynamics and mixing in the near-field of a multiple port outfall diffuser is postulated. It employs the equations for gross conservation of mass, momentum, and buoyancy of the fluid in the discharge jet or plume. These equations are obtained by assuming flow similarity and then integrating over the cross-sectional area of the plume. Two distinct interactions of the discharge jets or plumes are included in the model. These are the interaction of the individual round jets from the diffuser ports and the merging of the plume from either side of the diffuser, over the top of the diffuser. The resulting equations are closed by the "entrainment assumption" and solved numerically. Results provide the velocity, width, and dilution of the jet or plume. Calculations were made for a number of cases where experimental results were available. The model gives reasonable agreement with the experiments over a wide range of discharge conditions and over the complete range of flow patterns. In most cases it slightly underestimates the mixing or dilution. Therefore the model should be useful in determining the minimum dilution that can be expected from any marine outfall.

Introduction

A rather common problem in hydraulics is the disposal or discharge of a quantity of waste liquid into a large volume of surrounding ambient water. The situation encountered most often is the disposal of wastewater from a sewage treatment plant or the discharge of condenser cooling water from power generating facilities. If the amount of toxic materials in the effluent is small, it is usually possible to achieve an acceptable environmental or public health impact simply by diluting the effluent with the background water. The problem then becomes the fluid mechanics of how to mix the effluent with the background water as much and as rapidly as possible. This has received considerable attention in the past 20 years, primarily because of the construction of rather large waste treatment and power generating facilities.

The usual geometric arrangement to promote mixing is to inject the effluent through a multiple port diffuser at the end of the discharge pipe. This type of diffuser consists of a series of holes or ports spaced at certain intervals along the pipe. The ports are usually located on each side of the pipe and alternated to prevent flow instabilities via oscillating flow between the ports. A typical configuration is shown in Fig. 1 and Brooks [1] has given a rather complete summary of design considerations for this type of outfall diffuser.

As is shown in Fig. 1, the discharge from a multiple port (multiport) diffuser initially consists of a series of round horizontal jets. These jets are driven outward by the discharge momentum and usually upward because the effluent is less dense than the background fluid. As the round jets entrain fluid, their diameter increases and ultimately the individual
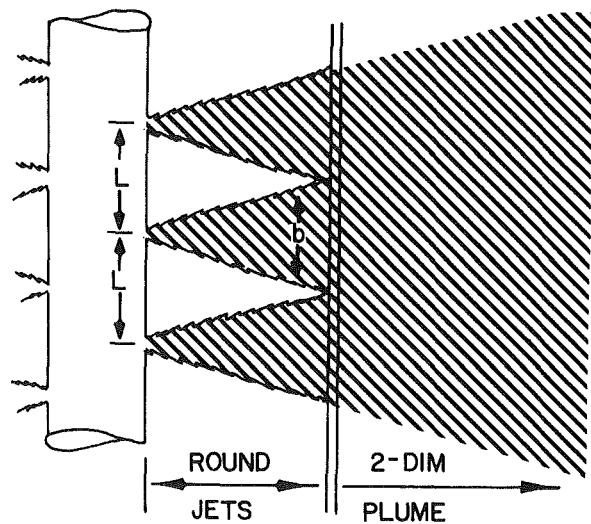
Fig. 1   Schematic of round jet interference plan view

jets begin to interfere with each other. It is generally accepted (Koh and Fan [2], Jirka and Harleman [3], and Shiranzi and Davis [4]) that the individual round jets interact to form a two-dimensional or slot jet. The situation is depicted in Figs. 1 and 2, where the resulting flow field, after interaction of the round jets, is a two-dimensional buoyant plume rising from either side of the diffuser pipe. These plumes continue to entrain fluid as they rise. Because there is a limited volume of background fluid between the two plumes, they move toward each other due to conservation of the mass between the two plumes. If the receiving water is sufficiently deep, the two-

SINGLE VERTICAL
PLUME
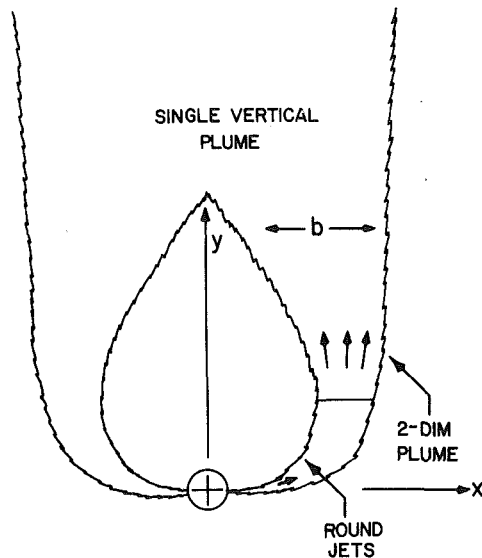
Fig. 2 Schematic of two-dimensional plume merging to single vertical plume. End view.

dimensional plumes will eventually merge together as they rise and form a single vertically rising plume. It is a plume in the true sense, because the horizontal discharge momentum has been canceled and the only driving mechanism is the buoyancy of the less dense effluent. The merging or joining of the two-dimensional plumes has been observed in the field and has been demonstrated by the laboratory experiments of Liseth [5].

Therefore, although the effluent discharge from a multiport diffuser begins initially as a series of round horizontal jets, these jets usually interact very quickly to form a two-dimensional plume. The plumes on either side of the diffuser then merge over the diffuser and result in a single vertically rising plume. If the diffuser is located in deep water, the details or fine structure of the flow patterns do not greatly alter the final flow geometry or dilution of the effluent as it reaches the surface (or a terminal level). This has been demonstrated by the numerical experiments of Wallis [6]; and, in fact, Koh and Brooks [7] have utilized this observation to obtain preliminary estimates of dilution by simply considering only a vertical plume. The reason this is accurate is because the discharge momentum is quickly dissipated, by turbulent entrainment, and thus the primary long term driving mechanism is buoyancy.

In shallow water, however, the round jet interaction and the subsequent merging of the two-dimensional plumes may not have been completed before the rising effluent reaches the background water surface (or the terminal level). Here the dilution, velocity, and configuration of the discharge plume does depend on the degree of interference that has occurred between the jets. Therefore an accurate calculation of the

mixing requires an analysis of the round jet interference and of the merging of the two-dimensional plume. This paper provides a rather simple model for these two processes, but one that agrees reasonably well with existing experimental data.

In some cases, particularly in shallow water, high volume thermal discharges may modify the flow field far from the diffuser. This situation has been considered by Jirka and Harleman [3] and is not considered here. However, the present interaction model would still apply for the near-field. Finally, most design calculations are for "worse case" conditions or the set of circumstances that produces the least mixing. Usually this is zero current, although the recent work of Nospal and Tatinclaux [8] indicates that this may not always be the case. Therefore this paper deals with multiple jet interaction in the near-field and with zero background current.

Model

The model utilized has its origin in the classical work by Morton, Taylor, and Turner [9] and by Priestley and Ball [10]. They assume quasi-similarity in the sense that the mean flow is self-similar and that the turbulent entrainment can be directly related to the mean flow. In this approach, the equations of motion are integrated over the cross-sectional area of the jet or plume to give "gross-flux equations." For example, the equations used by Morton, Taylor, and Turner [9] are conservation of mass, momentum, and buoyancy. They close the system of equations by the "entrainment assumption," which asserts that the velocity at which the background fluid is drawn into the jet or plume (the entrainment velocity) by turbulent diffusion can be related to the mean flow parameters. One of the first applications of this approach to outfalls was by Fan [11] and by Fan and Brooks [12]. There have been numerous other approaches and improvements basically using this method. Morton [13] gives an excellent discussion of the various different conservation equations that have been used and the particular advantages of each. When using the entrainment assumption, the entrainment velocity is usually related to the mean flow velocity at the jet or plume centerline by use of an entrainment coefficient. The entrainment velocity being the entrainment coefficient times the mean velocity at the centerline. The question of the functional relation between the entrainment coefficient and the mean flow quantities has been considered in detail by List and Imberger [14]. At approximately the same time, Jirka and Harleman [3] suggested a specific relation for the two-dimensional buoyant jet, based in part on the work of Fox [15]. In the work considered here, the discharge momentum is very quickly dissipated and for most of the calculation the discharge is essentially a plume. Therefore, the present calculation uses a constant value of entrainment coefficient, typical of that recommended by Brooks [16] for plumes. The actual values are given in Table

─────── **Nomenclature** ───────

b = jet or plume width	r = radial coordinate normal to plume axis (round plume)	θ = angle of plume axis with horizontal
Fo = densimetric Froude No. based on port diameter	s = distance along jet or plume axis	λ = spreading coefficient (λ^2 = Schmidt no.)
g = acceleration of gravity	u = jet or plume velocity	$\rho(s)$ = density of fluid in jet or plume
H_m = height of plume use before merging	V_e = entrainment velocity	$\Delta\rho$ = density of difference between jet or plume fluid and background fluid
K = plume translation coefficient	V_n = plume translation velocity	
L = port spacing (cf., Fig. 1)	x = horizontal coordinate	ρ_0 = density of background fluid at discharge port
n = coordinate normal to plume axis (two-dimensional plume)	y = vertical coordinate	
	α = entrainment coefficient	ρ_a = density of background fluid

Table 1 Values of entrainment coefficient α and spreading ratio λ used for the calculations

	α	λ
Round jets	0.082	1.16
Slot and vertical plume	0.14	1.0

1. When the assumptions and restrictions that follow are considered, the use of a constant entrainment coefficient seems appropriate.

The discharge leaves the diffuser as a series of round jets and the model starts by applying the procedure to the individual round jets. Initial conditions are the jet diameter and velocity, as computed from the hydraulic analysis (cf., Sorrell [17]). These are corrected for the transition from approximately uniform flow out of the port to the assumed Gaussian velocity profile by using the results of Albertson, et al. [18]. This results in a velocity profile of the form:

$$u(r,s) = u(s)\, e^{-r^2/b^2} \qquad (1)$$

where u = centerline velocity, s = distance along the jet or plume axis, r = the coordinate normal to the plume axis, and b = the (local) plume diameter. In order to allow for different rates of spreading (different effective diameters) between mass and momentum, the density profiles are represented by:

$$\frac{\rho_a - \rho(s,r)}{\rho_0} = \frac{\rho_a - \rho(s)}{\rho_0}\, e^{-r^2/(\lambda b)^2} \qquad (2)$$

where ρ_0 = the ambient or background density at the discharge location, ρ_a = the ambient density, $\rho(s)$ the density of the fluid in the jet or plume, and λ_1 = the ratio between the mass transfer diameter and the momentum transfer diameter of the jet or plume. As such λ_1^2 is the turbulent Schmidt number which is assumed constant and is usually found to be somewhat larger than one.

These profiles are then integrated over the area of the jet or plume to yield gross flux conservation equations. In the present approach, equations for conservation of mass, momentum, and buoyancy are obtained. Brooks [16] gives a summary of this calculation and a report by Ditmars [19] provides a detailed description of the procedure as applied to a single round jet. After integration and some subsequent manipulation, one obtains a set of total differential equations for the centerline velocity, u, the jet or plume diameter, b, the buoyancy $\rho - \rho(s)$, the angle of the jet or plume axis with the horizontal, θ and the x and y coordinates of the axis. These equations are:

$$\frac{du}{ds} = \frac{2g\lambda_1^2(\rho_a - \rho)\sin\theta}{u\rho_0} - \frac{2\alpha_1 u}{b} \qquad (3)$$

$$\frac{du}{ds} = \frac{2\alpha_1 g\lambda_1^2(\rho_a - \rho)\sin\theta}{u^2\rho_0} \qquad (4)$$

$$\frac{d(\rho_a - \rho)}{ds} = \frac{1 + \lambda_1^2}{\lambda_1^2}\frac{d\rho_a}{dy}\sin\theta\,\frac{2\lambda_1(\rho a - \rho)}{b} \qquad (5)$$

$$\frac{d\theta}{ds} = \frac{2g\lambda_1^2(\rho_a - \rho)\cos\theta}{u^2\rho_0} \qquad (6)$$

$$\frac{dx}{ds} = \cos\theta \qquad (7)$$

$$\frac{dy}{ds} = \sin\theta \qquad (8)$$

Using the previously established initial conditions, these equations are then integrated numerically. Two numerical procedures were used. One was an extrapalation algorithm developed by Bulirsch and Stoer [20] and the other was a modified Adams predictor-corrector algorithm developed by

Gear [21]. Neither technique proved superior to the other, either in computational costs or in accuracy. The use of two different computational techniques does increase confidence in the accuracy of the results. The calculation proceeds assuming a round jet until the diameter of the jet, b, equals some fraction of the port spacing L (cf., Fig. 1). At this time, the computation switches the model from a round jet to a two-dimensional or slot plume. This approach to round jet interference had been suggested previously by Cedewall [22] and utilized by Jirka and Harleman [3]. An alternate criteria for transition has been suggested by Koh and Fan [2] based on equal entrainment rates. While this may be more satisfactory from a philosophical view, the result is essentially the same as the previously proposed criteria. Implicit in this procedure is the assumption that the transition from a self-similar round plume to a self-similar two-dimensional plume is quite rapid.

The model thus produces transition from round to slot plumes when the round plume width equals some fraction of the port spacing. Present calculations were made using equivalence of the two, $b = L$. The transition provides a slot plume whose initial width is that of the round plume before transition, which is also the port spacing L (cf., Fig. 1). The initial centerline velocity and concentration in the slot plume are assumed to be equal to those of the round plume immediately before transition. The initial conditions for the slot plume are thus established.

If merging of the slot plumes is not a consideration, the integral technique can then be used to continue the calculation. The equations and procedure have been summarized by Brooks [16]. A detailed description with constant entrainment coefficient is given by Sotil [23] and with a variable entrainment coefficient by Jirka and Harleman [3]. However, if the merging of the two slot plumes from either side of the diffuser is to be considered, some modification of this procedure is required.

In order to model the merging of the slot plumes, the following mechanism is postulated. Before the round plumes begin to interact, the volume of background fluid between these plumes is basically unrestricted and thus there is very little, if any, tendency for the round plumes on either side of the diffuser to move toward each other. After formation of the two-dimensional or slot plume, flow of the background fluid into the region between the plumes can occur only at the ends of the diffuser and is thus severely restricted. Accordingly, merging of the two-dimensional plumes is assumed to begin after the transition from the round to the two-dimensional plumes. When this occurs, the two-dimensional plume is shifted, normally to the centerline, toward the diffuser. This is because the background fluid between the two plumes is restricted in volume and is being entrained into the plume. Moreover, it is argued that the shift of the plumes (toward each other, see Fig. 2) is directly related to the entrainment velocity. The present model assumes that the plumes move toward each other at some fraction of the entrainment velocity. Implicit in this is the assumption that the entrainment is unchanged by the merging process.

The gross-flux equation for the slot plume is thus modified by inclusion of a velocity normal to the plume axis. This velocity is:

$$V_n = KV_e \qquad (9)$$

where V_n is the velocity of the plume normal to its axis (see Fig. 2), V_e is the entrainment velocity, and K is some constant less than or equal to one. Using the concept of an entrainment coefficient, α_2, the equation becomes:

$$V_n = K\alpha_2 u \qquad (10)$$

where u is the centerline velocity. It is reasonable to expect the merging to become more pronounced (larger shift normal to the plume axis) as the plume rises. Therefore, the original

intention was to vary K through the calculation and to determine the most accurate way to do this from experiments. However, as discussed in the next section, due to a lack of relevant experimental results, simply selecting $K = 1$ was all that reasonably could be done.

Again, Gaussian profiles are assumed for the velocity and density distributions in the two-dimensional plume. That is the two-dimensional velocity given by

$$u(n,s) = u(s) e^{-n^2/b^2} \qquad (11)$$

where $u =$ the center velocity as before, $n =$ the coordinate normal to the plume axis, and $b =$ the (two-dimensional) plume width. The profile of density deficiency with respect to the ambient density is given by

$$\frac{\rho_a - \rho(s,n)}{\rho_0} = \frac{\rho_a - \rho(s)}{\rho_0} e^{-n/\lambda_2^2 (b)^2}$$

where the density symbols, ρ, take the same meaning as in equation (2). Again λ_2^2 is the turbulent Schmidt, but, in this case, for a two-dimensional plume rather than the round jet or plume. Values that were used for α_1 and α_2 and of λ_1 and λ_2 are provided in Table 1; these values have been suggested by Brooks [16]. Using these expressions, the two-dimensional plume is also integrated over its area to yield gross flux conservation equations. These equations, including the terms to account for the merging of the plumes, are as follows:

$$\frac{du}{ds} = \frac{\sqrt{2}g\lambda_2(\rho_a - \rho)\sin\theta}{u\rho_0} - \frac{2\alpha_2 u}{\sqrt{\pi}b} \qquad (12)$$

$$\frac{db}{ds} = \frac{4\alpha_2}{\sqrt{\pi}} - \frac{\sqrt{2}g\lambda_2(\rho_a - \rho)b\sin\theta}{u^2\rho_0} \qquad (13)$$

$$\frac{d(\rho_a - \rho)}{ds} = \frac{(1+\lambda_2{}^2)^{1/2}}{\lambda_2{}^2} \frac{d\rho a}{dy}\sin\theta - \frac{2\alpha_2(\rho_a - \rho)}{\sqrt{\pi}b} \qquad (14)$$

$$\frac{d\theta}{ds} = \frac{\sqrt{2}g\lambda_2}{\rho_0}(\rho_a - \rho)\frac{\cos\theta}{u^2} + \left[\frac{K\alpha_2}{[x^2+y^2]^{1/2}}\right] \qquad (15)$$

$$\frac{dx}{ds} = \cos\theta - [k\alpha_2\sin\theta] \qquad (16)$$

$$\frac{dy}{ds} = \sin\theta + [k\alpha_2\cos\theta] \qquad (17)$$

All symbols in these equations have been defined previously. The terms on the right of equations (15–17) (enclosed by the square brackets) are the additional terms added to model the merging process.

The trajectory of the two-dimensional plume is computed and the inner and outer edges of the plume calculated at each step. This edge is defined as the width where velocity has decreased to $1/e^2$ of centerline velocity. The inside edge of the plume is that side closest to the diffuser. If the inside edges of both plumes overlap, the plumes are then assumed to have merged. Because the flow pattern is symmetric, this occurs at $x = 0$. Therefore, the merging criteria is when the inner edge of the plume intersects the $y -$ axis. After this occurs, the model makes the transition to a single vertically rising plume. The initial conditions for the vertical plume are an initial width of twice the single plume (two individual plumes have merged), and initial velocity and concentration equal that of the two-dimensional plumes before merging. The calculation is then completed, i.e., carried to the surface or to the computed terminal level, as a single vertically rising plume. Numerically, this is a special case of the two-dimensional plume and is quite easily carried out. Figure 3 shows a graph of the previously defined edges of a plume. The calculation is for 9.15 cm (0.30 ft) dia ports, spaced 731 cm (24 ft) apart on each side of the diffuser and with a discharge velocity of 192 cm/s (6.3 ft/s).
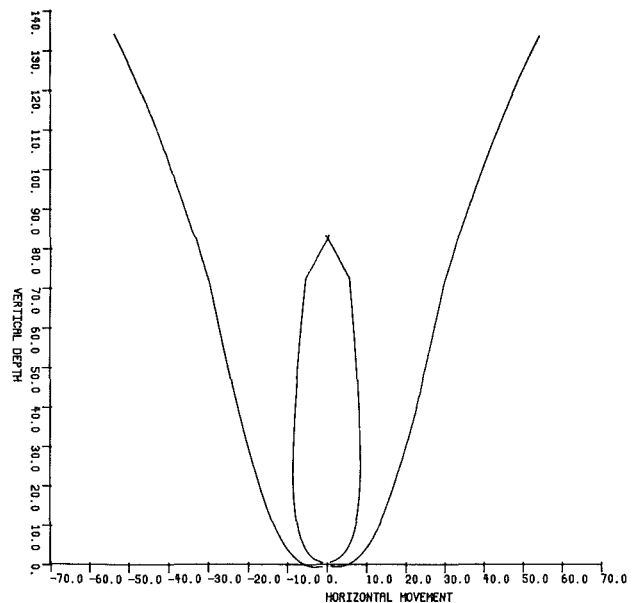
Fig. 3 Computer plot of calculated plume geometry

The discharge is fresh water into weakly stratified seawater. The seawater density at the diffuser is 1.025 gm/cm^3. The transition from round to a two-dimensional plume occurs at a height of 2130 cm (70 ft) above the bottom. The foregoing parameters were chosen to model the Orange County, Calif., marine outfall.

In summary, the model considers two distinct interactions: (a) The interaction of the individual round jets from the diffuser ports to form a two-dimensional plume. The interaction criteria is based on a comparison of the round jet width to spacing or distance between jets. (b) Merging of the two-dimensional plumes rising on either side of the diffuser. Merging criteria are based on overlapping of the inner edge of the plumes.

Results

Because of the large number of parameters that are used in a complete calculation, it was not considered feasible to give general results either in tabular or graphical form. Rather, specific results are given for prescribed discharge conditions, stratification, and diffuser parameters (dia, spacing). One of the first objectives was to compare computed and experimental results. This was done not only to investigate the validity of the model, but also to try to determine the proper range of values for K as defined by equation (9). It is interesting that, in view of the large quantity of high quality analysis devoted to this problem, only a meager amount of experimental work has been undertaken. Of the experiments reported in the literature, those by Liseth [5] seem the only one suited for the present purposes. These experiments were on the discharge from a model of a multiport diffuser and were conducted in the laboratory. Liseth [5] reports results from a large number of experiments in which he measured dilution at the jet or plume centerline. In addition, some concentration profiles normal to the axis of the diffuser were also measured and pictures were taken of the flow pattern. These were the only data found from which the location that the plumes merged could be determined. In order to evaluate several choices for K, the numerical model was run at all the cases where there was experimental data for the height at which the plume merged. The results indicated that a value of $K = 1$ gave reasonable agreement. Because this was a larger value than expected, an additional approach was used.

In a number of the experiments, the port spacing (L in Fig.

Table 2 Comparison of computed and experimental values

Diffuser characteristics

Port dia = 0.373 cm Port spacing = 10 cm Discharge vel. = 84 cm/s	Froude no. = 24	

Computed Values

Round jets merge s = 25 cm	Height = 12 cm	
Vertical plume s = 106 cm	Height = 92 cm	
Comparison at s = 40	Height = 25 measured	calculated
Width	22–24 cm	19.5 cm
Dilution	41–43	34

Fig. 4 Comparison of calculated and measured values of dilution
○ single round jet
□ Round jet plus two-dimensional plume
△ Round jet plus two-dimensional plume plus vertical plume

1) was sufficiently close that the round jets interact very quickly. In this situation, transition into the two-dimensional plume occurs very near the diffuser and the subsequent merging into a single vertical plume should be primarily because of entrainment into the two-dimensional plumes. Thus the merging must occur relatively independent of the round jet interaction. This was modeled numerically by assuming an equivalent two-dimensional plume initially, that is, beginning at the diffuser. This model should merge at least as quickly as the experiments, and thus the value of K determined in this manner should be a minimum value. The value so determined was approximately $K = 1$. On the other hand, the maximum value that one would expect from consideration of mass conservation is $K = 1$. Therefore this value was chosen for the subsequent calculations.
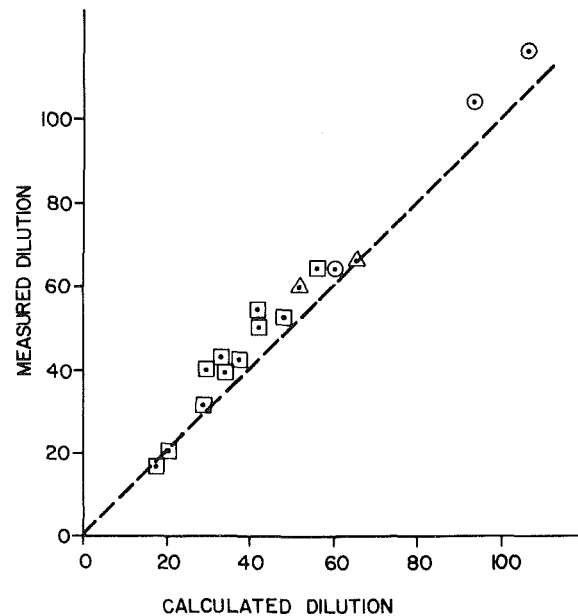
It is rather surprising that in order to achieve merging of the two-dimensional plumes as rapidly as observed experimentally, they must move toward each other with a velocity at least as large as the entrainment velocity. This observation is relatively independent of the processes that occur in the round jet or plumes and thus it would appear to validate the assumption that the merging begins only after transition to the two-dimensional plume. It would therefore rule out some motion toward each other before transition to two-dimensional plumes as an explanation of the relatively large value required for K. A possible explanation is the generation of a pressure field that would promote merging in addition to that which occurs from simple mass conservation. Clearly, the model is too crude and the experiments too sparse to explore this further.

In analysis of his experiments, Liseth [5] also developed a criteria for merging of the plumes above the diffuser. He found that the height at which the plumes merge, H_m, could be given approximately by:

$$\frac{H_m}{L} = \text{Fo}$$

where L is the port spacing and Fo the densimetric Froude no. at the discharge port. While this expression probably agrees with data, as well as the presently proposed model, it is related more to the round jet parameters than to the two-dimensional plume parameters. Inclusion of the port spacing does mean that the location of the transition from round to two-dimensional plume is considered indirectly. However, if the presently proposed model is an accurate description of the process, Liseth's expression for the merging height would appear to put too much dependence on the round jet characteristics. Additional experiments over a wider range of port spacing and Froude no. would certainly help clarify the situation.

Using a value of $K = 1$, the numerical model was employed to make a comparison with most of the experimental results of Liseth [5]. Table 2 provides a comparison of data where the width of the plume was measured. These data are after the round jet interaction has occurred, but before the single vertical plume is established. Thus they do not provide a test for the merging of the plume. The calculated and measured widths agree reasonably well; however, the measured values of dilution are significantly larger than the computed values. Recall that these are centerlines or maximum values of concentration (minimum dilution). One explanation is that it may be difficult to experimentally measured the local minimum value of dilution. This is partially because the location of the jet or plume centerline may not be known very accurately. With the computer model, however, it is a simple matter to extract the maximum concentration. This is possibly one reason the measured values of dilution are always larger than the computed values.

This observation points to an inherent difficulty in using concentration or dilution for comparison of results. Although the dilution is the parameter ultimately desired, it is an insensitive indicator of the actual flow pattern or flow dynamics. Measurement of flow velocity or of plume width would provide more precise and useful data for comparison with theory or other experiments.

Most of the data provided by Liseth [5] is in the form of centerline dilution for various discharge and diffuser conditions. In an attempt to provide a concise comparison of all results from the present model and these experiments, the format shown in Fig. 4 was chosen. This provides a plot of measured dilution versus computed dilution for the complete range of flow patterns and discharge parameters given by Liseth [5]. Figure 4 indicates reasonable agreement over the entire range and is probably the best argument for confidence in the model. As with the previous comparison, all measured values of dilution are as large or larger than the computed values. A possible reason for this was mentioned earlier. Because the model consistently underestimates the dilution (as compared to experiments), it provides a conservative estimate of the dilution from any diffuser design.

Summary and Conclusions

The discharged effluent in the near-field or mixing zone from a multiport diffuser was modeled. The model uses the

gross-flux equations of mass, momentum, and buoyancy and is closed by the entrainment assumption. The interaction of the round jets from the individual diffuser ports was modeled by a transition from round jets to a single two-dimensional plume. This was assumed to occur when the width of the jet reaches some fraction of the port spacing. The resulting two-dimensional plumes from either side of the diffuser then merge over the top of the diffuser. This is believed to occur because the volume of background fluid available to be entrained into the plumes is restricted by the plumes themselves. It is modeled by assuming the plumes translate toward each other at some fraction of the entrainment velocity.

Results calculated by this model were compared with previously reported experimental data and it is found that translating the plumes at the entrainment velocity yields good agreement. Although this is a higher velocity than expected from physical reasoning, it does appear to provide the best agreement. This can be because too few experimental data points were available to permit an accurate comparison; or because an additional mechanism, other than entrainment of the background fluid, causes the plumes to merge together.

The dilution as computed by the model was compared with experimentally measured values over as wide a range of discharge conditions as there was experimental data. In view of the large amount of analysis on this particular problem, there has been surprisingly little experimental work. Thus there was not a great deal of data with which to compare the model. Additional data on the process by which the plumes merge is especially needed. Moreover, it is concluded that while dilution is the parameter of greatest interest to the engineer, it is a fairly insensitive measure of the flow dynamics in the mixing zone. Therefore, the measurement of the velocity profile or possibly some other parameter would be more useful in understanding the details of the near-field and in comparing different results.

The present model does give reasonable agreement with the experiments over a fairly wide range of discharge conditions and over the complete range of flow patterns. In most cases, it slightly underestimates the dilution. Thus the model should be a useful tool in helping design engineers determine the minimum mixing that will occur in the discharge from any multiport diffuser.

Acknowledgment

References

1 Brooks, N. H., "Conceptual Design of Submarine Outfalls - II. Hydraulic Design of Diffusers," W.M. Keck Lab. TM 70-2, 1970.

2 Koh, R. C. Y., and Fan, L. N., "Mathematical Models for the Prediction of Temperature Distribution Resulting from the Discharge of Heated Water in Large Bodies of Water," EPA WPCR Series 16130 DWO, 1970.

3 Jirka, G., and Harleman, D. R. F., "The Mechanics of Submerged Multiport Diffuser for Buoyant Discharges in Shallow Water," M. I. T. Parsons Rept. 169, 1973.

4 Shirazi, M. A., and Davis, L. R., Workbook on Thermal Plume Prediction, Vol. 1, EPA WPCR Series 16130, 1972.

5 Liseth, P., "Mixing of Merging Buoyant Jets from a Manifold in Stagnant Receiving Water of Uniform Density," Univ. of Calif., Berkeley, Hyd. Engr. Lab., TR Hel 23-1, 1970.

6 Wallis, I. G., "Initial Dilution with Deepwater Diffusers," J. Water Pollution Control Fed., Vol. 99, July 1977, p. 1621.

7 Koh, R. C. Y., and Brooks, N. H., "Fluid Mechanics of Waste-Water Disposal in the Ocean," Ann. Rev. Fluid Mech., Vol. 7, 1975, pp. 187–211.

8 Nospal, A., and Tatinclaux, J., "Design of Alternating Diffuser Pipes," J. Hyd. Div., ASCE, Vol. 102, No. HYA, Apr. 1976.

9 Morton. B. R., Taylor, G. I., and Turner, J. S., "Turbulent Gravitational Convection from Maintained and Instantaneous Sources," Proc. Roy. Soc. (London), Series A, Vol, 234, 1956, p. 1.

10 Priestley, R. B., and Ball, F. K., "Continuous Convection from an Isolated Source of Heat," Quar. J. Roy. Meteorol. Soc., Vol. 81, 1955, p. 144.

11 Fan, L. N., "Turbulent Buoyant Jets into Stratified of Flowing Fluids," C.I.T., W.M. Keck Lab., Rept. KH-R-15, 1969.

12 Fan, L. N., and Brooks, N. H., "Numerical Solutions of Turbulent Buoyant Jet Problems," C.I.T. Keck Rept. KH-R-18, 1969.

13 Morton, B. R., "The Choice of Conservation Equations for Plume Models," J. Geophysics Res., Vol. 76, No. 30, 1971,, p. 7409.

14 List, E. J., and Imberger, J., "Turbulent Entrainment in Buoyant Jets and Plumes," J. Hyd. Div., ASCE, Vol. 99, No. HY9, Sept. 1973, p. 1461.

15 Fox, D. G., "Forced Plume in a Stably Stratified Fluid," J. Geophys. Res., Vol. 17, 1970, pp. 6818–6835.

16 Brooks, N. H., "Dispersion in Hydrologic and Costal Environments," Keck Lab. Rept. KH-R-29 (also EPA Rept. 660/3-73-010), 1973.

17 Sorrell, F. Y., "Outfall Diffuse Hydraulics as Related to North Carolina Costal Wastewater Disposal," UNC Sea Grant Pub. UNC-SG-78-01.

18 Albertson, M. L., Dia, Y. B., Jensen, R. A., and Rouse, H.," Diffusion of Submerged Jets," Trans. ASCE., Vol. 115, 1950, pp. 639–697.

19 Ditmars, J. D., "Computer Program for Round Buoyant Jets into Stratified Ambient Environment," C.I.T. Keck Tech Memo 69-1, 1969.

20 Bulirsch, R., and Stoer, J. R., "Numerical Treatment of Ordinary Differential Equations by Extrapolation Methods," Numerische Mathematik, 1966, Vol. 8, p. 1.

21 Gear, C. W., "DIFSUB for Solution of Ordinary Differential Equations," Comm. A.C.M. Vol. 14, 1971, pp. 185–190.

22 Cederwall, K., "Buoyant Slot Jets into Stagnant of Flowing Environments," C.I.T. Keck Rept. KH-R-25, 1971.

23 Sotil, C. A., "Computer Program for Slot Buoyant Jets into Stratified Ambient Environments," C.I.T. Keck Tech Memo 1971, pp. 71–72

Transverse Oscillations of a Vertical Pile in Waves

F. Angrilli

V. Cossalter

Institute of Applied Mechanics,
Padua University, 35100 Padua, Italy

A cantilevered pile, flexible only in the transverse direction, has been submitted to wave action. It has been found that resonance transverse vibrations, with natural frequency f_n, are induced by eddies shedding in waves having frequency $f_w = 1$, $1/2$, $1/3$, $1/4 f_n$. A lock-in effect has been observed within the range of $0.9 f_n \leq f_w \leq 1.1 f_n$. Results of a simple mathematical model find reasonable support in the experiments.

Introduction

It is well known how a rigid cylinder, placed in a steady stream, is subjected to a fluctuating lift force due to vortex shedding, acting in a direction perpendicular to the flow. The frequency of vortex shedding is correlated by the Strouhal number with the flow velocity and with the diameter of the cylinder.

If the cylinder is flexible, or elastically mounted in the direction perpendicular to the stream, vibrations are induced by the vortex shedding. When the natural frequency of the cylinder approaches the Strouhal frequency, its oscillations can increase and can drive the eddies to shed with natural frequency or with a frequency ranging between natural frequency and that of Strouhal [1]. The effect of synchronization is that of increasing the eddies' strength [2] and the in-line drag force [3]; aside from expanding at the same time the resonance range of velocity in which the cylinder oscillates with large amplitudes, leading to possible negative consequences.

Keulegan and Carpenter [4] have made measurements on submerged horizontal cylinders placed in the node of a standing wave and have shown that the eddy shedding frequency is primarily dependent on a nondimensional group, subsequently called Keulegan-Carpenter number, KC $= U_M T/D$ in which U_M = the maximum horizontal water particle velocity; T = the wave period; and D = the cylinder diameter. The physical meaning of this parameter is a measure of the ratio of the water particle displacement to the cylinder diameter. For a rigid cylinder in oscillating flow, eddy separation has not been observed for KC less than approximately 4, so that in this range there is no lift force due to vortex shedding.

Sarpkaya [5] has studied the dependence of lift coefficient C_L on KC for a horizontal cylinder immersed in a bidimensional harmonically oscillating fluid. He found the possibility of four lift frequencies f_v, for a given flow cycle, with a predominant lift frequency twice the frequency f_w of the oscillating flow. The measured lift coefficient C_L shows a maximum at KC $\simeq 10$ with $f_v = f_w$ or $f_v = 2f_w$ respectively corresponding to the shed of one or two vortices in a half

cycle. Another maximum is found at KC $\simeq 18$; for this value of KC, the dominant vortex shedding frequency is $f_v = 2f_w$ corresponding to the shed of two vortices in a half cycle.

For a vertical cylinder in waves, there are important differences from the case of a cylinder in harmonic oscillating flow where the particle paths are straight. We should notice that the former is more interesting when it comes to applications. Water particle displacement in waves diminishes with depth, while the particle paths are orbital. Such differences are sharper for deep water waves than for shallow water waves.

Isaacson and Maull [6] have studied the lift force acting on a rigid vertical cylinder in a wave oscillating flow as a function of the Keulegan-Carpenter number, of the Reynolds number, and of two other dimensionless groups: the water depth parameter $Nd = 2\pi d/L$ and the wave steepness parameter $Np = 2\pi H/L$. Here d is the mean water depth, L the wave length, and H the wave height (trough to crest). They have found an effective dependence of the lift coefficient on KC and Nd. They have observed that for KC < 2 no vortex formation is discernible. For KC $\simeq 4$, a pair of vortices are formed, but they do not break off the cylinder. In the range $6 <$ KC < 15, one eddy is shed per half cycle, while for KC $= 16$, two eddies separate completely in a half cycle.

Chakrabarti, et al. [7], by analyzing the spectra of lift force acting on a rigid vertical cylinder in waves, have found that for KC < 7, f_v/f_w is 1; for $7 <$ KC < 15, f_v/f_w is 2; for KC > 15, f_v/f_w is 3. They have also found that the lift force for KC $= 15$ is greater than in line force.

Recent papers [8, 9], have reported that the reduced velocity $U_r = U_M/f_n D$ is one of the most important parameters governing the resonant oscillations. Here f_n is the in-water natural frequency of the cylinder.

Sarpkaya and Rajabi [8] have shown that perfect lock-in occurs when the reduced velocity assumes a value of 5.5, and have found that, at perfect synchronization, the lift coefficient C_L is amplified by a factor of about two related to that for a nonoscillating cylinder in harmonic flow.

Zedan, et al. [9], have investigated the dynamics of cantilever piles in response to wave excitation under vortex shedding in lock-in conditions.

To correlate the results of different tests, they had identified a nondimensional number $G = (y_{RMS}/D) (EI/\rho U_M^2 C_L d^4)$ called top transverse deflection parameter.
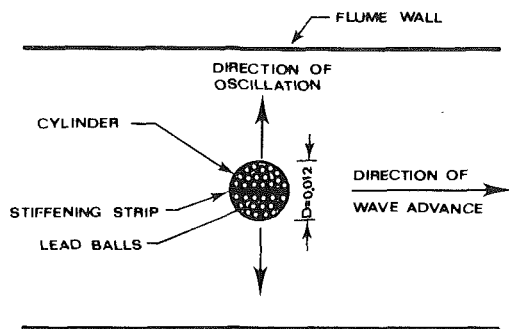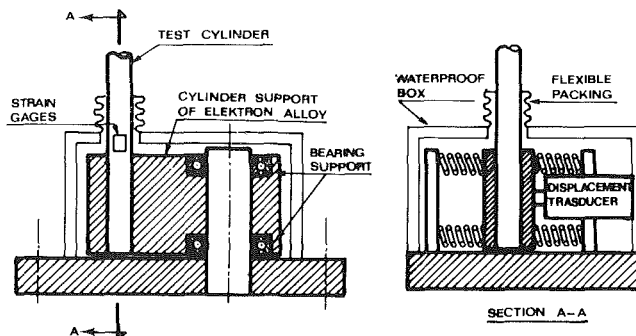
Fig. 1 Sketch of cylinder (not to scale)

Fig. 2 Force and moment measuring setup

The parameter G is proportional to the root mean square top displacement y_{RMS}, to the pile stiffness EI/d^3, and inversely proportional to the forcing lift function $\rho U_m^2 C_L Dd$. Perfect lock-in occurs in their tests for $U_r = 5.5$, $U_r = 5.75$, $U_r = 7.3$.

The work herein reported may be considered as a first approach to the analysis of the interaction between the eddy shedding in waves and the motion of a flexible cylinder.

After having observed in a previous preliminary work [10] the complexity of the phenomena, when the pile is left free to oscillate in all directions, it was decided to study separately the response of a flexible cylinder only in the in-line direction and, afterwards, the response in the transverse direction.

The results of the former research have been summarized in paper [11], so we report here only the results of the second case.

Description of the Apparatus

The experimental channel was a concrete tank with glass windows having an overall length of 30 m, a width of 1.0 m, and a depth of 1.1 m.

A water depth of 0.9 m was used for the experiments described here.

At one end of the channel, the waves were generated by an oscillating paddle, pivoted on the bottom. At the other end of the channel, the wave energy was absorbed by a beach. A network steel filter was installed between the wave generator and the experimental section for the regularization of the wave profiles.

The wave heights and periods were varied by adjusting the control mechanism of the wave generator. The water level in the experimental section was continuously recorded by means of a two-wire immersed conductance-transducer and amplified carrier-bridge.

The test cylinder was a 0.012 m diameter PVC pipe. A strip of spring steel was inserted to stiffen the cylinder only in the inline direction, and the rest of the cavity was filled with little lead balls, Fig. 1. The free oscillation period of the cylinder in still water was 0.76 s. The physical characteristics of this pile are summarized in Table 1.

Table 1 Model pile characteristics

Height	$h = 0.9$ m
Outside diameter	$D = 0.012$ m
Mass of the cylinder per unit length	$\mu = 0.545$ Kg/m
Bending stiffness in the in-line direction	$EI = 44$ Nm^2
Bending stiffness in the transverse direction	$EI = 2.62$ Nm^2
Log decrement in air	$\delta = 0.082$

Nomenclature

A = cross sectional area of the cylinder

c = viscous damping coefficient

C_D = coefficient of drag

C_I = coefficient of added mass

C_L = coefficient of lift

d = mean water depth

D = cylinder diameter

EI = flexural stiffness of the cylinder

f = frequency of oscillations

f_n = natural frequency of the cylinder in water

f_v = frequency of vortex shedding

f_w = frequency of flow oscillations and frequency of waves

$f(t)$ = motion generalized coordinate

F = overall force

F_D = drag force

F_{DT} = component of the drag force in the transverse direction

F_L = lift force

F_{LT} = component of the lift force in the transverse direction

g = acceleration of gravity

$G, \bar{G}$ = top transverse deflection parameter

h = length of the cylinder

H = wave height (through to crest)

k = wave number

k^* = reduced stiffness

KC = Keulegan-Carpenter number

L = wave length

m^* = reduced mass

M = dynamic magnification factor

n = number of vortices formed in half cycle

Nd = water depth parameter

Np = wave steepness parameter

p = weight of cylinder per unit length

$q(x)$ = shape function

t = time

T = wave period

U = horizontal water particle velocity

U_M = maximum horizontal water particle velocity at mean water level

U_r = reduced velocity

V = relative velocity between the cylinder and water particle

x = x-axis

y = y-axis, displacement of the top pile

y_M = maximum top transverse amplitude of oscillations

$\bar{y}_M$ = mean top amplitude

y_{RMS} = root mean square top displacement

α = angle of attack

β = frequency coefficient

δ = log decrement in air

η = water surface elevation at the pile

ζ^* = reduced damping ratio

μ = mass density of cylinder per unit length

μ_t = the mass of the cylinder including the added mass, per unit length

ν = kinematic viscosity

ρ = mass density of water

ϕ = phase between the lift force and the wave particle velocity

ω_n = natural circular frequency

Fig. 3 Wave tank test setup

Table 2 Wave parameters and amplitudes for vibrating cylinder

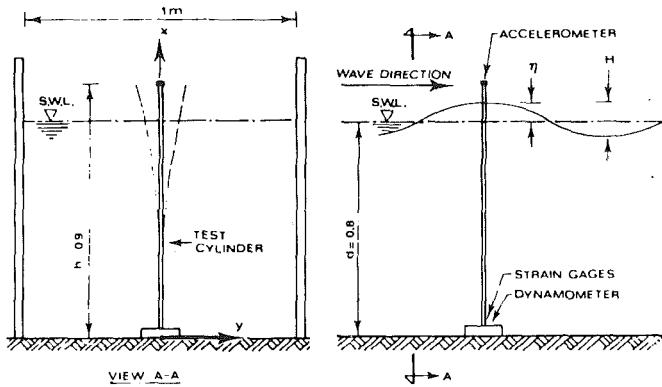| Run	1	2	3	4
Frequency ratio f_w/f_n	1	1/2	1/3	1/4
Wave period T (s)	0.76	1.52	2.28	3.04
Wave height H (m)	0.067	0.040	0.048	0.076
Reduced velocity U_r	17.54	5.75	5.93	8.98
KC	17.54	11.51	17.79	35.92
Nd	5.65	1.53	0.88	0.62
Vortex frequency ratio $\dfrac{f_v}{f_w}$	3	2	3	4
Top pile resonance amplitude y_M/D	0.87	1.25	1.42	1.54

The cylinder was cantilevered at the bottom by means of a dynamometer (Fig. 2) which measured the overall transverse forces. The measured natural frequency of the dynamometer, with the cylinder test in air, was 47 Hz. Two strain gages were bonded near the clamped end to measure the bending moment.

The velocity and displacement of the cylinder top were measured through electronic integration by means of a light $(2 \cdot 10^{-3}$ Kg) strain-gage accelerometer, Philips PR 9366/20, fixed at the free end of the pile. The electronic integrator was a Loetscher Electronic Type BD1 with linear response ($\pm$ 2 percent for double integration) starting from 0.2 Hz.

All transducers were individually calibrated before each set of runs.

The wave gages were calibrated in still water by lowering and raising the probe and recording the output on the galvanometer oscillograph.

A calibration control of displacement was made by photographic technique. On the top of the pile, a little glass sphere had been bonded for reflecting a beam of light, and a reference ruler had been placed near the cylinder and parallel to the oscillation plane. A photograph of the path of the little sphere was used to measure the amplitude of the motion, with an accuracy greater than 0.5 mm.

The dynamometer was calibrated with two different procedures. In the first procedure, the output of the overall force was compared with the indication of a spring mechanical dynamometer. The second procedure was performed by hanging weights to the pile by means of a silk thread and a little teflon pulley. The results of these calibration tests indicated a maximum error of $\pm$ 3 percent in respect to the nominal straight line.

The sensitivity of the force meter in the line direction was proved; no force was detected.

In the same tests, the moment-meter was calibrated by measuring the lever of the applied force.

Experimental Results

The cylinder described in the previous section was installed in the wave tank as shown in Fig. 3.

The experiments were carried out by increasing uniformly the frequency of the waves from 0.2 Hz to 2 Hz and afterwards decreasing it from 2 Hz to 0.2 Hz. The total time of the sweeping was 600 s. In this sweeping test, it was not possible to keep constant the height of the waves. The fundamental aim of this test was identifying the frequencies at which the lock-in occurs. A continuous record of the measured quantities has been performed. The experiments have given the following results.

During the passage of a wave, a wake was generated behind the cylinder. The vortices shed from the cylinder were visible on the water surface. The eddy pattern around the cylinder was dependent on the wave frequency, on the shedding

frequency, and on the motion of the cylinder, if any. For particular wave frequencies, the cylinder oscillated with amplitudes and frequencies near to resonance conditions, and the motion was steady. Permanent resonant oscillation of the cylinder occurred for the frequency ratios used $f_w/f_n = 1$, 1/2, 1/3, 1/4.

In the four resonant conditions, the experiments were repeated with different wave heights in order to achieve amplitude of the oscillations large enough for the accurate measurement of the phenomenon, yet still remaining in the linear domain.

The records of the top transverse displacement y and of the wave height H, presented in Figs. 4(a-d), show the resonance phenomenon of the pile with wave frequencies subharmonic of the pile frequency.

Table 2 presents experimental data obtained in the four runs. The amplitude of the recorded quantities was not exactly constant with time. The variations were within about $\pm$ 6 percent. The values presented in Table 2 are the mean values of many measurements.

In this table, the Keulegan-Carpenter number and the reduced velocity have been evaluated with the horizontal velocity of water U_M, calculated at the mean water level, using Airy theory.

It may be noted that the values of the reduced velocity for run 2, $U_r = 5.75$, and for run 3, $U_r = 5.93$, are very close to that found by Sarpkaya [8] and Zedan, et al. [9].

Figure 5 reproduces our experimental results together with those obtained by Sarpkaya and by Chakrabarti, et al. The data by Sarpkaya are referred to fixed cylinders in a two-dimension harmonic oscillating flow; those of Chakrabarti, et al., refer to vertical rigid cylinders in regular waves. The actual four cases are obtained, instead, with an oscillating cylinder in regular waves.

The dependence of the vortex frequency on the Keulegan-Carpenter number KC for actual cases is in agreement with that observed on fixed cylinders.

The motion of the cylinder is produced by the lift alternating force due to the vortex shedding. The lift force frequency f_v is equal to $n f_w$ where n is the number of vortices formed in half a cycle.

To be in resonant condition, the lift force frequency must be equal to the natural frequency f_n of the pile. In runs 2, 3, 4, this occurrence is clearly verified. In run 1, the lift frequency is three times the natural frequency; however, the dependence of the lift force amplitude on the relative velocity produces a fundamental lift component, larger than the other component, with frequency f_n. This aspect is shown in Fig. 10(a), obtained by the simplified mathematical model presented in the next section.

When the waves have a frequency close to f_n or close to its integer submultiple $(f_w = 1, 1/2, 1/3, 1/4 \, f_n)$, regular oscillations of the pile near to its resonance conditions are observable. For wave frequencies far from these conditions, the pile motion is small and irregular.

By gradually increasing and decreasing the wave frequency

a) $f_w = f_n$

b) $f_w = \frac{1}{2} f_n$

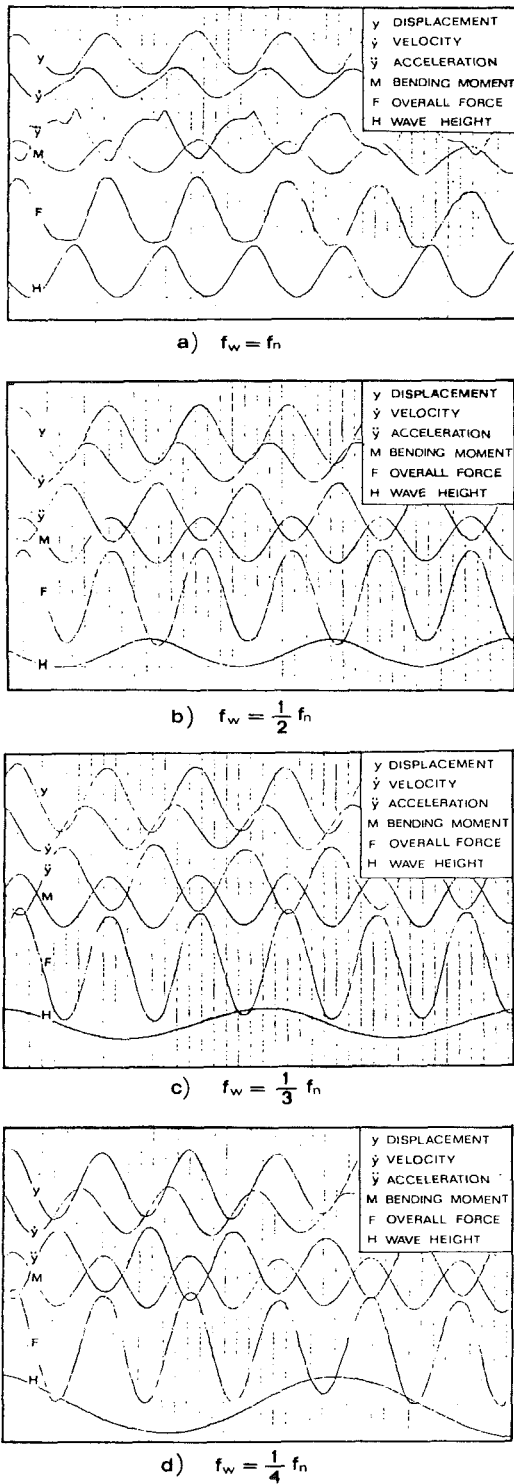c) $f_w = \frac{1}{3} f_n$

d) $f_w = \frac{1}{4} f_n$

Fig. 4 Sample of recorded test data on waves, overall forces, bending moments, acceleration, velocity, and displacement of cylinder top, showing subharmonical resonance phenomena

Fig. 5 Normalized vortex shedding frequency versus Keulegan-Carpenter parameter for rigid cylinders in harmonic flow [5], or in waves [7], and for a flexible cylinder in waves
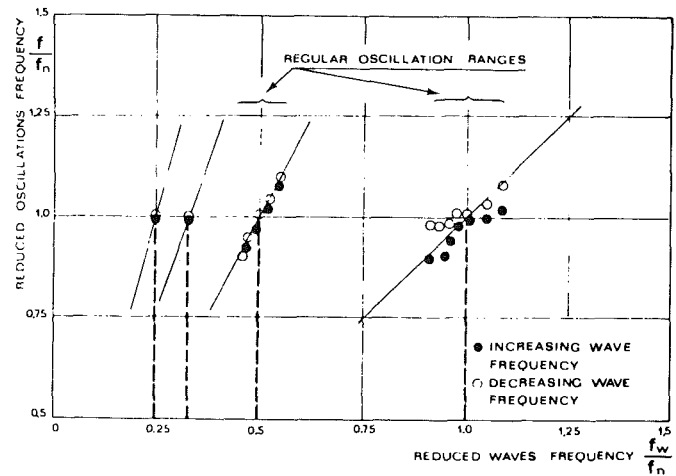
Fig. 6 Oscillation frequency versus waves frequency for the test cylinder

around the four conditions in which the resonance of the pile takes place, different situations are found (Fig. 6).

In runs 3 and 4, the oscillations grow suddenly only when the frequencies are in an exact integer ratio. A very little variation of the frequency of the waves from the value $1/3f_n$, $1/4f_n$, suppresses the oscillations.

In run 2, there is a range of wave frequency around $1/2f_n$ in which regular oscillations occur, and the pile is forced to vibrate with wave frequency.

Finally in run 1, regular oscillations in a frequency range

centered around f_n are also found. But they may be produced by a lock-in effect in which the frequency of eddies is driven by pile motion. This synchronization phenomenon is present with a form of hysteresis.

Therefore, starting with a frequency $f_w \simeq 0.9 \ f_n$ and gradually increasing it, the motion of the pile always has the same frequency of the waves until $f_w = f_n$.

A further increase of the wave frequency above $f_w = f_n$ does not produce a corresponding variation of pile frequency. The pile, instead, continues to respond at its natural frequency f_n, even though with reduced amplitude.

Conversely as the wave frequency is reduced from $f_w \simeq 1.1$ f_n, the pile responds at the wave frequency until $f_w = f_n$. Then from $f_w = f_n$ to $f_w \simeq 0.9 \ f_n$, the pile responds at its natural frequency f_n.

At the boundaries of the synchronization range, the lock-in is intermittent. The vortex shedding synchronizes alternately with the cylinder and with the waves; the instability of this phenomenon is shown by a beating vibration of the cylinder.

In the case $f_w = 1/2f_n$, the displacement of the pile top has been measured for frequencies close to the resonant one.

The results of these tests are given in Fig. 7 where we have plotted the nondimensional parameter

$$\bar{G} = \frac{y_{RMS}}{D} \frac{EI}{h^3 \rho U_M^2 C_L d}$$

versus the frequency ratio f_v/f_n. The parameter $\bar{G}$ is slightly different from that used by Zedan, et al. [9]:
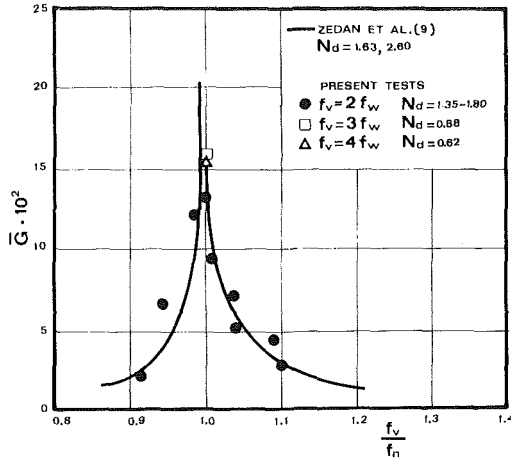
Fig. 7 Dimensionless top transverse displacement response parameter $\bar{G}$ versus frequency ratio

$$G = \frac{y_{RMS}}{D} \frac{EI}{\rho U_M^2 C_L d^4}$$

which is independent from the total length of the pile.

They assumed the equivalent stiffness of the pile proportional to EI/d^3 while we are assuming the same quantity proportional to EI/h^3.

In this manner, we are able to correlate tests with different values of the ratio between the water depth and the total length of the pile d/h. In Fig. 7, the continuous line, corresponding to the results of Zedan, et al. $(d/h = 0.63)$, is compared with the data of present tests $(d/h = 0.89)$.

Although the experiments were performed with different values of the ratio d/h, of the wave number Nd, and with different physical characteristics of the piles, the agreement seems rather good.

Analysis in Resonance Conditions

The total force per unit length on the cylinder, in the transverse direction, is given by the sum of the drag and lift components (Fig. 8):

$$F_T(x,t) = F_L(x,t)\cos\alpha + F_D(x,t)\sin\alpha$$
$$= F_{LT}(x,t) + F_{DT}(x,t) \qquad (1)$$

where

$$\alpha = \arctan\left[-\frac{\dot{y}(x,t)}{|U(x,t)|}\right]. \qquad (2)$$

A simple formula for the oscillating lift force due to vortices is:

$$F_L(x,t) = \frac{1}{2}\rho D\, V^2(x,t)\, C_L \sin(2\pi f_v t + \phi) \qquad (3)$$

in which ρ = the mass density of water; D = the diameter of the pile; C_L = the lift coefficient; ϕ = the phase angle of the lift force with respect to the wave particle velocity; $f_v = n f_w$ is the vortices frequency where f_w is the wave frequency and n is the number of eddies shed during a half cycle of wave; $V(x,t)$ is the relative velocity between the cylinder and the water flow:

$$V(x,t) = [U^2(x,t) + \dot{y}^2(x,t)]^{\frac{1}{2}} \qquad (4)$$

The drag force per unit length is:

$$F_D(x,t) = \frac{1}{2}\rho D\, C_D\, |V(x,t)|\, V(x,t) \qquad (5)$$

in which C_D is the drag coefficient.

The horizontal components of water particles velocity $U(x,t)$ are determined by the second order Stokes theory.

Introducing $\cos\alpha = |U(x,t)|/|V(x,t)|$ and $\sin\alpha =$

$-\dot{y}(x,t)/|V(x,t)|$, equation (1) can be rewritten as:

$$F_T(x,t) = \frac{1}{2}\rho D[\,|V(x,t)|\,|U(x,t)|\,C_L\sin(2\pi n f_w t + \phi)$$
$$- C_D\,|V(x,t)|\,\dot{y}(x,t) \qquad (6)$$

The equation of motion for the elastic cylinder may be written as:

$$\mu_t \frac{\partial^2 y(x,t)}{\partial t^2} + c\frac{\partial y(x,t)}{\partial t} + \frac{\partial^2}{\partial x^2}\left[EI\frac{\partial^2 y(x,t)}{\partial x^2}\right]$$
$$+ \frac{\partial}{\partial x}\left[p(h-x)\frac{\partial y(x,t)}{\partial x}\right] = F_T(x,t) \qquad (7)$$

where μ_t = the mass of the cylinder, including the added mass of entrained fluid per unit length; c = the viscous damping coefficient per unit length; EI = the flexural stiffness; h = the length of the cylinder; p = the weight per unit length of the cylinder (for the submerged part p is the unit weight of the pile in water). The last term at the left-hand side expresses the axial effect of the gravity.

Equation (7) is a nonlinear, partial, differential equation whose complete solution would be an expensive and rather complex process.

In resonance, a much simpler, approximate solution can be obtained assuming that the pile may deflect only in a single known shape. So that it is possible to reduce the continuous system to an equivalent one deg system. It is assumed: $y(x, t) = q(x) f(t)$ in which: $q(x) = (1 - \cos \pi x/2h)$ is a commonly approximate shape function for a cantilever beam, and $f(t)$ is the amplitude of the motion.

The equation of motion, in which the Ritz-Galerkin technique [12] for the reduced system is used, may be written as:

$$m^*\ddot{f}(t) + 2m^*\zeta^*\omega_n\dot{f}(t) + k^*f(t) = F_T^*(t) \qquad (8)$$

in which:

$$m^* = \mu\int_0^h q^2(x)\,dx + \rho\,AC_I\int_0^{d+\eta} q^2(x)\,dx \qquad (9)$$

is the reduced mass, including added mass of fluid; where A is the cross-sectional area of the cylinder, C_I is the added mass coefficient and $\eta = H/2\,\sin2\pi f_w t$ is the water surface elevation;

$$\zeta^* = \frac{c}{2m^*\omega_n}\int_0^h q^2(x)\,dx \qquad (10)$$

is the reduced damping ratio;

$$k^* = EI\int_0^h\left[\frac{\partial^2 q(x)}{\partial x^2}\right]^2 dx - p\int_0^h (h-x)\left[\frac{\partial q(x)}{\partial x}\right]^2 dx \quad (11)$$

is the reduced stiffness due to the elastic property of the cylinder and to the effect of the axial gravity load, where p is given as $p = (\mu - \rho)g$ for $0 \le x \le d + \eta$, $p = \mu g$ for $d + \eta \le x \le h$;

$$F_T^*(t) = \int_0^{d+\eta} F_T(x,t)\,q(x)\,dx \qquad (12)$$

is the reduced force.

Numerical Results

The choice of the coefficients C_I, C_D, C_L and of the phase ϕ for the numerical computation should be carefully made. Our experiments are performed in a poorly explored dynamical condition and we have to extrapolate the values of the coefficients from simpler cases.

For instance, the static lift and drag coefficients, which are functions of KC and of the frequency parameter $\beta = D^2/\nu T$, are deduced from Sarpkaya's data [13] obtained in a bidimensional flow and not in waves.
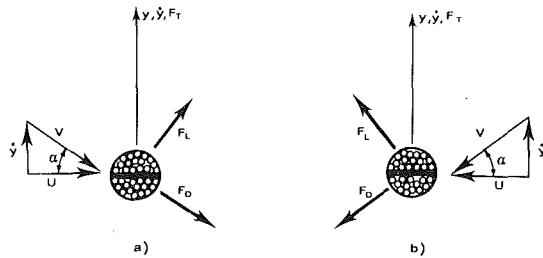
Fig. 8 General layout and forces on cylinder,
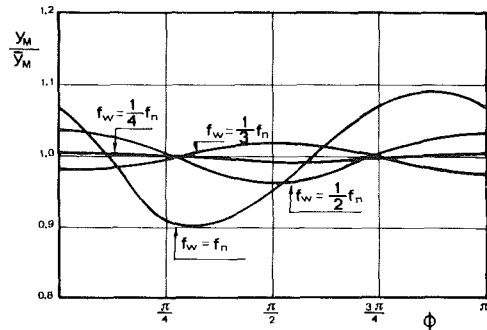(a) Velocity in wave crest
(b) Velocity in wave trough

Fig. 9 Calculated top transverse displacement ratio versus phase ϕ

Furthermore, the synchronization causes an amplification of lift force. Therefore, the value of the static coefficient C_L must be multiplied by a dynamic magnification factor M.

No data are available on M for a pile in waves. For an elastically-mounted cylinder in harmonic flow, Sarpkaya [8] gives a value of about 2.

To find a criterion for the choice of phase ϕ between the lift force F_L and the particle velocity U, the effect of its variation on the motion of the pile has been investigated.

From Fig. 9, it clearly appears that this dependence is very weak. The maximum of variation of the response ratio $y_M(\phi)/\bar{y}_M$, where $\bar{y}_M$ is the mean amplitude obtained varing ϕ from 0 to π, is less than $\pm$ 10 percent in run 1. In the other cases, by increasing the frequency ratio f_v/f_w, the dependence of response from the phase becomes weaker and weaker.

Table 3 Numerical results

Run	1	2	3	4
Experimental top amplitude y_M/D	0.87	1.25	1.42	1.54
Calculated top amplitude y_M/D (C_L and C_D obtained from Sarpkaya's data)	1.20	1.49	1.64	1.59
Dynamic magnification factor M	1.4	1.7	1.6	1.9
Phase ϕ (rad)	1.17	0	1.57	0

In Table 3, the experimental and numerical results are summarized. the calculated top amplitudes are the mean values in a wave cycle and have been obtained assuming: C_L and C_D from Sarpkaya's data [13], the factor $M=2$ as suggested by Sarpkaya [8], and phase $\phi = 0$.

We observe that the values calculated in all the runs are greater than the experimental ones. The extrapolation of the coefficients obtained in harmonic flow to the tests in waves is not completely satisfactory.

The values of magnification factor M reported in Table 3 are deduced by experimental results in order to give calculated amplitudes equal to the experimental ones.

Figures 10(a–d) show the comparison between the measured and calculated values of the instantaneous dispalcement, of the overall force, of the lift force (only analytical), and of the wave height as a function of time.

The agreement between the numerical and experimental

a) $f_w = f_n$
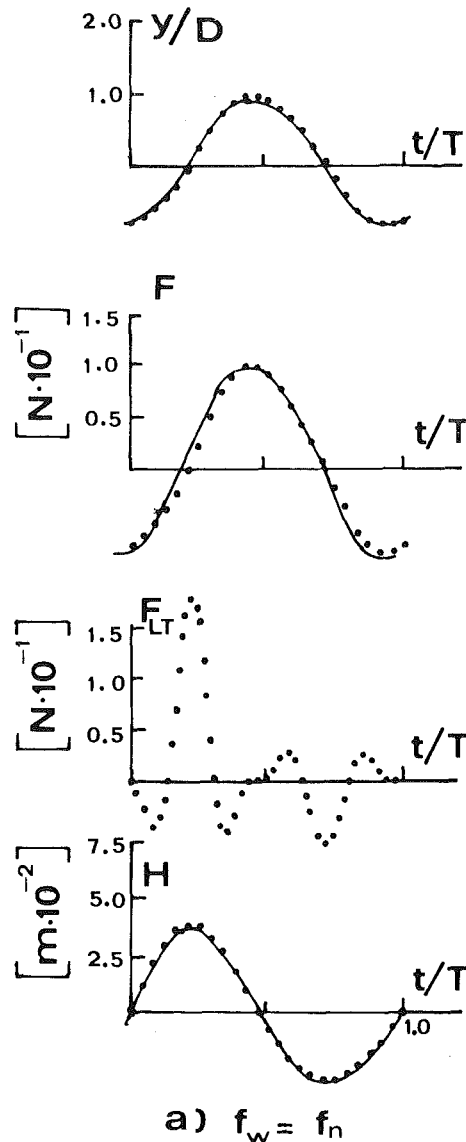
Fig. 10(a)

results has been obtained with the values of M and ϕ reported in Table 3.

Conclusions

The results presented in this work lead to the following conclusions:

1 A flexible structure can reach the resonance condition in the transverse direction with wave frequencies equal to its natural frequency or to submultiples of it: $f_w = 1, 1/2, 1/3, 1/4 f_n$.

2 The occurrence of a lock-in effect $(0.9f_n \le f_w \le 1.1f_n)$ increases the range of substantial transverse oscillations of the pile, taking control of the shedding.

3 Perfect synchronization occurs for $f_w = 1/2f_n$ at $U_r = 5.75$, for $f_w = 1/3f_n$ at $U_r = 5.93$, and for $f_w = 1/4f_n$ at $U_r = 8.98$. The values of the reduced velocity U_r are comparable to those found by other authors [8, 9].

4 The use of the dimensionless top transverse deflection parameter $\bar{G} = (y_{RMS}/D) (EI/h^3 \rho U_M{}^2 C_L d)$ permits a good correlation of our results with those of Zedan, et al. [9]. The values of $\bar{G}$, in the three cases of perfect synchronization, with subharmonical waves $(f_w = 1/2, 1/3, 1/4f_n)$, are, respectively, 0.130, 0.156, and 0.152.

5 By means of a simple mathematical model, the

b) $f_w = \frac{1}{2} f_n$

Fig. 10(b)

c) $f_w = \frac{1}{3} f_n$
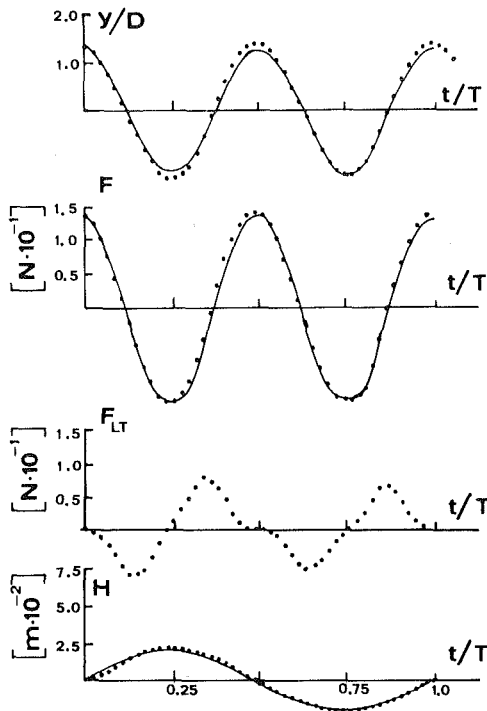
Fig. 10(c)

magnification factor M of the static lift coefficient has been calculated. The values obtained for the four cases, varying from 1.4 to 1.9, are comparable to the one obtained in two dimensional harmonic flow by Sarpkaya [8] who found a factor of about 2.

6 A simple mathematical model permits us to verify that the transverse lift component keeps the pile in motion with a phase angle appropriate to resonant conditions even in case 1, in which the vortex frequency is three times the natural frequency of the pile.

d) $f_w = \frac{1}{4} f_n$

Fig. 10(d)

Fig. 10 Measured (———) and predicted (·······) wave height, overall force and top pile displacement; lift transversal force (calculated only)

References

1 Di Silvio, G., Angrilli, F., and Zanardo, A., "Fluidelastic Vibrations: Mathematical Model and Experimental Result," Meccanica, No. 4, Vol. X, 1975, pp. 269–279.

2 Griffin, O., and Ramberg, S. E., "The Effects of Synchronized Cylinder Vibrations on Vortex Formation and Strength, Velocity Fluctuations, and Mean Flow," Paper No. 3 presented at the Symposium on Flow Induced Structural Vibrations, Karlsruhe, Germany, Aug. 1972.

3 Bishop, R. E. D., and Hassan, A. Y., "The Lift and Drag Forces on a Circular Cylinder in a Flowing Fluid," Proc. Roy. Soc., London, Series A, 277, 1964, pp. 51–75.

4 Keulegan, G. H., and Carpenter, L. H., "Forces on Cylinders and Plates in an Oscillating Fluid," J. of Res., NBS, Vol. 60, 1958, pp. 423–440.

5 Sarpkaya, T., "Forces on Cylinder and Spheres in a Sinusoidally Oscillating Fluid," ASME Journal of Applied Mechanics, Mar. 1975, pp. 32–37.

6 Isaacson, M. Q., and Maull, D. J., "Transverse Forces on Vertical Cylinders in Waves," J. of Waterways, Harbors, and Coastal Eng. Div., Feb. 1976, pp. 49–60.

7 Chakrabarti, Subrata K., et al., "Wave Forces on Vertical Circular Cylinders," J. of Waterways, Harbors, and Coastal Eng. Div., May 1976, pp. 203–221.

8 Sarpkaya, T., and Rajabj, F., "Dynamic Response of Piles to Vortex Shedding in Oscillating Flows," Offshore Technology Proceedings, OTC, Paper No. 3647, May 1979, pp. 2523–2528.

9 Zedan, M. F., et al., "Dynamic Response of a Cantilever Pile to Vortex Shedding in Regular Waves," Offshore Technology Proceedings, OTC, Paper No. 3799, May 1980, pp. 45–59.

10 Angrilli, F., and Zanardo, A., "Forze Agenti su un Cilindro Flessibile Sollecitato da Moto Ondoso Indagine Sperimentale," Ingegneria Meccanica, Vol. 6, 1975, pp. 43–50.

11 Angrilli, F., Cossalter, V., and Zanardo, A., "Wave Induced Vibrations of Flexible Piles," World Offshore, Nov. 1979, pp. 17–24.

12 Clough, R. W., and Penzien, J., Dynamics of Structures, McGraw-Hill, 1975, pp. 29–38.

13 Sarpkaya, T., "In-Line and Transverse Forces on Cylinders in Oscillatory Flow at High Reynolds Numbers," Offshore Technology Proceedings, OTC, Paper No. 2533, May 1976, pp. 95–108.

DISCUSSION

M. F. Zedan[1]

The problem of flow induced oscillations has received considerable attention in recent years because of a number of structural failures that are believed to be caused by vortex shedding lock-in. However, understanding of many aspects of the phenomenon is still far from complete. More experimental data are needed to enhance understanding of these aspects. This will eventually help develop physically sound computer models and provide more accurate correlations for use in the design of offshore and marine structures. Most of the studies in the literature have dealt with vortex shedding induced by currents or by two-dimensional harmonic flow. Studies on vortex shedding induced oscillations on vertical piles in waves are very scarce. In fact, the present study is the second major investigation of the problem (after that of reference [1]) and is, therefore, very timely.

The agreement of most of the results of the present study, where pile motion was suppressed in the in-line direction, with the results of reference [1] where the pile was free to oscillate in all directions, is quite interesting. Both studies have shown that the shedding frequency is not affected by the flexibility of the cylinder and thus can be predicted using correlations developed for fixed cylinders. At perfect lock-in, both studies showed large and regular (monoharmonic) oscillations while outside the "lock-in" range the motion was irregular and small in magnitude; at boundaries of lock-in, the beating phenomenon was observed.

The agreement of the response results of this study with the $\bar{G}$ versus f_v/f_n correlation developed by Zedan et al. [1] is quite important indicating the soundness of their dimensional argument. The authors use of $h^3 d$ instead of d^4 in the denominator of $\bar{G}$ is quite appropriate for generalization of the correlation. The agreement also indicates that response parameter $\bar{G}$ (which represents some sort of dynamic amplification) depends mainly on f_v/f_n and its dependence on other parameters (Nd, Re, and KC) which were different in the two experiments, is negligible. Of course more experimental data (preferably at higher Re and KC) are required to confirm this correlation which can be of great practical importance.

Table 2 shows that lock-in was achieved at $U_r = 17.54$, 5.75, 5.93, and 8.98 in runs 1 through 4, respectively. A plot of Y_m/D versus U_r for each run could have been much more informative. Such plots in the experiment of Zedan et al [1], showed double peaks; for Nd = 1.63 the peaks were sharp and occurred at $U_r = 5.5$ and 6.2 while for Nd = 2.6 which represents deeper water, the peaks were broad and occured at $U_r = 5.75$ and 7.3. These results may explain some observations in the present study. For example, the authors report that very little variation of wave frequency from exact values required for perfect "lock-in" supressed oscillations in runs 3 and 4, while it did not in run 2. The values of Nd listed in Table 2 indicate that run 2 represents deeper water as compared to runs 3 and 4. This behavior follows the same trend of the results of Zedan et al. discussed earlier.

The occurrence of lock-in in run 1 where $f_w/f_n = 1$, $f_v/f_n = 3$, Nd = 5.65 and $U_r = 17.54$, is quite surprising. The explanation given by the authors may be acceptable; however more details will be helpful. As for the analytical method developed in the paper, it appears that with appropriate values of lift amplification factor (M), excellent agreements

with experimental results are obtained. The authors point out that they used M = 2, which is based on data obtained in two dimensional harmonic flow [2], because of the absence of similar data in waves. This value seems high compared to values obtained recently by Zedan and Rajabi [3] ($M = 1.6$ to 1.9) for a cantilever pile in waves. Incidently, the authors of the paper under discussion used values of M ranging from 1.6 to 1.9 to bring agreement between the analytical and experimental results in runs 2, 3, and 4 and used $M = 1.4$ in run 1.

Additional References

1 Zedan, M. F., Yeung, J. Y., Salane, H. J., and Fischer, F. J., "Dynamic Response of a Cantilever Pile to Vortex Shedding in Regular Waves," *Proceeding*, Offshore Technology Conference, Houston, Texas, May, 1980. A slightly revised version appeared in the ASME *Journal of Energy Resources Technology*, Vol. 103, Mar. 1981, pp. 32-40.

2 Sarpkaya, T., and Rajabi, F., "Dynamic Response of Piles to Vortex Shedding in Oscillating Flows," *Proceedings*, Offshore Technology Conference, Houston, Texas, May 1979.

3 Zedan, M. F., and Rajabi, F., "Lift Forces on Cylinders Undergoing Hydroelastic Oscillations in Waves and Two-Dimensional Harmonic Flows," *Symposium on Hydrodynamics in Ocean Engineering*, the Norwegian Institute of Technology, Trondheim, Norway, Aug. 1981.

Authors' Closure

We appreciate Dr. Zedan's comments, and we agree in general with him.

We want to add the following remarks for completeness.

Attending his suggestion we have plotted, in Fig. 11, the available data of case 2 in order to correlate Y_{RMS}/D and U_r. The values of Nd in this case are ranging between 1.35 and 1.8. Since these are the only data we have at present, we are not in a position to verify the existence of the double peak found by Zedan.

We are very pleasant that Zedan et al. found agreement between their theoretical and experimental results using for M values between 1.6 and 1.93, since the same values (in cases 2, 3, 4,) are being obtained independently by us.

The run 1 which gives $M = 1.4$ is quite different from the other cases. In run 1 in fact Nd is equal to 5.65 (deep water) and the frequency of the lift is three times the natural frequency of the pile. Therefore the minor efficiency of energy transfer between the fluid and the elastic system is reasonable.
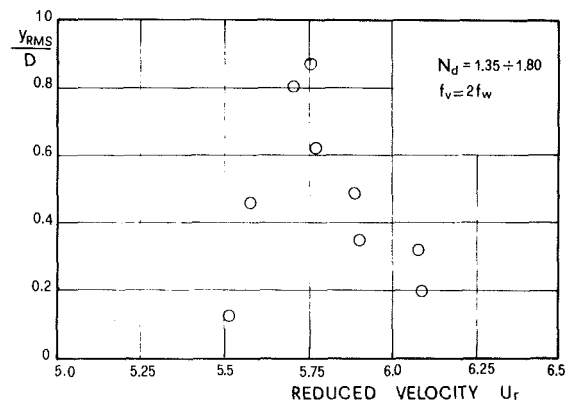

Fig. 11 Dimensionless root mean squad top displacement versus reduced velocity.

A Flow Model for the Effect of a Slanted Base on Drag

R. Sedney

Launch and Flight Division,
U.S. Army Ballistic Research Laboratory,
ARRADCOM,
Aberdeen Proving Ground, Md. 21005

Experiments by Morel have shown that slanting the base of a bluff body causes large variations in the drag, as the slant angle changes. For a particular, critical slant angle the drag changes discontinuously. This phenomenon was correlated with a drastic change in the type of base flow. A mechanism to explain this change, and therefore, the discontinuity in drag, is proposed. The basis of the mechanism is breakdown of the side edge vortices. An estimate of the swirl angle in these vortices is obtained using a swept-back mixing zone solution. This swirl angle and the other elements of the theory provide an estimate for the critical slant angle that is entirely consistent with the observed value.

Introduction

In the search to reduce drag of road vehicles, it has become clear that a more basic understanding of the complex flows about such bodies is required. Many investigations of drag and flow phenomena exist; see [1] for surveys of recent work.

A particularly interesting phenomenon is the effect that slanting the base has on the drag of a bluff body. Following up on work by Janssen and Hucho, partially reported in reference [1], Morel did a comprehensive study of that effect, see [1] and [2]. Janssen and Huccho observed an overshoot in drag and a change in separation pattern in tests on a model of a hatch-back car when the angle of the slanted portion of the roof was varied over a small range. In order to examine this effect more closely and gain some understanding of it, Morel, [1] and [2], made extensive tests on two models (see Fig. 1): (*a*) an ogive cylinder with a slanted base, mounted in the center of a wind tunnel to minimize wall effects; and (*b*) a vehicle-like model simulating a hatch-back car, mounted in the center of the tunnel and close to the tunnel wall. Because the wind tunnel models are simpler to discuss and there are more experimental details, the results of Morel will be used in this paper.

The most striking result from the tests of Morel was the extremely rapid change in drag coefficient, C_D, as the slant angle, β, is varied. In fact the data show, essentially, a discontinuity in C_D for a certain $\beta = \beta_c$. The results of Janssen and Hucho are qualitatively the same, but the variation of c_D with β is smooth, i.e., there exists no discontinuity. (The term discontinuity is used here for convenience and its descriptive accuracy, even though a mathematical discontinuity, does not exist.)

Visualizing the flow with smoke, Morel showed that there are two distinct types of base flow. For $\beta > \beta_c$ a closed base flow, typical of blunt-based axisymmetric bodies, was found. For $\beta < \beta_c$ streamwise vortices were formed at the side edges with a resultant 3-D separation pattern. It was concluded that switching from one separation pattern to the other caused the discontinuity in C_D.
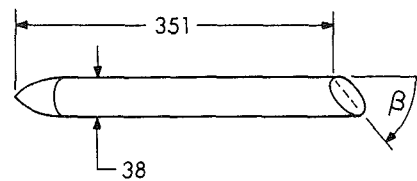
Fig. 1(a)   Ogive-cylinder model
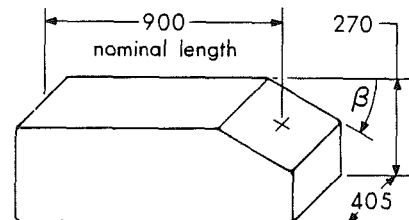
Fig. 1(b)   Vehicle-like model
Fig. 1   Models tested by Morel [2]. Dimensions in mm.

Additional evidence for the existence of the streamwise vortices springing from the side edges is given by Carr, [3]. He used the surface indicator (oil flow) method to visualize the flow and found clear and distinct edge vortices for $\beta = 25$ deg but not for $\beta = 35$ deg. Carr also discusses the downwash produced by, and the effect on the rear lift force of the side edge vortices.

The primary purpose of this paper is to propose a flow mechanism to explain the change in separation pattern and the discontinuity in C_D. The mechanism involves breakdown of the side-edge vortices. Vortex breakdown has been relatively well studied and is partially understood; the work on this subject through 1972 has been reviewed by Hall, [4], and later work by Leibovich, [5]. To make use of the empirical knowledge on vortex breakdown, a model for the flow over a side edge is required. For an idealized side edge configuration, a flow model is constructed which allows a simple estimate of the swirl in the vortex. Empirical evidence shows that breakdown occurs for a value of swirl corresponding to $\beta = \beta_c$, approximately. The consistency of this theoretical result and the experimental data is sufficient to warrant further examination of this mechanism and to test it in additional experiments.
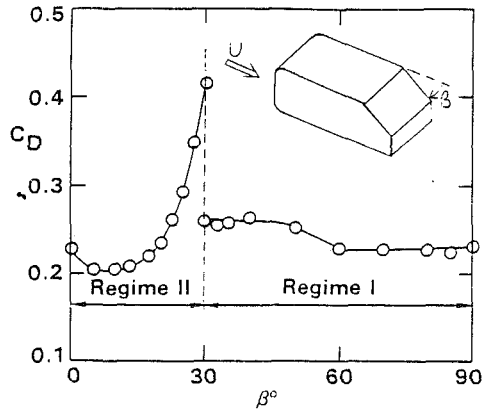
Fig. 2 Drag coefficient of the vehicle-like model in the free stream location, from [2]

(a) Quasi-axisymmetric Separation Pattern
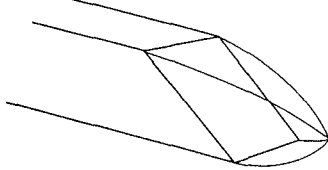
(b) 3-D Separation Pattern
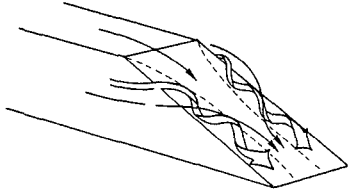
Fig. 3 The two types of base flows for a body with a slanted base: (a) The closed type exists in regime I; (b) the open type with side edge vortices exists in regime II.

Fig. 4 Rear view of a slanted base showing part of the surface flow pattern. The flow along the side (out of the plane of the paper) separates at the side edge and reattaches at the dashed line; sketched from a photograph in [3].
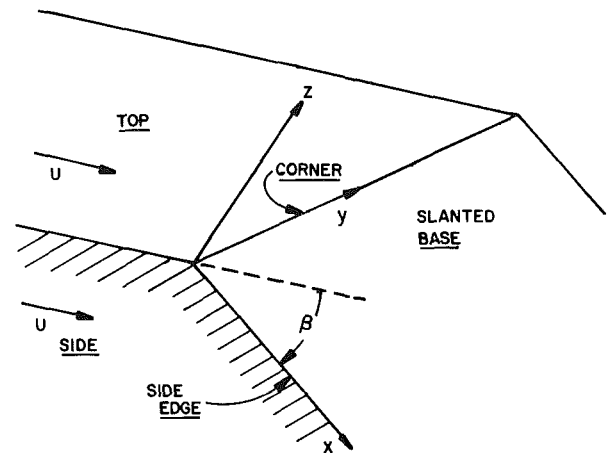
Fig. 5 A wedge, semi-infinite in the y-direction, as an idealized configuration for side edge flow. The freestream velocity, U, is parallel to the top and the side. The slanted base is $z = 0, x > 0, y > 0$.

The Experimental Evidence

For the two models tested by Morel, (see Fig. 1) the β_c were different. It is simpler to discuss the vehicle-like model because it has a straight side edge. Some discussion of the ogive-cylinder model is given later.

The drag coefficient, based on projected frontal area, as a function of β is shown in Fig. 2. The base flows corresponding to Regimes I and II are shown in Fig. 3. In Fig. 3(a), for Regime I, the base flow is essentially like that of an axisymmetric body; in the mean the base flow is a closed region. In Fig. 3(b), for Regime II, a vortex springs from each side edge; between them there is attached longitudinal flow. In [3], Carr quotes the work of Potthoff, 1969, who pointed out the existence of the side edge vortices and the fact that they can prevent the slanted base flow from separating for β as large as 30 deg or even greater with suitable shaping of the body sides.

For Carr's model, which had a short "boot length" at the end of the slant base, $\beta = 25$ deg. The surface flow pattern clearly showed the trace of the side edge vortices. A part of this pattern is sketched in Fig. 4, which shows the rear view of the slanted part of the roof, i.e., slanted base. The flow along

the side separates at the side edge and reattaches along the dashed line. The surface streamlines, which are easily visible in the oil film used for the visualization and which emanate from the dashed line, are typical of reattachment, forming what is often called a herringbone pattern close to the reattachment line. Using the reattachment line to indicate the inboard boundary of the vortex, this result shows that the vortices extend over about one-half of the width of the slant base, for this case.

There is enough evidence to conclude that side edge vortices exist for $\beta < \beta_c$. For smaller β, say $\beta < 10$ deg, they probably exist but would be difficult to detect because they are weak. As pointed out by Morel, [1] and [2], the initial decrease in C_D, for $0 \leq \beta \leq 10$ deg, may be a boattail type of effect, familiar in the design of projectiles, rather than a side edge vortex effect. The latter probably begin to dominate for $\beta > 10$ deg. For $\beta = \beta_c$ the discontinuity in C_D occurs and the side

———— Nomenclature ————

C_D = drag coefficient based on frontal area	U = free stream velocity	β_c = angle of slanted base dividing Regimes I and II
C_P = pressure coefficient	V_θ = azimuthal velocity in vortex	ϕ = swirl angle in vortex
O = order of magnitude symbol	w = velocity in z-direction	σ = mixing coefficient
S = see (2)	x,y,z = Cartesian coordinates, see Fig. 5	**Subscripts**
u = axial velocity in vortex and velocity in x-direction	β = angle of slanted base	r,s = reattachment and separation
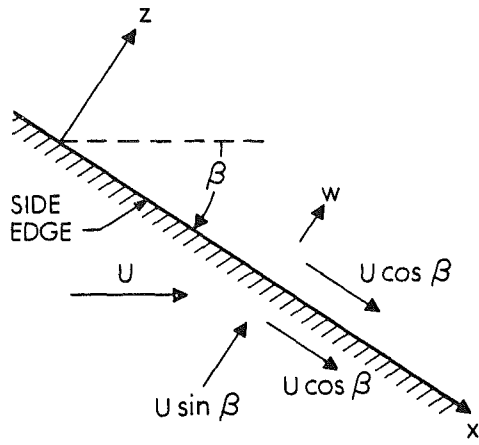
Fig. 6(a) The view in the plane $y = 0$
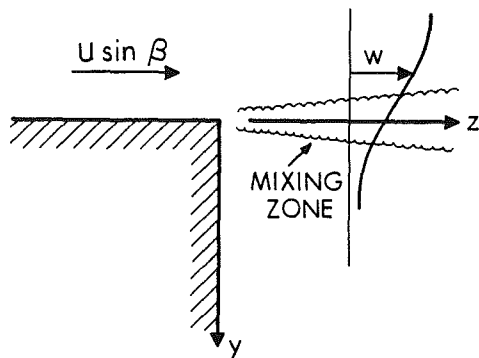
Fig. 6(b) The view in the plane x = constant. The flow separates from the side edge, forming a free shear layer or mixing zone.

Fig. 6 Flow over an infinite, yawed side edge at $y = 0, z = 0$

edge vortices disappear. This massive change in the slanted base flow field occurs suddenly, for a small change in β.

Before discussing the flow mechanism for this sudden change, some estimates of the side edge flow are necessary.

The Side Edge Flow

A description of the complete flow field over either of the models shown in Fig. 1 by analytical methods would be very difficult. To obtain a tractable idealization the local flow at the side edge should be examined. One possibility is shown in Fig. 5 where the side edge is along the x-axis and the leading edge of the slanted base, or corner, is along the y-axis. The z-axis is normal to the base and forms a right-handed, rectangular, Cartesian coordinate system. The external flow, U, is parallel to the top and side surfaces. The boundary layer would be neglected until the flow reaches the side edge and corner. This is an idealization, however, but will not yield the simple estimates needed here.

As a further simplification, appropriate to the side edge flow away from the corner, consider an infinite, slanted, or yawed, side edge. That is, there is no corner. The side view, $y = 0$ and the back view, x = constant, are shown in Figs. 6(a) and 6(b) respectively. The solution to this problem is independent of x. This kind of idealization is basic in the study of swept wings. As an additional approximation the incoming flow, U, is taken to be the free stream velocity over the model in Fig. 1(b). The thickness of the boundary layer, before it separates from the edge, is neglected. This is the same assumption made in the classic Görtler solution for the 2-D, free, turbulent, shear layer, often called the mixing zone problem. We obtain this problem, discussed in [6], if $\beta = 90$ deg. This idealization of the side edge flow can be called a combination of the 2-D mixing zone solution with the sweepback principle.
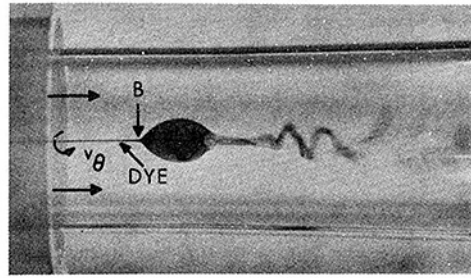

Fig. 7(a) Bubble type
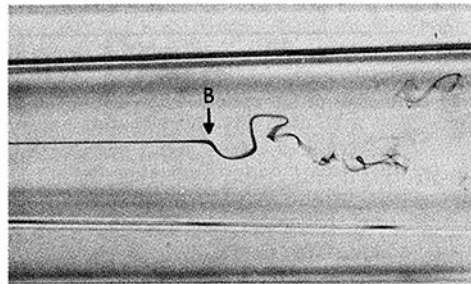
Fig. 7(b) Spiral type

Fig. 7 Vortex breakdown in a duct flow, made visible with dye introduced into the flow, from [6]. B is the breakdown point.

However, an additional caution must be discussed. In most applications of the sweep-back theory the independence principle holds, i.e., the flow in the (y,z) plane can be computed, and then the flow in x-direction determined. For laminar flow this is always possible but, because of the Reynolds stress terms in the momentum equations, the independence principle is not strictly valid for turbulent flow. It will be assumed here that the independence principle holds; this assumption should cause a small error in the swept-back mixing zone problem.

Therefore, from Fig. 6, the mixing zone flow is determined for the external velocity $U \sin \beta$. The velocity, w, in the z-direction, in the mixing zone is given by the well known solution, (see [6])

$$w = (1/2)U\sin\beta[1 + \mathrm{erf}(-\sigma y/z)] \qquad (1)$$

where $\sigma \simeq 12$ is the mixing coefficient. The vorticity, $\partial w/\partial y$, is solely in the x-direction. The velocity parallel to the edge, $U \cos \beta$, is constant for all z. This is as far as the idealization can be carried. Specifically, in the absence of pressure gradients, the free shear layer cannot reattach to the wall $z = 0$.

On the actual model, the separated flow must reattach on the slanted base in order to form the vortex. Only empirical criteria for reattachment are available and these require knowledge of the pressure. The criterion given by Crabtree [7] for leading edge bubbles on airfoils is $S \lesssim 0.35$ where

$$S = (C_{pr} - C_{ps})/(1 - C_{ps}) \qquad (2)$$

and C_{pr} and C_{ps} are the pressure coefficients at reattachment and separation, respectively. Using Morel's pressure data [1] reattachment is indicated by Crabtree's criterion. At this stage this is only a consistency statement. It would be useful deductively if estimates of the pressure could be obtained.

The most important quantity that can be estimated from the solution to the swept-back mixing zone problem is the swirl in the side edge vortex. Assume that the flow over the actual model reattaches on the slanted base. The swirl angle is defined as

$$\phi = \tan^{-1}(v_\theta/u),$$

where v_θ is the azimuthal velocity in the vortex and u is the velocity in the x-direction, i.e., axial velocity in the vortex. ϕ varies with position in the vortex because v_θ and u vary. The

estimate for v_θ is obtained from (1) and that for u from $U\cos\beta$. Thus,

$$v_\theta = 0 \quad (U\sin\beta)$$
$$u = 0 \quad (U\cos\beta) \quad,$$

so that

$$\phi = 0 \quad (\beta) \quad.$$

This result for ϕ will be used as approximate relation

$$\phi \simeq \beta \quad. \tag{3}$$

The velocities v_θ and u could be measured using a laser Doppler velocimeter to obtain a check on this result.

An estimate of ϕ is needed to relate breakdown of the side edge vortex to the discontinuity in C_D. The error in this estimate may be considerable, but it should decrease as x increases. Since only the ratio, v_θ/u, is used to estimate ϕ and it may have smaller error than v_θ and u.

The Vortex Breakdown Hypothesis

Vortex breakdown has been observed in a number of flows, e.g., flow over highly swept wings and flow in ducts. Breakdown is one of the more remarkable aspects of vortex cores. Although it has been studied vigorously, there is no completely satisfactory theory for it. The description of it given by Hall [4] will be quoted here; he refers to flow in a duct with swirl imparted by vanes at the duct entrance. "If we follow the fluid as it spirals along the duct we find, typically, that the structure of the vortex, as indicated for example by the velocity distribution over a cross section of the duct, varies only slowly in the axial direction and then, suddenly and, at first sight, unexpectedly, there is an abrupt change in the structure with a very pronounced retardation of the flow along the axis and a corresponding divergence of the stream surfaces near the axis." This abrupt change is called vortex breakdown. Since Hall's review many papers on the subject have appeared, too numerous to mention here. Leibovich [5] reviews the recent work. The important facts for present purposes are the abruptness of the change in the vortex core flow and its sensitivity to small changes in flow conditions. Vortex breakdown occurs in two forms, mainly seen in reference [5]. One is called the bubble type and is nearly axisymmetric, at least close to the breakdown region; the second is called the spiral type and is highly asymmetric. These are illustrated in Fig. 7(a) and 7(b), respectively. In the duct flow a filament of dye is introduced along the axis which then gives a visual record of the breakdown.

Most of the quantitative information on vortex breakdown is obtained from duct flows because it is more difficult to run a controlled experiment in other flows. It seems that the phenomenon was first discovered in flows over highly swept wings; see [4] for references and a smoke flow photograph. This photograph shows a bubble type breakdown on one side of a delta wing and a spiral type on the other. Clearly the flow over a wing, with vortices on each side of the plane of symmetry, is more representative of the slanted base flows discussed here than duct flows. For typical wings, the spanwise separation of the vortices is much greater than in slanted base flows; the interaction beween the vortices is then quite different.

According to Hall [4] the necessary conditions for breakdown are: 1) the maximum $\phi \geq 40$ deg; 2) an adverse pressure gradient; 3) stream tube divergence in the vortex core. Conditions (2) and (3) are satisfied for the side edge vortices. The estimate obtained from the swept-back mixing zone problem gave $\phi \simeq \beta$ so that condition (1) would give $\beta \simeq 40$ deg for breakdown.

Condition (1) is clearly approximate. It was deduced by Hall from the limited experimental data available at the time. Since then laser-Doppler anemometry has come into wide use

Table 1*

Re	Type of breakdown	ϕ_m (deg)	Core expansion ratio
1920	spiral	31.7	1.64
	bubble	30.4	2.54
2812	spiral	30.6	1.78
	bubble	30.8	1.97
3348	spiral	33.5	2.10
	bubble	29.9	2.76

*Data from [5].

and is ideal for velocity measurements in vortex breakdown flow fields because no probe is introduced into the flow; a probe in the breakdown region can introduce large perturbations in the flow field. Results from many experiments on duct flows, using laser-Doppler anemometry, are presented by Leibovich [5]. In particular, his Table 1 summarizes data for the velocity in the approach flow, i.e., the flow to within about 1.5 vortex core diameters upstream of the breakdown point. Both bubble and spiral types of breakdown were observed and measured at three Reynolds numbers, which is based on the axial velocity far from the axis and the vortex core diameter. From those data, Table 1 was constructed.

The swirl angle, ϕ_m, presented in Table 1 is defined as

$$\phi_m \equiv \tan^{-1}(v_{\theta_{max}}/u_{max}).$$

It is calculated using certain functional forms for v_θ and u; the parameters in those forms are determined from a best fit to the data. The value of ϕ_m is a measure of the swirl angle for vortex breakdown; it is more reliable than the criterion given in condition (1).

In Table 1, ϕ_m varies between 29.9 and 33.5 deg. No trend in the variation of ϕ_m with Reynolds number can be detected; the average value of ϕ_m is 31.9 deg for the spiral type, 30.4 deg for the bubble type, and 31.2 deg if both types are considered. For purposes of estimation, $\phi_m \simeq 30$ deg can be used. Assuming that ϕ_m approximates the estimate of ϕ in (3), breakdown of the side edge vortex is estimated to occur at $\beta = 30$ deg.

Another feature of vortex breakdown that enters the proposed mechanism to explain the discontinuity in C_D is the increase in size of the vortex core after breakdown. Downstream of the breakdown region a new vortex is formed, in the wake region. The ratio of the wake-core radius to that in the flow upstream of breakdown is called the core expansion ratio, given in Table 1. The core radius is defined as the radial coordinate of the maximum in the azimuthal velocity. The smallest entry in the table gives a 64 percent increase in the size of the core.

One of the major results of the aforementioned theory is that breakdown of the side edge vortices is possible for the range of parameters covered in Morel's experiments. Assuming it does occur, its relations to the sudden change in C_D can be described as follows. Before breakdown the two vortices occupy a substantial part of the slanted base; see the discussion of Fig. 4, above. The sudden billowing of these vortices, as measured by the core expansion ratio, will cause the mutual interaction between them and their interaction with the outer stream to increase. The adverse pressure gradient acting on the vortices will increase and cause the breakdown region to move further upstream, etc. Rapid movement of the breakdown region is observed in duct flow experiments. The 3-D separation pattern, or open base flow, then collapses into the quasi-axisymmetric base flow. The final stage of this collapse cannot be described by the model.

The estimates of swirl, the relationship between swirl and

slant angle, $\beta \simeq \phi$, and the model proposed here can now be combined. They give the critical slant angle for the discontinuity in C_D, $\beta_c \simeq 30$ deg. Morel's experiments give (Fig. 2) $\beta_c = 30$ deg. Considering the idealizations made in arriving at the theoretical result, its agreement with the experimental value must be considered fortuitous. The proper conclusion is that the theory is consistent with the available experimental findings.

For the ogive-cylinder wind tunnel model tested by Morel ([2], Fig. 1(a)) the C_D versus β variation was generally the same as that in Fig. 2. However, the discontinuous decrease in C_D, from 0.62 to 0.3 in this case, occurs at $\beta_c = 43$ deg rather than $\beta_c = 30$ deg as for the straight side-edge. Development of a flow model for the ogive-cylinder slanted base, where the edge is an ellipse, will not be attempted. Some understanding of the flow for $\beta < \beta_c$ can be obtained by isolating three modules of the base flow field, assuming steady flow. 1) At the top of the base the flow separates. The scale of this separated region, measured by the location of reattachment line, is a small fraction of the major axis. 2) In the neighborhood of the side of the base the flow separates and side-edge vortices are formed. The flow pattern would be topologically the same as that in Fig. 4. The scale of the separation region is a significant fraction of the minor axis. 3) At the bottom of the base the flow has, at most, a small scale separated region.

It appears reasonable to neglect first order interaction between these three modules; then some portion of the base surface streamlines can be sketched. For small enough β the side-edge vortices must depart from the base either by reaching the edge or by lifting off. It is conjectured that for $\beta \simeq 30$ deg either the swirl is decreased below the critical value before they depart the surface or they break down off the surface. In the former, larger β is required for breakdown on the surface. In the latter, their mutual interaction and that with the outer stream, which is necessary to explain the sudden change in base flow and C_D, is relatively weak. Stronger vortices, i.e., larger β, would be required to have breakdown on the surface and the required interaction. In either case the conclusion is consistent with the observed larger β_c.

Discussion

More refined estimates for the swirl in the side edge vortices are possible, e.g., using the configuration of Fig. 5, but would require much more analysis. It would be preferable to test the central hypothesis of this theory experimentally. Introduction of a blunt body along the center of the vortex core, which is known to promote breakdown, could be useful as a diagnostic tool.

An explanation of the discontinuity in C_D at $\beta = \beta_c$ requires a process with the abruptness (almost explosive nature) of vortex breakdown. Theories based on some other hypothesis are possible, however. One of these could be based on the inability of the free shear layer to reattach for $\beta > \beta_c$.

In addition to an understanding of the phenomena that lead to the discontinuity in C_D, it would be desirable to be able to predict drag, especially for $\beta < \beta_c$. Linearized theory might be useful for the case of small β. Otherwise, only numerical methods could be successful.

References

1 Sovran, G., Morel, T., and Mason, W. T., Jr., *Aerodynamic Drag Mechanisms of Bluff Bodies and Road Vehicles*, Symposium held at the General Motors Research Laboratories, Plenum Press, New York, 1978.

2 Morel, T., "Aerodynamic Drag of Bluff Body Shapes Characteristic of Hatch-Back Cars," Research Publication GMR-2581, General Motors Research Laboratories, Nov. 1977. See also S.A.E. Technical Paper 780267, 1978.

3 Carr, G. W., "Influence of Rear Body Shape on the Aerodynamic Characteristics of Saloon Cars," Motor Industry Research Association, Report No. 1974/2, Nuneaton, Warwickshire, Feb. 1974.

4 Hall, M. G., "Vortex Breakdown," *Annual Review of Fluid Mechanics*, Vol. 4, Annual Reviews, 1972.

5 Leibovich, S., "The Structure of Vortex Breakdown," *Annual Review of Fluid Mechanics*, Vol. 10, Annual Reviews, 1978.

6 White, F. M., *Viscous Fluid Flow*, McGraw-Hill, New York, 1974, p. 509.

7 Crabtree, L. F., "Effects of Leading-Edge Separations on Thin Wings in Two-Dimensional Incompressible Flow," I.A.S. Preprint 659, Jan. 1957.

Complete Velocity Profile and "Optimum" Skin Friction Formulas for the Plane Wall-Jet

G. P. Hammond

Lecturer,
School of Mechanical Engineering,
Cranfield Institute of Technology,
Bedford, MK43 0AL,
England

An analytic expression for the complete velocity profile of a plane, turbulent wall-jet in "stagnant" surroundings is obtained by coupling Spalding's single formula for the inner layer with a sine function for the "wake component." This expression is transformed at the velocity maxima to yield an "optimum log-law" for skin friction. An approximate skin friction formula based on the "initial conditions" of the wall-jet is also presented. The formulas are generally in good agreement with experimental data. The complete velocity profile does not exhibit the conventional "law of the wall" behavior and modifications are consequently recommended to the usual treatment of the near-wall region in numerical calculation procedures for wall-jet flows. The use of the "Clauser plot" method of skin friction measurement is similarly shown to be in error when applied to wall-jets.

1 Introduction

Wall-jets of various types are widely used for applications such as gas turbine film cooling, aircraft blown flaps, and in heating and air-conditioning practice. Some of these flow geometries involve additional shear layer interactions and rates of strain superimposed on the classical plane wall-jet in nominally stagnant surroundings: coflowing external streams and streamline surface curvature are two common examples. Wall-jets also constitute part of more complex flows as in the case of impinging-jets, where they form the flow regime downstream of the impingement zone. Nevertheless, the classical plane wall-jet continues to be of considerable importance; directly, in applications such as heating and air-conditioning, and indirectly as a "limiting case" for validating the new calculation methods and turbulence models being developed for more complex wall-jet geometries.

Since the mid-1960's, an extensive literature has developed on plane wall-jets (see, for example, the review by Rajaratnam [1]), although the results lack a consistency comparable to that found with experimental data for other turbulent wall shear layers. (This is illustrated by the data scatter for the near-wall velocity profile and skin friction coefficient subsequently shown.) There is also a disparity in the interpretation of the available data which is reflected in the values for the log-law constants adopted by different workers and given in Table 1. These authors have identified a near-wall region for which the log-law expression:

$$u^+ = \frac{1}{\kappa}\ln y^+ + B = \frac{1}{\kappa}\ln(Ey^+) \tag{1}$$

is assumed to hold. These values may be compared with those

recommended by Brederode and Bradshaw [9] for turbulent boundary layers of $\kappa = 0.41$ and $B = 5.2$ (or $E = 8.4$). Their choice for the additive constant, B, was made to insure agreement with Patel's direct calibration for "Preston tube" skin friction measurements. It is clear that some of the wall-jet investigators of Table 1 consider there to be a log-law region similar to that found in turbulent boundary layers at moderate pressure gradients, while others imply that this region has quite a different character.

The present contribution has two main purposes. First, to obtain an analytic expression for the complete velocity profile in the fully-developed flow regime of a plane, turbulent wall-jet in stagnant surroundings: extending from the wall to the free edge of the jet. Second, to transform this expression in order to yield an "optimum log-law" for skin friction. The results of this analysis are subsequently used to resolve the anomalies, previously identified, in the log-law constants adopted by previous workers for plane wall-jets. They also lead to recommendations concerning the treatment of the near-wall region in numerical calculation methods for wall-jets, as well as the use of the Clauser plot method of skin friction measurement in such flows.

2 Complete Velocity Profile

The velocity profile for turbulent boundary layers may be well represented by an equation of the form:

$$u^+ = \frac{1}{\kappa}\ln y^+ + B + C\omega\left(\frac{y^+}{\delta^+}\right) \tag{2}$$

outside the viscous sublayer. This is essentially the log-law expression, equation (1), modified by Coles' "law of the wake" [10]. Spalding [11] chose a cosine form for the wake component, $\omega(y^+/\delta^+)$, to represent plane, turbulent wall-jets, but suggested that the agreement with experiment could be improved by a better choice of wake function; possibly

Table 1 Plane wall-jet log-law constants

Authors	Date	Data Source	Log Law Constants		
			κ	B	E
Myers, et al. [2]	1963	Authors	0.411	4.90	7.48
Pai and Whitelaw [3]	1969	Bradshaw and Gee [4]	0.507	10.48	200.00
Pai and Whitelaw [3]	1969	Kruka and Eskinazi [5]	0.522	9.00	107.50
Mabuchi and Kumada [6]	1972	Authors	0.406	5.10	7.94
Alcaraz, et al. [7]	1977	Tailland and Mathieu [8] (Corrected)	0.555	8.00	84.90

using a polynomial. The procedure used by Spalding [11] for evaluating the coefficient C is equivalent to setting $u^+ = 0$ at $y^+ = \delta^+ (\equiv D_1 b_u^+)$ and gives:

$$C = -\left\{ \frac{1}{\kappa} \ln(D_1 b_u^+) + B \right\} \tag{3}$$

In the present contribution, a sine relation is adopted to represent the wake function itself:

$$\omega\left(\frac{y^+}{\delta^+}\right) = \sin\left\{ D_2 \pi \left(\frac{y^+}{b_u^+}\right) \right\} \tag{4}$$

The use of equation (2) implies that the velocity profile results from an interaction between the near-wall (log-law) and "free-jet" (wake component) regions of the wall-jet. It is therefore logical to employ boundary layer values for the log-law constants and Brederode and Bradshaw's recommendations [9] are used here: $\kappa = 0.41$ and $B = 5.2$. In order to evaluate the coefficients D_1 and D_2 in the wake function, equations (3) and (4), the following boundary conditions must be satisfied:

$$\frac{u}{u_m} = 0.5 \text{ at } \frac{y^+}{b_u^+} = 1$$

$$\omega\left(\frac{y^+}{\delta^+}\right) = .1 \text{ at } \frac{y^+}{\delta^+} = 1 \tag{5}$$

These coefficients, obtained using an iterative solution procedure, are found to be closely represented by the "power law" relations:

$$D_1 = 2.27 R_m^{0.00962} \tag{6}$$

$$D_2 = 12.6 R_m^{-0.00962} \tag{7}$$

for $2000 < R_m < 35,000$ (the range covered by the experimental literature) and with the foregoing choice of log-law constants. The Reynolds number dependence of these coefficients reflects slight streamwise dissimilarity in the velocity profile, due to the differing character and development of the inner and outer layers of the wall-jet. The present wake function is in reasonable agreement with the plane wall-jet data of Bradshaw and Gee [4] as shown in Fig. 1. It also agrees well with the "plane flow" version of Starr and Sparrow's tabular wake function [12] derived from their cylindrical wall-jet, which was subsequently used by Mabuchi and Kumada [6] for comparison with their own plane wall-jet data.

In order to obtain an expression for the complete velocity profile in a plane wall-jet, it is necessary to allow for the deviation of the mean (time-average) velocity from that given by equation (2) within the viscous sublayer. A single analytic function for the profile in the buffer zone between the "linear" sublayer and the log-law region of a turbulent boundary layer has been derived by Spalding [13] in the form:

$$y^+ = f(u^+) \tag{8}$$

where

$$f(u+) = u^+ + e^{-A}\left[e^{\kappa u^+} - 1 - \kappa u^+ - \frac{(\kappa u^+)^2}{2!} \right.$$

$$\left. - \frac{(\kappa u^+)^3}{3!} - \frac{(\kappa u^+)^4}{4!} \right] \tag{9}$$

and

$$A = \kappa B \tag{10}$$

Equation (9) asymptotes to the outer layer profile and combining it with equation (2), in a similar manner to that

Nomenclature

A = κB

b_u = cross-stream distance from the wall to the point where $u/u_m = 0.5$

b_u^+ = $u_\tau b_u / \nu$

B = log-law additive constant

C = "wake function" coefficient

c_f = skin friction coefficient, $\tau_w / \frac{1}{2}\rho u_m^2$

c_F = skin friction coefficient, $\tau_w / \frac{1}{2}\rho u_e^2$

D^+ = van Driest damping function "constant"

D_1 = δ^+ / b_u^+

D_2 = sine coefficient in wake function

E = log-law "integration" constant

h = effective height of flattened pitot tube

K_b = jet spread parameter, db_u/dx

K_u = jet peak velocity decay constant

1 = Prandtl's mixing length

1^+ = $u_\tau 1/\nu$

n = jet peak velocity decay exponent

Re_s = slot Reynolds number, $u_e s/\nu$

R_m = local Reynolds number, $u_m y_m / \nu$

s = slot width

u = mean velocity component in the x-direction

u^+ = u/u_τ

u_e = slot exit velocity

u_m = jet velocity maxima (peak) at given x-position

u_m^+ = u_m/u_τ

u_τ = "friction velocity," $(\tau_w/\rho)^{1/2}$

x,y = coordinate directions parallel and normal to the wall, respectively

x_0 = virtual origin of the jet

y^+ = $u_\tau y/\nu$

y_m = cross-stream distance from the wall to the point where $u = u_m$

y_m^+ = $u_\tau y_m / \nu$

y_s = viscous sublayer thickness at $y^+ = 50$

α = "free-jet" region mixing length constant

δ = wall-jet thickness

δ^+ = $u_\tau \delta / \nu$

κ = von Karman's constant

ρ, ν = density and kinematic viscosity, respectively

σ = standard deviation about mean value

τ_t = total (viscous plus turbulent) shear stress
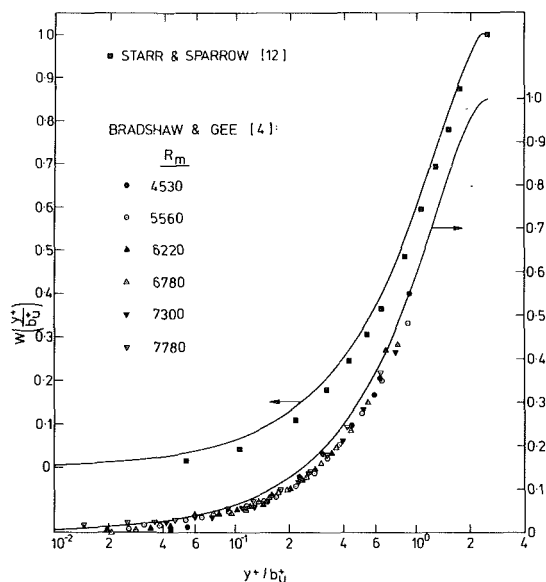
τ_w = local wall shear stress

τ^+ = τ_t / τ_w

Fig. 1 Plane wall-jet wake function (normalized to $\delta^+/b_u{}^+ = 2.48$, with $\kappa = 0.41$ and $B = 5.2$)

Fig. 2 Complete velocity profile for the plane wall-jet ($R_m = 9500$)

proposed by Dean [14] for turbulent boundary layers, gives a two-part expression for the complete velocity profile of a plane wall-jet in the form:

$$y^+ e^{\kappa C \omega (y^+/b_u^+)} = f(u^+) , y^+ < 150$$

$$y^+ e^{\kappa C \omega (y^+/b_u^+)} = e^{(\kappa u^+ - A)} , y^+ > 150 \qquad (11)$$

where the partitional value of y^+, separating the influence of the viscous sublayer from that of the outer layer, is rather arbitrary within the range $70 < y^+ < 170$. This is because the influence of the viscous sublayer, reflected in the first part of the formulation, is negligible for y^+ greater than about 30-50. However, this first part of the expression cannot be used in the outer layer, free-jet region, where u^+ falls to zero but viscous effects do not influence the profile shape. Thus both parts of equation (11) yield identical results for about $y^+ > 70$ and $u^+ > 13$, although not otherwise. (Dean [14] was able to employ a single expression, similar to the first part of equation (11), for the complete velocity profile in turbulent boundary layers, as u^+ for this outer layer never falls below about 20.)

The outer layer form of equation (11) simply reproduces the results of equation (2). A typical velocity profile obtained using equation (11) is shown in Fig. 2. The complete velocity profile satisfies the following five boundary conditions:

$$u^+ = 0, du^+/dy^+ = 1 \text{ at } y^+ = 0$$

$$u^+ = 0.5u_m^+ \text{ at } y^+ = b_u^+$$

$$u^+ = 0, du^+/dy^+ = 0 \text{ at } y^+ = \delta^+ \qquad (12)$$

The complete velocity profile formula is compared with experimental data for the plane wall-jet in Fig. 3. Agreement is seen to be reasonable in the outer layer but, in order to assess the causes for the obvious deviation in the near-wall region, it is necessary to consider the experimental techniques employed by the investigators ([2], [4], [8]). Very close to the wall (for about $y^+ < 5$), the mean velocity variation should conform to the "linear" profile, and the discrepancies in all three experimental studies is therefore likely to be due to measurement "errors." It is, of course, notoriously difficult to make measurements within the viscous sublayer as a result of its very small width. (Such problems are possibly the reason for the existence of so few data sets covering the near-wall
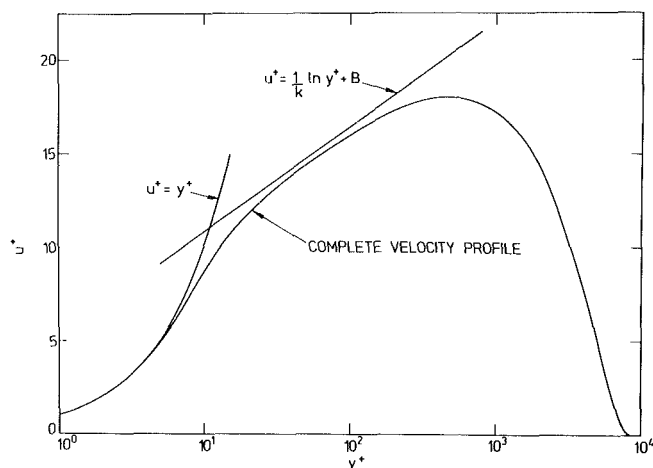
region of plane wall-jets in the literature.) The data of Bradshaw and Gee [4] was obtained using a flattened pitot tube for mean velocity and a "Stanton tube" for skin friction measurement. An indication of the spatial resolution of velocity measurements in the viscous sublayer may be obtained from the ratio of the effective height of the probe, h, to the sublayer thickness, y_s. Defining y_s as the thickness corresponding to $y^+ = 50$ enables an estimate of h/y_s to be made, and this is found to be about 0.340 in Bradshaw and Gee's experiments [4]. In contrast, for Myers, et al. [2], who used a flattened pitot tube and a hot-film technique to measure mean velocity and skin friction, respectively, the ratio h/y_s is estimated to be approximately 0.056. This improved spatial resolution is likely to be the reason for the generally closer agreement with the linear sublayer requirement in the data of Myers, et al. [2], although their scatter is greater than the other studies. Tailland and Mathieu [8] obtained mean velocities with a pitot tube and skin friction data by extrapolating hot-wire, turbulent shear stress measurements to the wall. They were conscious of errors in the latter procedure resulting from the cooling effect of the wall on the hot-wire itself. Mathieu and his co-workers ([7], [8], [15]) have gone to some lengths to assess the magnitude of this error in their earlier data. The measurements presented in Fig. 3 have been corrected for the cooling effect by using the skin friction correlation of Alcaraz and Mathieu [15] based on the "floating surface element" technique. It is clear that, although this improves the outer layer agreement with the present complete velocity profile formula, the near-wall experimental data still does not conform to the linear profile. It seems likely that this is again due to the problem of spatial resolution, but the relative size of the measurement probe cannot be estimated as Tailland and Mathieu [8] do not give the dimensions of their pitot tube. The foregoing discussion would seem to support the contention that the present complete velocity profile, given by equation (11), is physically more plausible in the near-wall region than the available experimental data.

In engineering practice, the wall-jet velocity profile is often required in a form based on the local, mean-flow velocity and length scales; u_m and b_u, respectively. The definitions for the skin friction coefficient, c_f, "friction" (or wall shear) velocity, u_τ, and local, mean-flow Reynolds number, R_m, may be used to transform the velocity profile formula equation (2) (which neglects the influence of the viscous sublayer) into such a form:

$$\frac{u}{u_m} = \left(\frac{c_f}{2}\right)^{1/2} \left[\frac{1}{\kappa} \ln\left\{R_m\left(\frac{c_f}{2}\right)^{1/2}\left(\frac{b_u}{y_m}\right)\left(\frac{y}{b_u}\right)\right\} + B\right]$$

$$+ C\sin\left\{D_2\,\pi\left(\frac{y}{b_u}\right)\right\}\Big]\qquad(13)$$

This expression may be solved for a prescribed slot Reynolds number, Re_s, and streamwise distance, x/s, via the formulas relating initial and local flow properties hereafter obtained (equation (22)). Typical velocity profiles obtained from equation (13) are shown in Fig. 4 together with Verhoff's commonly used expression [16] (which, for $y/b_u < 1$, closely follows the present velocity profile corresponding to a value of $\mathrm{R}_m = 2000$). Verhoff's relation is based on an inner layer velocity profile described by a one-seventh power law, similar to Blasius' near-wall formula for turbulent pipe-flow, and an error function for the profile in the free-jet region. This expression is in good agreement with the plane wall-jet experimental data reviewed by Rajaratnam [1] and Verhoff [16] for about $0.2 < y/b_u < 1.2$. The present velocity profile formula, equation (13), is in better agreement with experimental data, particularly close to the wall and toward the free edge of the jet.

3 Optimum Log-Law for Skin Friction

Dean [17] has recently employed the log-law velocity profile formula for turbulent wall shear layers to obtain an "optimum log-law" for skin friction in two-dimensional, rectangular duct-flow. This approach is adopted here to obtain an analogous expression for the plane wall-jet from equation (2). The latter may be transformed at the velocity maxima, where $y = y_m$, noting that:

$$u_m^+ \equiv \frac{u_m}{u_\tau} = \left(\frac{2}{c_f}\right)^{1/2}, y_m^+ \equiv \frac{u_\tau y_m}{\nu} = \mathrm{R}_m\left(\frac{c_f}{2}\right)^{1/2}\quad(14)$$

This gives the optimum log-law for skin friction in the form:

$$\left(\frac{2}{c_f}\right)^{1/2} = \frac{1}{\kappa}\ln\left\{\mathrm{R}_m\left(\frac{c_f}{2}\right)^{1/2}\right\} + B + C\sin\left\{D_2\,\pi\left(\frac{y_m^+}{b_u^+}\right)\right\}\quad(15)$$

The location of the velocity peak, y_m^+/b_u^+, is simply obtained by differentiating equation (2) to find its maxima as a function of b_u^+ (or R_m). The optimum log-law, equation (15), may then be easily solved iteratively. A consequence of this procedure is that b_u^+ is found to be linearly related to R_m, within the range $2000 < \mathrm{R}_m < 35{,}000$, and given by

$$b_u^+ = 0.385\mathrm{R}_m\qquad(16)$$

which may be retrospectively used to solve equations (11), (13), and (15)[1]. The location of the velocity peak may then be expressed in the form:

$$\frac{y_m^+}{b_u^+} = 2.60\left(\frac{c_f}{2}\right)^{1/2}\qquad(17)$$

using equation (16).

A comparison of the optimum log-law with experimental data and data correlations for skin friction in plane wall-jets within nominally stagnant surroundings is shown in Fig. 5. This comparison is limited to data obtained with direct techniques for skin friction measurement as indirect methods of the "Clauser plot" type [20], employed by several workers ([2], [6], [19]), presume the existence of a conventional log-law region within the inner layer and necessitate prior specification of log-law constants. Myers, et al. [2], presented their data in terms of the wall-jet "initial conditions" (c_F, Re_s, and x/s) and these have been converted to their local, mean-flow equivalent. This was performed by using the empirical peak "velocity decay" and jet spreading rate of Myers, et al., together with Verhoff's [16] value for the location of the peak velocity ($y_m^+/b_u^+ = 0.1654$). The resulting

---

[1] These equations have interrelated boundary conditions and were originally solved "simultaneously."
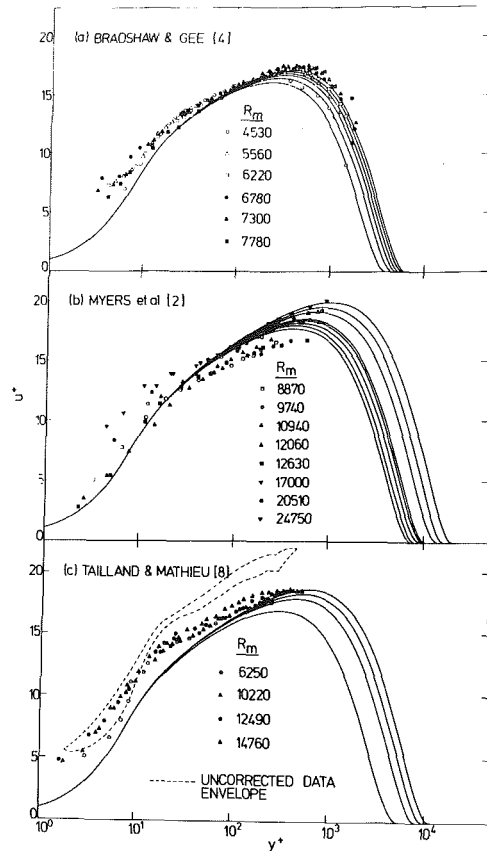
Fig. 3 Complete velocity profile compared with experimental data
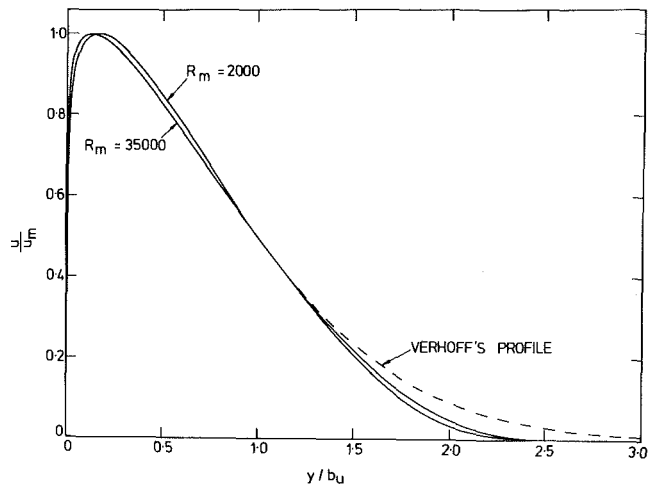
Fig. 4 Wall-jet velocity profile scaled on mean-flow properties

skin friction correlation exhibits a slight residual dependence on x/s in addition to that associated with R_m. The optimum log-law is consequently seen (in Fig. 5) to be in good agreement with both the magnitude and trend of the available, directly-measured skin friction data.

4 Approximate Skin Friction Formula

Myers, et al. [2], have emphasized the desirability for engineering design purposes of presenting wall-jet skin friction data in terms of the jet's easily identified initial conditions (also, G. E. Myers, private communication, 1978). In order to convert the optimum log-law to this basis, it is

Table 2 Mean-flow properties of plane wall-jets: Experimental data

| Authors | Date | Experimental range | | | Velocity decay | | | |
		S(mm)	Re_s	x/S	K_u	n	K_b	x_0/S
Sigalla [18]	1958	7.95	22,620–51,690	<64	3.45	0.500	0.0633	8.02
Schwarz and Cosart [21]	1961	25.40	13,510–41,600	18–66	5.42	0.555	0.0678	11.20
Bradshaw and Gee [4]	1962	0.46	6039	350–2150	3.96	0.549	0.0741	NA
Myers, et al. [2]	1963	12.70	7100–56,500	<180	3.45	0.490	0.0787	4.43
Giles, et al. [22]	1966	<0.64	20,000–100,000	NA	NA	NA	0.0768	NA
Tailland and Mathieu [8]	1967	6.25	11,000–30,000	<192	3.85	0.500	0.0705	8.00
Gartshore and Newman [23]	1969	7.72	30,800	<124	4.55	0.538	0.0660	9.40
Paizis and Schwarz [24]	1975	NA	NA	90–400	3.70	0.500	0.0860	NA
Wilson and Goldstein [25]	1976	6.09	3500–16,500	25–127	5.28	0.525	0.0780	7.50
Guitton and Newman [19]	1977	7.62	30,000	<207	NA	NA	0.0710	NA

NA = not available
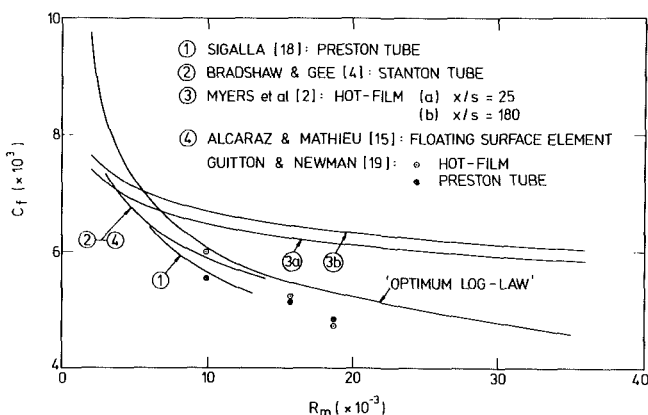
Fig. 5 "Optimum log-law" for skin friction beneath plane wall-jets

Fig. 6 Approximate skin friction formula for plane wall-jets: · · · · · · uncertainty due to mean-flow properties.

necessary to make estimates of the mean-flow properties of the jet; specifically, the peak velocity decay and jet spread. These are conventionally written in the form:

$$\frac{u_m}{u_e} = K_u \left(\frac{x}{s} \right)^{-n} \tag{18}$$

and

$$\frac{b_u}{s} = K_b \left(\frac{x}{s} + \frac{x_0}{s} \right) \tag{19}$$

where the spread constant, K_b, is equal to the far-field spreading rate (db_u/dx) and x_0/s is the so-called "geometric" virtual origin of the jet [26]. The experimental values for the constants appearing in these expressions are given in Table 2. The variability observed in the experimental data[2] does not seem to justify a choice for the velocity decay exponent, n, other than 0.5. Adopting this exponent, then the experimental uncertainty in the constants may be represented by the following deviation about the mean values:

$$K_u = 3.73 \, (\sigma = 0.57)$$

$$K_b = 0.073 (\sigma = 0.007)$$

$$x_0/s = 8.10 (\sigma = 2.20)$$

The optimum log-law for skin friction, equation (15), may be approximated by the simple relation:

$$c_f = 0.0667 \text{R}_m^{-0.258} \tag{20}$$

for $2000 < \text{R}_m < 35,000$ with an error of about 3 percent. This error is small in comparison with the foregoing uncertainty in the mean-flow properties required to obtain an approximate

skin friction formula based on the jet initial conditions. Equation (20) has therefore been transformed in terms of these initial conditions by using equations (18) and (19) together with the mean values for their characteristic constants to give:

$$c_F = 1.38 \text{Re}_s^{-0.23} \left(\frac{x}{s} \right)^{-1.10} \tag{21}$$

for $3000 < \text{Re}_s < 140,000$ and $30 < x/s < 3000$. This approximate skin friction formula is shown in Fig. 6 with an uncertainty band, obtained by the method of Kline and McClintock [27], which corresponds to one standard deviation in the mean-flow properties. The approximate formula is also compared in Fig. 6 with experimental data correlations ([2], [4], [18]). The correlations for Bradshaw and Gee [4] and Sigalla [18] were obtained by transforming their local skin friction correlations using their corresponding mean-flow data (except that in the latter case Verhoff's [16] value for the cross-stream velocity peak location was employed). The discrepancy between the approximate skin friction formula and Bradshaw and Gee's transformed correlation is mainly due to the deviation of their velocity decay data from the mean values used here (as can be observed in Fig. 5, where their *local* skin friction is seen to be in quite good agreement with the optimum log-law). The skin friction correlation of Alcaraz and Mathieu [15], transformed using the mean-flow data of Tailland and Mathieu [8], is very close to that of equation (21) for $20 < x/s < 190$. It is therefore not included in Fig. 6 for reasons of clarity. The approximate

---

[2] This variability does not exhibit any consistent dependence on either Re_s or x/s and appears to reflect experimental uncertainty.

skin friction formula is seen to be in good agreement with the available experimental data, except for that of Bradshaw and Gee [4] as previously discussed.

The mean-flow properties of the wall-jet, given by equations (18) and (19), may also be used to obtain an expression for the local Reynolds number, R_m, in terms of the jet initial conditions. Adopting the experimental average values for these properties (as employed aforesaid) gives:

$$R_m = 0.215 \, Re_s^{0.89} \left(\frac{x}{s} \right)^{0.40} \qquad (22)$$

with an uncertainty of about ∓ 24 percent, based on one standard deviation in the mean-flow properties. Equation (22) may be used to solve the complete and cross-stream scaled velocity profile, and optimum skin friction formulas, equations (11), (13), and (15), respectively, for prescribed initial conditions.

5 Some Implications of the Wall-Jet Inner Layer

The complete velocity profile formula for a typical local, mean-flow Reynolds number ($R_m = 9500$) is compared with the conventional log-law for a turbulent wall shear layer in Fig. 2. It is clear that plane wall-jets do not exhibit a well-defined log-law region due to the "strong" interaction between the near-wall and free-jet regions. The wall-jet profile is also seen to fall below the conventional log-law curve and this has important implications for both the calculation of wall-jet flows using modern numerical techniques and the experimental determination of wall-jet skin friction from methods of the Clauser plot type.

The significance of the wall-jet inner layer can be illustrated by considering the treatment of the near-wall region in two, well-tested finite-difference calculation procedures for turbulent thin shear layers: the Patankar-Spalding method [28], incorporated in the GENMIX code, and the Keller-Cebeci "box" method used by Cebeci and Smith [29]. The former bridge the steep property gradients close to the wall by employing "wall functions" based directly on the log-law, equation (1). Conversely, Cebeci and Smith [29] perform calculations within the viscous sublayer using a damping function of the van Driest type [30] applied to the near-wall mixing length distribution. Cebeci and Smith [29] give the resulting velocity profile in the form:

$$u^+ = \int_0^{y^+} \frac{2}{1+\sqrt{1+4a}} \, dy^+ \qquad (23)$$

where $a = (\kappa y^+)^2 \, [1 - \exp(-y^+/D^+)]^2$. The damping length, D^+, has a conventional value of 25.5 corresponding to a value for the log-law additive constant, B, of 5.2. The total shear stress in the inner layer is given by:

$$\tau^+ = \frac{du^+}{dy^+} + 1^{+2} \left| \frac{du^+}{dy^+} \right| \frac{du^+}{dy^+} \qquad (24)$$

where there is a region, outside the viscous sublayer, for which $1^+ = \kappa y^+$. Thus, experimental mean velocity and turbulent shear stress measurements may be used to evaluate κ from equation (24). However, there is a scarcity of such data sets for plane wall-jets and those available ([4], [8], [25]) would not seem to support a choice for κ other than the usual value of about 0.41. Adopting this value enables D^+ in the damped mixing length distribution:

$$1^+ = \kappa y^+ [1 - \exp(-y^+/D^+)] \qquad (25)$$

to be evaluated by matching the velocity obtained from equation (23) with the wall-jet velocity profile, equation (11), in the region $70 < y^+ < 170$. Equation (23) has been integrated numerically and the resulting dependence of D^+ on R_m may be represented by the power-law relation:

$$D^+ = 8.61 R_m^{0.107} \qquad (26)$$

for $2000 < R_m < 35,000$. The corresponding expression for the dependence of the log-law "constant" E in the wall functions of Patankar and Spalding [28] is:

$$E = 1.06 R_m^{0.204} \qquad (27)$$

The use of these expressions for calculating the inner layer of wall-jet flows is only approximate as they still imply log-law behavior in the region $70 < y^+ < 170$. Nevertheless, they will insure better agreement with the known physical characteristics of wall-jets than the use of methods based on the near-wall properties of "conventional" turbulent wall shear layers.

The Clauser plot method of obtaining skin friction data from mean velocity measurements [20] assumes, as previously noted, the existence of a log-law region with conventional values for the constants, κ and B. The error in the use of this technique for wall-jets may be estimated by comparing the skin friction coefficient derived from it (employing Brederode and Bradshaw's recommendations for the log-law constants [9]) with coefficients obtained by fitting "effective" log-law constants to the complete velocity profile in the region $70 < y^+ < 170$. The Clauser plot values are found to be low by about 25 percent at $R_m = 2000$ with the error reducing to 1 percent at $R_m = 35,000$. However, the problem is complicated by measurement errors in mean velocity data for the inner layer. These mean velocities are higher than the complete velocity profile and therefore alter the apparent error in the corresponding Clauser plot skin friction data. The corrected mean velocity data of Tailland and Mathieu [8] implies an increased skin friction error, while Bradshaw and Gee's data [4] slightly reduces it and that of Myers, et al. [2], almost eliminates this error. The latter is undoubtedly the reason that Myers, et al., found Clauser plot data to be in good agreement with their hot-film measurements. The inconsistency in the effect of the data of different workers appears to be due to the separate influences of the error in the inner layer velocity measurements and the range of R_m. In view of the foregoing uncertainties in the application of the Clauser plot, its use is not recommended for wall-jet flows.

6 Concluding Remarks

An analytic expression for the complete velocity profile of a plane wall-jet in stagnant surroundings has been obtained by coupling Spalding's single formula for the inner layer with a sine function for the wake component. The profile is shown to satisfy the wall boundary conditions and to exhibit near-wall behavior which is physically more plausible than the available experimental data, due to measurement errors inherent in the latter. The complete velocity profile results from the strong interaction between the near-wall and free-jet regions and does not display a well-defined log-law region. The complete profile is dependent on the local, mean-flow Reynolds number and the inner layer profile falls below the conventional law of the wall for turbulent thin shear layers. The variation in the log-law constant adopted by previous investigators (noted in the Introduction and Table 1) has therefore resulted from attempts to fit a log-law relation to this inner layer at differing Reynolds numbers. Recommendations have consequently been made to modify the usual treatment of the near-wall region in numerical calculation methods for wall-jet flows. The complete velocity profile also provides a basis for generating the "starting profiles" in such methods.

The complete velocity profile formula has been transformed at the velocity maxima to yield an "optimum log-law" for skin friction. This was then used to develop an approximate skin friction formula based on the initial conditions of the wall-jet. Both formulas have been shown to be in generally good agreement with the available experimental

data. The Clauser plot method of deriving skin friction coefficients from measured velocity profiles has been shown to be unreliable for wall-jet flows, due to both the necessity of specifying log-law constants and the measurement errors in near-wall velocity data.

Acknowledgments

References

1 Rajaratnam, N., *Turbulent Jets*, Elsevier, Amsterdam, 1976.

2 Myers, G. E., Schauer, J. J., and Eustis, R. H., "Plane Turbulent Wall Jet Flow Development and Friction Factor," ASME *Journal of Basic Engineering*, Vol. 85, 1963, pp. 47–54.

3 Pai, B. R., and Whitelaw, J. H., "Simplification of the Razor Blade Technique and Its Application to the Measurement of Wall-shear Stress in Wall-jet Flows," *Aeronautical Quarterly*, Vol. 20, 1969, pp. 355–364.

4 Bradshaw, P., and Gee, M. T., "Turbulent Wall Jets With and Without an External Stream," ARC R&M 3252, 1962.

5 Kruka, V., and Eskinazi, S., "The Wall-jet in a Moving Stream," *Journal of Fluid Mechanics*, Vol. 20, 1964, pp. 555–579.

6 Mabuchi, I., and Kumada, M., "Studies on Heat Transfer to Turbulent Jets with Adjacent Boundaries (1st Report: Flow Development and Mass Transfer in Plane Turbulent Wall Jet)," *Bulletin of the JSME*, Vol. 15, 1972, pp. 1236–1245.

7 Alcaraz, E., Charnay, G., and Mathieu, J., "Measurements in a Wall Jet over a Convex Surface," *Physics of Fluids*, Vol. 20, 1977, pp. 203–210.

8 Tailland, A., and Mathieu, J., "Jet Pariétal," *Journal de Mécanique*, Vol. 6, 1967, pp. 103–131.

9 Brederode, V., and Bradshaw, P., "A Note on the Empirical Constants Appearing in the Logarithmic Law for Turbulent Wall Flows," Imperial College (London Univ.), Aero. Report 74-03, 1974.

10 Coles, D., "The Law of the Wake in the Turbulent Boundary Layer," *Journal of Fluid Mechanics*, Vol. 1, 1956, pp. 191–226.

11 Spalding, D. B., "A Unified Theory of Friction, Heat Transfer and Mass Transfer in the Turbulent Boundary Layer and Wall Jet," ARC CP 829, 1965.

12 Starr, J. B., and Sparrow, E. M., "Experiments on a Turbulent Cylindrical Wall Jet," *Journal of Fluid Mechanics*, Vol. 29, 1967, pp. 495–512.

13 Spalding, D. B., "A Single Formula for the Law of the Wall," ASME *Journal of Applied Mechanics*, Vol. 28, 1961, pp. 455–458.

14 Dean, R. B., "A Single Formula for the Complete Velocity Profile in a Turbulent Boundary Layer," ASME JOURNAL OF FLUIDS ENGINEERING, Vol. 98, 1976, pp. 723–727.

15 Alcaraz, E., and Mathieu, J., "Mesure des Vitesses Moyennes prés d'une Paroi par Anémométrie à fil Chaud," *C.R. Acad. Sci. Paris*, Vol. 280A, 1975, pp. 737–740.

16 Verhoff, A., "The Two-dimensional, Turbulent Wall Jet With and Without an External Free Stream," Princeton University Report 626, 1963.

17 Dean, R. B., "Reynolds Number Dependence of Skin Friction and Other Bulk Flow Variables in Two-dimensional Rectangular Duct Flow," ASME JOURNAL OF FLUIDS ENGINEERING, Vol. 100, 1978, pp. 215–223.

18 Sigalla, A., "Measurements of Skin Friction in a Plane Turbulent Wall Jet," *Journal of the Royal Aeronautical Society*, Vol. 62, 1958, pp. 873–877.

19 Guitton, D. E., and Newman, B. G., "Self-preserving Turbulent Wall Jets over Convex Surfaces," *Journal of Fluid Mechanics*, Vol. 81, 1977, pp. 155–185.

20 Clauser, F. H., "Turbulent Boundary Layers in Adverse Pressure Gradients," *Journal of the Aeronautical Sciences*, Vol. 21, 1954, pp. 91–108.

21 Schwarz, W. H., and Cosart, W. P., "The Two-dimensional Turbulent Wall-jet," *Journal of Fluid Mechanics*, Vol. 10, 1961, pp. 481–495.

22 Giles, J. A., Hays, A. P., and Sawyer, R. A., "Turbulent Wall Jets on Logarithmic Spiral Surfaces," *Aeronautical Quarterly*, Vol. 17, 1966, pp. 201–215.

23 Gartshore, I. S., and Newman, B. G., "The Turbulent Wall Jet in an Arbitrary Pressure Gradient," *Aeronautical Quarterly*, Vol. 20, 1969, pp. 25–56.

24 Paizis, S. T., and Schwarz, W. H., "Entrainment Rates of Turbulent Shear Flows," *Journal of Fluid Mechanics*, Vol. 68, 1975, pp. 297–308.

25 Wilson, D. J., and Goldstein, R. J., "Turbulent Wall Jets with Cylindrical Streamwise Surface Curvature," ASME JOURNAL OF FLUIDS ENGINEERING, Vol. 98, 1976, pp. 550–557.

26 Flora, J. J., and Goldschmidt, V. W., "Virtual Origins of a Free Plane Turbulent Jet," *AIAA Journal*, Vol. 7, 1969, pp. 2344–2346.

27 Kline, S. J., and McClintock, F. A., "Describing Uncertainties in Single-sample Experiments," *Mechanical Engineering*, Jan. 1953, pp. 3–8.

28 Patankar, S. V., and Spalding, D. B., *Heat and Mass Transfer in Boundary Layers*, 2nd Ed. Intertext, London, 1970.

29 Cebeci, T., and Smith, A. M. O., *Analysis of Turbulent Boundary Layers*, Academic Press, New York, 1974.

30 Van Driest, E. R., "On Turbulent Flow Near a Wall," *Journal of the Aeronautical Sciences*, Vol. 23, 1956, pp. 1007–1011.

data. The Clauser plot method of deriving skin friction coefficients from measured velocity profiles has been shown to be unreliable for wall-jet flows, due to both the necessity of specifying log-law constants and the measurement errors in near-wall velocity data.

Acknowledgments

References

1 Rajaratnam, N., *Turbulent Jets*, Elsevier, Amsterdam, 1976.

2 Myers, G. E., Schauer, J. J., and Eustis, R. H., "Plane Turbulent Wall Jet Flow Development and Friction Factor," ASME *Journal of Basic Engineering*, Vol. 85, 1963, pp. 47–54.

3 Pai, B. R., and Whitelaw, J. H., "Simplification of the Razor Blade Technique and Its Application to the Measurement of Wall-shear Stress in Wall-jet Flows," *Aeronautical Quarterly*, Vol. 20, 1969, pp. 355–364.

4 Bradshaw, P., and Gee, M. T., "Turbulent Wall Jets With and Without an External Stream," ARC R&M 3252, 1962.

5 Kruka, V., and Eskinazi, S., "The Wall-jet in a Moving Stream," *Journal of Fluid Mechanics*, Vol. 20, 1964, pp. 555–579.

6 Mabuchi, I., and Kumada, M., "Studies on Heat Transfer to Turbulent Jets with Adjacent Boundaries (1st Report: Flow Development and Mass Transfer in Plane Turbulent Wall Jet)," *Bulletin of the JSME*, Vol. 15, 1972, pp. 1236–1245.

7 Alcaraz, E., Charnay, G., and Mathieu, J., "Measurements in a Wall Jet over a Convex Surface," *Physics of Fluids*, Vol. 20, 1977, pp. 203–210.

8 Tailland, A., and Mathieu, J., "Jet Pariétal," *Journal de Mécanique*, Vol. 6, 1967, pp. 103–131.

9 Brederode, V., and Bradshaw, P., "A Note on the Empirical Constants Appearing in the Logarithmic Law for Turbulent Wall Flows," Imperial College (London Univ.), Aero. Report 74-03, 1974.

10 Coles, D., "The Law of the Wake in the Turbulent Boundary Layer," *Journal of Fluid Mechanics*, Vol. 1, 1956, pp. 191–226.

11 Spalding, D. B., "A Unified Theory of Friction, Heat Transfer and Mass Transfer in the Turbulent Boundary Layer and Wall Jet," ARC CP 829, 1965.

12 Starr, J. B., and Sparrow, E. M., "Experiments on a Turbulent Cylindrical Wall Jet," *Journal of Fluid Mechanics*, Vol. 29, 1967, pp. 495–512.

13 Spalding, D. B., "A Single Formula for the Law of the Wall," ASME *Journal of Applied Mechanics*, Vol. 28, 1961, pp. 455–458.

14 Dean, R. B., "A Single Formula for the Complete Velocity Profile in a Turbulent Boundary Layer," ASME JOURNAL OF FLUIDS ENGINEERING, Vol. 98, 1976, pp. 723–727.

15 Alcaraz, E., and Mathieu, J., "Mesure des Vitesses Moyennes prés d'une Paroi par Anémométrie à fil Chaud," *C.R. Acad. Sci. Paris*, Vol. 280A, 1975, pp. 737–740.

16 Verhoff, A., "The Two-dimensional, Turbulent Wall Jet With and Without an External Free Stream," Princeton University Report 626, 1963.

17 Dean, R. B., "Reynolds Number Dependence of Skin Friction and Other Bulk Flow Variables in Two-dimensional Rectangular Duct Flow," ASME JOURNAL OF FLUIDS ENGINEERING, Vol. 100, 1978, pp. 215–223.

18 Sigalla, A., "Measurements of Skin Friction in a Plane Turbulent Wall Jet," *Journal of the Royal Aeronautical Society*, Vol. 62, 1958, pp. 873–877.

19 Guitton, D. E., and Newman, B. G., "Self-preserving Turbulent Wall Jets over Convex Surfaces," *Journal of Fluid Mechanics*, Vol. 81, 1977, pp. 155–185.

20 Clauser, F. H., "Turbulent Boundary Layers in Adverse Pressure Gradients," *Journal of the Aeronautical Sciences*, Vol. 21, 1954, pp. 91–108.

21 Schwarz, W. H., and Cosart, W. P., "The Two-dimensional Turbulent Wall-jet," *Journal of Fluid Mechanics*, Vol. 10, 1961, pp. 481–495.

22 Giles, J. A., Hays, A. P., and Sawyer, R. A., "Turbulent Wall Jets on Logarithmic Spiral Surfaces," *Aeronautical Quarterly*, Vol. 17, 1966, pp. 201–215.

23 Gartshore, I. S., and Newman, B. G., "The Turbulent Wall Jet in an Arbitrary Pressure Gradient," *Aeronautical Quarterly*, Vol. 20, 1969, pp. 25–56.

24 Paizis, S. T., and Schwarz, W. H., "Entrainment Rates of Turbulent Shear Flows," *Journal of Fluid Mechanics*, Vol. 68, 1975, pp. 297–308.

25 Wilson, D. J., and Goldstein, R. J., "Turbulent Wall Jets with Cylindrical Streamwise Surface Curvature," ASME JOURNAL OF FLUIDS ENGINEERING, Vol. 98, 1976, pp. 550–557.

26 Flora, J. J., and Goldschmidt, V. W., "Virtual Origins of a Free Plane Turbulent Jet," *AIAA Journal*, Vol. 7, 1969, pp. 2344–2346.

27 Kline, S. J., and McClintock, F. A., "Describing Uncertainties in Single-sample Experiments," *Mechanical Engineering*, Jan. 1953, pp. 3–8.

28 Patankar, S. V., and Spalding, D. B., *Heat and Mass Transfer in Boundary Layers*, 2nd Ed. Intertext, London, 1970.

29 Cebeci, T., and Smith, A. M. O., *Analysis of Turbulent Boundary Layers*, Academic Press, New York, 1974.

30 Van Driest, E. R., "On Turbulent Flow Near a Wall," *Journal of the Aeronautical Sciences*, Vol. 23, 1956, pp. 1007–1011.

DISCUSSION

P. Bradshaw[3]

Although velocity profile families are not used very often in calculation methods these days, skin friction formulas derived from them are always useful. An explanation of the departure from the conventional law of the wall is provided by the analysis of Townsend[4] who shows that the convex-upwards profile found in wall jets is to be expected if the shear stress falls rapidly with distance from the wall while the "mixing length" remains linearly proportional to y. In principle, the Reynolds number dependence of D_2 implies viscous effects in the outer part of the wall jet, contrary to what one would expect, and one wonders whether the very slow variation quoted in equations (7) is really significant. However, equation (15) is a neat extension of the conventional boundary layer analysis, and might perhaps be further extended to wall jets below an external stream.

Authors' Closure

The author is grateful to the discusser for his comments and suggestions on the present work. It is perhaps appropriate to record that Professor Bradshaw's many publications on turbulent shear flows have been a source of enlightenment to the author, and much of the terminology of the paper bears witness to this influence.

The shear stress distribution in Townsend's linear-stress layer [31] may be written in the form:

$$\tau^+ = 1 + \alpha^+ y^+ \qquad (28)$$

The rather limited data available [4, 8, 25] suggests that for wall-jets in stagnant surroundings this layer extends for about $40 < y^+ < 800$ (see the inset of Fig. 7) and that $\alpha^+ \simeq -0.0044$ (corresponding to $R_m \simeq 8250$), although α^+ is strictly a function of R_m. If $1^+ = \kappa y^+$, then it can be shown that the velocity distribution in the linear-stress layer is given by the following expression:

$$u^+ = \frac{1}{\kappa} \ln y^+ + B - \frac{2}{\kappa} \ln\left(\frac{1 + \sqrt{\tau^+}}{2}\right) + \frac{2}{\kappa}\left(\sqrt{\tau^+} - 1\right) \quad (29)$$

The form used here is that employed by Cebeci et al. [32]. Unfortunately the shear stress is negative for $y^+ > 227$, and

the last two terms on the right of equation (29) become imaginary. However, it is possible to study the qualitative behaviour of the distribution implied by equation (29) if the trend of these last two terms are extrapolated. The resulting curve is shown in Fig. 7 (where the dashed curve represents the extrapolation), and can be seen to exhibit a "convex-upwards" profile similar to that of the complete velocity profile. Indeed agreement can be regarded as very good in view of the uncertainty in the value of α^+. It is therefore clear that, although $1^+ \neq \kappa y^+$ across the whole of the linear-stress layer, and even equation (29) cannot be exactly solved for $y^+ > 230$, Professor Bradshaw's explanation of the profile shape is certainly qualitatively correct. It should be noted, of course, that the linear-stress distribution itself results from the strong interaction between the inner and outer (free-jet) layers: the dominant physical mechanism in wall-jets.

The question of the Reynolds number dependence of the "wake component" coefficients, D_1 and D_2, was also raised by one of the referees. It results from a solution of the velocity profile formula for prescribed boundary conditions, which are very restrictive in the case of the wall-jet (no flow-specific empirical data were employed in the present solution). In this sense the Reynolds number dependence is a "real" effect which, it may be argued, is simply another reflection of the strong interaction between, and different streamwise development of, the inner and outer layers. Support for this view comes from Glauert's classic analytical paper [33] which also demonstrates the slight nonsimilarity and Reynolds number dependence of the velocity profile in turbulent wall-jets. In more recent work [34], the author has attempted to apply the present formulation as a consistency check on Irwin's self-preserving wall-jet [35] (in which the ratio of the peak to free-stream velocity was maintained at 2.65:1). It was found that in this case the sinusoidal wake function did not satisfy the required boundary conditions: the sine form is thus of only limited application. To overcome this problem a quartic wake function was adopted which satisfied even more boundary conditions than the present formulation, although it required an empirical specification of δ^+/b_u^+. (The results were found to be relatively insensitive to the choice of this parameter.) It is interesting to note that the wake function coefficients, four in this case, were again Reynolds number dependent. Whether or not this dependence may be interpreted as implying direct viscous effects on the large "eddies" in the outer layer is open to doubt. The mean-flow Reynolds number, R_m, is defined using velocity and length scales at the overlap position between the wall-jet inner and outer layers; the velocity peak. Although these scales should be independent of near-wall viscous effects, they are determined by the interaction of two layers of quite different character. There is no counterpart to this strong interaction in boundary layers, where so-called 'Reynolds number similarity' of the large eddies is observed. Similarly, in duct and pipe-flows where the weakly interacting layers are symmetrically opposite. It may therefore be tentatively argued that R_m simply reflects scaling of the wall-jet overlap properties conveniently rendered dimensionless by the kinematic viscosity of the fluid.

The author will certainly consider Professor Bradshaw's suggestion of extending profile analysis to obtain a skin friction formula for wall-jets below an arbitrary external stream. It would seem appropriate to undertake this in the context of the author's more recent work [34]. However, it might be anticipated that the wake function coefficients
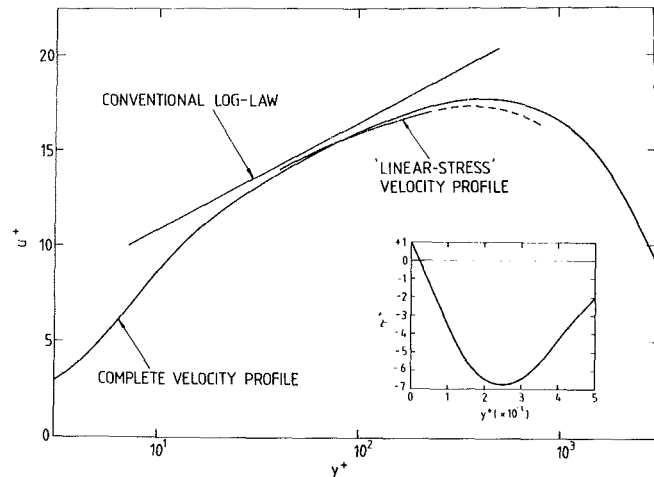

Fig. 7 Comparison of the "complete" and "linear-stress" velocity profiles ($\alpha^+ = -0.0044$, $R_m = 8250$) for the plane wall-jet

would strictly depend on the upstream 'history' of the peak to free-stream velocity ratio. The resulting formulation may therefore lack simplicity and/or "exactness."

Finally, a referee also questioned the usefulness of velocity profile families in the age of 'differential field' computational methods. It is the author's view that fluid dynamicists would be unwise to dismiss any of the tools available: analytical, computational or experimental. Each approach may well have a complementary rather than competitive role to play in aiding the understanding of complex turbulent flows. Indeed, the author's interest in profile analysis actually developed from an attempt at turbulence modelling for wall-jet flows and the consequent need for near-wall boundary conditions. A reliance solely on experimental measurements can be equally misleading. According to a recent paper by Ljuboja and Rodi [36], Professor B. E. Launder and Dr. W. Rodi concluded from a review of experimental data that the conventional log-law holds for wall-jets, at least in the limited range $30 < y^+ < 50$. This is contrary to the present results and the authors were presumably misled by the inherent errors in near-wall measurements discussed in the present paper. Professor Bradshaw is, of course, an exponent of the complementary use of different "tools," and this is evident, for example, in the recent paper of Cebeci et al. [32]. Here the starting profiles for a differential field method were generated using a boundary layer version of Coles' profile expression, equation (2), in much the same way as advocated in the present paper.

Additional References

32 Cebeci, T., Chang, K. C., and Bradshaw, P., "Solution of a Hyperbolic System of Turbulence-Model Equations by the 'Box' Scheme," *Comp. Meth. Appl. Mech. Engng.*, Vol. 22, 1980, pp. 213–227.

33 Glauert, M. B., "The Wall Jet," *Journal of Fluid Mechanics*, Vol. 1, 1956, pp. 625–643.

34 Hammond, G. P., "Similarity Profile Analysis of the Self-Preserving Plane Wall-Jet," Cranfield Institute of Technology Report SME/J/81/02, in preparation Sept. 1981.

35 Irwin, H. P. A. H., "Measurements in a Self-Preserving Plane Wall Jet in a Positive Pressure Gradient," *Journal of Fluid Mechanics*, Vol. 61, 1973, pp. 33–63.

36 Ljuboja, M., and Rodi, W., "Prediction of Horizontal and Vertical Turbulent Buoyant Wall Jets," ASME *Journal of Heat Transfer*, Vol. 103, 1981, pp. 343–349.

Draining of Tanks With Submerged Outlets or Without Vacuum-Relief

Franklin T. Dodge

Staff Engineer.
Fellow ASME

Edgar B. Bowles

Research Engineer.
Assoc. Mem. ASME

Department of Mechanical Sciences,
Southwest Research Institute,
San Antonio, Texas 78228

It is shown that the gravity-induced draining of liquid from a tank does not cease when the pressure differential at the outlet is zero if the liquid level is still above the outlet. Instead, either air or exterior liquid is ingested, depending on whether or not the tank outlet is submerged. Analytical models are developed to predict both the onset of ingestion and the subsequent discharge rates; experimental results are used to guide these developments. The models are shown to agree well with tests of draining during air ingestion and during water ingestion when the tank liquid is denser than water. When the tank liquid is less dense than water, however, the predictions of water ingestion are only in qualitative agreement with tests. Some possible reasons for this discrepancy are advanced.

Introduction

It is a common observation that gravity-draining of liquid from a tank into air requires a tank vent or vacuum-relief valve. Otherwise, a partial vacuum is created in the tank ullage, and the liquid outflow becomes intermittent as air is periodically ingested through the tank outlet. It is perhaps not so widely observed that when the tank outlet is below the surface of a surrounding liquid the exterior liquid can be ingested into the tank even if the tank is vented. In both cases, the rate of discharge is markedly reduced during the time the ingestion occurs.

A prediction of the discharge rate during ingestion is needed in some cases of interest. For example, the cargo tank of a ship may be punctured below the waterline, or if it is punctured above the waterline, the tank vacuum-relief valve may be jammed shut. These kinds of tanker-safety considerations prompted the present study,[1] but the results are applicable to other situations as well. A literature review showed that mathematical or physical models for computing discharges from tanks when air or liquid is ingested through the outlet are not available, although the somewhat related problem of the conditions required for a liquid discharge pipe to run full has been treated [1]. Consequently, the models described herein have been developed practically from first principles, using experimental results to guide and verify the models.

Tank Draining With Air Ingestion

Analysis. The ullage pressure P_u of an unvented tank decreases as the liquid contents are discharged. Eventually the pressure difference ΔP across the outlet can become zero. If the liquid level is still above the outlet, the discharge does not

---

[1] As part of a broader investigation of accidental discharges from punctured ship tanks sponsored by the U.S. Coast Guard, Contract DOT-CG-73623-A.
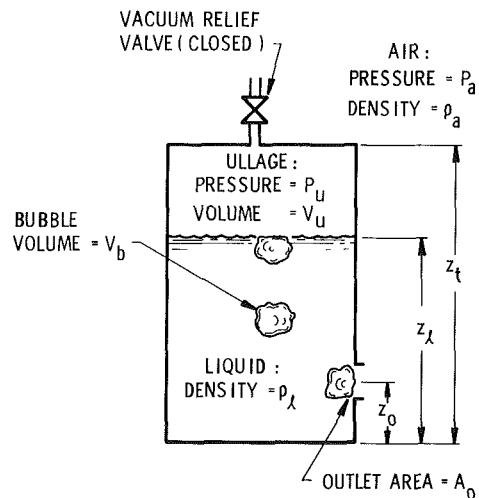
Fig. 1 Air Ingestion in an unvented tank

cease since a vertical, stationary, liquid-gas interface is unstable except for interfaces so small that surface tension can stabilize them. Instead, air is ingested through the outlet to relieve the ullage vacuum. Additional liquid is thereby allowed to discharge. But the outflow becomes intermittent because the ingested air bubble temporarily blocks the outlet. After the bubble clears the outlet, the discharge resumes until P_u again decreases to the point where air is ingested. This process is repeated continually until the liquid level falls to the outlet, as depicted schematically in Fig. 1. (For long, vertically oriented outlets, the hydrostatic head may vary substantially along the outlet, and the air bubbles may block only the top part of the outlet; these kinds of outlets are not considered here.)

Predicting when the outlet flow decreases to such a low value that the outlet cannot run full or when the flow momentum cannot restrain the entrance of bubbles into the

outlet (whichever is the governing mechanism) would require a sophisticated analysis beyond the scope of this paper. Instead, the hypothesis is made that bubbles are ingested when the momentum flux $\rho_l v^2$ (i.e., the force per unit area that must be overcome by the bubbles) decreases to some critical value:

$$\frac{\frac{1}{2} \rho_l v^2}{p_a} = \frac{P_u - P_a}{P_a} + \frac{\rho_l g (z_l - z_o)}{P_a} = K_1 \quad (1)$$

where K_1 is a nondimensional parameter. This hypothesis is in accord with our tests, which gave $0.001 \leq K_1 \leq 0.002$ and indicated that K_1 did not depend on the size of the outlet or on ρ_l.

The volume of air ingested must be known in order to predict the increase ΔP_u of the tank pressure. Each cycle of air inflow will be completed when either (1) the tank pressure increases to the point that a liquid outflow is re-established, or (2) an instability related to surface tension "pinches off" the bubble at the outlet. Our experiments did not cover a sufficiently wide range of parameters to make a definite choice between these two alternatives. But after both measuring the sizes of many bubbles from photographs and inferring bubble volumes from the measured ΔP_u for many cycles, it seemed to us that the bubble was pinched off by an instability, independently of the pressure increase. The experiments indicated that an average bubble had a volume equal to that of a sphere whose diameter was about 1.8 times the diameter of the outlet:

$$V_b = 4.2 (A_o)^{3/2} \quad (2)$$

Equation (2) correlates the bubble volume data to about ±50 percent. Because of this substantial scatter, nothing definite can be said about the nondimensional parameters that influence the constant in equation (2). If our hypothesis is correct, however, it could be a weak function of the Bond number, $\rho g A_o / \sigma$, where σ is air-liquid interfacial tension.

The discharge rate during the intervals between air ingestion events can be computed by the standard steady-state orifice-flow relation:

$$Q = A_o C_d \{2[(P_u - P_a)/\rho_l + g(z_l - z_o)]\}^{1/2} \quad (3)$$

The relation between Q and z_l is simply

$$\frac{dz_l}{dt} = -Q/A \quad (4)$$

The ullage gas pressure is assumed to expand adiabatically during periods of outflow and to be compressed adiabatically during the time when the outflow is momentarily halted and the ingested air is added:

$$\frac{\Delta P_u}{P_u} = \gamma \left(\frac{\rho_a V_b}{\rho_u V_u} \right) \approx \gamma \left(\frac{V_b}{V_u} \right) \quad (5)$$

The last approximation assumes that the ullage gas density is essentially the same as air.[2]

A computerized solution must be used to compute the intermittent flows predicted by equations (1–5).

Tests. The tests used a cylindrical tank 27.6 cm in diameter, made of transparent arcylic plastic and having a total capacity of 36.5 liters; see Fig. 2. Circular outlets 3.2 cm and 2.2 cm in diameter were drilled into the 1.2-cm-thick wall at a point 4.2 cm above the bottom; their discharge coefficients were determined experimentally to be 0.72. Ullage pressure was measured by a vacuum pressure gage having a total range of 127 cm of water and a least count of 2.5 cm of water. Liquid levels were measured visually by scribed marks spaced 2.54 cm (1.0 in.) apart on the tank wall. A stop watch, with a least count of 0.1 s, was used for time measurements. Most of the tests were conducted with water, but carbon tetrachloride and isopropyl alcohol were also used.

The tank was fitted with a manually adjustable vacuum relief valve so that the start of air ingestion could be controlled independently of the initial liquid and ullage volumes for some tests; the valve was left at its last setting after the ingestion started. For other tests, the valve was always closed. The ullage pressure oscillated each time air was ingested, and the nominal pressure gradually approached P_a; at the instant the outlet was uncovered, P_u was in fact indistinguishable from P_a.

The value of K_1 was determined in several tests by noting the liquid level and ullage pressure at the onset of ingestion. Since both P_u and z_l could only be measured to within one-half of the least count of their measurements methods, there was an uncertainty of about 0.001 atmosphere in these determinations, which accounts for the range specified in equation (1) for K_1.

Model-Test Comparisons. A quantitative comparison of the computerized model and a typical test result is shown in Fig. 3. The effects of the vacuum relief valve were simulated by continually adjusting the volume of air in the ullage prior to ingestion so as to maintain a vacuum pressure of 15.2 cm of water, in accordance with the conduct of the test. After ingestion was predicted to start, the effects of the relief valve were simulated by adding air to the ullage whenever P_u fell to a vacuum of less than 15.2 cm water; these quantities were relatively small compared to the quantity ingested through the outlet. The predicted time for the start of ingestion was 22.3 s, compared to 21.6 s in the test; at the start of ingestion, the drop in the initial liquid level was predicted to be 6.2 cm, while the measured drop was 8.0 cm. These model-test discrepancies are primarily the result of the uncertainty in the

---

[2] When the liquid is volatile, this assumption is invalid and evaporation from the liquid into the ullage must also be accounted for. See [2].

———— Nomenclature ————

A	=	tank cross-sectional area	ΔP	=	pressure differential across outlet
A_o	=	tank outlet area	ΔP_u	=	change in P_u when air is ingested
A_{ol}	=	outlet area occupied by outflow	ΔP_w	=	pressure differential across ingested water column
A_{ow}	=	outlet area occupied by inflow	Q	=	tank liquid volumetric outflow rate
C_d	=	discharge coefficient	Q_w	=	exterior liquid volumetric inflow rate
g	=	acceleration of gravity			
K_1	=	empirical constant, see equation (1)	t	=	time
P_a	=	atmospheric absolute pressure	V_b	=	volume of ingested air bubble
P_u	=	tank ullage absolute pressure	V_u	=	volume of tank ullage

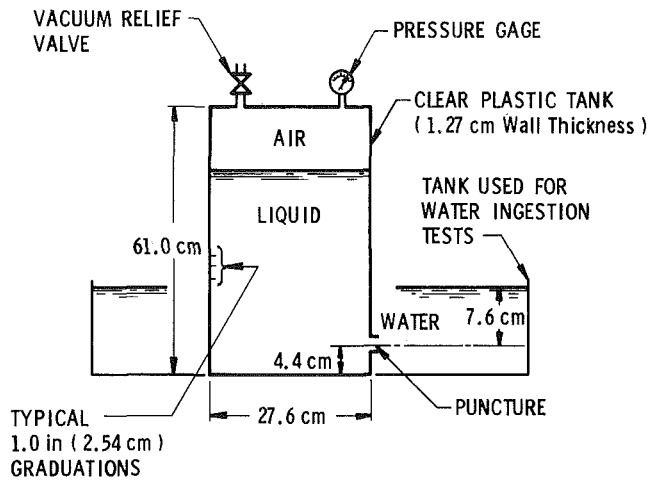|		
z_l	=	tank liquid level above bottom
z_o	=	tank outlet level above bottom
z_t	=	height of tank
z_w	=	exterior liquid level above tank bottom
z_{wl}	=	ingested liquid level above tank bottom
γ	=	ratio of specific heats
ρ_l	=	density of tank liquid
ρ_w	=	density of exterior liquid
σ	=	air/liquid interfacial tension

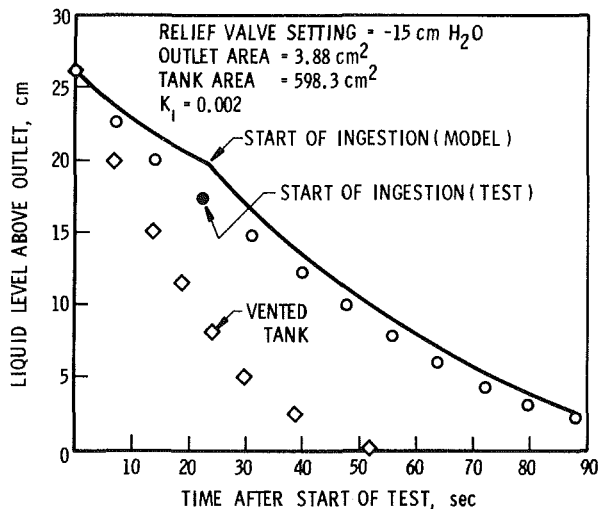Fig. 2 Test apparatus for air and water ingestion studies

Fig. 3 Comparison of air ingestion model predictions and typical test results

value of K_1 used in the model. The actual discharge rate predicted by the model after the start of air ingestion compares well with the tests. The total discharge time was predicted to be 86.0 s, compared to the 88.1 s measured in the test. When the tank was fully vented, the corresponding discharge time was 51 s.

Tank Draining With Water Ingestion

Analysis. If the tank outlet is submerged, outside liquid will be ingested when the hydrostatic pressure outside the outlet equals the interior pressure. Once again, however, the discharge will not stop when this condition of zero ΔP occurs. For immiscible tank and exterior liquids, as is assumed here, the discharge will in fact continue until the exterior liquid covers the outlet on both the inside and the outside. Our preliminary tests showed, moreover, that the discharge does not become intermittent, as it does for air ingestion; instead a steady inflow and outflow simultaneously share the outlet area.

Since the discharge is steady or changing very slowly, the ΔP at the outlet must also be steady or changing very slowly. ΔP cannot increase, since this would lead to an increase of the discharge velocity, which is illogical, but it may decrease, so as to approach zero as the outflow ceases. In any case, the change in ΔP is so slow that an important proportionality between the inflow and outflow rates can be derived by assuming that $d(\Delta P)/dt \approx 0$. There are two cases to be con-

sidered: $\rho_l > \rho_w$ and $\rho_l < \rho_w$. (For definiteness, the exterior liquid is assumed to be water, and the tank liquid is called the cargo.)

When $\rho_l > \rho_w$, the ingested water rises to the cargo surface. As depicted in Fig. 4, the pressure differential at the outlet is

$$\Delta P = P_u + \rho_w g(z_{wt} - z_l) + \rho_l g(z_l - z_o)$$
$$- [P_a + \rho_w g(z_w - z_o)] \qquad (6)$$

Assuming that the tank is vented so that P_u remains constant, the requirement of $d(\Delta P)/dt = 0$ thus leads to

$$\rho_w g \frac{d}{dt}(z_{wt} - z_l) + \rho_l \frac{dz_l}{dt} = 0 \qquad (7)$$

Since $Q = -A(dz_l/dt)$ and $Q_w = A(dz_{wt}/dt - dz_l/dt)$, equation (7) reduces to

$$\rho_w Q_w = \rho_l Q \qquad (8)$$

That is, the weight of the water ingested per unit time is equal to the weight of the cargo discharged per unit time. Ingestion continues until all the cargo above the outlet is discharged, i.e., until $z_l = z_o$.

When $\rho_l < \rho_w$, the ingested water sinks to the tank bottom. The pressure differential at the outlet is

$$\Delta P = P_u + \rho_l g(z_l - z_o) - [P_a + \rho_w g(z_w - z_o)] \qquad (9)$$

Thus, $d(\Delta P)/dt = 0$ gives $dz_l/dt = 0$, or

$$Q_w = Q \qquad (10)$$

That is, the volume of water ingested per unit time must be equal to the volume of the cargo discharged per unit time. The water continually lifts the cargo until all the cargo below the outlet is discharged, i.e., until $z_{wt} = z_o$.

When the tank is unvented, P_u may not remain constant. If $\rho_l > \rho_u$, the relation corresponding to equation (7) is

$$\rho_w Q_w = \rho_l Q \left\{ \frac{g(z_t - z_{wt}) + \gamma P_u/\rho_l}{g(z_t - z_{wt}) + \gamma P_u/\rho_w} \right\} \qquad (11)$$

If $\rho_l < \rho_w$, the cargo level z_l does not change, so $P_u = $ constant $< P_a$, and equation (10) remains valid. Equations (8), (10), and (11) were verified in our experiments.

Predicting the onset of ingestion theoretically again requires stability analyses beyond the scope of this paper. Our tests showed that an equation of the form of (1) seemed to control the onset, but with P_a replaced by the total exterior pressure, $P_a + \rho_w g(z_w - z_o)$. ΔP at the onset can thus be evaluated as $K_1[P_1 + \rho_w g(z_w - z_w)]$. But since ΔP remains nearly constant thereafter during the ingestion, it must always be nearly equal to the onset value of ΔP. Since the discharge velocity is proportional to $\sqrt{\Delta P}$, the numerical value of K_1 would play a much more important role for water ingestion than for air ingestion. In fact, very accurate experimental data for K_1 would be required. We therefore chose to compute the point of ingestion as follows. When ΔP neared zero in our computerized model, the discharge rate for the next time interval Δt computed by assuming that water ingestion had not yet begun was compared to that computed by assuming that it had, using the flow equations given below. At some ΔP, the discharge without ingestion was less than with ingestion, even though the discharge stream during ingestion has to share the outlet area with the inflow stream. This ΔP was selected as the onset of ingestion. The same thing can be accomplished analytically by finding the ΔP where dQ/dt is greater with water ingestion than without it. Our procedure has some physical merit since it is believed that ingestion should occur so as to maximize the discharge.

Knowing ΔP, the discharge velocity can be computed. However, neither Q nor Q_w can be determined until the corresponding outlet areas are known. One relation for predicting this is
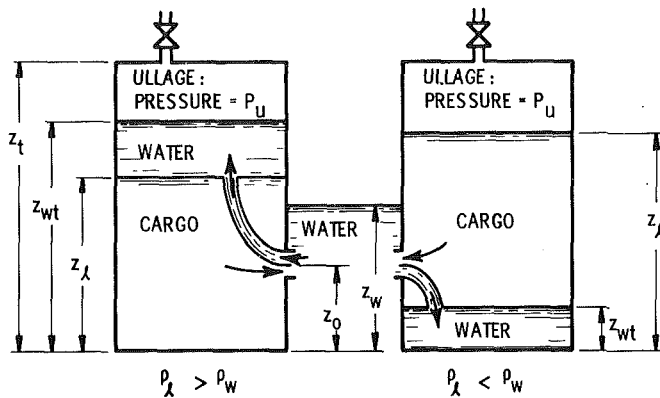
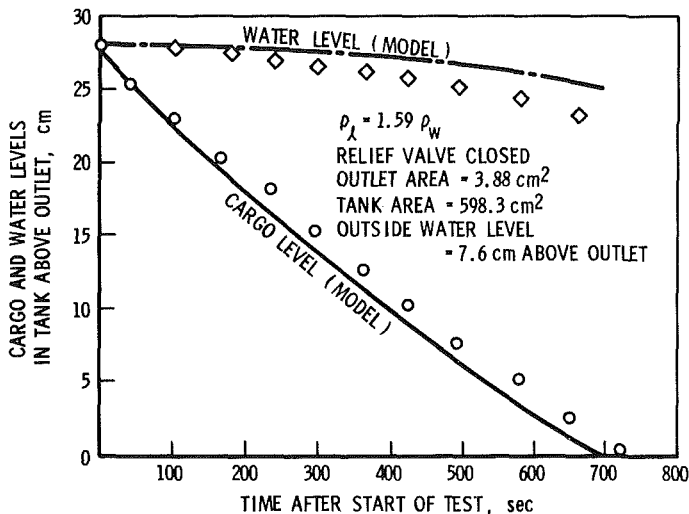**Fig. 4 Water ingestion phenomena as a function of tank liquid density**

Fig. 5 Comparison of water ingestion model predictions and typical test results for $\rho_l > \rho_w$

Equations (8), (10), (12), (13), and (15) (or (11) and (14) instead of (8) and (13)), along with the ΔP determined as described earlier, are sufficient to predict the discharge rate after the ingestion begins.

Tests. The tank used in the air-ingestion studies was placed in a much larger diameter tank that could be filled with water to cover the outlet. The tank liquid for most of the tests was either carbon tetrachloride ($\rho_l = 1.59\,\rho_w$) or isopropyl alcohol ($\rho_l = 0.78\,\rho_w$), both of which are virtually immiscible with water. In order to emphasize the effects of water ingestion, the vacuum-relief valve was kept closed for all the tests. Thus, the ullage pressure almost immediately dropped to a sufficiently high vacuum to cause water ingestion.

Model-Test Comparisons. The tests qualitatively confirmed the primary assumptions of the analytical models. Table 1 shows typical test results. During both the carbon tetrachloride and isopropyl alcohol tests, the ΔP at the outlet remained small and nearly constant. Further, the discharge continued until the outlet was covered on both sides by water. The relative efficiency of air-ingestion and water-ingestion can also be seen from these tests, since an air-ingestion test using the same initial conditions required less than 200 s to drain the tank.

Figure 5 gives a quantitative comparison of a typical test and the model predictions for a case with $\rho_l > \rho_w$. The test is predicted very well in all of its particulars. The comparison for tests with $\rho_l < \rho_w$ were, however, not as good. For example, the predicted discharge time for one isopropyl alcohol test was 194 s, compared to a measured 610 s, although the predicted ullage vacuum was in fair agreement with the test. It seems evident that equation (14) must overpredict the driving force for the water ingestion when $\rho_l < \rho_w$, even though the corresponding equation (13) for $\rho_l > \rho_w$ apparently is a valid approximation. There were no observed differences in the behavior of the liquids during the tests that explain this contradictory result.

Conclusions

It has been demonstrated that the gravity-induced draining of liquid from a tank does not cease when the pressure differential at the outlet is zero if the liquid level is still above the outlet. Instead, either air or outside liquid (e.g., water) is ingested into the tank through the outlet, depending on whether or not the outlet is submerged. If air is ingested, the discharge becomes intermittent because of the blockage of the outlet by the ingested air bubbles. The vacuum in the ullage is alternately relieved by the ingested air and then drawn down again by the subsequent liquid discharge. On the other hand, if outside liquid is ingested, the outflow remains steady but shares the outlet area with the steady inflow. The ullage vacuum also remains steady after the ingestion begins.

Analytical models have been developed which predict both the onset of ingestion and the discharge rates. For unsubmerged outlets, air is ingested when the outlet ΔP falls to about 0.2 percent of atmospheric pressure. An empirical value of the air volume ingested per ingestion cycle is used in the model to help predict the discharge rate. For submerged outlets, liquid ingestion begins at a point that maximizes the discharge rate; the outlet ΔP for these conditions is also of the order of 0.1 percent of the exterior pressure. The inflow rate is related to the discharge rate such that ΔP at the outlet remains approximately constant after ingestion begins; for vented tanks, this requires equal inflow and outflow mass flow rates, of $\rho_l > \rho_w$, and equal volumetric flow rates, if $\rho_l < \rho_w$. The driving pressure for liquid ingestion is taken to be the positive or negative buoyancy of a column of the exterior liquid in the tank liquid.

$$A_{ol} + A_{ow} = A_o \tag{12}$$

but one more relation is required, which is here chosen to be a prediction of inflow velocity. The driving force for the ingestion is the negative or positive buoyancy of the water relative to the cargo. The tests showed that the water stream entering the tank soon broke up into discrete droplets, but it is assumed here that the entrance velocity is the same as if the water remained in a continuous streamtube, as shown in Fig. 4. The ΔP_w acting on the streamtube, if $\rho_l > \rho_w$, is

$$\Delta P_w = g(\rho_l - \rho_w)(z_l - z_o) \tag{13}$$

If $\rho_w > \rho_l$, ΔP_w is

$$\Delta P_w = g(\rho_w - \rho_l)(z_o - z_{wt}) \tag{14}$$

These equations can be derived by considering the various hydrostatic heads, starting at the outside air, proceeding through the outside water, through the outlet, and then along the streamtube to the interface between the water and the cargo inside the tank; since ΔP is small compared to ΔP_w, it is neglected in computing ΔP_w. As can be seen, the net ΔP_w is just the buoyancy force per unit area acting on a submerged column of water of length $z_l - z_o$, for $\rho_l > \rho_w$, or $z_o - z_{wt}$, for $\rho_w > \rho_l$. Equation (13) or (14) predicts the trends of the inflow velocity observed in the tests; namely, the inflow velocity is greatest at the start of ingestion and smallest just as the outlet is cover··.., this is the physical justification of the stream tube assumption. The water inflow rate is computed by

$$Q_w = A_{ow} C_d \sqrt{2\Delta P_w / \rho_w} \tag{15}$$

Table 1 Pressure Differential at Outlet for Typical Water Ingestion Studies[1]

Carbon Tetrachloride Test, $\rho_l = 1.59\,\rho_w$

Cargo Surface z_l, cm	Water Surface z_{wt}, cm	Ullage Pressure P_u, cm H$_2$O	Outlet ΔP cm H$_2$O	Time t, s
32.3	32.3[2]	−33.0	3.7	~0
22.2	31.4	−28.0	1.9	245
4.4	27.6	−19.0	1.0	665

Isopropyl Alcohol Test, $\rho_l = 0.78\rho_w$

Cargo Surface z_l, cm	Water Surface z_{wt}, cm	Ullage Pressure P_u, cm H$_2$O	Outlet ΔP cm H$_2$O	Time t, s
32.5	0	−12.7	1.5	~0
31.7	5.5[3]	−12.7	1.0	610

---

[1] All distances measured from tank bottom; outlet centerline = 4.4 cm above bottom; outlet = 2.2 cm; water level outside tank = 12 cm, or 7.6 cm above outlet centerline
[2] Water layer thickness = $z_{wt} - z_l$, equals zero at $t = 0$.
[3] Top of outlet

The analytical model predictions of both air and water ingestion, when $\rho_l > \rho_w$, are in excellent qualitative and quantitative agreement with tests. For water ingestion, when $\rho_l < \rho_w$, the model overpredicts the discharge rate substantially, although the postulated proportionality between the volumetric inflow and outflow rates was shown to be valid. There is no evident reason why the assumptions upon which the model is based should give good results when $\rho_l > \rho_w$, but not when $\rho_l < \rho_w$. In order to understand this contradiction, a stability analysis of a stream of negatively buoyant liquid ingested into a tank liquid may be required; perhaps the assumptions of an effective driving pressure for the ingestion can be modified or corrected by such an analysis.

References

1 Wallis, G. B., Crowley, C. J., and Hagi, Y., "Conditions for a Pipe to Run Full When Discharging Liquid into a Space Filled With Gas," ASME JOURNAL OF FLUIDS ENGINEERING, Vol. 99, June 1977, pp. 405–413.

2 Dodge, F. T., Bowles, E. B., Mann, J. E., and White, R. E., "Experimental Verification and Revision of the Venting Rate Model of the Hazard Assessment Computer System and the Vulnerability Model," Final Report, Contract DOT-CG-73623-A, Southwest Research Institute, San Antonio, Texas, July 1980.

D. M. Rooney

Assistant Professor.

R. D. Peltzer

Research Assistant.
Assoc. Mem. ASME

Aerospace and Ocean Engineering
Department,
Virginia Polytechnic Institute
and State University,
Blacksburg, Va. 24061

The Effects of Roughness and Shear on Vortex Shedding Cell Lengths Behind a Circular Cylinder

Circular cylinders of aspect ratio $L/D = 17$ were tested in a wind tunnel under a wide range of spanwise upstream velocity shears. The correlation between upstream shear, characterized by a nondimensional shear parameter β, and the spanwise lengths of constant vortex shedding frequency was sought for both smooth and rough cylinders in transitional Reynolds numbers flows. Among the significant conclusions are that the spanwise range in shedding frequencies decreases with increasing roughness, the average constant shedding frequency cell length increases with increasing roughness for constant shear, and the average cell length decreases with increasing upstream shear for constant roughness.

1 Introduction

Before discussing details of vortex shedding phenomena behind circular cylinders, it is instructive to review briefly the terminology which the authors use to characterize the various flow regimes encountered by the cylinder. Those regimes are the subcritical, critical, supercritical, and transcritical, in order of occurrence with increasing Reynolds number.

The upper limit of the subcritical regime usually occurs around Re = 2×10^5, when the drag coefficient begins to decrease as the separation point moves downstream on the cylinder surface. During the critical regime, laminar separation bubbles appear, and the drag coefficient reaches its minimum value. Regular vortex shedding occurs in both subcritical and critical flows. The supercritical regime is characterized by the disappearance of discernible vortex shedding and a gradual rise in drag coefficient. Finally, in transcritical flow, vortex shedding reemerges, turbulent separation occurs, and the surface pressure pattern resembles that of subcritical flow. The exact Reynolds numbers marking the limits of each regime depend on cylinder surface roughness and freestream turbulence levels.

Previous studies devoted to determining the effects of a freestream velocity shear on vortex shedding frequency begin with the work of Maull and Young [1], who first verified the existence of coherent cells for a single value of upstream shear by examining the power spectral density of the velocity fluctuations behind a bluff body with a long trailing edge. They explained the presence of four distinct cells by maintaining "that the coherence of the shed vortices requires a constant frequency over certain lengths." They theorized that

the cell divisions are marked by longitudinal vortices created by the rolling up of the freestream vorticity of the shear flow. Mair and Stansby [2] determined an optimum endplate design to minimize interference with coherent vortex shedding behind a cylinder. They noted, however, that to produce appreciable values of the shear parameter (proportional to the cylinder diameter), the aspect ratio was forced to be low enough such that end effects caused a variation in base pressure coefficient (C_{pb}) across the entire cylinder span. They attributed the lack of a measured cellular shedding structure in some results (particularly in runs with no endplates) to fluctuations in cell boundaries which registered on successive time-averaged spectra as a continuous change in peak frequency. Stansby [3] investigated lock-on effects between mechanically produced cylinder vibrations and periodic vortex shedding at Reynolds numbers less than 10^4. His studies of stationary cylinders included two shear levels (corresponding to aspect ratios of 8 and 16) so no comprehensive evaluation of the relationship of shear to cell structure was possible. Davies [4] approached the problem by analyzing the variation in C_{pb} for a highly sheared, highly turbulent (4 to 7 percent) flow about a cylinder of low aspect ratio ($L/D = 6$) in the critical Reynolds number range. The high turbulence levels reduced the onset of the critical Reynolds number by a factor of ten. He attributed the disappearance of measurable vortex shedding to the variation in spanwise wake patterns at a centerline Reynolds number of 1×10^5, which decreased spanwise correlations in C_{pb}.

In an earlier investigation by the present authors, [5] test results derived from measurements around a 6-in. (15-cm) dia cylinder placed in a 6 ft × 6 ft (1.8 m × 1.8 m) wind tunnel were obtained. Those tests were primarily directed toward determining the surface mean and fluctuating pressures around the cylinder, and seeking to identify a cellular

organization of eddy shedding frequencies behind the cylinder in transitional Reynolds number (5×10^5) flow. Given that the maximum Reynolds number achievable in the tunnel was about 5×10^5, the test cylinder was knurled to a roughness $K/D = 0.001$ (where K is the depth of a roughness element, and D is the diameter). The surface roughness was expected to trigger a transcritical wake pattern around the cylinder. The relatively low aspect ratio ($L/D = 9.3$) permitted only a two-cell shedding structure behind the cylinder. Therefore an estimate of the lengths of cells of constant shedding frequency could not be made. However, the investigation demonstrated for the first time that a cellular structure identical to that observed in subcritical flow reappeared in transcritical flow.

The present study was planned to incorporate improvements in design of the test model and data gathering capability in order to achieve certain results which the previous program was unable to arrive at. Specifically, three goals were envisioned:

(a) determination of eddy shedding cell lengths as a function of upstream shear. Optimal endplate design and larger aspect ratio were the chief steps taken toward attaining this objective.

(b) determination of minimum shear level producing cellular shedding patterns. A wider range of upstream velocity shears was to be tested than in any previous study.

(c) Detailed analysis of the effect of roughness on shedding patterns. A very smooth cylinder was to be tested under the same conditions as a roughened cylinder, and the two sets of results compared.

2 Experimental Setup

Experiments were conducted in the 6 ft $\times$ 6 ft (1.8 m $\times$ 1.8 m) cross section Stability Wind Tunnel located on the VPI&SU campus. An upstream velocity shear was generated in the tunnel by a series of six wire screens, incorporating vertical rods in a nonuniform cross-tunnel distribution. The screens were located approximately 15 ft upstream of the test model and could be arranged in any combination to produce a variety of freestream shear levels.

The test cylinder, represented by a 3.5 in. (9 cm) dia, 60 in. (152 cm) long hollow aluminum pipe, spanned the tunnel midway between the floor and the ceiling of the test section. The pipe was rigidly attached to rectangular steel endplates, approximately 0.05 in. (1.3 mm) thick, and 24 in. (60 cm) high and 52 in. (132 cm) long. The cylinder axis was 9 in. (23 cm) behind the leading edge of the plates and midway in height. The downstream parts of the endplates were fastened to the instrumentation traverse to minimize any vibration of the plates induced by the wind. The main features of the experimental setup (without the traverse) are shown in Fig. 1.

A significant parametric limitation was imposed by the dimensions of the cylinder. The advantage gained in increasing the aspect ratio was offset to a degree by the decrease in Reynolds number attainable because of the smaller cylinder diameter employed. One technique which has been advocated (by Szecheny [6] among others) to simulate higher Reynolds
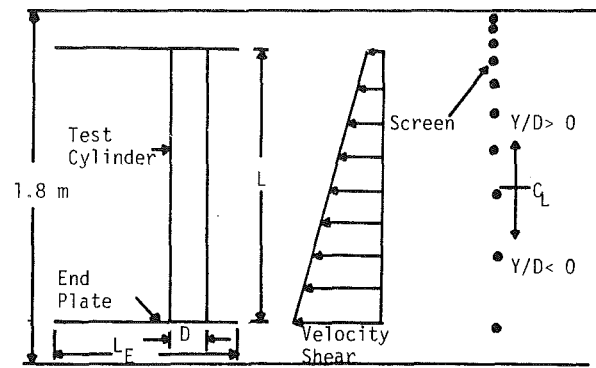

Fig. 1 Wind tunnel test configuration (top view)

number flow is to roughen the cylinder surface. The conditions under which, according to Szechenyi, transition to transcritical flow occurs are that the roughness Reynolds number ($\mathrm{Re}_K = U_c K/v$, where U_c = centerline velocity, K = roughness height, v = kinematic viscosity) exceeds 200, but that the dimensionless surface roughness K/D is kept below 2.2×10^{-3} in order to generate clear periodic shedding. These criteria put a lower limit on the transcritical cylinder Reynolds number of $\mathrm{Re} \approx 1 \times 10^5$. Accordingly, two models of identical dimensions were constructed to determine whether roughening the surface negated the Reynolds number decrease. One cylinder was diamond knurled to a roughness $K/D = 1 \times 10^3$, while the other was machined smooth.

Both cylinders were drilled with four circumferential series of 1/16 in.-dia ports at spanwise distances of $y/D = -5.4$, -2, 1.4, and 4.9 (where y is the actual spanwise distance from the cylinder center and D is the diameter). Each circumferential series contained 24 ports spaced 15 deg apart, so that complete coverage of the pressure distribution around the cylinder was provided at the four locations. In addition, two ports at the front center of the cylinder 2 in. (5 cm) apart measured the centerline stagnation pressure. Plastic tubing of 1/16 in. (1.6 mm) dia connected them to a Setra Systems Model 237 pressure transducer. A Scanivalve pressure switch successively sampled the pressure readings at each port, with the output recorded on a Hewlett-Packard Model 7100B strip chart recorder. Output from the two centerline ports was channeled to a Hewlett-Packard Model 3476 B Multimeter which displayed the d-c digital readout corresponding to the centerline velocity.

An electronically controlled tranverse was situated about 3 ft downstream of the position to be occupied by the test model. The traverse controls permitted positioning of a probe mount to within any 0.04 in. (1 mm) increment along the span of the cylinder. In addition, vertical adjustment was possible within a limited height range. The traverse mount held a hot-wire anemometer probe, which was positioned approximately 5 diameters (18 in. or 45 cm) behind the base of the cylinder. The traverse was found to have a negligible effect on the flow conditions around the cylinder.

To examine the spectral characteristics of the shear layer between the wake and the freestream flow behind the cylinder, a single hot-wire probe was connected to a Thermo-Systems,

─────── **Nomenclature** ───────

C_p = pressure coefficient
C_{pb} = base pressure coefficient
D = cylinder diameter, m
f = frequency, 1/s
K = depth of roughness element, m
L = cylinder length, m
Re = Reynolds number

Re_c = Reynolds number based on centerline velocity
St_c = Strouhal number based on centerline velocity
U = freestream velocity, m/s
U_c = centerline freestream velocity, m/s

y = spanwise distance from cylinder midpoint, m
β = shear parameter
θ = circumferential angle from cylinder stagnation point

Inc. Model 1051-6 constant temperature anemometer. The filtered anemometer signal was transmitted to a ZTL Inc. Multichannel FFT Processor. Real-time visual inspection of the signal was available through simultaneous monitoring on a Tektronix Type 561A Oscilloscope. A two-channel Data Memory System received and quantitized the incoming data and performed the spectral analysis. The output, in the form of a power density spectrum (log amplitude versus frequency), was plotted on a Tektronix Model 4010 Graphics Display Terminal. Through keyboard commands, variables such as sampling rate, number of spectral averages, and frequency range of the displayed spectrum could be specified. A hard copy of the results was obtained by photographing the terminal screen with high speed Type 5710 Polaroid film loaded in a Graflex camera.

3 Test Procedures

A. Upstream Velocity Profiles. Velocity profiles in the undisturbed flow far upstream of the test cylinders were determined from total head tube readings at 25 stations across the tunnel. Each sheared profile corresponded to a given set of screens placed in slots 15 ft upstream from the cylinder. Each screen configuration also produced a different turbulence level, which varied from 0.03 percent for no screens, up to 0.8 percent for the full set of screens. Shear levels are characterized by a dimensionless parameter β, defined as $D/U_c \, dU/dy$ (where $D=$ cylinder diameter, $U_c =$ centerline velocity and $dU/dy =$ spanwise velocity gradient. Plots of the mean velocity profiles and freestream turbulence profiles as a function of the shear parameter are contained in reference [7].

B. Surface Pressure Measurements. One approach used to determine the flow regime experienced by a circular cylinder is to examine the surface pressure coefficient distribution around the cylinder circumference. Subcritical pressure plots are characterized by relatively low values of the pressure coefficient ($C_p \approx -1.2$) near circumferential angles perpendicular to the oncoming flow. In the critical regime this maximum value becomes more negative, until at the initiation of supercritical flow (marked by an asymmetric separation bubble and followed by the cessation of discernible shedding), peak values of $C_p = -2.5$ are attained. As the Reynolds number continues to increase, $C_{p_{max}}$ becomes less negative, and a profile very similar to that of the subcritical case is realized.

One of the goals of the present study was to determine the effect of roughness on the shedding characteristics in a shear flow. In addition, it was hoped to ascertain better the ability of roughness to place a flow regime in a transcritical state despite centerline Reynolds numbers around 2×10^5, as Szechenyi has demonstrated can be done in two-dimensional (uniform upstream flow) cases. Consequently, plots of the pressure coefficient for both the rough and smooth cylinder cases will be compared for three-dimensional flow regimes.

C. Eddy Shedding Characteristics. The traverse mechanism supporting the hot-wire probe located 5 diameters behind and 2 diameters above the cylinder was positioned to take readings along the shear layer behind the cylinder in increments of 9 cm (approximately one cylinder diameter), to determine the spanwise eddy shedding characteristics. At each setting, a spectral analysis of the signal was performed, usually consisting of 25 averages of individual spectra, with the dominant energy level yielding the shedding frequency. A complete set consisted of 17 points along the cylinder, although for a number of cases where the shedding pattern was nonexistent or relatively uniform, fewer readings were taken.

When the maximum spanwise shedding frequency was expected to occur at less than 100 Hz (as was the case for all

test runs at Re $= 1.6 \times 10^5$), the output was plotted on the 0 to 100 Hz frequency scale, with a resolution bandwidth of 0.2 Hz. When the 0 to 250 Hz scale was used, the resolution bandwidth was 0.5 Hz.

A complete listing of all test runs is given in the table below. All cases for which pressure distributions alone were taken are marked by an asterisk. The remainder of the cases was analyzed for both pressure and eddy shedding characteristics. For $\beta = 0$, only one spanwise setting was required to determine the shedding frequency, and therefore a large number of Reynolds numbers were investigated, to ascertain the dependence of Strouhal number on Reynolds number.

Table of test runs for smooth and rough cylinders

Shear parameter $(\beta = D/U_c \, dU/dy)$	Reynolds Number $(Re = U_c D/\nu)$
0.000	$1.6 \times 10^5 - 3.6 \times 10^5$
0.007	1.6×10^5
	2.2×10^5
	2.6×10^5
	3.0×10^5
0.016	1.6×10^5
	$2.2 \times 10^{5*}$
	2.6×10^5
	3.0×10^5
0.021	1.6×10^5
	$2.2 \times 10^{5*}$
	2.6×10^5
0.033	1.6×10^5
	$2.2 \times 10^{5*}$
	2.6×10^5
0.041	1.6×10^5
	2.2×10^5

4 Results and Discussion

A. Surface Pressure Distributions. All C_p distributions discussed in the following section were obtained at the set of circumferential pressure taps located at $y/D = -2$.

Figures 2(*a*), (*b*), and (*c*) show a plot of pressure coefficient, C_p, as a function of circumferential angle, θ, for the three cases of unsheared flow examined. From Fig. 2(*a*), it is apparent that even for Re $= 3.2 \times 10^5$, the C_p distribution (with a maximum negative $C_p \approx 1.6$) did not reach the typical initial supercritical profile, recognizable by peak suction values of $C_p \approx -2.5$. Nevertheless, since for Re $= 1.6 \times 10^5$, C_p was only -1.2 at $\theta = 90$ deg, the highest Reynolds number case was in the critical, or transition, regime. Figure 2(*b*) is the corresponding plot for the rough cylinder in uniform flow with freestream turbulent intensities of 0.2 percent. At the lowest speed, with Re $= 1.6 \times 10^5$, a subcritical profile was produced. At Re $= 2.2 \times 10^5$, one side of the cylinder revealed a peak suction $C_p = -2.0$, while on the other side $C_p = -1.3$. This asymmetry in C_p distribution reflects the condition noted by Bearman [8] regarding the separation bubble phenomenon in flow over a smooth cylinder at Re $= 3.4 \times 10^5$, just prior to entry into the supercritical regime. At Re $= 2.6 \times 10^5$, the base pressure coefficient reached its least negative value and a symmetric peak suction developed. Beyond Re $= 2.6 \times 10^5$, the rough cylinder pattern assumed the expected symmetrical supercritical shape, with increasing base pressure coefficient and decreasing peak suction.

With an order of magnitude decrease in freestream turbulence to about 0.03 percent the C_p distribution over the rough cylinder was as shown in Fig. 2(*c*). Again, a subcritical profile existed at Re 1.6×10^5, but at Re $= 2.2 \times 10^5$, the flow (as demonstrated by the maximum $C_p = -1.5$) was not as far into the transition stage as in the previous case. At Re $= 2.6 \times 10^5$, the largest symmetrical peak suction ($C_p = -2.0$) and least negative base pressure coefficient ($C_{pb} = $
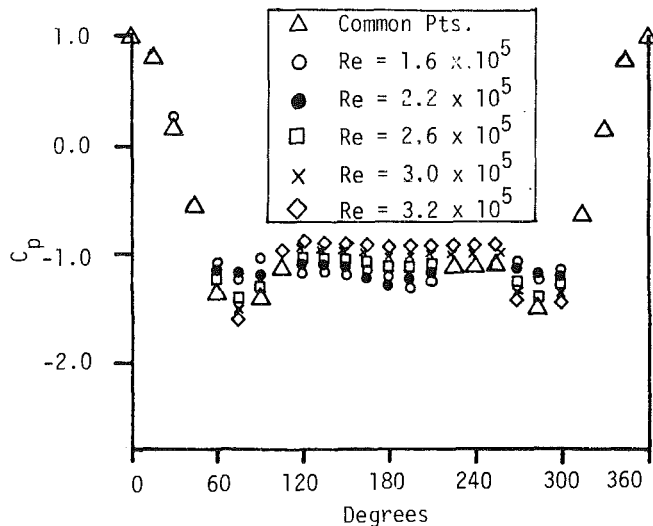
△	Common Pts.
O	Re = 1.6 x.10^5
●	Re = 2.2 x 10^5
□	Re = 2.6 x 10^5
X	Re = 3.0 x 10^5
◇	Re = 3.2 x 10^5

Fig. 2(a)   Smooth cylinder

△	Common Pts.
O	Re = 1.6 x 10^5
●	Re = 2.2 x 10^5
□	Re = 2.6 x 10^5
X	Re = 3.0 x 10^5
◇	Re = 3.2 x 10^5

Fig. 2(b)   Rough cylinder

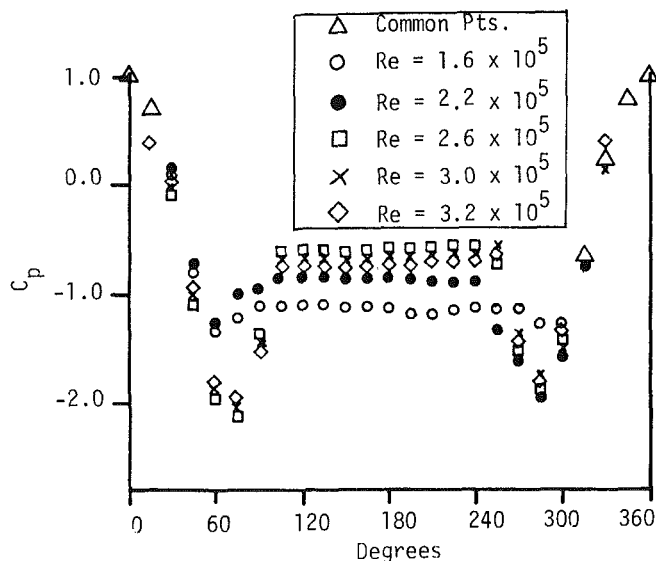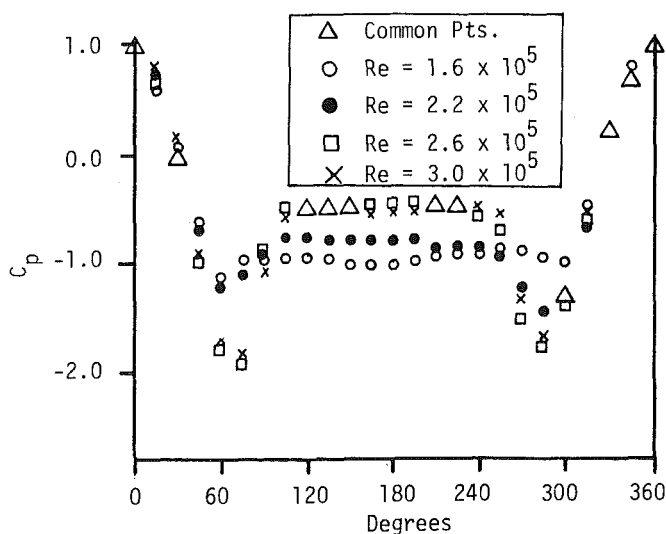| △ | Common Pts. |
O	Re = 1.6 x 10^5
●	Re = 2.2 x 10^5
□	Re = 2.6 x 10^5
X	Re = 3.0 x 10^5

Fig. 2(c)   Rough cylinder, low turbulence

Fig. 2   Circumferential pressure distributions ($\beta = 0.0$)

-0.44), signaled entry into the supercritical regime. The highest Reynolds number examined, $Re = 3.0 \times 10^5$, was slightly less developed that at the same Reynolds number at the higher turbulence level. Therefore, an increase in freestream turbulence from a negligible amount (0.03 percent) to a small amount (0.20 percent) had a measurable effect in transforming the flow regime to transcritical at a lower Reynolds number. This phenomenon will be brought out again when shedding frequencies are examined later.

A similar conclusion was reached by Batham [9], who noted that increased turbulence "promoted earlier transition in the shear layers and this effect was more pronounced than the effect of roughness" at $Re = 1.1 \times 10^5$. At a higher Reynolds number, surface roughness effects superseded those of freestream turbulence. In general, he concluded that "the critical range of Reynolds number is narrower for high roughness and wider for high turbulence." Since no tests were performed on the smooth cylinder with turbulence levels of 0.03 percent, a more complete qualitative comparison with Batham's results is not possible. However, a cursory comparison of Figs. 2(a) and (b) amply testifies to Batham's other observation "that cylinders in uniform streams which exhibit critical mean C_p distributions are highly sensitive to surface roughness."

The effects of varying roughness and freestream turbulence on the flow regimes experienced by the cylinders is brought out more dramatically in Fig. 3, a plot of drag coefficient as a function of Reynolds number. For comparison, some results obtained by Bearman are also plotted on the graph. For the rough cylinder, C_p values clearly demonstrate the slight shift downward in Reynolds number of a given regime with increased freestream turbulence. Also noteworthy is the fact that the minimum drag coefficient for a smooth cylinder was about 0.23 (according to Bearman) whereas on a rough cylinder, a minimum of 0.37 was measured. This difference is in accord with results obtained by Achenbach [10], Szecheny [6], and Buresti and Martini [11], who observed that an increase in surface roughness produces higher minimum drag coefficients.

Figures 4(a) and (b) show the pressure coefficient plots (where C_p is still based on the centerline velocity) for the smooth and rough cylinders at $\beta = 0.016$, which represent a typical set of sheared flow results. The values were obtained at $y/D = -2$. The smooth cylinder results correspond closely with the unsheared results, although the minimum base pressure coefficient was attained at a lower centerline Reynolds number than in the uniform case, Fig. 2(a). Likewise, the rough cylinder results follow closely those in Fig. 2(b). The peak suction ($C_p = -2.7$) attained at $Re_c = 2.6 \times 10^5$ is slightly higher, and the base pressure coefficient ($C_{pb} = -0.6$) slightly more negative, but the Reynolds numbers marking the transition from one regime to the next are not altered by the introduction of a spanwise shear. Obviously, the local Reynolds number is the significant parameter here since, when tests are being performed in the transitional range, a change of flow regime along the cylinder span take place if the shear level is great enough.

B. Vortex Shedding Patterns for Smooth and Rough Cylinders in Uniform Flow. Three cases were examined, and the results are plotted in Fig. 5. First the smooth cylinder was placed in the unsheared flow generated by a single screen. The energy in the peaks remained concentrated around a narrow frequency band as the Reynolds number increased.

Measurements for the knurled cylinder indicated that organized shedding activity disappeared just above $Re = 2.2 \times 10^5$, and began to reappear around $Re = 3.2 \times 10^5$. An attempt was then made to estimate the influence of freestream turbulence on the shedding characteristics by removing the single uniform wire screen from the upstream end of the
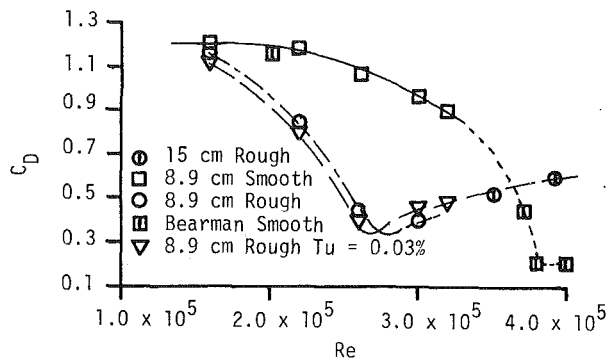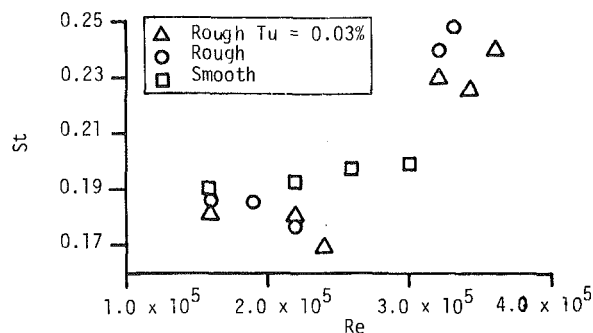
Fig. 3 Drag coefficients ($\beta = 0.0$)

Fig. 5 Strouhal number versus Reynolds number ($\beta = 0.0$)
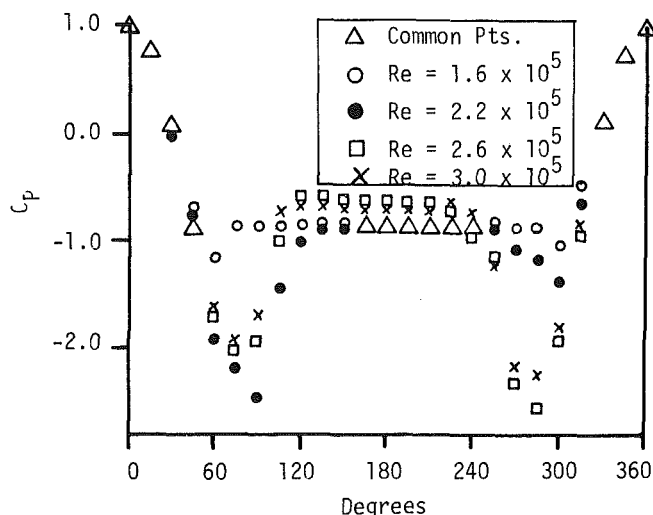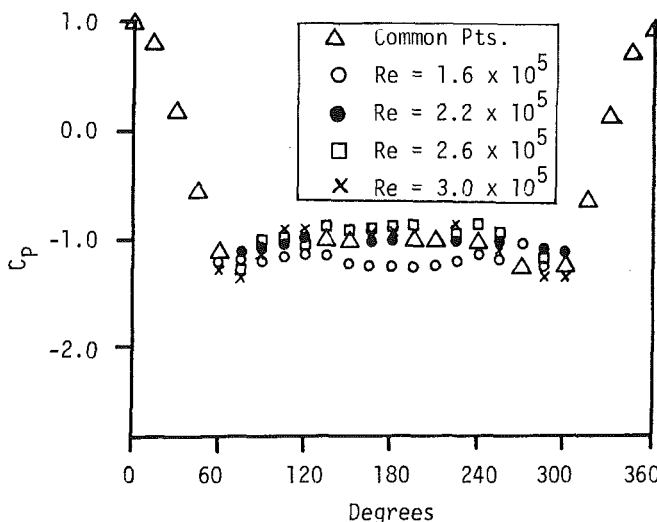

Fig. 4(a) Smooth cylinder

Fig. 4(b) Rough cylinder

Fig. 4 Circumferential pressure distributions ($\beta = 0.016$)

tunnel. For this third case, with no screens impeding the flow, the tunnel turbulence decreased to about 0.03 percent. An additional point (at Re $= 2.4 \times 10^5$) is included to indicate a slightly greater persistence of the subcritical peak. However, the transcritical peak at Re $= 3.3 \times 10^5$ was weaker than for the higher turbulence level. Without the screen in the test section, results could be obtained for Reynolds numbers up to 3.6×10^5, for which the power spectral density of the velocity fluctuations appeared to correspond to those at Re $= 3.3 \times 10^5$ for the higher turbulence knurled case. Therefore the

effects of an increase in freestream turbulence is seen to be a shift downward in the Reynolds number range for the transition regime with no discernible eddy structure. Exactly the same conclusion was reached from an analysis of the surface pressure distribution.

The supercritical regime for the smooth cylinder was not reached. Bearman has shown that on a perfectly smooth cylinder in uniform flow, periodic narrow band shedding occurs up to Re $= 5.5 \times 10^5$, which he defined as the end of the critical regime. Around Re $= 3.4 \times 10^5$, the formation of laminar separation bubbles occurs, and he reported an upward change in Strouhal number to 0.32 and then to 0.46 at Re $= 3.8 \times 10^5$, before it disappeared. The broadband shedding at higher Reynolds numbers has been documented by Roshko [12].

In the present set of tests, for subcritical Reynolds numbers, the Strouhal number ($St_c = FD/U_c$, where $f =$ frequency in Hz, and the other symbols are so previously defined) was fairly constant around 0.18. When the shedding reemerged around Re $= 3.2 \times 10^5$ (depending of the freestream turbulence level) the Strouhal number was 0.24. For the smooth cylinder, a value between 0.19 and 0.20 was observed. The smooth cylinder data are entirely consistent with Bearman's results, but the 0.24 value for the rough cylinder suggests that (if it is maintained at even higher Reynolds numbers) roughness causes transcritical shedding to occur at a much lower frequency than on a smooth cylinder. Buresti's results for a sandpaper roughened ($K/D = 0.91 \times 10^{-3}$) circular cylinder in unsheared flow indicate, at subcritical Reynolds numbers, a shedding frequency range of $0.183 \leq St \leq 0.189$. The shedding ceased around Re $= 1.5 \times 10^5$, and transcritical shedding reappeared at Re $= 2.7 \times 10^5$ at St $= 0.226$, a value consistent with the present rough cylinder ($T_u = 0.03$ percent) value. For a rougher cylinder ($K/D = 1.20 \times 10^{-3}$) he found that transcritical shedding occurred at St $= 0.24$. The discrepancy in the Reynolds numbers characterizing the disappearance and reappearance of shedding can be attributed to the differences in the types of roughness elements employed in the tests (knurling versus sandpaper). Alemdaroglu et al [13], along with Buresti, further show that with increasing Re, the transcritical shedding frequency rapidly decreases to a constant value of St $= 0.22$. The jump in Strouhal number from subcritical to transcritical is exactly that noted by Roshko [12], although his values (0.20 and 0.26) were somewhat higher for his smooth cylinder. Another interesting feature of both rough cylinder data plots, at subcritical-critical Reynolds numbers, is that as the cylinder proceeds into the critical regime, the values of St decrease. This result confirms a finding Alemdaroglu that "the beginning of the transitional regime is seen by the lowering and spreading of the relevant peak in the spectrum."

Further careful tests are required to clarify the effect of roughness on shedding frequencies in the critical Reynolds number range.

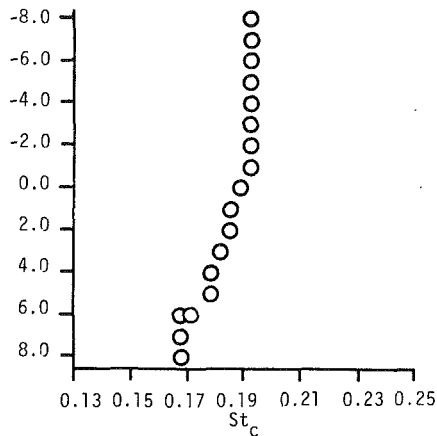It should be noted that Szechenyi [6] has presented a graph

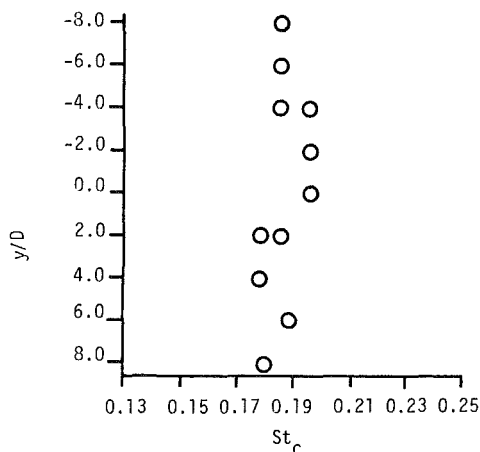Fig. 6(a) Smooth cylinder, $Re_c = 1.6 \times 10^5$

Fig. 6(b) Rough cylinder, $Re_c = 1.6 \times 10^5$

Fig. 6 Spanwise variation of eddy shedding frequency ($\beta = 0.007$)

of Strouhal number as a function of roughness Reynolds number (in which the diameter of a roughness element is the length scale) which gives consistently higher values of Strouhal number for all flow regimes than do the present results. He also locates the supercritical regime between Re = 1.5×10^5 and Re = 2.0×10^5, assuming a perfect equivalence of the effect of a glass bead coated surface and a knurled surface of the same depth.

C. Vortex Shedding Patterns for Smooth and Rough Cylinders in Sheared Flow. For each of the sheared flow cases examined, a plot of Strouhal number (still defined as $St_c = FD/U_c$) as a function of y/D for the given case is presented, where the Strouhal number is, like the Reynolds number, based on the centerline freestream velocity. A spanwise vortex shedding cell is identifiable as a segment of y/D over which the Strouhal number is constant. A particular station for which the signal has a broad peak is represented by points at the upper and lower limits connected by a bar. A station for which two separate identifiable peaks were measured is represented by two unconnected points; a very weak, yet still discernible peak is shown as a dotted point.

The following analysis proceeds from the lower to the higher shear cases with a comparison of smooth and rough cylinder results for each case.

Figure 6(a) shows the frequency distribution along the smooth cylinder at $Re_c = 1.6 \times 10^5$ for the lowest shear level, $\beta = 0.007$. A single rather broad peak at $St_c = 0.192$ persisted from the high velocity end to the center of the cylinder, a length of about eight diameters. The next few peaks appeared to move gradually to a lower frequency, which then stabilized at $St_c = 0.168$ over the last three diameters of the cylinder.

Reference to Fig. 5 shows a uniform flow peak at $St_c = 0.188$. Clearly then, a tendency toward an organized cell structure is evident even for very small shear values. The apparent gradual change of the peak near the center of the cylinder reflects the unsteadiness of the boundary between the two cells. As noted previously, Mair and Stansby [2] put forward this explanation for some of their results, observing "that a vortex that is shed must have some length in the spanwise direction, and the time interval between two successive vortices cannot change continuously along the span." As the present sets of spectra were averaged over a two minute period, there was ample opportunity for contributions from both end peaks to be included in midspan spectral averages.

The shedding pattern developed behind the rough cylinder at $Re_c = 1.6 \times 10^5$ (Fig. 6(b)) was somewhat more confused than in the corresponding smooth cylinder case. For example, between $y/D = -8$ and $y/D = -4$, a peak at $St_c = 0.185$ was measured, whereas in the lower velocity region from $y/D = -4$ to $y/D = 0$, a peak at $St_c = 0.195$ was measured. The lower value is evidently the result of endplate effects. The maximum velocity was only 4 percent greater than the centerline velocity for $\beta = 0.007$, so the endplate region may have generated a cell based on a slightly lower boundary velocity. Including the end cell, a total of perhaps three separate cells may be discerned, although the final one (from $y/D = 2.0$ to $y/D = 8.0$) was not very well defined. A significant difference from the smooth cylinder result can be seen in the decreased St_c range (0.196 to 0.178) from the high to the low velocity ends. When the centerline Reynolds number was raised to 2.6×10^5 and 3.0×10^5, the flow pattern assumed supercritical characteristics, unlike the smooth cylinder case, which was still critical, as has already been noted in the analysis of the surface C_p distributions. Consequently, no significant amount of energy was concentrated at a Strouhal frequency, except at $y/D = -4.0$ at $Re_c = 3.0 \times 10^5$, where a broadband signal emerged at a Strouhal number of about 0.260, or about 25 percent higher than the corresponding Strouhal number at the same location on the smooth cylinder at $Re_c = 3.0 \times 10^5$.

Doubling the shear parameter produced a range of shedding frequencies, shown in Fig. 7(a), from $St_c = 0.204$ at $y/D = -8.1$ down to $St_c = 0.161$ at $y/D = +8.1$, for the smooth cylinder at $Re_c = 1.6 \times 10^5$. However, the associated cell structure was still not very coherent. A four diameter long cell appeared at the high velocity end, but the mid-span near continuous variation of Strouhal number with y/D closely paralleled the low shear results. An examination of the spectra revealed that a number of peaks were relatively broadband. Elaborating on the observation of Mair and Stansby on the fluctuations in cell boundaries, one may conclude that with a number of cells (at least three) a change in boundaries also changes the mean velocity of the cell, therby changing the shedding frequency. In the averaged spectra this appears as a wide band of high energy frequencies, which gradually shifts with the mean velocity profile.

Rasing the centerline Reynolds number to 2.6×10^5 served again to clarify the cell structure. The peaks recorded at the high velocity end were very narrow, indicating a near periodic shedding frequency. The mid-span section was characterized by weaker energy levels, before another strong signal emerged at $y/D = 2.0$ and was maintained up to the low velocity endplate. The spectrum at $y/D = 6.1$ showed evidence of a second peak at the frequency of the weak mid-span cell. The Strouhal number range was from 0.205 to 0.169, again showing the shift upward with increasing Reynolds number.

The previously noted phenomenon associated primarily with the lower shear rough cylinder results was most pronounced at $\beta = 0.016$ and $Re_c = 1.6 \times 10^5$. At the high velocity end, from $y/D = -8.1$ to $y/D = -4.0$, the dominant frequency of the cell corresponded to $St_c = 0.186$. The second cell, as can be seen in Fig. 7(b), was at a significantly higher
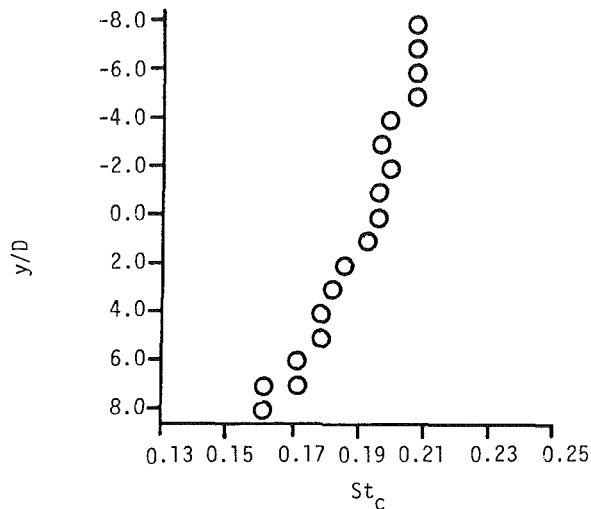
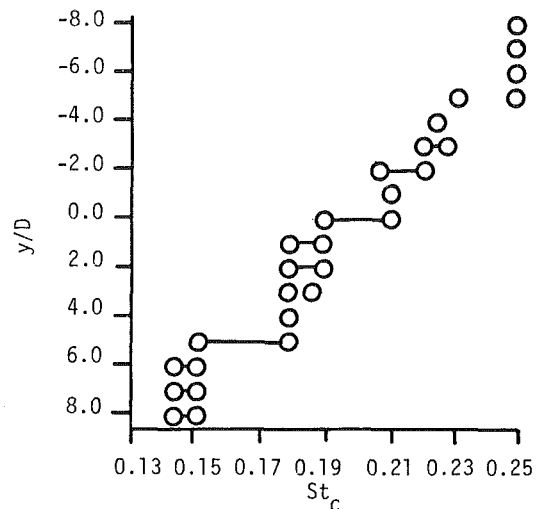**Fig. 7(a) Smooth cylinder, $Re_c = 1.6 \times 10^5$**
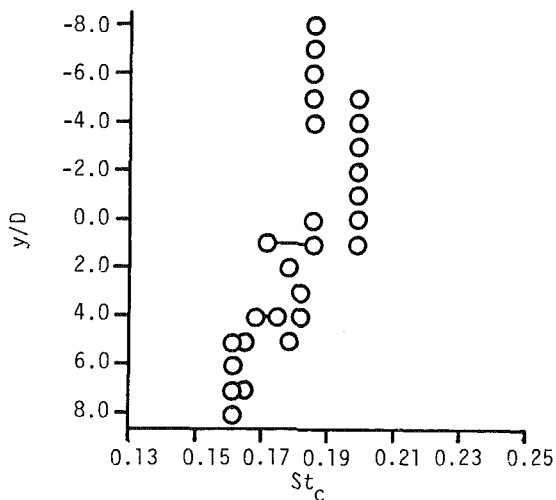

Fig. 7(b) Rough cylinder, $Re_c = 1.6 \times 10^5$

Fig. 7 Spanwise variation of eddy shedding frequency ($\beta \approx 0.016$)

Fig. 8(a) Smooth cylinder, $Re_c = 1.6 \times 10^5$

Fig. 8(b) Smooth cylinder, $= Re_c = 2.2 \times 10^5$

Fig. 8(c) Rough cylinder, $Re_c = 1.6 \times 10^5$

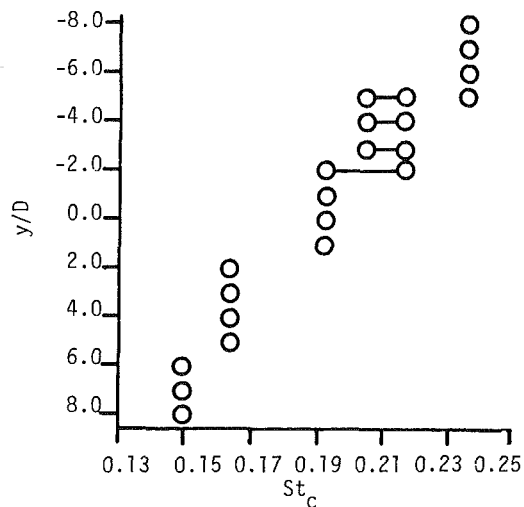**Fig. 8 Spanwise variation of eddy shedding frequency ($\beta = 0.041$)**

frequency, even though the mean velocity at the center of the second cell was about 3 percent lower than in the first. No irregularities in the mean and fluctuating velocity profiles existed on the high velocity side of the cylinder. Also, cylinder blockage effects could not have been responsible since no such reverse cell was documented in the corresponding smooth cylinder results. It has already been postulated that an endplate effect was the cause, even though the actual endplate boundary layer thickness was much smaller than 1 in. Two important differences from the smooth cylinder flowfield which would tend to magnify the endplate effect on a rough cylinder must be taken into account: *a*) the surface roughness promoted a more homogeneous cylinder boundary layer which could permit further penetration of endplate boundary layer effects, and *b*) the rough cylinder flowfield was much closer to critical conditions that the smooth cylinder flowfield, and therefore may have been much more sensitive to small scale effects of the order of the endplate boundary layer.

With an increase in upstream shear to $\beta = 0.021$ and $\beta = 0.033$ more stable cell boundaries appeared for both the smooth and rough cylinder cases, particularly as the Reynolds numbers entered the critical regime. The Strouhal number range was consistently narrower for the rough cylinder results for a given Reynolds number, in accord with the trend already observed above for the low shear cases.
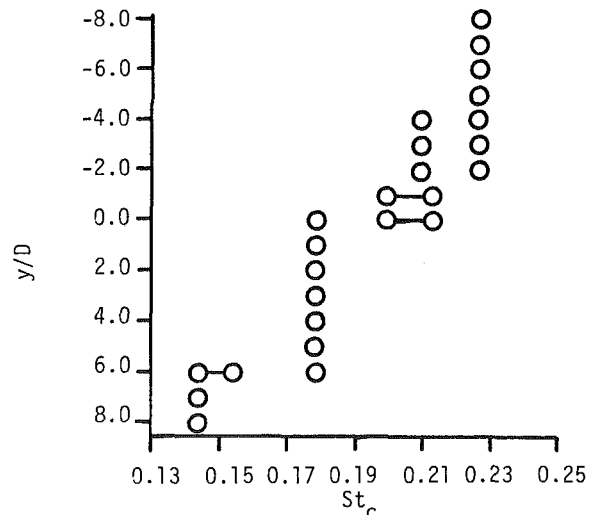
The series of tests run under the highest shear conditions attainable in the wind tunnel demonstrated the clearest pattern of multiple cellular shedding.

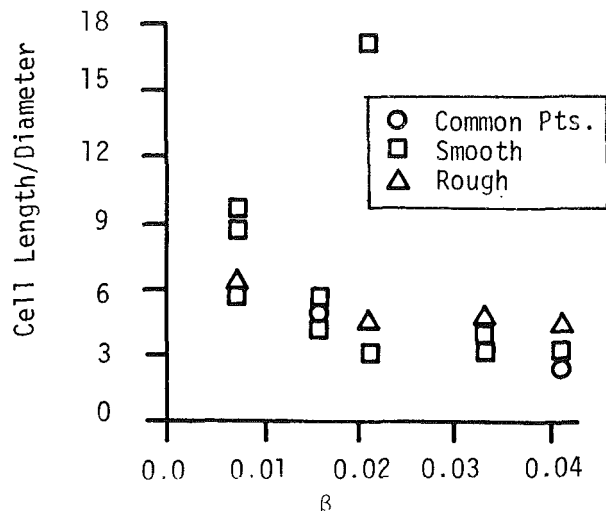The smooth cylinder results at $Re_c = 1.6 \times 10^5$, shown in

Fig. 9 Average cell length versus shear parameter β

Fig. 10 Spanwise Strouhal number range versus $\beta(Re_c = 1.6 \times 10^5)$

Fig. 8(a), exhibited broadband peaks but significant changes in their frequencies occurred over short length scales, so cells were well defined. The Strouhal number of the high velocity endplate cell was 0.244. At $y/D = -5.1$, an equally prominent peak appeared, but quickly gave way to a third cell. It is difficult to determine whether one or two cells were present in the length from $y/D = -5.1$ to $y/D = 0$. The next cell persisted down to $y/D = 4.0$, and finally an endplate peak centered around $St_c = 0.144$ formed the fourth (or fifth) cell. Each cell boundary was marked by a jump in Strouhal number of about 0.020.

At the higher Reynolds number, $Re_c = 2.2 \times 10^5$, the relative lengths of the four major cells were virtually unchanged, as indicated in Fig. 8(b). The uniform flow Strouhal number for this case was 0.192. With $\beta = 0.041$, the high velocity end cell shed at $St_c = 0.236$ and was followed successively by peaks at $St_c = 0.205$ to 0.217, 0.193, 0.164 and 0.149. The spanwise spread in Strouhal numbers decreased slightly from the previous case, but the low velocity end cell was much more coherent and therefore centered at a higher mean velocity. Again the cell boundaries were marked by very large discontinuities in Strouhal number.

The rough cylinder exhibited a well-defined four cell structure at $Re_c = 1.6 \times 10^5$, as indicated by Fig. 8(c). The relative lengths and amplitudes of the peaks were somewhat different than in the corresponding smooth cylinder case. The highest frequency cell shed at $St_c = 0.226$ extended almost half the cylinder length and was extremely well-defined. A second peak at $St_c = 0.205$ gave way to another sharply defined cell at $St_c = 0.178$ and the final cell was centered at $St_c = 0.144$. The range in Strouhal numbers was again smaller than for the corresponding smooth cylinder case. A physical explanation of this phenomenon is in order. It is evident from a comparison of the results at $\beta = 0.041$ that the high velocity end peak in the rough cylinder tests penetrates much further down the cylinder than it does on the smooth one. Therefore the peak is centered at a lower mean velocity, hence the smaller shedding frequency. The rough surface probably acts to homogenize flow conditions over a large area, permitting a wider coherence in the shedding pattern. The average cell size would then be expected to be larger for a rough cylinder. An attempt will be made in the next section to examine that conclusion more thoroughly based on the results of the entire set of test runs.

When the rough cylinder was tested at $Re_c = 2.2 \times 10^5$, the high shear level produced two very distinct flow regimes along the cylinder span. Along the low velocity side, distinct peaks at a Strouhal number of 0.150 were observed, while the high
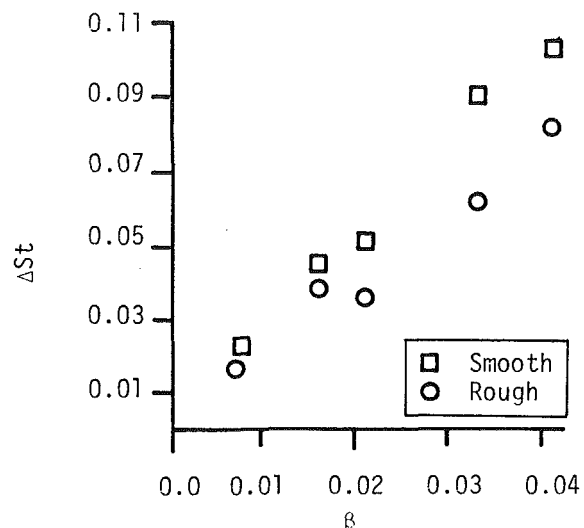
velocity side, obviously in the supercritical regime, was devoid of shedding activity except for one weak endplate peak caused by the boundary effect noted before.

D. Effect of Shear on Cell Length. An attempt was made to determine whether a definite correlation between upstream shear level and size of cells of constant shedding frequency could be extracted from the data plotted and analyzed in the preceding section.

The result is the graph in Fig. 9, plotting cell length as a function of β. Before drawing any conclusion from the graph, one must bear in mind two physical limitations which make the process of identifying cells quite difficult. The first is the unsteadiness of many cell boundaries, which can even obscure the existence of a cell, let alone its length. The second is the effect of the endplates. It has been observed that the endplates contaminated the rough cylinder results up to $\beta = 0.021$ by imposing a lower velocity cell over some spanwise distance down from $y/D = -8.1$.

The coherent cells discernible at both ends of the cylinder, even when the central region showed no cellular organization, were clearly forced by the endplates, and cannot be attributed primarily to the shear in the upstream flow. Ideally an aspect ratio greater than 20 would be desirable to permit a central spanwise segment uncontaminated by the end effects, but the reduction in cylinder diameter necessary to produce high aspect ratios would have limited the test runs to solely subcritical flow regimes. The mid-span cells observed at high shear values were clearly produced by the upstream shear, and it is their variation as a function of surface roughness and Reynolds number which most clearly demonstrates the conclusion that cell length increased with increasing roughness, as can be seen in Fig. 8, for example.

Nevertheless, two trends are apparent in Fig. 9. The first is that an increase in β generally resulted in a decreased cell size, where each point plotted represents the average cell size for a particular case tested. The one noteworthy exception is the single point at $\beta = 0.021$, which was observed to have been affected by the endplate.

The second trend which developed (above $B = 0.021$) is the tendency for the rough cylinder to generate longer cells than the smooth cylinder. The increased homogeneity in wake structure caused by roughness elements is hypothesized to spread the influence of a single cell, diminishing the number of cells, and producing the narrower range in shedding frequencies which was documented in the rough cylinder results.

Finally, a plot of the spanwise variation in Strouhal number

as a function of the shear parameter β is displayed in Fig. 10. The comparison of smooth and rough cylinder results is made at $Re_c = 1.6 \times 10^5$, at which the smooth cylinder was definitely in the subcritical regime and the rough cylinder was entering the critical regime. The smooth cylinder consistently exhibited a wider range in shedding frequencies. It has already been stated that roughness tends to homogenize the cylinder boundary layer and stabilize cell structure, with longer cells resulting from this process. Corroborating evidence for this phenomenon has been observed in instantaneous surface pressure measurements [7], in which a smooth cylinder at $Re_c = 2.6 \times 10^5$ registered much greater fluctuations than a rough cylinder. The fluctuations apparently diminish as the cylinder progresses through the critical regime. Therefore, since roughness enhances the onset of critical flow, it also stabilizes the pressure field, and fixes cell boundaries. A decrease in spanwise shedding values necessarily follows.

5 Conclusions

The following new conclusions have been arrived at from the results discussed above:

1 Any linear shear in the upstream velocity profile will trigger a cellular vortex shedding pattern in critical Reynolds numbers, with the cells becoming more distinct at higher shear levels further into the critical regime.

2 In tests where end effects and fluctuating cell boundaries were not predominant, the average cell length along a rough cylinder is greater than along a smooth cylinder. There is a decrease in cell length with increasing upstream shear for both smooth and rough cylinders.

3 The spanwise Strouhal number range is substantially reduced with increasing roughness on a cylinder in the subcritical-critical Reynolds number range.

6 Experimental Uncertainty

The maximum uncertainty in the mean C_p distributions, and their corresponding C_D values, was ±6 percent of reading. This value of uncertainty was a result of two factors: the uncertainty caused by the fluctuation in the C_p values, and the instrument uncertainty. The largest factor affecting the uncertainty in spectral data was the number of spectral averages selected. During the program 25 averages were taken, although to be statistically valid, at least ten times as many averages are usually required. The limitations on available wind tunnel time required that a relatively low number be selected. It was determined, through comparing specific spectra obtained using 25 and 250 averages, that the only significant benefit realized by the larger number of averages was a smoothing of the small fluctuations in the spectra away from the peaks. The fairly narrow banded high energy signal, measured at most test positions, virtually eliminated the need for a large number of averages.

References

1 Maull, D. J., and Young, R. A., "Vortex Shedding from Bluff Bodies in a Shear Flow," *Journal of Fluid Mechanics*, Vol. 60, 1973, pp. 401–409.

2 Mair, W. A., and Stansby, P. K., "Vortex Wakes of Bluff Cylinders in a Shear Flow," *SIAM Journal of Applied Mathematics*, Vol. 28, 1975, pp. 519–540.

3 Stansby, P. K., "The Locking-On of Vortex Shedding Due to the Cross Stream Vibration of Circular Cylinders in Uniform and Shear Flows," *Journal of Fluid Mechanics*, Vol. 74, 1976, pp. 641–667.

4 Davies, M. E., "The Effects of Turbulent Shear Flow on the Critical Reynolds Number of a Circular Cylinder," *National Physical Laboratory (U.K.) NPL Report Mar. Sci. R. 151*, Jan. 1976.

5 Rooney, D. M., and Peltzer, R. D., "The Effects of Shear on Vortex Shedding Patterns in High Reynolds Number Flow: An Experimental Study," *Proceedings of Sixth OTEC Conference*, Washington, D. C., June 19–22, 1979.

6 Szechenyi, E., "Supercritical Reynolds Number Simulation for Two-Dimensional Flow Over Circular Cylinders," *Journal of Fluid Mechanics*, Vol. 70, Part 3, 1975, pp. 529–542.

7 Peltzer, R. D., "The Effect of Upstream Shear and Surface Roughness on Vortex Shedding Patterns and Pressure Distributions Around a Circular Cylinder in Transitional Re Flows," M. S. thesis, VPI&SU, Apr. 1980, 176 pp.

8 Bearman, P. W., "On Vortex Shedding From a Circular Cylinder in the Critical Reynolds Number Regime," *Journal of Fluid Mechanics*, Vol. 37, Part 3, 1969, pp. 577–585.

9 Batham, J. P., "Pressure Distributions on Circular Cylinders at Critical Reynolds Numbers," *Journal of Fluid Mechanics*, Vol. 57, 1973, pp. 209–228.

10 Achenbach, E., "Influence of Surface Roughness on the Cross-Flow Around a Circular Cylinder," *Journal of Fluid Mechanics*, Vol. 46, Part 2, 1971, pp. 321–335.

11 Buresti, G., and Martini, G., "Experimental Research on the Effects of Surface Roughness on the Cross-Flow Around Circular Cylinders," *Atti Istituto Di Aeronautica (Italy)*, Report Number AIA 80-2, May 1980.

12 Roshko, A., "Experiments on the Flow Past a Circular Cylinder at Very High Reynolds Numbers," *Journal of Fluid Mechanics*, Vol. 10, 1961, pp. 345–356.

13 Alemdaroglu, N., Rebillat, J. C., and Goethals, R., "An Aeroacoustic Coherence Function Method Applied to Circular Cylinder Flows," *Journal of Sound and Vibration*, Vol. 69, 1980, pp. 427–440.

E. Kordyban
Professor,
University of Detroit,
Detroit, Mich. 48221
Mem. ASME

Oil Thickness Variation on Wavy Water in the Presence of Wind

The effect of the wind on the distribution of an oil layer on wavy water has been examined analytically and the results are compared with experimental values. It is found that the wind tends to decrease the difference between the oil layer thickness at the wave crest and the wave trough, but for sinusoidal waves this effect is small.

Introduction

The large number of oil spills in recent years and increased recognition of their deleterious effects on the environment has brought about an interest which resulted in development of a great number of devices for oil containment and clean-up [1]. This gave rise to the need for better understanding of the behavior of the oil layer on open water surface. In spite of considerable literature that has appeared in recent years the various mechanisms governing the behavior of the oil layer are not completely understood. This is particularly true in the presence of wind and waves, a frequent occurrence in nature, where complex effects are introduced into the distribution of the oil layer. When left unperturbed, the oil layer will eventually spread to a thickness of less than a millimeter and under such conditions the local variation in thickness is probably not very important for practical purpose, but when the oil slick is retained by an oil boom it may become quite thick and the thickness variation will be important.

The behavior of the oil layer on wavy water has been studied both under laboratory [2] and field conditions [3] and it was found that the oil layer becomes thicker at the wave crest than at the wave trough. Leibovich [4] has examined this problem analytically, but his results are limited to "extremely thin" oil layers while Chung [5] extended this analysis to greater thicknesses. Both analyses confirmed the experimentally observed thickness variations. This author [14] has measured local thicknesses of oil layer on waves and found that, for some wave lengths, the difference in oil thickness was substantially larger than predicted by Chung's analysis.

All of the above studies were conducted on waves in the absence of wind and, yet, it is rarely that the waves exist in nature without the wind also being present. It is well known that the wind affects the liquid surface both by shear forces and by virtue of the presence of normal pressure variations which bear a definite relationship to the phase of the wave.

The effect of the wind on the wavy water surface has been studied extensively both theoretically [6, 7] and experimentally [8, 9] mostly in search of a plausible mechanism of wave growth, but the literature on the effects of wind on the local distribution of an oil layer is conspicuous by its absence.

This paper presents the analysis of the wind effect on the oil layer. Furthermore, the tests conducted to confirm the theoretical results are described and their results are compared to the theoretical predictions.

Theory

While the wind affects the wavy liquid surface by both the surface shear and normal pressure variation, the former seems to be of secondary importance, as concluded by Miles [6]. Consequently, only the effect on normal pressure variations will be examined here. Oil viscosity and surface tensions will also be neglected.

Chung [5] derives the following equations for the velocity potential of oil, using linearized wave theory

$$\phi^o = ia\left\{\left[\frac{\omega}{k}\bar{\rho}\coth kh + \frac{g}{\omega}(1-\bar{\rho})\right]\cosh kz \right.$$

$$\left. + \frac{\omega}{k}\sinh kz\right\}e^{i(kx-\omega t)} \tag{1}$$

and of water

$$\phi^w = ia\frac{\omega}{k}\frac{\cosh k(z+h)}{\sinh kz}e^{i(kx-\omega t)} \tag{2}$$

Using the condition that the pressure at the air-oil interface is zero the following equation was obtained by Chung for the wave frequency

$$\omega^4(\bar{\rho}\coth kh \coth kh_o + 1) - \omega^2\bar{\rho}(\coth kh_o$$
$$+ \coth kh_o)gk + (\bar{\rho}-1)g^2k^2 = 0 \tag{3}$$

with the following approximate solution applicable to external waves

$$\omega^2 = gk\tanh k(h+h_o) \tag{4}$$

Using equations (1), (2), and (4) the expressions for the elevations of air-oil interface and oil-water interface are obtained.

When the wind is present the condition of zero pressure at the wave surface no longer holds. We shall assume that the aerodynamic pressure is composed of a component proportional to negative surface elevation and component proportional to wave slope. Neglecting the effect of surface tension the pressure at air-oil interface can be expressed as

$$\frac{p}{\rho_o} = -A\eta^o + B\frac{\partial\eta^o}{\partial x} \tag{5}$$

The boundary condition for the air-oil interface then is

$$-A\eta^o + B\frac{\partial \eta^o}{\partial x} = -\frac{\partial \phi^o}{\partial t} - g\eta^o$$

or

$$\frac{\partial \phi^o}{\partial t} = -(g-A)\eta^o - B\frac{\partial \eta^o}{\partial x} \tag{6}$$

using the kinematic condition

$$\frac{\partial \phi^0}{\partial z} = \frac{\partial \eta^o}{\partial t}$$

equation (6) becomes

$$\frac{\partial^2 \phi^o}{\partial t^2} = -(g-A)\frac{\partial \phi^o}{\partial z} - B\frac{\partial^2 \phi^o}{\partial x \partial z} \tag{7}$$

Substituting from equation (1) into equation (7)

$$ia\left\{\left[-\frac{\omega^3}{k}\bar{\rho}\coth kh - g\omega(1-\bar{\rho})\right]\cosh kz - \frac{\omega^3}{k}\right.$$

$$\left.\sinh kz\right\}e^{i(kx-\omega t)} = ia(g-A)\left\{\left[-\omega\bar{\rho}\coth kh\right.\right.$$

$$\left.-\frac{gk}{\omega}(1-\bar{\rho})\right]\sinh kz - \omega\cosh kz\right\}e^{i(kx-\omega t)}$$

$$+aB\left\{\left[\omega k\bar{\rho}\coth kh + \frac{qk^2}{\omega}(1-\bar{\rho})\right]\sinh kz\right.$$

$$\left.- \omega k\cosh kz\right\}e^{i(kx-\omega t)}$$

At the wave surface $z = h_o$, and the foregoing expression becomes

$$\omega^4(\bar{\rho}\coth kh\coth kh_o + 1) + \omega^2\{gk(1-\bar{\rho})\coth$$

$$kh_o - (g-A)\bar{\rho}k\coth kh - (g-A)k\coth kh_o$$

$$- i[Bk^2\bar{\rho}\coth kh + Bk^2\coth kh_o]\} - g(g-A)$$

$$k^2(1-\bar{\rho}) - iBgk^3(1-\bar{\rho}) = 0$$

For $\bar{\rho} \to 1$ we have

$$\omega^4\bar{\rho}\coth kh\coth kh_o + 1 - \omega^2 k(g-A)(\bar{\rho}\coth kh$$

$$+ \coth kh_o) + iBk^2(\bar{\rho}\coth kh + \coth kh_o) = 0$$

The first approximate root of this equation, applicable to external waves is

$$\omega^2 = \frac{\coth kh + \coth kh_o}{\coth kh\coth kh_o + 1}(g-A)k + iBk^2$$

or

$$\omega^2 = [(g-A)k + iBk^2]\tanh k(h+h_o) \tag{8}$$

The wave frequency ω is now a complex number

$$\omega = \omega_R + i\omega_i$$

where ω_R represents the real frequency while ω_i represents a growth factor.

If we limit our analysis to cases where A and B are small in comparison with g, equation (8) can be expressed as follows

$$\omega_R + i\omega_i \approx \left[1 - \frac{1}{2}\frac{k(A-iBk)}{(gk)}\right]\left[(gk\tanh k(h+h_o))\right]^{1/2}$$

from which

$$\omega_R = \left[(gk)^{1/2} - \frac{1}{2}kA\right]\tanh^{1/2}k(h+h_o) \tag{9}$$

Thus, within specified limitations, the component of pressure in phase with the wave slope has no effect on the wave frequency.

Using equations (1), (2), and (9) the following equations are obtained for the elevations of air-oil and oil-water interfaces

$$\eta^o = a\left\{\left[\bar{\rho}\coth kh - \frac{g}{g-A}\cdot\frac{\bar{\rho}-1}{\tanh k(h+h_o)}\right]\right.$$

$$\left.\sinh kh_o + \cosh kh_o\right\}\cosh(kx-\omega t) + h_o \tag{10}$$

and

$$\eta^w = a\cos(kx-\omega t) \tag{11}$$

From equation (10) it may be noted that the effect of the wind tends to increase the second term by a factor of $g/g-A$ and thus to reduce the amplitude of the wave on the air-oil interface.

Using equations (10) and (11) the difference in oil layer thickness is

$$\Delta t = 2a\left\{\left[\bar{\rho}\coth kh - \frac{g}{g-A}\frac{\bar{\rho}-1}{\tanh k(h+h_o)}\right]\right.$$

$$\left.\sinh kh_o + \cosh kh_o - 1\right\} \tag{12}$$

For deep water $\coth kh \to 1$, $\tanh k(h+h_o) \to 1$, while for small kh_o, $\sinh kh_o \to kh_o$ and $\cosh kh_o \to 1$. Under these conditions equation (12) becomes

$$\Delta t = 2a\left[1 - \frac{A}{g}(\bar{\rho}-1)\right](kh_o) \tag{13}$$

In order to determine the effect of the wind quantitatively it is necessary to find the value of A. This may be accomplished by considering irrotational flow of air past a wave surface. Equation for stream function is

$$\psi^a = U(-z + be^{kz}\sin kx) \tag{14}$$

Neglecting the surface tension effects the pressure at air-oil

---

Nomenclature

a = amplitude of water wave
A = constant defined in test
b = amplitude of wave on air-oil interface
B = constant defined in text
c = wave speed
f = wave frequency, cps
g = acceleration of gravity
h = depth of water
h_o = mean oil layer thickness
k = wave number
L = wave length

p = pressure at the wave surface
t = time
Δt = difference in oil thickness between wave crest and wave trough
U = air velocity relative to wave
U_c = air velocity at wave crest relative to wave
U_T = air velocity at the wave trough relative to wave
U_1 = 2.5 U^*
U^* = friction velocity
x = longitudinal coordinate

z = transverse coordinate
α, β = constants defined in text
η^o = elevation of oil-air interface
η^w = elevation of oil-water interface
ρ_a = density of air
ρ_o = density of oil
ρ_w = density of water
$\bar{\rho}$ = ρ_w/ρ_o
ϕ^o = velocity potential for oil
ϕ^w = velocity potential for water
ψ^A = stream function for air
ω = wave frequency

interface is identical for both oil and air. Applying the Bernoulli equation at the interface

$$\frac{p}{\rho_a} = \text{const.} - gz - \frac{1}{2} U^2 [1 - 2be^{kz}\sin kx + \ldots]$$

Setting const. $-1/2U^2 = 0$ and neglecting the gravity term for air

$$p = -U^2 \rho_a bk\sin kx \qquad (15)$$

Since the equation of surface elevation is $\eta^o = b\sin kx$

comparing to equation (5) we have

$$A = \frac{\rho_a}{\rho_o} U^2 k \qquad (16)$$

and equation (13) becomes

$$\Delta t = 2a\left[1 - \frac{\rho_a U^2 k (\bar{\rho} - 1)}{\rho_o g}\right]kh_o \qquad (17)$$

U is the velocity of the air relative to the waves in an ideal case, but it is well known that in nature the wind velocity varies with the vertical distance from the water surface. For such a case Miles [6] has assumed the aerodynamic pressure in the form

$$p_{as} = (\alpha + i\beta)\rho_a U_1^2 k\eta$$

where $U_1 = 2.5U^*$

Miles, however, did not suggest a method for calculating α, since his prime interest lay in β, the growth factor.

The actual pressure measurements at the wave surface under laboratory conditions were taken by Shemdin and Hsu [10] using apparatus which followed the surface of the waves. The average wind velocity in their channel varied from 1.7 to 7.2 m/s and for this range the coefficient β increases with air velocity. Comparing one value of β at an average velocity of 6.22 m/s it is found that the measured pressure variation at the water surface is about 50 percent larger than predicted by equations (5) and (16). It may be thus concluded that equation (16) yields approximate results but further study is needed to establish more accurate values.

Experimental Work

Equipment. The experiments conducted for the purpose of verification of the developed theory were performed in a wave channel made of acrylic plastic, 10 cm deep, 15 cm wide, and about 7 m long. The downstream end of the channel is equipped with a sloping beach made of gravel and screens to minimize the reflection of the waves. The upstream end contains a piston-type wave generator and the air inlet. The wave generator was used to produce longer and better defined waves than those produced by the wind. Both the frequency and the length of travel of the generator could be varied.

The air was supplied by a blower and was admitted to the channel tangentially to the liquid surface. The air flowrate was measured by a laminar flowmeter which also served to

reduce the turbulence in the incoming air. The channel was filled with water to a depth of 6 cm and then 2000 ml of kerosene was added to simulate oil. The static kerosene thickness was 2.9 mm, but it was significantly modified both by the waves and the wind.

Instrumentation. The measurements taken were those of air flowrate, local oil layer thickness, and the amplitudes of water waves. The instrumentation to measure the oil thickness was developed for this study and it is shown schematically in Figs. 2 and 3. Its development and calibration were described in detail in [11]. In essence, it consists of a probe which follows the surface of water and is similar in principle to that used in
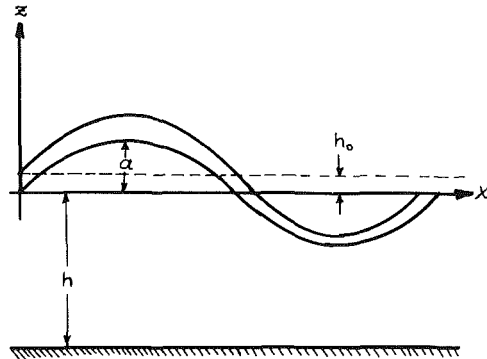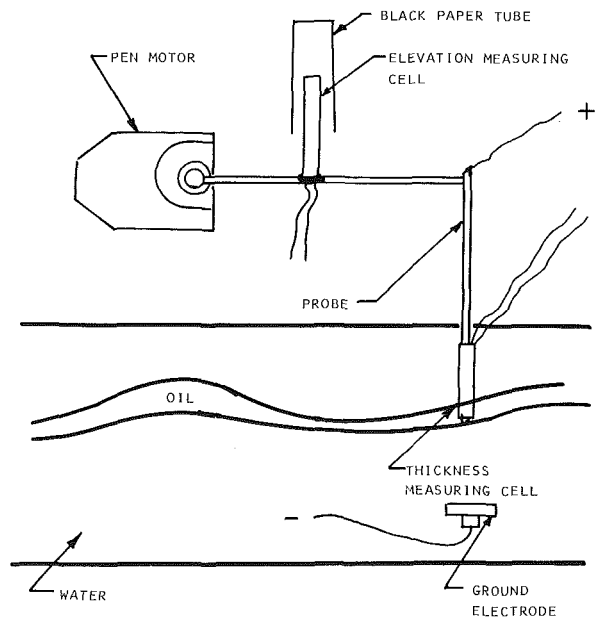

Fig. 1 Pictorial representation of a wave

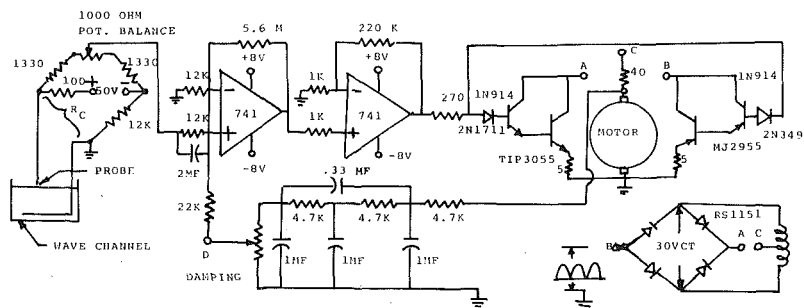Fig. 2 Schematic of oil thickness measuring instrumentation

Fig. 3 Circuit diagram for servo amplifier

Fig. 4 Ratio of oil thickness amplitude to oil thickness amplitude at zero air velocity as a function of air velocity; uncertainty estimate: ratio 12 percent, velocity 5 percent

AIR VELOCITY, M/SEC

Fig. 6 Maximum oil thickness variation over a wave as a function of air velocity; uncertainty estimate: thickness 8 percent, velocity 5 percent

Once it is known that the probe tip is at the water surface, it is only necessary to measure the depth to which the probe is submerged in oil in order to determine local oil thickness. This was accomplished by the use of a light sensitive cell made in the form of a thin strip 2.5 mm wide and 32 mm long which was attached to the probe in such a way that its lower edge was slightly above the probe point.

Since the kerosene is normally transparent it was dyed a dark color to provide good resolution for the measurement of submergence.

The light sensitive cell was also equipped with a scale which permitted visual observation of the depth to which it was submerged. This served as a coarse check on the oscillograph readings to assure that no gross errors were being committed. Such errors are possible with a light sensitive cell when the shadow of the wave or the light reflected from the wave surface is permitted to fall upon the cell.

The wave amplitude was measured by a similar cell attached to the movable motor arm. As the probe point followed the water surface the cell moved into and out of a black paper tube producing a signal on the oscillograph from which local water surface elevation could be determined.

Tests. The tests were conducted in the following manner. The channel was filled with water and the kerosene was added and permitted to reach the equilibrium thickness. At this point the wave generator was started at a predetermined frequency. Due to wave drift the oil layer became thicker at the downstream end; again, sufficient time was allowed to reach the equilibrium and then the record of the local oil thickness and of water surface elevation was made in proper phase relationship between them. After this the blower was started and the flowrate adjusted to the lowest value. After the equilibrium was attained the readings were taken again and the air flowrate increased to the next value. In all, the readings were taken without the air flow and for four values of flowrate at a particular frequency; this was repeated for six
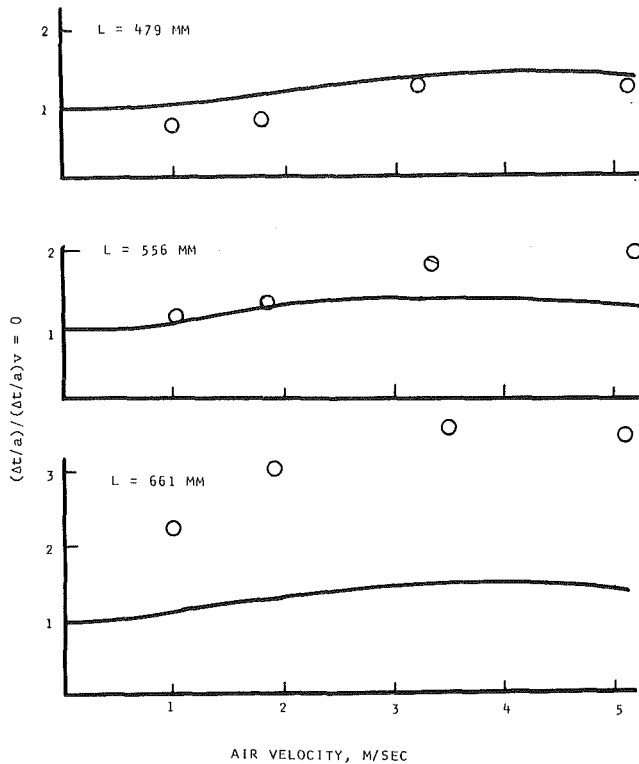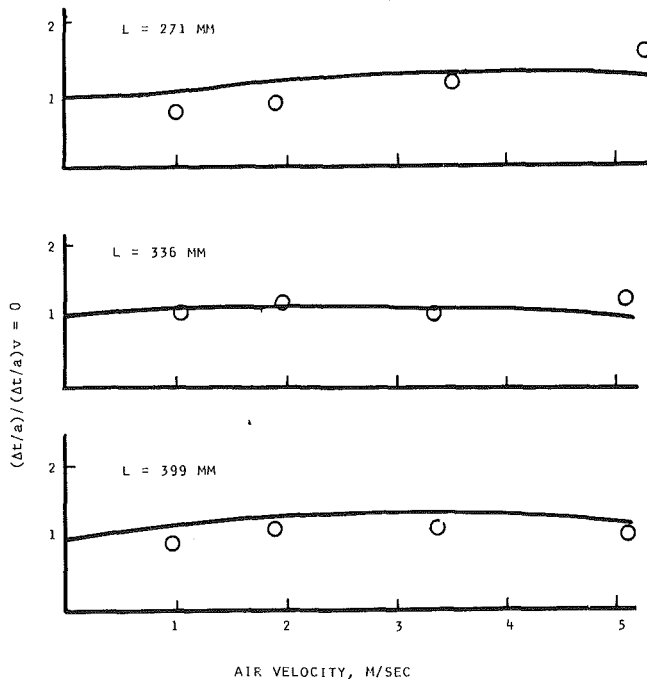

AIR VELOCITY, M/SEC

Fig. 5 Ratio of oil thickness amplitude to oil thickness amplitude at zero air velocity as a function of air velocity; uncertainty estimate: ratio 12 percent, velocity 5 percent

[3]. This is accomplished by placing a ground electrode in water while the probe tip serves as the positive electrode. When the probe tip comes in contact with the water surface, a small current flows between the electrodes and this current serves as a signal for the amplifier circuit shown in Fig. 3 to drive the probe in such a way that its tip remains always in contact with the water surface.
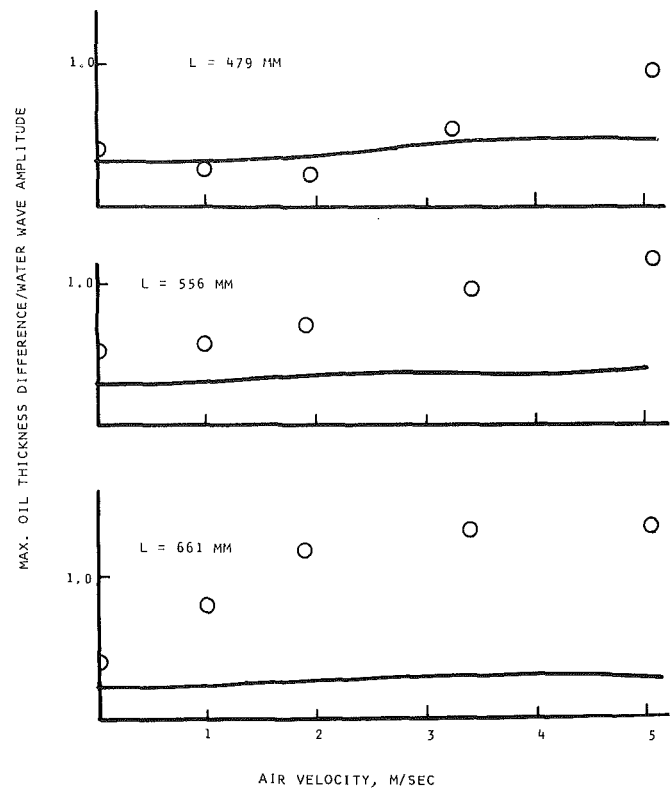
Fig. 7 Maximum oil thickness variation over a wave as a function of air velocity; uncertainty estimate: thickness 8 percent, velocity 5 percent
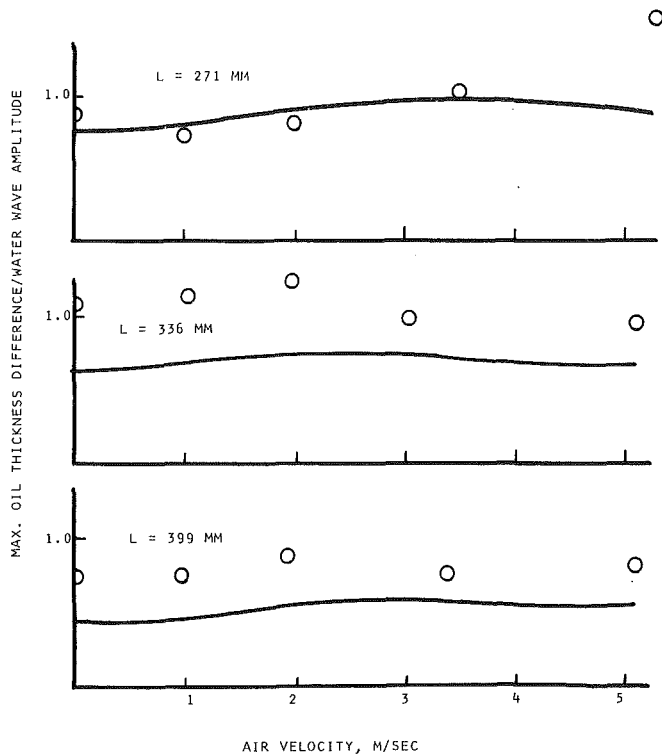

Fig. 8 Comparison of growth rates of water waves under oil and for bare water waves; uncertainty estimate: ratio 12 percent, velocity 5 percent

different frequencies. At each point the record of about 20 waves was obtained; the differences between individual waves were usually small and the average for the set was used as the value for that point. The final value for each point represents the average of five to eight tests.

It was found that as the air velocity increased the mean oil thickness also increased while the wave frequency dropped slightly.

The instruments were calibrated before each test and occasionally after tests by attaching the arm of the probe to a micrometer mechanism and submerging the probe in dyed kerosene through known distances.

Water wave growth tests were performed in a manner similar to that just described, except no oil was added to water.

Results

From the records obtained during the tests the local oil thickness and the elevation of the water surface could be found as a function of wave phase for a range of a wave frequency and air velocities. The wave frequency which was found from the oscillograph records permitted calculation of the wave length from

$$L = c/f$$

by assuming the wave speed to be

$$c = \left(\frac{g}{k} \tanh kh \right)^{1/2} \tag{18}$$

It should be noted that equation (18) was checked in the author's previous work [12] for water waves in the presence of an oil layer and was found to produce satisfactory results.

The average air velocity was found by calculation of the mean liquid level from the oscillograph data. The flowrate was then divided by the cross-sectional area of the air passage.

In Figs. 4 and 5 the ratio of oil thickness variation amplitude to the amplitude at zero air velocity is presented as a
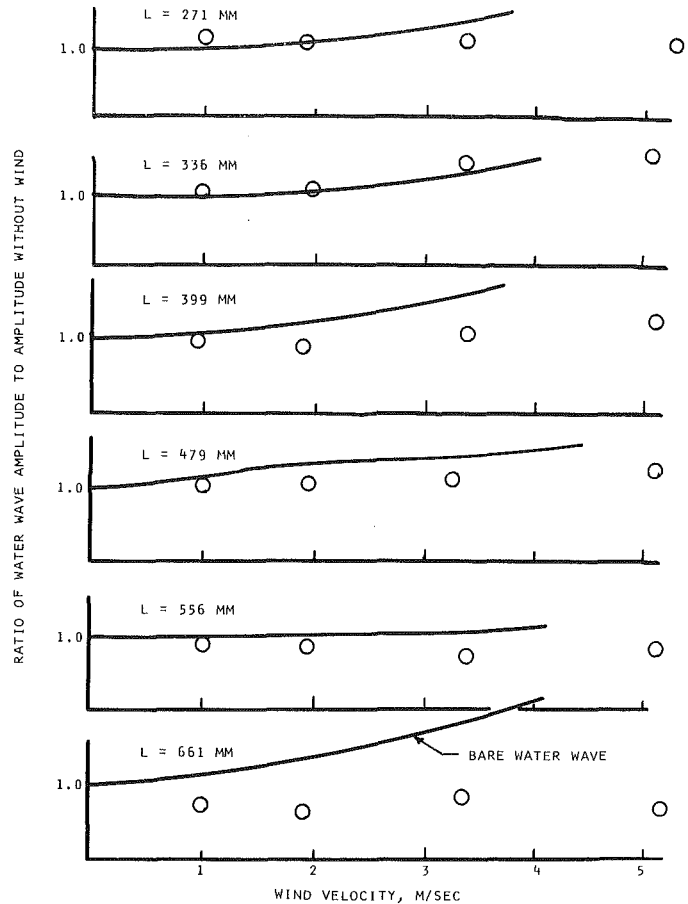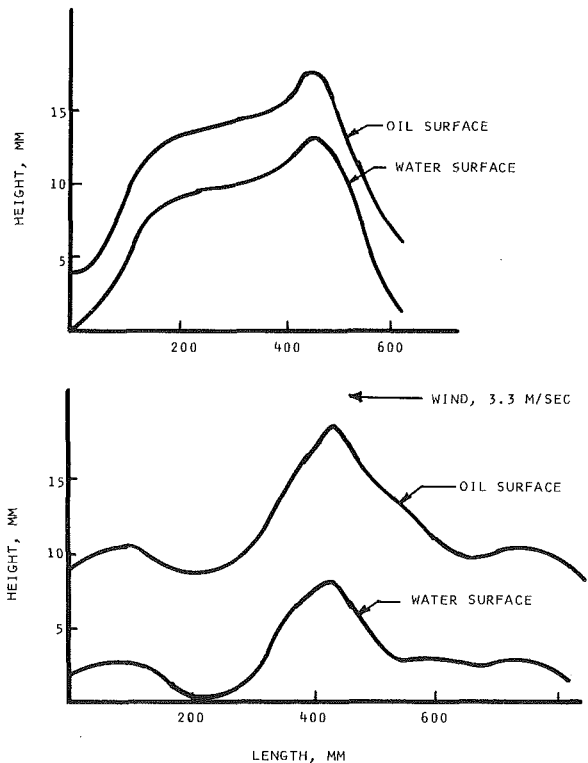
Fig. 9 Wave profile for the longest wave: a) no wind; b) wind velocity = 4 m/s
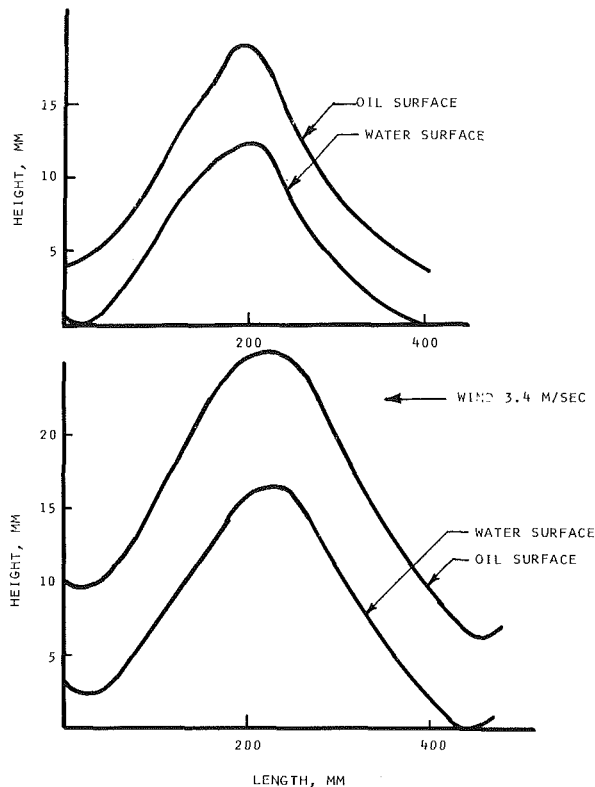
Fig. 10 Wave profile for representative waves: a) no wind; b) wind velocity = 4m/s

Fig. 11 Photograph showing the oil thickness variation on waves 270 mm in length with 1 m/s wind velocity

Fig. 12 Photograph showing the oil thickness variation on a wave 270 mm in length with 4.5 m/s wind velocity

Fig. 13 Photograph showing oil distribution on a breaking wave. Wave length is 270 mm and air velocity is 4.5 m/s.

function of air velocity for the series of wave lengths. The predicted values are shown as curves. They were obtained by using actual observed values of mean oil layer and water depth.

Figures 6 and 7 show the comparison between the maximum oil thickness variation observed and predicted theoretically.

In Fig. 8 a comparison is shown between the growth of the waves on the oil-water interface and the growth of water waves with the oil being absent as a function of air velocity. All values were obtained from tests in the same channel.

Figure 9 represents the profile of the longest wave for which unusually large growth of thickness variation is noted in Fig. 4. Figure 10 shows the wave profile more representative of the waves in the bulk of the tests.

Figure 11 shows a photograph of the shortest wave at low (1 m/s) air velocity, while Figs. 12 and 13 show the photographs of the same wave length at high (4.5 m/s) air velocity; wave breaking and large accumulation of oil at the crest may be observed there.

Discussion

From analysis of equation (17) it will be evident that the effect of wind tends to reduce the variation of oil thickness from crest to trough, but at moderate speeds and sinusoidal waves it is rather small. In fact, the numerical values found by using this equation show that, for a 1 m wave the specific gravity of oil equal to 0.8, a 19.40 m/s air velocity is needed to produce a 10 percent reduction in the oil thickness variation amplitude. At this velocity, however, large breaking waves would be produced and, consequently the range of validity of the developed theory would be greatly exceeded.

From observation of Figs. 4 and 5 it will be noted that there is good agreement between the observed points and predicted values except, very noticeably, at the longest wave length; there the oil thickness variation grows quite rapidly with the air velocity. In order to uncover the reason for this
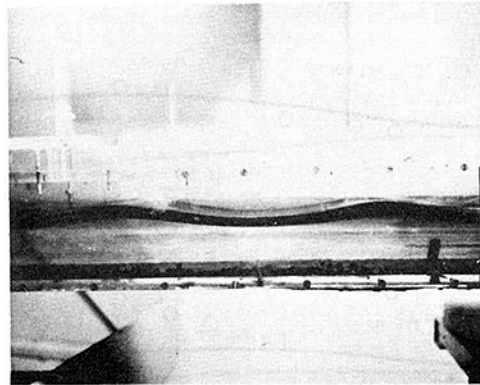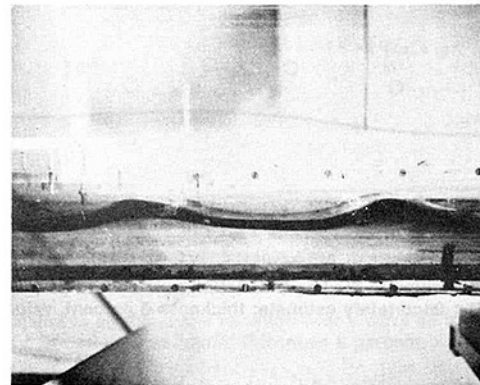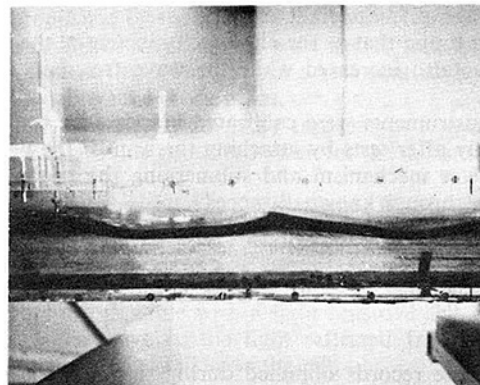
discrepancy these waves were studied in greater detail, but the results were found to be repeatable. On the other hand, as may be observed from Fig. 9, the wave profile is quite irregular and, furthermore, it changes significantly with increasing air velocity. Apparently, the developed theory is not directly applicable to this case. For the majority of the tests the waves were much closer to sinusoidal shape as may be observed from Fig. 10. There is also some disagreement, although less noticeable, for the short waves at highest air velocities. At such velocities the waves begin to exhibit typical nonlinearities as sharper crests and wave breaking as shown in Figs. 12 and 13; such effects apparently serve to increase the oil thickness at the crests significantly.

The conditions under which the tests were run differ substantially from the assumptions which underlie equation (17). The depth of water was limited and the values of kh_o

could not be considered small. Furthermore, the aerodynamic pressure distribution at the wave surface was affected significantly by the proximity of the upper wall of the channel. Consequently, the oil thickness variation was calculated from equations (10) and (11) while the pressure distribution was determined from

$$p = \frac{1.81}{2} \rho_a (U_T^2 - U_C^2) \qquad (19)$$

Equation (19) was taken from the author's work [13] in which the pressure distribution over water waves was determined in the same channel.

The reason for the increase in the oil thickness amplitude with air velocity, as evident in Figs. 4 and 5 and in apparent conflict with the prediction of equation (17), is due to the fact that the mean oil thickness increased with increasing air velocity.

While the agreement between predicted and measured values of the growth rates of the oil thickness amplitude is good, the actual values of oil thickness variation are not well predicted by the developed equations as is evident from Figs. 6 and 7. These variations are generally greater than predicted. This was also found to be the case in previous work [14] where the oil thickness variations were measured in the absence of wind and compared to Chung's theory.

It may be also of interest to examine the growth of the water wave amplitude under oil with increasing air velocity and to compare it to the growth of bare water waves under the same conditions; this is shown in Fig. 8. As may be seen, the growth rate of the water wave under oil shown as points is generally smaller than the growth rate of bare water waves. For the case of the longest wave there is actually a significant decrease in amplitude indicating that the energy is transferred to oil which may account for the large growth of the oil thickness variation. The reduction of water wave amplitude can be also deduced from equations in [4] and [5].

Conclusions

The examination of theoretical equations dealing with the effect of wind on oil distribution on wavy water shows that the wind tends to reduce the thickness difference, but for moderate wind speeds on sinusoidal waves this effect is small.

The results of tests performed to measure the oil thickness variations in the presence of wind and waves show a good agreement with the theory when dealing with percentage change of oil thickness amplitude with wind velocity, but, in general, the theory tends to underpredict the oil thickness difference.

References

1 Sittig, M., *Oil Spills Prevention and Removal Handbook*, Noyes Data Corp., Park Ridge, N.J., 1974.

2 Lindenmuth, W. T., et al., "Studies of Oil Retention Boom Hydrodynamics," The U.S. Coast Guard Report No. 714102/A/008, AD719294, prepared by Hydronautics, Inc., 1970.

3 Alchorn, T., and Chung, J. S., "Test Report, High Seas Oil Recovery Systems; Transportability and Oil Recovery Test," in the U.S. Coast Guard Report No. CG-D-150-75, prepared by Lockheed Missiles and Space Co., Sunnyvale, Calif., 1975.

4 Leibovich, S., "Hydrodynamic Problems in Oil Spill Control and Removal," *Proceedings of the Offshore Technology Conference*, Houston, Tex., May 1975.

5 Chung, J. S., "Thickness Variations of an Oil Spill on Waves," *Cavitation and Polyphase Flow Forum*, ASME Publication, 1977.

6 Miles, J. W., "On the Generation of Surface Waves by Shear Flows," *Journal of Fluid Mechanics 2*, Vol. 3, 1957, p. 185.

7 Phillips, O. M., "On the Generation of Waves by Turbulent Wind," *Journal of Fluid Mechanics 2*, Vol. 3, 1957, p. 417.

8 Wu, J., "Laboratory Studies of Wind-Wave Interaction," *Journal of Fluid Mechanics*, Vol. 34, 1968, p. 91.

9 Gottifredi, J. C., and Jameson, G. J., "The Growth of Short Waves on Liquid Surfaces Under the Action of Wind," *Proc. Royal Society*, A319, 1970, p. 393.

10 Shemdin, O. H., and Hsu, E. Y., "Direct Measurement of Aerodynamic Pressure Above a Simple Progressive Gravity Wave," *Journal of Fluid Mechanism*, Vol. 30, Part 2, 1967, p. 403.

11 Kordyban, E., and Cuker, S., "Instrumentation to Measure the Oil Thickness on Wavy Water Surface," *Rev. Sci. Instr.*, Vol. 49, No. 9, 1978.

12 Kordyban, E., "Variation of Oil Thickness on Wavy Water," *Cavitation and Polyphase Forum*, ASME Publication, 1979.

13 Kordyban, E., "Experimental Study of Aerodynamic Pressure at the Wave Surface in Two-Phase Flow," Submitted for publication.

14 Kordyban, E., "The Effect of Waves on Oil Distribution on Water," Submitted for publication.

J. Lee
Senior Research Engineer,
Research and Development Division,
Babcock & Wilcox Co.,
Alliance, Ohio 44601

C. T. Crowe
Professor,
Mechanical Engineering Dept.,
Washington State University,
Pullman, Wash. 99164

Scaling Laws for Metering the Flow of Gas-Particle Suspensions Through Venturis

An experimental investigation was undertaken to determine those scaling parameters applicable to measuring the mass flow rate of gas-particle suspensions through venturis. It was found that Stokes number and the particle/gas loading ratio are the two most important parameters. The results show that pressure drop increases linearly with loading ratio and decreases monotonically with increasing Stokes number. The results also indicate that β-ratio and orientation of venturi do not significantly affect the pressure drop. Data for irregularly shaped pulverized coal particles show higher pressure drop compared with those for spherical particles. A quasi one-dimensional numerical model overpredicts the pressure drop, but a two-dimensional model demonstrates improved agreement.

Introduction

The reliable metering of the solids mass-flow rate in a gas stream is important to many energy related industrial processes such as gasification and combustion of pulverized coal, air-pollution control systems, pneumatic transport of granular materials, and in many other fields of engineering and science. In contrast to many data available for metering single phase fluids, there is yet little information on metering gas-solids flows through venturis and flow nozzles.

Because of the growing need and importance of the continuous monitoring of the solids mass-flow rate, many different meter designs and concepts have been introduced. Techniques which measure particle speed and density separately to obtain solids mass-flow rate include the radioactive tracer and β-ray absorption [1], microwave [2], and acoustic/ultrasonic techniques [3]. Another concept is the target or impact flow meter [4] which measures the momentum imparted by the particle cloud but a second measurement of particle density is also required. A third type of flow meter which measures the mass flow rate of solids directly includes the eddy current flow meter [5], noise correlation technique [6], and measurement of capacitance charge of the solids [7]. Common to all these meters, except pressure differential-type meters, are the complexity of the systems, calibration, limitations on operating conditions and, subsequently, the difficulty of establishing general scaling laws for different operating conditions. For industrial applications the meter should be simple, reliable, and should yield mass flow rate directly.

Pressure differential meters have been studied by many because of the simplicity in design and monitoring the flow rate once scaling laws have been established. However, application of these meters to full-scale systems has not been entirely successful. The original study in this area was conducted by Carlson, et al. [8]. They tried to measure both particles and gas flow rates with a venturi-orifice combination in series. Their design was successful on a laboratory scale but failed for large-scale application. A more extensive experimental study of the venturi meters for gas-particle flow was undertaken by Farbar [9]. He also developed a simple model for pressure drop but it was inadequate for general design purposes because the parameters important to scaling were not included. Other studies [10, 11] also failed to include those parameters important to the scaling. Also, the range of experimental conditions was very limited.

Subsequent studies [12, 13] based on dimensional analysis for gas-particle flow suggest that the pressure drop across the venturi depends primarily on Stokes number and solids loading ratio provided the gravitational effect is not important.

The Stokes number is defined as the ratio of the particle relaxation time to gas relaxation time. If the Stokes number is small, the particles have sufficient time to maintain near-velocity equilibrium with gas (equilibrium flow condition) and thereby a large pressure gradient is required to achieve acceleration of the gas-particle mixture. In fact, in the limit of gas-particle velocity equilibrium, the mixture can be regarded as a single phase fluid with modified properties.

On the other hand, if the Stokes number is large, the particles have insufficient time to be accelerated and the particle motion is almost completely unaffected by the gas flow (frozen-flow condition); i.e., the gas flow behaves as though the particles were essentially absent. This reasoning explains some of the early data obtained with gas-particle flow through a venturi and an orifice in series in which it was found that the orifice essentially measures the gas flow rate while a venturi measures the mixture flow rate. Also, the fact that Stokes number is dependent on meter size explains the failure of previous studies to apply as anticipated to a large-scale system.

The other important parameter, loading ratio, is defined as
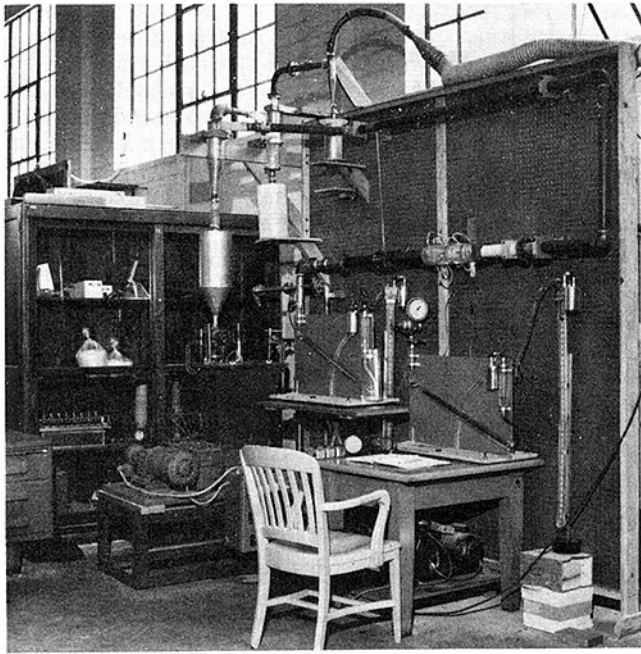
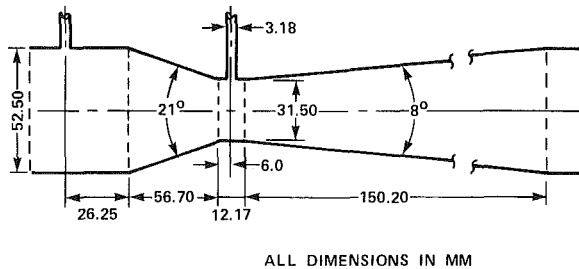**Fig. 1 Photograph of the experimental setup**

ALL DIMENSIONS IN MM

Fig. 2 Geometry of standard ASME venturi with β-ratio of 0.6

the ratio of the particles' mass flow rate to gas mass flow rate. Obviously, this ratio significantly affects the pressure distribution by increasing the mass of the accelerating mixture.

Virtually no data were available which demonstrated the dependence of pressure drop on Stokes number and loading over a sufficiently wide range for practical use. The purpose of this study is to obtain a reliable base to establish the scaling laws for metering the flow of gas-solids suspensions through venturi by carrying out experiments over a wide range of flow conditions.

Experimental Program

Experiments were undertaken to investigate the effects of Stokes number, loading, β-ratio and orientation of venturis, and nonsphericity of particles on the pressure drop across a venturi.

The experimental setup is shown in Fig. 1. The facility consists of flanged-connected steel conduits (0.0525 m inside diameter), an inlet air supply, metered by an orifice, an auger powder feeder to feed particles into the airstream, a gas-

particle mixing section, a test section for installation of venturis and finally, a series of cyclone separators to remove particles from the airstream and return them to the powder feeder forming a closed loop system.

The powder hopper is connected by a pressure line to a point very near the mouth of the powder feeder to minimize the effect of a pressure difference between hopper and the mouth of the feeder on the mass feed rate of solids. Calibration tests demonstrated that the powder feed rate varies linearly with auger speed. In situ verification of the particle mass flow rate was also checked by isokinetic sampling.

The mass flow rate of air through an orifice and pressure drop across venturis were measured by slant tube manometers with a maximum resolution of 5 pascals.

The pressure taps were continuously purged by an inconsequentially small air flow to prevent dust accumulation in the tap. There was no effect of this purging air on the measurement of the pressure drop.

Three types of spherical particles were used in the experiment: micro-balloons, glass particles, and ballotin-impact beads. Also, Utah coal as obtained from a commercial pulverizer was used. A coulter counter was utilized to analyze the particle sizes. The maximum feed rate of each particle type and their characteristics are shown in Table 1.

Using these particles in the experimental rig provided Stokes numbers from 0.15 (close to the equilibrium flow) to 13 (close to frozen flow) and a loading ratio from 0 to 2.

Table 1 Characteristics of particles used in experiments

particle type	maximum feed rate (gr/s)	density (kg/m^3)*	mass median dia. (μm)*	shape
micro-balloons	10	325 ± 5	29 ± 1.0	#
glass beads	70	2900 ± 5	36 ± 1.0	#
Ballotin-impact beads	77	2420 ± 5	65 ± 2.0	#
pulverized coal	28	1340 ± 5	43 ± 1.0	+

* 20:1 odds   # spherical   + irregular

The majority of the experiments were conducted with standard ASME venturis with β-ratios of 0.5, 0.6, and 0.7. The venturi with a β-ratio of 0.6, which is shown in Fig. 2, was tested in both the horizontal and vertical orientations.

The tests were carried out for a given venturi geometry and particle type by maintaining a constant air mass flow rate and increasing the powder feed rate to increase the loading. The pressure drops across the venturi were measured. This yielded data at one Stokes number. Tests were repeated for other air flow rates to establish the repeatability of the data. Next, different types of powder and/or air flow conditions were set to obtain data for other Stokes numbers.

Results

The results of the experimental program are summarized below.

Effect of Loading Ratio. Data typical for the effect of loading ratio on the pressure drop are shown in Fig. 3 for Stokes number of 3.8 and 10.7. The pressure drop is nor-

<hr>

Nomenclature

P_r = pressure ratio parameter

ΔP_g = pressure drop across a venturi for gas-phase only

ΔP_{tp} = pressure drop across a venturi for gas-particle flow

St = Stokes number

z = loading ratio (mass flow rate of particles/mass flow rate of gas)

β = beta ratio of the venturi (throat diameter/inlet diameter)

Journal of Fluids Engineering

malized with respect to the pressure drop which would exist if no particles were present (loading ratio equal to zero). One notes a strong linear correlation of the pressure drop ratios with loading which persisted throughout. The steeper slope of pressure drop ratio for the smaller Stokes number implies higher acceleration of particles under this condition. One can also infer that at very small Stokes number the pressure drop ratio will asymptotically approach $1 + z$, condition of equilibrium flow, while at very large Stokes number it approaches unity, the frozen flow condition.

The linearity of the pressure drop with loading allows one to account for loading by measuring the slope of the line. Thus, it is convenient to introduce a pressure ratio parameter defined as

$$p_r = (\Delta p_{tp} / \Delta p_g - 1)/z$$

which is independent of loading and a convenient parameter with which to represent the data.

Effect of Stokes Number. The effect of Stokes number on the pressure ratio parameter is shown in Fig. 4. One recognizes that the mean pressure ratio parameter monotonically decreases with increasing Stokes number. The nominal uncertainty in pressure ratio parameter is 5 percent with odds of 20 to 1. Clearly Fig. 4 shows that Stokes number is an important scaling parameter for metering gas-solids suspensions through venturis.

Effect of β-ratio. Figure 4 also shows no significant effect of β-ratio for Stokes numbers up to 5, which implies that β-ratio is not a significant parameter in this range. However, for Stokes numbers around 10, the venturi with larger β-ratios tend to have a smaller value of the pressure ratio parameter.

Effect of Orientation of Venturi. The effect of meter orientations on the pressure ratio parameter was tested using a venturi with a β-ratio of 0.6. The results are shown in Fig. 4. With a nondeposit flow condition of the gas-particle mixture and loading ratios up to 2, there appears to be no significant difference in data between the horizontal and vertical orientations.

Effect of Nonsphericity of the Particles. Most of the tests were undertaken with spherical particles. However, to investigate the effect of nonsphericity of particles on the pressure drop across venturi, experiments were conducted with irregularly shaped pulverized coal particles. The results in Fig. 4 show that the pressure ratio parameter for nonspherical particles is higher than that for the spherical particles. This result is consistent with the higher drag coefficient characteristics of irregularly shaped coal particles [14].

Comparisons of Experimental Result With Numerical Predictions. Figure 5 shows the experimental results and predictions by quasi one-dimensional [13] and two-dimensional [15] numerical models for the dependence of pressure drop ratios on loading ratio at a Stokes number of 3.85. The quasi-one-dimensional model consistently overpredicts the pressure drop over all loading ratios. This deviation is attributed primarily to the inability of a one-dimensional model to account for the two-dimensional channeling effect of the particles. However, the two-dimensional model incorporates this two-dimensional channeling behavior of particles predicts the pressure drop ratios very well over the loading ratio of experiment. The slight nonlinearity of the prediction by a two-dimensional model is attributed to compressibility effects unaccounted for in the model.

Based on the experimental results obtained to date, the following summary can be made.

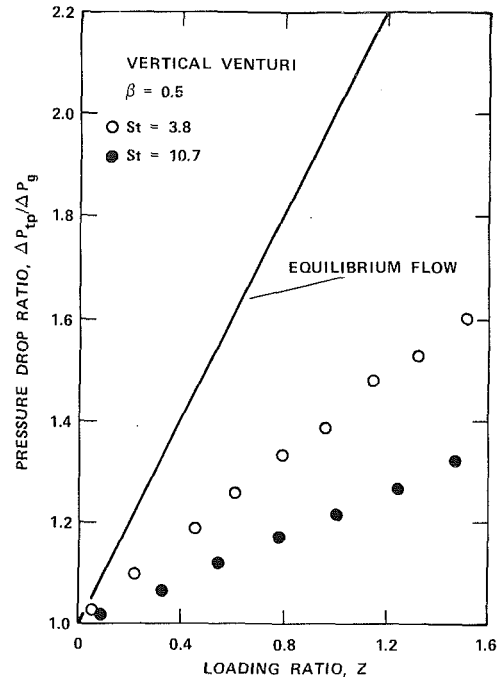1 Stokes number and loading ratio are the two dominant

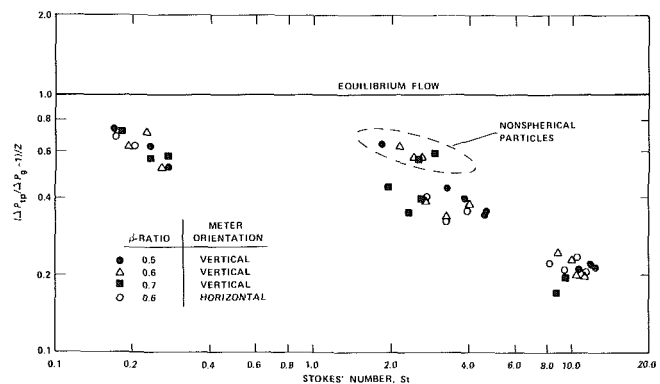Fig. 3 Measurement of pressure drop ratio versus loading ratio

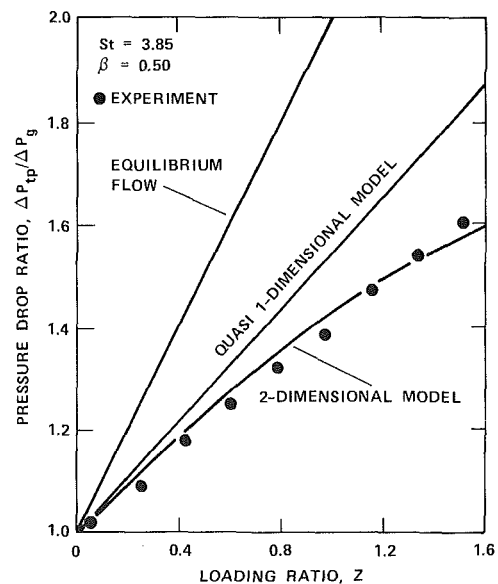Fig. 4 Variation of pressure ratio parameter with Stokes number

Fig. 5 Comparison of experimental result with numerical model predictions

nondimensional parameters controlling pressure drop of gas-particle flows in a venturi.

2 Pressure drop at a fixed Stokes number varies linearly with solids loading.

3 The pressure ratio parameter decreases monotonically with increasing Stokes number.

4 The β-ratio of venturi appears only to have an effect at higher Stokes number.

5 Pulverized coal has a higher pressure ratio parameter than spherical particles at the same Stokes number.

6 Orientation of venturi for the nondeposit flow condition appears to have no significant effect on pressure drop.

Conclusion

Pressure drop across a venturi with gas-particle flow is primarily dependent on loading ratio and Stokes number. These two nondimensional numbers constitute the primary scaling parameters.

Acknowledgments

References

1 Hours, R. M., and Chen, C. P., "Application of Radioactive Tracers and β-Rays Absorption Techniques to the Measurement of Solid Particles Velocity and Space Concentration in a Two-Phase Air-Solid Flow at High Mass Rate," Paper B3, *Third International Conference on the Pneumatic Transport of Solids in Pipes*, BHRA Fluid Engineering, Cranfield, England, 1976.

2 Howard, A. V., "A Microwave Technique for Monitoring the Mass Flow Rate of Pneumatically Transported Solids in Pipes," BHRA Fluid Engineering, Cranfield, England, 1976.

3 Lynnworth, L. C., "Industrial Application of Ultrasound—A Review, II. Measurements, Tests, and Process Control Using Low-Intensity Ultrasound," *IEEE Transactions on Sonics and Ultrasonics*, Vol. SU-22, No. 2, Mar. 1975, pp. 71–101.

4 Gibson, H. G., and Fasching, G. E., "Metering Device for Pulverized Coal Suspensions," *Pneumatic Transportation Symposium*, Oct. 1965.

5 Wiegand, D. W., "The Eddy Current Flowmeter," ANL-7554, 1969.

6 Randall, R. L., "Flow Measurements Using Noise Analysis Techniques," NAA-SR-MEMO-9787, 1964.

7 Beck, M. S., Hobson, J. H., and Mendies, P. J., "Mass Flow and Solids' Velocity Measurement in Pneumatic Conveyors," Paper D3, *First International Conference on the Pneumatic Transport of Solids in Pipes*, BHRA Fluids Engineering, Cranfield, England, 1971.

8 Carlson, H. M., Frazier, P. M., and Engdahl, R. B., "Meter for Flowing Mixtures of Air and Pulverized Coal," *Trans. ASME*, July 1953, p. 943.

9 Farbar, L., "Metering of Pulverized Solids in Gas-Solids Mixtures," *Ind. and Eng. Chem.*, Vol. 44, No. 12, 1952, pp. 2947–2955.

10 Graczyk, C., "The Application of the Venturi Tube to the Measurement of the Rate of Coal Dust Flow Transported in Air," *Acta Imeko*, 1961, pp. 251–275.

11 Antikayan, P. A., "Measurement of Pulverizer Coal Flow in an Air Stream," *Teploenergetika*, Vol. 3, No. 12, 1956, p. 35.

12 Boothroyd, R. B., *Flowing Gas-Solids Suspension*, Chapman and Hall, 1971.

13 Sharma, M. P., and Crowe, C. T., "A Novel Physico-Computational Model for Quasi-One-dimensional Gas-Particle Flow," ASME JOURNAL OF FLUIDS ENGINEERING, Vol. 100, No. 3, 1978, pp. 343–349.

14 Kline, S. J. and McClintock, F. A., "Describing Uncertainties in Single Sample Experiments," *Mechanical Engineering*, Jan. 1953, p. 2.

15 Clift, R., Grace, J. R., and Weber, M. E., *Bubbles, Drops and Particles*, Academic Press, 1978.

16 Lee, J., *Scaling Laws for Metering the Flows of Gas-Particle Suspensions through Venturis*, Ph.D. dissertation, Washington State University, Pullman, WA, 1980.

M. R. Ghassemzadeh

Development Engineer,
Combustion Systems,
Babcock & Wilcox Co.,
Barberton, Ohio 44203

S. Carmi

Professor,
Mechanical Engineering Department,
Wayne State University,
Detroit, Mich. 48202
Mem. ASME

Drag Reduction in Flow of Coal-Oil Suspensions

Pipe flow characteristics of coal-oil mixtures (C.O.M.) are studied by a pipe flow facility consisting of a Tri-Rotor positive displacement pump, which draws fluid from a reservoir tank and discharges through a pipeline at regulated pressures. Pipe flow tests are carried out to study the drag reduction effect of the polymer carboxymethylcellulose (CMC) on the flow of coal-oil mixtures. Addition of CMC reduces friction drag on the average by 10 percent. Preliminary results are presented covering appropriate ranges of operating parameters (coal concentration and temperature) which influence the drag reduction. A brief discussion will evaluate the significance of these results.

Introduction

The purpose of our study was to investigate the possible drag reduction in the flow of coal-oil mixtures (C.O.M.) and the potential benefit in applying this technique to commercial systems dealing with C.O.M. preparation and treatment prior to combustion.

Drag reduction has been observed to occur in the flow of several additive systems, such as in solutions of synthetic as well as natural polymers and suspensions of solid particles. The mechanism of polymer drag reduction is believed to reside in the viscoelastic properties of such dilute polymer solutions. Some excellent reviews on polymer drag reduction have been published [1—3], but no previous application to C.O.M., to our knowledge, was reported.

Experimental Apparatus

Pipe-Flow Facility. Our drag reduction study has been carried out in a facility consisting of a 5 gal reservoir tank, a Tri-Rotor positive displacement pump, which can discharge fluid at a pressure as high as 50 psig and a 10 ft long commercial ¼ in. pipe with an inside diameter of 0.354 in. The apparatus can be operated batchwise using the pump as the driving force. An accurately calibrated pressure gage was used to measure the pressure drop. Flow rates were measured batchwise by collecting and weighing the sample in a receiver downstream for a measured period of time using a stop watch. The insulated pipe system was wrapped with heating tapes and the temperature was monitored constantly by a digital temperature readout controlled by a temperature controller.

Sample Preparation and Experimental Uncertainty. The C.O.M. fuel samples are prepared from No. 6 oil and pulverized coal 80 percent 200 mesh (80 percent of the coal particles are 75 μ or less in diameter). The #6 oil serves as a baseline fuel. Samples at concentrations of 0, 30, 35, 40, 45, and 50 percent coal by weight in the mixture were prepared. In the sample preparation, a 0.25 percent BASF stabilizing agent

heated to 120°F is added to the oil to which the pulverized coal is added up to the required concentration while the mixture, kept at 140°F, is stirred continuously by a mixer. The polymer was heated to 120°F and was then added to the mixture.

The uncertainty involved in measuring the flow rate of coal-oil mixtures with or without the polymer additive is about 0.1 percent. Using the Kline and McClintock uncertainty method with 20:1 odds, the overall uncertainty in drag reduction computations for each test condition was determined.

Drag Reduction Results

The drag reduction in the present study is attained by adding the polymer carboxymethylcellulose (CMC) to the C.O.M. Samples. Although many oil-soluble drag-reducing polymers are known, the CMC, which has a rather limited solubility in oil, was chosen because of its easy availability and the preliminary nature of this experimental investigation. Detailed studies with drag-reducing polymers which are more oil-soluble should be pursued. Viscosity, concentration, and temperature parameters which affect the drag were measured and analyzed (for details see [4]). Two sets of identical experiments with and without the polymer additive, using No. 6 oil and coal-oil mixture samples were conducted in order to show the effect of the presence of the polymer on the drag.

It was observed that for a constant pressure drop, the samples with the CMC additive had a higher flow rate, measured batchwise, than the samples without the additive. The experiments were performed in a temperature range of 130–150°F. The data qualitatively demonstrates drag reduction by the polymer additive.

The magnitude of drag reduction can be quantitatively defined by using the following expression:

$$\text{D.R.} = 1 - \frac{(\Delta P)_{\text{sample}+\text{CMC}}}{(\Delta P)_{\text{sample}}} \bigg|_{Q=\text{constant}}, \tag{1}$$

where D.R. = drag reduction and ΔP = pressure drop. It is convenient to write the definition of D.R. as

$$\text{D.R.} = 1 - \left(\frac{t_{\text{sample}+\text{CMC}}}{t_{\text{sample}}} \right)^2 \tag{2}$$
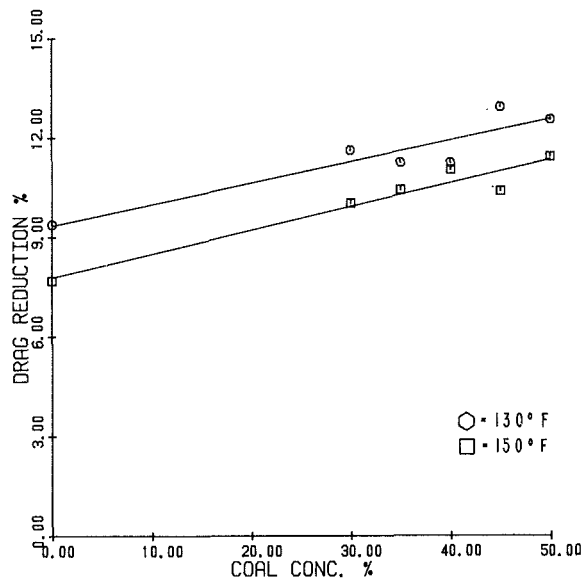
Fig. 1 Drag reduction (%) versus coal concentration (%); with temperature (°F) as a parameter

where t = flow time (time for the given volume of effluent to flow out of the reservoir) is proportional to Q = flow rate for a fixed volume sample while Q^2 is proportional to ΔP for turbulent flow. Two different concentrations of CMC were used, 250 PPM and 500 PPM by weight, respectively, and the D.R. was found to be very similar for both. Limited solubility of CMC in oil might be the reason for this result. Results for 250 PPM of CMC are summarized in Fig. 1.

Conclusions

The purpose of this study was to investigate the effect of this particular polymer additive CMC on flow of coal-oil mixtures under different flow conditions and at various temperatures and the potential of applying this technique to commercial systems dealing with the preparation and transportation of C.O.M. prior to combustion. On the average, adding CMC to coal-oil mixtures reduced drag by about 10 percent. This reduction is equivalent to a 10 percent reduction in ΔP which corresponds to 5 percent on Q or t. The drag reduction results, although preliminary, are quite encouraging. As can be noted in Fig. 1, the drag reduction increases with concentration but decreases with temperature. More tests involving different polymer additives with a higher solubility in oil than CMC are necessary to ascertain if higher drag reduction can be attained.

Acknowledgment

References

1 Hoyt, J. W., "The Effect of Additives on Fluid Friction," ASME *Journal of Basic Engineering*, Vol. 94, 1972, pp. 258–285.

2 Little, R. C., Hansen, R. J., Houston, D. L., Kim, O. H., Patterson, R. L., and Ting, R. Y., "The Drag Reduction Phenomenon, Observed Characteristics, Improved Agents, and Proposed Mechanisms," *Industrial Engineering Chemical Fundamentals*, Vol. 14, 1975, pp. 283–296.

3 Virk, P. S., "Drag Reduction Fundamentals," *American Institute of Chemical Engineering Journal*, Vol. 21, 1975, pp. 625–656.

4 Ghassemzadeh, M. R., 1980, Ph.D. thesis, Department of Mechanical Engineering, Wayne State University, Detroit, Mich.

R. Oba
Professor.

T. Ikohagi
Assistant.

K. T. Kim
Graduate Student.

Institute of High Speed Mechanics,
Tohoku University,
Sendai, Japan

Cavitation in an Extremely Limited Flow Through Very Small Orifices

In order to clarify the role of cavitation nuclei upon inception, the behavior of inception was carefully investigated in an extremely limited water flow through very small orifices less than 1.0 mm in diameter under a prescribed nuclei condition. The following facts of technical interest were determined: a) The desinent cavitation number (σ_d) decreased rapidly and exponentially with the orifice diameter d, up to one hundredth in magnitude; and b) the cavitation appearance in such limited flows was quite different from that in fully turbulent flows through larger orifices.

Introduction

Cavitation and associated troubles so often arise in such extremely limited regions of technical interest as tip clearances of impellers, throats of control valves, small fluidic branched pipes, and so on. In such regions, the effects of cavitation nuclei may be significant, since the regions are approximately one to two orders of magnitude greater than the size of the nuclei.

According to literature [1, 2], many investigations on the cavitation in the oil hydraulic restrictors have been made not in the laminar flows of present interest, but in the fully turbulent flows. In the Coulter counter [3] which has been often used for cavitation nuclei measurements, there arises a question whether the cavitation occurs in the so-called micro-orifice installed in it.

At present, the understanding of cavitation mechanism seems to be far from complete. This is suggested by the recent finding of "Johnsson effects" [4], namely, that cavitation inception exhibits a wide variety of appearances on the ITTC standard body in different test facilities, even under almost the same conditions for Reynolds number as well as cavitation number.

The first step in this investigation to clarify the role of nuclei in inception was to study the behavior of inception in low turbulent water flows through very small orifices under prescribed nuclei conditions as well as for various hydrodynamic conditions. The orifices, also called "micro-orifices," were approximately one to two orders magnitude greater than the nuclei size [5]. Simultaneous measurements were also made on the cavitation appearances and the associated sound pressures.

Experimental Facilities

Water Tunnel and Test Orifices. The blow-down tunnel shown in Fig. 1 was built for the present investigation, in which capacities of the upper and the lower tank were designed much larger than that through the orifice, so as to keep prescribed flow rates for a sufficiently long time. All of
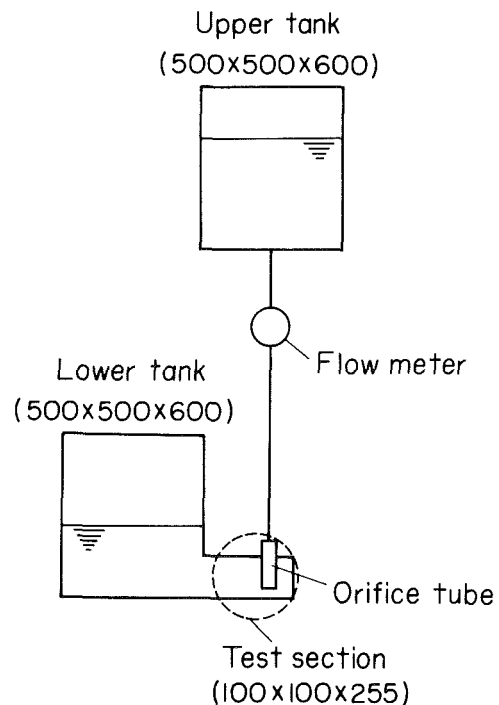
Fig. 1 Schematic diagram of blow-down tunnel. (All dimensions are in millimeters.)

the test section, tanks, and pipes were made of lucite to keep the water clean and for the purpose of observation.

Figure 2 shows the detail of the test section. The test orifice is a kind of long orifice, which is often applied to Coulter counters as well as to oil hydraulic systems. The diameter d is 0.2, 0.5, 0.8, and 1.0 mm, the length l is fixed as 0.5 mm, and the upstream pipe inner diameter D is 6.0 mm, so that the diameter ratio ($\beta = d/D$) is 0.033, 0.083, 0.133, and 0.167, respectively. The orifice plate is placed at the center of the rectangular test section. The upstream and the downstream pressure, p_1 and p_2, are measured on the inner wall at the points C_1 and C_2, respectively. Cavitation sound pressures are also measured by the PZT probe [6] shown in Fig. 2,

Fig. 2   Test section. (All dimensions are in millimeters.)

which is fixed on the outer surface of lucite wall whose acoustic impedance is very close to that of water. A kind of vaseline is plastered between the probe and the wall to match the acoustic impedance.

Coulter Counter. Since a marked difference in the test water cavitation nuclei, which are supposed to be microbubbles of about 0.01 ~ 0.1 mm in diameter, is believed to be one of the principal sources of "Johnsson effects," we tried to measure the nuclei by means of a newly made Coulter counter, without adding a little amount of salt to water.

Figure 3 shows the detail of the counter. A ruby orifice of 0.2 mm in diameter and 0.15 mm in length is located near the lower end of the glass-made Coulter tube. It is well known that 0.1 mm diameter orifices have been often applied to such counters [3, 7]. However, according to our experience, they are not necessarily suitable for accurate continuous nuclei measurements, because it is difficult to measure accurately the microbubbles of about 0.04 ~ 0.1 mm in diameter which are believed to have a most powerful effect on the inception, and also partly because the throats have been so often plugged by any motes.

A large number of nuclei measurements can be done, while the sample water being poured into the Coulter tube flows down very slowly through the orifice and fills up a 130 cm³ lucite vessel gradually.

Figure 4 is a block diagram of the counter system. The voltage pulses, which are proportional to the volumes of microbubbles or solid particles passing through the orifice, were fed to a multichannel analyzer through a high pass filter in order to eliminate noises, and then reduced to a level histogram according to their heights. The minimum measurable size of nuclei is restricted by the orifice diameter and by the noise caused inevitably in such systems. In our

Fig. 3   Coulter tube. (All dimensions are in millimeters.)

Fig. 4   Block diagram of Coulter counter system

system, it is about 0.008 mm which is supposed to be the minimum size of effective nuclei.

In the present nuclei measurements without any salt addition, the impedance between electrodes reaches several hundred kΩ. So we must be very careful of the signal treatment as well as of shielding to remove any noise. Figure 5 illustrates the typical nuclei size spectrum of the test water left undisturbed about two hours, and it is indicated that a number of effective nuclei above 0.04 mm are observable.

Instruments of Cavitation Sound Pressure. Here we used the previously reported instruments [8, 9]. A 20 mm diameter PZT probe, of which the receiver is 10 mm in diameter and 0.89 mm in thickness, and with natural frequencies of 2.25 MHz (thickness mode) and 400 kHz (radial mode), was calibrated by a comparative method by using a standard microphone. Since an amplifier was used to compensate the probe frequency response, the overall frequency characteristics of the measuring system was sufficiently flat.

Nomenclature

A = throat cross-sectional area, mm²
C = discharge coefficient
C_d = discharge coefficient at desinent condition
D = pipe inner diameter, mm
d = orifice diameter, mm
f = frequency, kHz
l = orifice length, mm
p_1, p_2 = upstream and downstream pressure, kPa

p_v = vapor pressure, kPa
P_{sm} = cavitation sound pressure, Pa
Q = flow rate, m³/s
$R_{e,D}$ = upstream Reynolds number
$R_{e,d}$ = orifice Reynolds number
t_w = water temperature, K
v_1, v_t = upstream velocity and mean throat velocity, m/s

α/α_s = air content ratio of the water
β = diameter ratio
ν = kinematic viscosity, m²/s
ρ = density, kg/m³
ρ_o = resistivity of water, Ω·m
σ = cavitation number
σ_d = desinent cavitation number

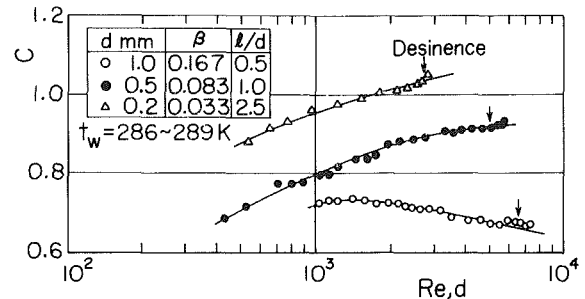**Fig. 5 Typical nuclei size spectrum of test water (uncertainty ±5 percent)**

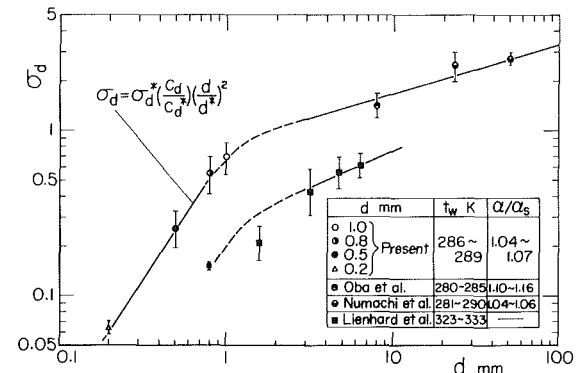**Fig. 6 Discharge coefficients of test orifices (uncertainty ±2 percent)**

Fig. 7 Desinent cavitation number σ_d versus orifice diameter d. (The symbol I indicates the uncertainty band for σ_d.)

In order to remove the statistical error as shown later, the cavitation sound pressures were once recorded on the data recorder, which is flat in frequency characteristics over a range from 0.2 to 100 kHz, and then they were analyzed by a frequency analyzer with a uniform bandwidth of 10 Hz.

Experimental Procedures

In each run, the fresh tap water was first poured into the upper tank. After two hours, when the cavitation nuclei were expected to be stabilized, the nuclei distribution was measured by means of the Coulter counter, to check whether the distribution fitted the prescribed one. Then, each run was started, after lowering the downstream pressure (p_2) by a vacuum pump until the prescribed state of cavitation was attained. In such experiments, therefore, mechanical vibration and acoustic noise were negligibly small. Here the resonant frequency was estimated in the test section to be about 12 Hz through the Lissajous's figures.

Since cavitation is essentially a stochastic phenomenon, as is well known, the corresponding experimental data should be sampled from the same population. In the present experiments, therefore, flow conditions, cavitation sound pressures, and cavitation photographs were simultaneously recorded and then analyzed statistically.

Cavitation inception has been scatteringly determined to be greatly dependent on the method of detection. In our experiments, the cavitation inception was detected in the desinent state both visually under a high intensity stroboscopic light and acoustically with the PZT probe. The acoustic detection was so selected that the cavitation sound pressures were only just detected within a 0.3 ms interval almost comparable to the usual frame interval of high speed movies.

The cavitation number (σ) and the discharge coefficient (C) are defined by the state of downstream where cavitation develops and by the pressure difference ($p_1 - p_2$) respectively, as follows:

$$\sigma = 2(p_2 - p_v)/\rho v_t^2,$$
$$C = Q/A\sqrt{2(p_2 - p_1)/\rho}$$

where v_t, ρ, p_v, A, and Q are the mean throat velocity, the

density of water, the vapor pressure of water, the throat cross-sectional area, and the flow rate (which is measured by a flow meter at a 1200 mm upstream position from the orifice), respectively.

The ranges of test conditions are $420 \sim 7300$ for the orifice Reynolds number ($R_{e,d} = v_t d/\nu$), $96 \sim 113$ kPa for the upstream pressure (p_1), $286 \sim 289$ K for the water temperature (t_w), and $1.04 \sim 1.07$ for the air content ratio of water (α/α_s) where α and α_s are the total and the saturated air content reduced to the normal condition (273.15 K, 101.3 kPa), respectively. Also, the upstream flow is considered to be perfectly laminar, because the upstream Reynolds number $R_{e,D} = v_1 D/\nu$ is 150 at most and partly because vibrations in the flow system are sufficiently eliminated, as mentioned above.

Results

In order to specify the flow conditions, the discharge coefficients C, which are an important factor for such flows, are shown in Fig. 6 for the Reynolds numbers $R_{e,d}$ and for various diameters d. As can be expected, the curves exhibit such typical characters of long orifices [10] as C increases with a decrease in d as well as in β. It is also indicated that in the present experiments the cavitation initiates in the laminar and/or the transitional region in the cases $d = 0.2$ mm and 0.5 mm, while in the near turbulent region for $d = 1.0$ mm.

Desinent Cavitation Number. How does the cavitation occur when the principal flow region is extremely limited by the orifice diameter d? In Fig. 7, the desinent cavitation number (σ_d) is shown for various d. It should be noted that σ_d determined acoustically and visually was scattered within the upper and the lower half of the uncertainty band, respectively. Here it is clearly seen that σ_d decreases rapidly and exponentially with decreasing d, up to one hundredth in magnitude, even in the present experimental range of 0.2 mm $\leq d \leq 1.0$ mm.

In general, the role of nuclei, vortex and turbulence effects should be considered as the factors of the marked diameter effects upon σ_d. The effect of vortex on σ_d has been evaluated
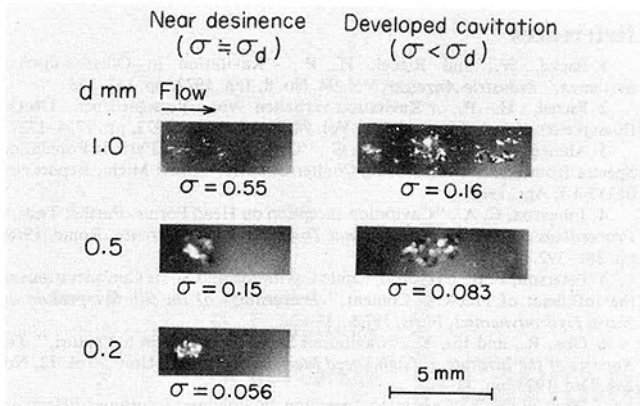
Fig. 8 Cavitation patterns (high speed photograph, exposure time 3µs)

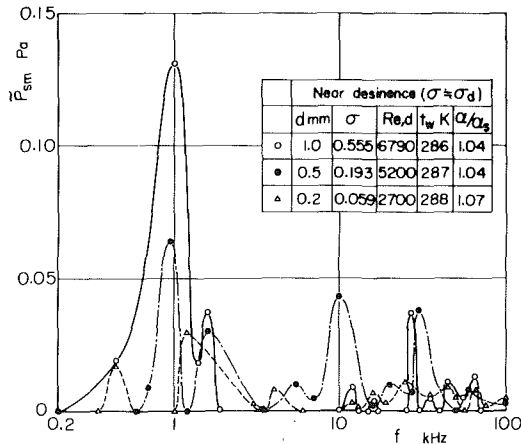| Near desinence ($\sigma \doteq \sigma_d$)				
d mm	σ	Re,d	t_w K	α/α_s
o 1.0	0.555	6790	286	1.04
• 0.5	0.193	5200	287	1.04
▵ 0.2	0.059	2700	288	1.07

Fig. 9 Spectra of cavitation sound pressures for the case of near desinence. (Uncertainties for $\tilde{P}_{sm}$ and f are ±10 and ±1 percent, respectively.)

Developed cavitation ($\sigma < \sigma_d$)				
d mm	σ	Re,d	t_w K	α/α_s
o 1.0	0.160	7290	286	1.04
• 0.5	0.083	5540	287	1.04

Fig. 10 Spectra of cavitation sound pressures for the case of developed cavitation

to be 50 percent at most [11], and the turbulence must be negligibly small in the present experiments. It is, therefore, concluded that the supply rate of nuclei plays a very important role in such rapid decrease in σ_d.

One would expect as the supply rate of nuclei decreases that σ_d should decrease. Furthermore, the nuclei supply rate is approximately proportional to the flow rate ($C_d d^2$) assuming that the nuclei are distributed homogeneously in time and in space. Thus if one assumes a linear relation then

$$\sigma_d = \sigma_d^* (C_d/C_d^*) (d/d^*)^2,$$

where the asterisk designates the reference state and C_d is the discharge coefficient at the corresponding desinent conditions. The present experiments for the micro-orifices can be said to fit to this relation, as indicated in Fig. 7. Here it is also confirmed that the cavitation hardly occurs in such micro-orifices applied to the Coulter counter.

Expectedly, the present data are smoothly connected with the larger diameter counterparts [8, 12] obtained in the natural tap water with the nearly same air content, while they significantly differ from the data [13] obtained in highly pressurized water at a high temperature where very few nuclei are present.

Next we shall examine the scale effects[1]. The result shown in Fig. 7 can be also interpreted as σ_d rapidly decreases with decreasing Reynolds number ($R_{e,d}$) in the range from the laminar region to the transitional one (thus considerable scale effects can be seen here). Therefore, further studies on such effects are absolutely needed in the near future. And it should be noted here that a factor (l/d) scarcely affects the inception within the present range of $0.5 < l/d < 2.5$ [14].

---

[1] Comparatively small changes in σ_d were observed in the well-developed region of $R_{e,d} > 10^4$, where most of the existing experiments were carried out.
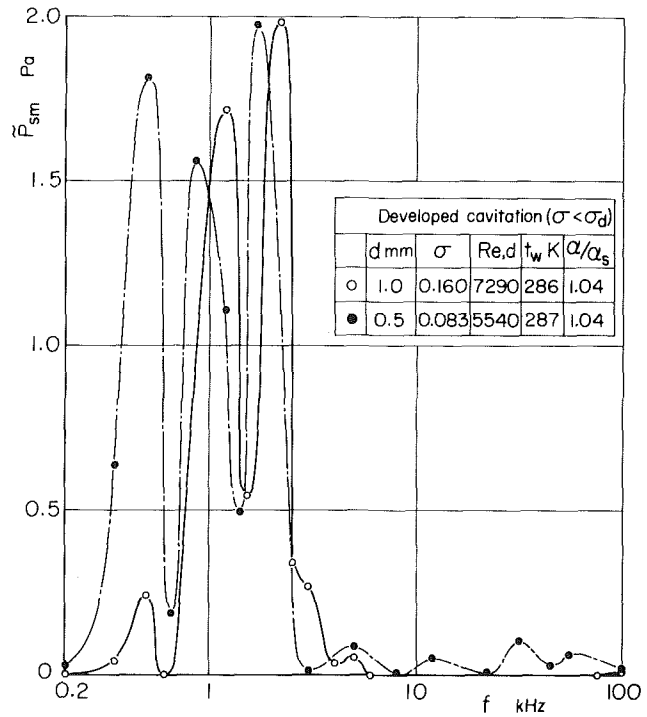
Cavitation Patterns. The cavitation patterns for the entire range from inception to developed state were photographed with a xenon flash lamp, whose exposure time was 3×10^{-6} s, as shown in Fig. 8. For the near turbulent case of $d = 1.0$ mm, nonspherical, rather small, bubbles mainly appear so as to spread widely downstream from the orifice, which seems to be similar in nature to that already observed in the fully turbulent flows through larger orifices [8], but are somewhat different in appearance. For the laminar and/or the transitional case of $d = 0.2$ mm or $d = 0.5$ mm, the appearance is a great contrast to what is observed above, that is, a mass of very fine bubbles, which appears in a period of about 1 kHz, is observed about 2 mm downstream intermittently. When the cavitation developes further, for $d = 1.0$ mm, the massive and the string bubbles increasingly and randomly appear approaching the orifice plate, while, for $d = 0.2$ and 0.5 mm, there is little difference in appearance and the mass of bubbles slightly grows in size and quantity downstream. Here, the considerable decrease in number of cavitation bubbles has also been clearly observed with decreasing the orifice diameter. Therefore, it can be suggested that the cavitation pattern as well as the occurrence region significantly varies with the orifice diameter, as if the nuclei play an important role.

Cavitation Sound Pressure. Here the cavitation sound pressures ($\tilde{P}_{sm}$) are analyzed in order to understand more clearly such cavitation aspects. Figures $9 \sim 10$ are the spectra of $\tilde{P}_{sm}$, measured on the outer wall downstream from the orifices. Of course, since the total energy contained in such flow is extremely small, the values of $\tilde{P}_{sm}$ are much smaller than the larger diameter counterparts, already reported [8]. Corresponding to the aforementioned facts, there appears such a great difference in the spectrum of near desinent state that the low frequency components become overwhelmingly predominant in comparison with the counterparts, as shown in Fig. 9. The spectrum of $\tilde{P}_{sm}$ exhibits a maximum at about 1 kHz, and local maxima at 10 and 30 kHz, respectively. At the well-developed state of cavitation, $\tilde{P}_{sm}$ further increases extremely in the neighborhood of 1 kHz, as shown in Fig. 10,

and especially in the laminar region for $d < 0.5$ mm another peak comes out at about 0.5 kHz.

Conclusion

The behavior of inception was experimentally investigated in low turbulent water flows through micro-orifices which were one to two orders of magnitude greater than the size of the nuclei, under a prescribed nuclei condition as well as various hydrodynamic conditions. The results are summarized as follows:

1 A very rapid decrease in the desinent cavitation number (σ_d) up to one hundredth in magnitude was actually observed in the present experimental range of 0.2 mm $\leqq d \leqq$ 1.0 mm. Being in proportion to the supply rate of nuclei, σ_d can be simply expressed as follows:

$$\sigma_d = \sigma_d^* (C_d / C_d^*) (d/d^*)^2 .$$

It is, therefore, evident that the nuclei play an important role on inception in such an extremely limited flow.

2 In such flows, the cavitation appearance is quite different from that in fully turbulent flows through larger orifices, and the mass of very fine bubbles appears about 2 mm downstream intermittently with a period of about 1 kHz.

3 The weak cavitation sound pressures ($\tilde{P}_{sm}$) whose spectra simply exhibit a maximum peak at about 1 kHz, are also detected within the audio frequency range. These facts may be quite consistent with the flow pattern as well as with the appearance.

4 It can be expected that no cavitation occurs in such micro-orifice as is installed in the Coulter counter.

Acknowledgments

The authors express their appreciation to Mr. J. Higuchi for his help in preparing the manuscript.

References

1 Backé, W., and Riedel, H. P., "Kavitation in Ölhydraulischen Systemen," *Industrie-Anzeiger*, Vol. 94, No. 8, Jan. 1972, pp. 153–158.

2 Riedel, H. P., "Kavitationsverhalten von Verschiedenen Druck-flüssigkeiten," *Industrie-Anzeiger*, Vol. 94, No. 71, Aug. 1972, pp. 1724–1727.

3 Ahmed, O., and Hammitt, F. G., "Determination of Particle Population Spectra from Water Tunnel Using Coulter Counter," Univ. Mich., Report No. 01357-4-I, Apr. 1969.

4 Johnsson, C. A., "Cavitation Inception on Head Forms. Further Tests," *Proceedings of the 12th International Towing Tank Conference*, Rome, 1969, pp. 381–392.

5 Peterson, F. B., "Hydrodynamic Cavitation and Some Considerations of the Influence of Free-Gas Content," *Proceedings of the 9th Symposium on Naval Hydrodynamics*, Paris, 1972.

6 Oba, R., and Ito, Y., "Cavitation Shock Pressures in a Venturi," *The Reports of the Institute of High Speed Mechanics*, Tohoku Univ., Vol. 32, No. 284, Dec. 1975, pp. 33–49.

7 Hoyt, J. W., "Cavitation Inception in Polymer Solutions. Effects of Polymers on Surface Tension, Dissolved Air, and Nuclei Count," *Proceedings of the 14th International Towing Tank Conference*, Ottawa, 1975, pp. 254–258.

8 Oba, R., Ito, Y., and Uranishi, K., "Effect of Polymer Additives on Cavitation Development and Noise in Water Flow Through an Orifice," ASME JOURNAL OF FLUIDS ENGINEERING, Vol. 100, No. 4, Dec. 1978, pp. 493–499.

9 Oba, R., Ito, Y., Kim, K. T., and Higuchi, J., "Velocity Dependence of Cavitation Shock Pressures in a Hydraulic Turbomachinery," *The Reports of the Institute of High Speed Mechanics*, Tohoku Univ., Vol. 39, No. 315, Feb. 1979, pp. 1–18.

10 Pearce, I. D., and Lichtarowicz, A., "Discharge Performance of Long Orifices with Cavitating Flow," *Proceedings of the 2nd Fluid Power Symposium*, Guildford, Paper D2, 1971, pp. 13–53.

11 Arndt, R. E. A., "Semiempirical Analysis of Cavitation in the Wake of a Sharp-Edged Disk," ASME JOURNAL OF FLUIDS ENGINEERING, Vol. 98, No. 3, Sept. 1976, pp. 560–562.

12 Numachi, F., Yamabe, M., and Oba, R., "Cavitation Effect on the Discharge Coefficient of the Sharp-Edged Orifice Plate," ASME JOURNAL OF BASIC ENGINEERING, Vol. 82, No. 1, Mar. 1960, pp. 1–11.

13 Lienhard, J. H., and Goss, C. D., "Influences of Size and Configuration on Cavitation in Submerged Orifice Flows," ASME Paper, 71-FE-39, 1971.

14 Backe, W., and Benning, P., "Uber Kavitationserscheinungen in Querschnittsverengungen von Olhydraulischen Systemen," *Industrie-Anzeiger*, Vol. 84, No. 63, Aug. 1962, pp. 1563–1571.

P. J. McNulty

I. S. Pearsall

National Engineering Laboratory,
East Kilbride, Scotland

Cavitation Inception in Pumps

Introduction

The principal effects of cavitation in pumps are loss of performance and erosion of the blading or casing. Up to now the criteria of assessment of cavitation have been in loss of performance and, to a lesser extent, erosion. The critical cavitation coefficient has been taken as the point where head (or efficiency) drops by 3 percent (sometimes 1 or 10 percent). This has been accompanied by the belief that if the performance was not affected, no cavitation occurred, and indeed where the head first started to drop was the point of cavitation inception. With the development of improved visual and acoustic detection devices, we know now that this is not true, and that incipient cavitation may exist long before the performance is affected. Cavitation numbers of between five and fifteen times the critical performance value are common. It appears also that cavitation erosion damage is most likely in this operating region between inception and performance breakdown. Evidence is available of the likely conditions for greatest risk, but no quantitative figures can yet be put on the values.

In the research program at NEL the cavitation and noise characteristics of typical centrifugal pumps have been measured. Additionally the critical assessment of inception has been made and compared with experimental results. An attempt has also been made to distinguish between cavitation noise and other noise sources with a view to using noise techniques to identify cavitation in a pump. Finally, hydraulic and cavitation noise tests were run on a series of geometrically similar pumps of different size at a number of speeds and flows.

Instrumentation

Noise measurements on a series of pumps of different sizes running at various speeds were made using miniature piezoelectric pressure transducers, a magnetic tape recorder, and a real-time analyzer, linked to a data-logging system, such that noise levels could be collected in digital form on paper tape. Figure 1 is a diagrammatic layout of the instrumentation system.

The transducers used were of the piezoelectric type with a nominal sensitivity of 15.8 pC/atm and a resonant frequency of 130 kHz. They were mounted in a 14 mm p.t.f.e. adapter, which was mounted flush with the inside of the pipe or pump inlet wall. Transducers were installed both at suction and discharge of the pumps under test.

The signal from the transducer was fed through a ½ m
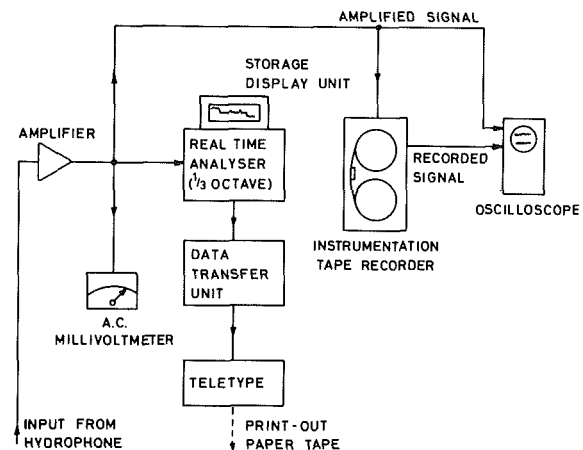
Fig. 1   Noise instrumentation layout

length of low noise cable to a low noise amplifier. A small high pass filter was placed at the amplifier input, to enable frequencies below 6.3 kHz to be rejected when required, thus allowing the remaining high frequency end of the spectrum to be further amplified without overloading the amplifier. The amplified signals from the transducers were fed directly to a magnetic tape recorder, operating at a speed of 30 in./s (760 mm/s) with 7-channel recording capability on ½-in. (13 mm) wide tape. Signals were recorded both in f.m. and a.m. modes for each transducer, thus providing recorded data from d-c to 150 kHz. Noise data could be reproduced from this system with very good repeatability and with an accuracy of ± 1 dB.

Each transducer could be linked (through a switch unit) to a 45-channel real-time analyzer. The analyzer covered the range 12.5 Hz to 160 kHz in ⅓-octave band filters. The digital output of the analyzer was fed through a data transfer unit to a printer, which provided a printout of the transducer signal, analyzed into each band, together with punched paper tape. The noise spectrum could be monitored visually on a display unit connected to the analyzer. Recorded and original signals were also monitored on a double beam oscilloscope and r.m.s. voltmeter.

Visual inception and cavity studies have been made using Perspex (Plexiglas) inlet sections or windows. Special sections were built allowing undisturbed views of the impeller, by ensuring that the Perspex/air interface is perpendicular to the line of sight; the Perspex/water interface is less important as the refractive indices are similar. Lighting is very important as misleading results can be obtained because of time effects. Stroboscopic lighting pulsed at once a revolution or at blade frequency gives a fairly good measurement; however, this will only show up cavities that are large enough or stable enough

to appear to be continuous at these frequencies. It will not show up transient cavities. It is better, therefore, to back up visual inspection by photographic records, either microsecond exposure single shots or high-speed films. In either case, it is preferable to photograph the same blades by a phasing system.

Many of the pumps reported on here were tested in the NEL high-power test house. Figure 2 shows a line diagram of this test circuit. Three possible test loops are available.

a) A closed circuit in which the pump draws water from the suction tank and discharges back to the tank through an electromagnetic flowmeter. In this case, the suction pressure at the pump can be altered by varying the suction tank pressure by means of a vacuum pump or a pressurizing pump connected to the tank.

b) This again is a closed circuit but does not include the suction tank. The pump discharges through the distribution manifold and returns to the pump inlet. The inlet pressure can be controlled by varying the pressure in the loop by means of the pressurizing pump which can be connected to either the inlet or discharge side of the loop.

c) In the third circuit, water can be drawn from the main sump by either one or both service pumps and its pressure increased, if necessary, by a third pump (booster pump) and then supplied to the test pump inlet. The test pump discharges through the manifold back to the main sump.

The flowrate was measured by an electromagnetic flowmeter which was calibrated against a weigh bridge method of flow measurement, before the tests and rechecked at intervals thereafter. Accuracy of flow measurement was 0.4 percent.

Inlet and discharge pressures were measured using pressure transducers of the unbonded strain gage type with an accuracy of 0.25 percent.

Temperature readings were taken using a resistance thermometer placed downstream of the discharge pressure transducer. Temperature was measured to an accuracy of 0.1 percent.

Some pumps were driven by a variable speed electric dynamometer, while others were driven by a variable speed d-c motor. Using a speed control unit the desired pump speed could be selected, and then maintained very accurately throughout the test, a phonic wheel being used to sense the test speed. Torque was measured using a torque tube with an accuracy of 0.2 percent.

Cavitation Inception in a Pump

In many of the tests both visual and acoustic inception could be detected. In most cases of blade cavitation, visual and acoustic inception occur at identical cavitation numbers. Occasionally, acoustic inception can occur at higher cavitation numbers, and this is usually associated with
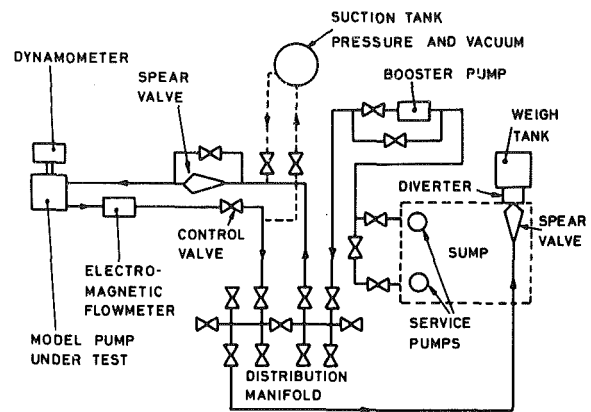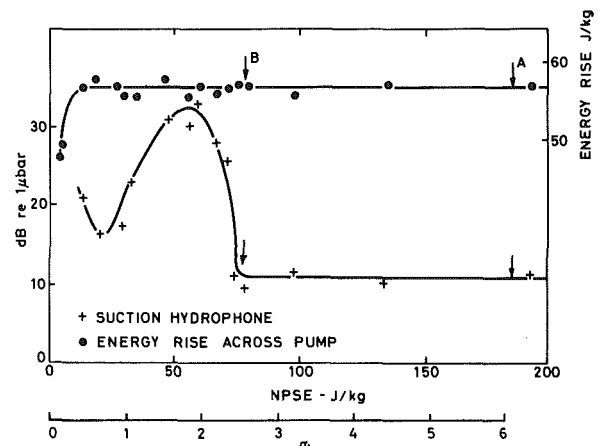

Fig. 2 Pump test circuit

Fig. 3 Typical high frequency noise output as NPSE is varied

cavitation in the wear rings, on the pressure face, or somewhere else in the machine.

Typical noise (at high frequency) and performance characteristics are shown in Fig. 3, for a cavitation test undertaken at a constant flow and speed. The high NPSE (or cavitation coefficient) points relate to the pump's best efficiency at the design point, A. As the suction pressure reduces at point B, cavitation inception occurs, often shown by an intermittent signal. This point corresponds to the visual inception. As the pressure is further reduced, cavitation and noise continue to increase up to a maximum after which, as the cavitation becomes more extensive, the noise drops and rises again until the point where the performance drops. There is strong evidence that the peak noise corresponds to the point where erosion danger is most severe. The reason for the drop

---

Nomenclature

BEP = best efficiency point

Ch = blade chord length, m

f = center frequency of one-third octave band Hz

Ks = suction specific speed

$$\left(\frac{\omega \sqrt{Q}}{\text{NPSE}^{3/4}} \right)$$

NPSE = net positive suction energy at pump inlet, J/kg

Q = volumetric flowrate, m³/s

Re = Reynolds number

$$\left(= \frac{W_i \text{Ch}}{v} \right)$$

St = Strouhal number, ft/U_t

t = impeller flow passage width at outlet tip, m

$U_{t,1}$ = impeller peripheral velocity at inlet tip, m/s

$V_{m,1}$ = meridional velocity at pump inlet, m/s

W_1 = impeller relative velocity at pump inlet, m/s

Y = specific energy (= gH), J/kg

v = kinematic viscosity

σ = cavitation number

$$\left(= \frac{\text{NPSE}}{W_1^2/2} \right)$$

σ_b = blade cavitation number

$$\left(= \sigma - \frac{\phi^2}{1 + \phi^2} \right)$$

ϕ = flow coefficient at inlet $(= V_{m,1}/U_{t,1})$

ω = rotational speed of pump, rad/s

in noise at pressures below the maximum point, appears to be bound up with absorption of sound by the large cavities in this region. The noise characteristic shown is for 40 kHz, but other frequencies show a similar trend. At low frequencies (<1 kHz) mechanical noise, for instance noise from blade and shaft frequencies, is more likely to interfere with the measurements. If background and flow noise are too great, the level noncavitation portion of the graph will be raised and an incorrect inception point measured.

These studies together with visual examinations show that cavitation occurs long before the pump performance is affected. Indeed the common practice of siting it with a factor of safety of 2 or 3 on the performance breakdown may well bring it to the peak of the noise curve where erosion is most likely. Values of breakdown and inception were evaluated for a number of centrifugal pumps of various types. These are compared in Table 1 on a basis of suction specific speed ratio or NPSE ratio. Ratios of between 3 and 20 have been noted for typical commercial pumps. The better-designed pumps corresponding to the lower ratios are nearer the theoretically attainable ratio. However, many commercial pumps have higher blade angles than the optimum, usually either to make the impellers easier to cast or improve the performance aspects. These cases include the pumps where cavitation performance is a secondary consideration. The high or low ratios are also often not related to the absolute performance in terms of cavitation breakdown performance. For performance breakdown, a critical figure of $K_s = 2.9$ (7200) is the average value quoted by the Hydraulic Institute, although 3.6 or even 4.8 (12,000) are possible. Values in parenthesis are in units of r/min, Imp. gal/min and ft/head.

Cavitation inception point is also affected by flowrate. As the flow is reduced, incidence increases and so σ_b would be expected to increase. Recirculation in the suction can however affect the local incidence and modify theoretical predictions. Figure 4 shows the characteristic much as would be expected. At the design point the minimum σ_b occurs with optimum blade incidence; increased σ_b occurs at lower flows (increased incidence) and again at higher flows as the incidence becomes negative and pressure side cavitation occurs. If the design point incidence is higher than optimum for performance reasons, the curve will be displaced to the right. Most commercial pumps are in this category, as shown in Fig. 5, which shows the relative values of σ_b to the best efficiency flow value for most of the pumps tested.

Cavitation Noise in the Pump

One of the original objectives of the work was to develop a technique for determining whether cavitation was occurring in the pump and its severity without visual examination or undertaking a performance test. As has been shown in Fig. 3 this has been achieved where it is possible to perform a cavitation test by varying NPSE. In field or plant tests this is rarely possible and the levels and spectra of cavitation noise have been studied to attempt to separate it. Firstly, it is necessary to identify the noncavitating pump noise. Correlation of total noise against specific speed allows the overall noise to be determined [1, 2]. Figure 6 shows measurements of the pump noise spectra, relative to total noise, we have measured on the pumps listed in Table 1. These are for noncavitating conditions corresponding to the flat portion of Fig. 3. Both amplitude and frequency have been multiplied by the ratio of tip width to tip speed and corrected for flowrate relative to design condition. The slope of the limiting curve shown for the right-hand side of the graph is −6 dB/octave spectral density.

When cavitation occurs, the high frequency noise increases above this limiting line, Fig. 7, with a mean slope of smaller
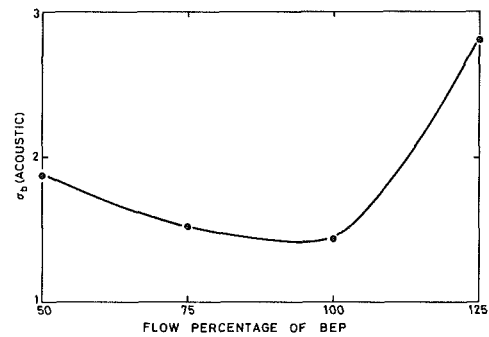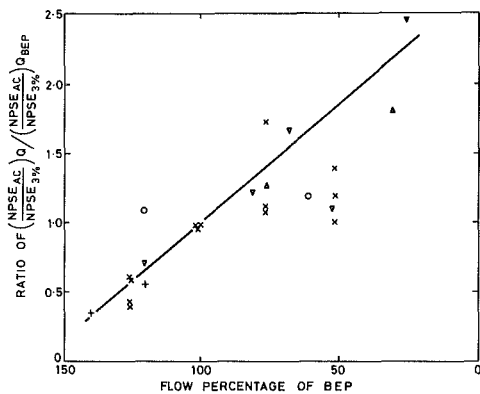

Fig. 4   Effect of flow on acoustic inception

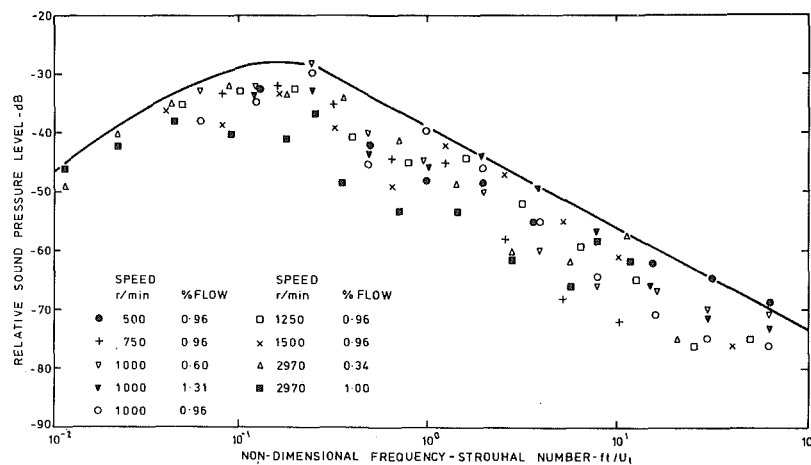Fig. 5   Acoustic inception ratio for off design conditions

| SPEED r/min	%FLOW	SPEED r/min	% FLOW
● 500	0·96	□ 1250	0·96
+ 750	0·96	x 1500	0·96
▽ 1000	0·60	△ 2970	0·34
▼ 1000	1·31	■ 2970	1·00
○ 1000	0·96		

Fig. 6   Correlation of noncavitating octave band spectra

Table 1 Comparison of inception and breakdown points for various pumps

Pump type	Specific speed	Flow compared to BEP %	K_s* inception	K_s** breakdown 3%	$\dfrac{K_s \text{ breakdown}}{K_s \text{ inception}}$	$\dfrac{\text{NPSE inception}}{\text{NPSE breakdown (3\%)}}$
Boiler feed pump (diffuser)	0.57 (1440)	100	0.48	3.36	7.0	13.3
Process pump (volute and diffuser)	0.31 (780)	24	0.25	2.0	8.0	16.0
		66	0.54	3.33	6.16	11.3
		100	0.7	2.87	4.1	6.5
		120	0.8	2.5	3.14	4.6
Double entry (volute)	0.96 (2395)	120	0.8	2.1	2.67	3.7
		100	<0.6	2.1	>3.64	>5.6
Centrifugal with diffuser and volute	0.55 (1372)	100	0.8	2.67	3.34	5.0
		75	0.6	2.41	4.02	6.4
Cooling water pump 1/5 model	1.35 (3370)	100	0.83	3.38	4.07	6.5
		75	0.60	3.69	6.16	11.3
		50	0.65	3.40	5.24	9.1
Cooling water pump 1/8 model	1.35 (3370)	125	1.07	2.45	2.28	3.0
		100	0.99	4.09	4.12	6.6
		75	0.78	3.44	4.40	7.2
		50	0.55	2.63	4.76	8.0
Cooling water pump 1/12 model	1.35 (3370)	125	0.72	1.60	2.22	2.9
		100	0.75	3.25	4.30	7.0
		75	0.99	4.66	4.71	7.9
		50	0.876	3.81	4.35	7.1
Volute pump	1.0 (2495)	120	1.21	2.47	2.05	2.6
		100	0.83	1.65	1.99	2.5
		60	0.76	1.74	2.28	3.0

*Uncertainty in K_s (inception ± 0.01; **Uncertainty in K_s (breakdown) ± 0.04
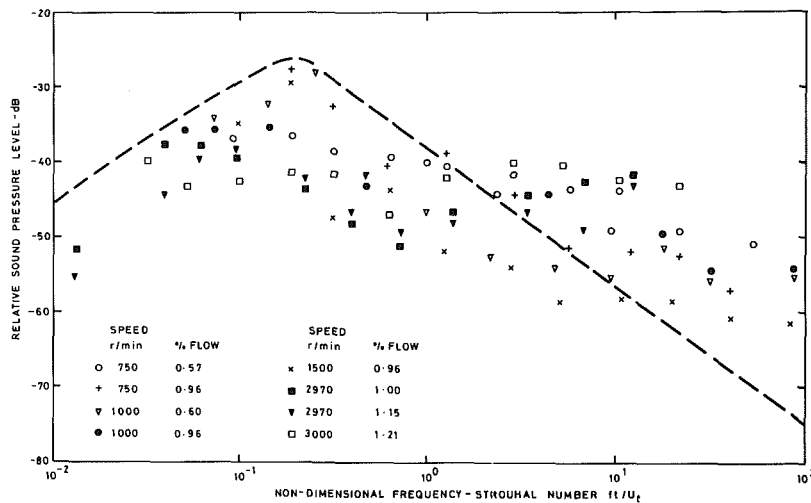
Fig. 7 Effect of cavitation on nondimensional spectra

gradient. Although this correlation seems promising, it is not completely reliable as another phenomenon capable of generating high frequency noise (such as clearance flows) could give misleading results. Also it does not distinguish between a well designed quiet pump and a badly designed noisy pump. Furthermore, it does not distinguish the source of cavitation noise, which could be, for instance, in the wear rings or in the diffuser blades. The technique does, however, provide a possible method for detecting cavitation.

Scale Effects on Cavitation Inception and Breakdown

Speed and size scale effects are of interest for scaling from models to prototype. It is usually only possible to perform extensive cavitation tests for performance and inception in the laboratory because of the facilities required. These results have then to be translated into prototype size and speeds. These effects have been investigated on three geometrically similar model centrifugal cooling water pumps. The pumps were 1/12, 1/8 and 1/5 models of the prototype, equivalent to

eye diameters of 200, 300 and 500 mm (8, 12 and 20 in.). Each pump was tested at four speeds (60, 75, 100 and 112 per cent) and four flows corresponding to 50, 75, 100 and 125 percent of design flow. The largest pump could not be tested at 125 percent flow as the NPSH available was insufficient. The pumps were tested over the range from cavitation inception to performance breakdown. The rig used is shown in Fig. 2.

The results are shown in Fig. 8 on the basis of blade cavitation number against Reynolds number for three pumps, four speeds and individual flows. The regression fit line is shown for each case and the indices of these lines are shown in Fig. 9 for both inception and performance breakdown. The results have been corrected for slight geometric differences between the impeller blades on the different pumps, on a basis of incidence where necessary. The different trends of the 125 percent flow from the others can be explained in that the incidence angle is negative (-1 deg) and pressure side cavitation is probably occurring.

## Table 2 Performance of original and new impeller

Impeller	Acoustic inception		Visual inception		Performance breakdown	
	NPSE J/kg	K_s	NPSE J/kg	K_s	NPSE J/kg	K_s
Original	105 ±1	0.83±0.01			26±0.5	2.48±0.04
New (design)	22.5±0.5	2.77±0.05	22.5±1	2.77±0.05	12.6±0.5	4.27±0.13
New (test)	110±1	0.84±0.01	34.3±1	2.02±0.02	13.7±0.5	4.01±0.11

Table 3 Uncertainty estimates for the figures

Fig. 3	Ordinate ± 1 dB	Abscissa ± 1 J/Kg
Fig. 4	Ordinate ± 4.5 percent	Abscissa ± 0.5 percent
Fig. 5	Ordinate ± 1.8 percent	Abscissa ± 0.5 percent
Figs. 6 & 7	Ordinate ± 2 dB	Abscissa ± 0.15 percent
Fig. 8	Ordinate ± 4.5 percent (acoustic)	Abscissa ± 0.25 percent
	Ordinate ± 1.7 percent (3 percent loss)	

Fig. 9

$$
\left.
\begin{array}{l}
\pm\ 0.24\ (125\ \text{percent flow}) \\
\pm\ 0.12\ (100\ \text{percent flow}) \\
\pm\ 0.20\ (75\ \text{percent flow}) \\
\pm\ 0.14\ (50\ \text{percent flow})
\end{array}
\right\} \text{acoustic}
$$

Abscissa ± 0.5 percent

$$
\left.
\begin{array}{l}
\pm\ 0.17\ (125\ \text{percent flow}) \\
\pm\ 0.14\ (100\ \text{percent flow}) \\
\pm\ 0.22\ (75\ \text{percent flow}) \\
\pm\ 0.10\ (50\ \text{percent flow})
\end{array}
\right\}
\begin{array}{l}
3\ \text{percent} \\
\text{head loss}
\end{array}
$$
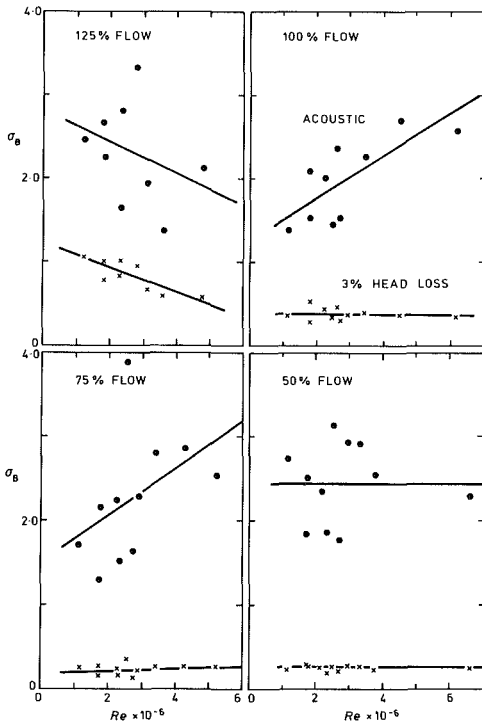
Fig. 8 Variation of inception with Reynolds number
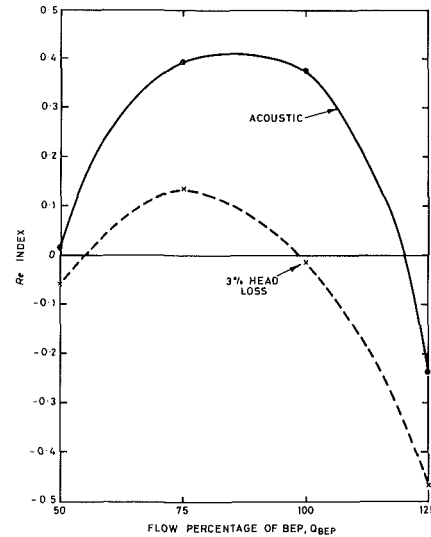
Fig. 9 Effect of flow on Reynolds number index

Theoretical Design and Evaluation

A commercial pump may have blade angles greater than optimum, and hence its inception point higher than theoretically possible. For instance, the cooling water pumps tested for the scale effect study have inception cavitation numbers between 1.4 and 2.5 (and breakdown 0.14). Theory would suggest values much lower than this, for instance a NACA 65 series symmetrical section can have an inception cavitation number as low as 0.25 and possible breakdown values of 0.08, at incidences of 3 or 5 deg. As part of a study of pumps with improved cavitation inception performance for breeder reactors, an attempt was made to produce a pump with low values as the theory suggested. The pump chosen was a centrifugal volute pump with a specific speed of 1. The new impeller was designed with a NACA 65 section blade with incidence of 3 deg corresponding to minimum cavitation

inception. The inlet diameter was optimized to give minimum NPSE or maximum suction specific speed for inception. The inlet blade angle was constant at 28 deg across the annulus.

Table 2 shows a comparison of performance for the original impeller and the new impeller. It can be seen that, although the breakdown point achieved was near the design, there was considerable difference between the test acoustic inception point and the design. Visual examination with the help of photographs gave an inception value much nearer the design. The inference was therefore that cavitation was occuring other than on the suction side of the blade that could be seen, and was occurring either on the pressure face or in the wear ring clearances.

Measurements of blade shape showed minor divergences from the design blade. Dressing of these to the correct shape did not improve matters and this has not been resolved at the time of writing.

It appears therefore that impellers designed to have a very good cavitation performance are much more sensitive to minor geometric variations or other factors causing cavitation in the pump.

Conclusions

Noise measurements particularly at high frequency (>4 kHz) are a reliable indication of whether cavitation is occurring in the pump. Provided background levels are sufficiently low, it can show the inception point and where performance breaks down. Values for typical pump show that cavitation is occurring at much higher NPSE than has often been supposed.

Scaling laws on speed and size follow substantially the dimensional similarity relationships. There seems to be little Reynolds number effect on performance breakdown, but a definite increase of σ_b with Reynolds number for cavitation inception.

Attempts to produce a pump impeller with much improved cavitation inception performance in accordance with theoretical predictions were not wholly successful, due it is thought, to cavitation occurring elsewhere in the pump.

Acknowledgments

References

1 Simpson, H. C., Magaskill, R., and Clark, T. A., "Generation of Hydraulic Noise in Centrifugal Pumps," *Symp. on Vibrations in Hydraulic Pumps and Turbines, Proc. Instruction of Mechanical Engineers*, Vol. 181, Part 3A, 1966-1967, pp. 84–108.

2 Deeprose, W. M., "Correlation of Pump Fluid-Borne Noise Data," Inst. of Acoustics Mtg. on Acoustics for Pumps, Paper 3, Risley, Warrington, UKAEA and NEL, April 18, 1978.

3 Pearsall, I. S., and McNulty, P. J., "Comparisons of Cavitation Noise with Erosion," *Cavitation Forum*, American Society of Mechanical Engineers, New York, 1968, pp. 6–7.

4 Numachi, F., "Ultrasonic Shock Waves Emitted by Cavitation," *Proc. 13th Congr. IAHR*, Kyoto, 1969, Vol. 5-3, pp. 85–117.

5 Yarga, J. J., and Sebestyen, Gy., "Noise Measuring as a Complementary and Checking Method for Pump Testing," Part 1, *IAHR Symposium*, Stockholm 1970, Trans., Paper 13.

6 Oba, R., Ito, Y., and Uranishi, K., "Effect of Polymer Additives in Cavitation Development and Noise in Water Flow Through an Orifice," ASME JOURNAL OF FLUIDS ENGINEERING, Vol. 100, No. 4, 1978, pp. 493–499.

7 Johnsson, C. A., "On Calculation of Pressure Fluctuation Around Propellers," *Proc. 12th Int. Towing Tank Conf.*, Rome, 1969, pp. 381–382.

Some Experiments With Specific Types of Cavitation on Ship Propellers

G. Kuiper

Research Engineer,
Netherlands Ship Model Basin,
Wageningen, The Netherlands

The influence of the boundary layer and of the nuclei content of the fluid on cavitation inception is investigated. Two models of ship propellers, displaying sheet cavitation and bubble cavitation respectively, are used. Generation of additional nuclei is obtained by electrolysis. It is shown that nuclei are necessary to create sheet cavitation when the laminar boundary layer separates. When the boundary layer is laminar, however, the absence of sheet cavitation is very persistent and independent of the nuclei content. Application of roughness at the leading edge of the propeller blades generates sheet cavitation independent of the nuclei content. Bubble cavitation is strongly affected by the nuclei content of the water. Roughness at the leading edge can indirectly affect bubble cavitation when nuclei are generated by the roughness elements.

Introduction

The cavitation behavior of ship propellers is generally predicted from model tests using the assumption that the cavity pressure is equal to the vapor pressure, while cavitation inception takes place at the vapor pressure. Especially with respect to the inception pressure on model scale large deviations are possible, however, as was recently demonstrated again by the ITTC Cavitation Committee [1]. In practice the extrapolation of cavitation observations on model scale therefore requires experience with respect to test conditions and interpretation of the observations. This experience is obtained by comparing predictions from model tests with full scale experiences.

The deviations between the inception pressure and the vapor pressure can lead to discrepancies between cavitation observations on model scale and full scale, as was illustrated in a case study [2] which initiated the present test program. After that, three propellers with some specific cavitation problems were investigated [3] and the deviations of the inception pressure from the vapor pressure were related with the state of the boundary layer and with nuclei in the fluid. Electrolysis of the water flowing into the propeller and roughness at the leading edge of the propeller blades were used to bring the inception pressure on model scale closer to the vapor pressure. This concerned mainly sheet cavitation. The behavior of bubble cavitation was still unclear. In the present paper some results are presented of two propellers which are specifically designed to display sheet and bubble cavitation respectively, in order to exhibit more clearly the phenomena observed in [3] with respect to sheet cavitation, and to investigate further the problems encountered with bubble cavitation. In general this paper attempts to relate the knowledge on cavitation inception, which is mainly obtained using headforms and foils, with experiences in propeller cavitation. The aim is to improve the testing technique and the
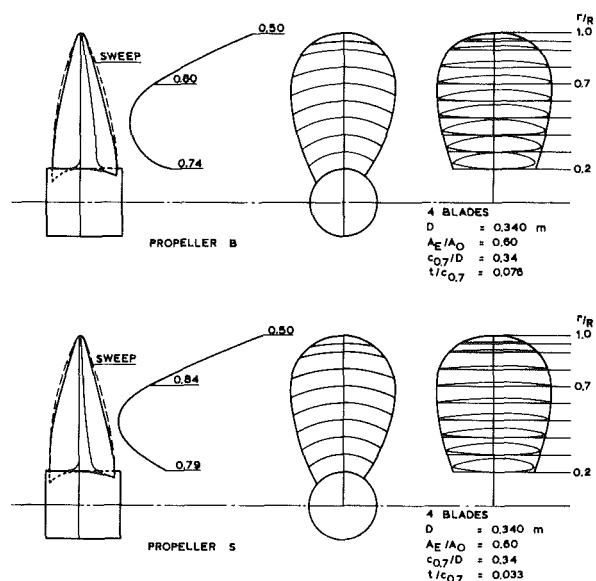
Fig. 1 Geometry of propellers

simulation of full-scale cavitation. This is especially important when phenomena caused or affected by cavitation are measured on model scale, e.g. radiated noise and induced pressure fluctuations.

Description of the Test Arrangement

The test program was carried out in the NSMB Depressurized Towing Tank because of its low nuclei content, which is independent of the test conditions.

To create different types of cavitation two propellers were designed (34 cm dia) which exhibited only one specific type of cavitation in a certain range of loading, viz. sheet cavitation (propeller S) and bubble cavitation (propeller B). The blade contour of both propellers is the same, the differences are in the camber and thickness distributions. The particulars of the two propellers are given in Fig. 1.

The propellers were tested in uniform axial flow. This was accomplished by mounting the propeller on a right angle drive, which was in turn mounted on a twin hull vessel, as shown in Fig. 2. Observation of the cavitating propellers was done by a remotely controlled camera mounted in one of the hulls. These observations do not give a complete picture of the cavity behavior. Only the type and the extent of the cavitation at a number of angular blade positions can be observed.

Electrolysis. To vary the nuclei content of the water, electrolysis was applied. A grid with six sets of 0.3 mm dia wires was mounted 1.6 m in front of the propeller disk as shown in Fig. 2. The lowest wire was at shaft height, so the bubbles only affected the upper half of the propeller plane. A constant current of 0.4 A/m was maintained during electrolysis in all conditions.

The nuclei spectrum generated by the electrolysis wires is unknown. A preliminary measurement with scattered light behind the wires showed that the maximum diameter of the nuclei at a distance of 1.5 m behind the wire was of the order of 50μm. These measurements were done at a low tank pressure (50 mbar). The total volume of gas created by electrolysis is proportional with the tank pressure and the tank pressure will therefore strongly influence the number and probably also the size of the generated nuclei. As an order of magnitude it is plausible that the bubbles generated by the wires are smaller than 100 μm in diameter.

Application of electrolysis might create additional turbulence in the flow, which can affect the boundary layer on the propeller. Some checks were made but no difference in the paint pattern (see next section) with and without wires could be observed. To avoid any confusion all tests were done with the electrolysis wires mounted in front of the propeller, also when no electrolysis was applied.

Boundary Layer Visualizations. The boundary layer on the propellers was visualized using a paint technique as described in reference [3]. The illumination of the fluorescent paint was done with U.V. light, which gave a very detailed picture of the limiting streamlines on the blades. From the direction of the streaks as well as from the thickness, the regions of laminar and turbulent flow could easily be distinguished. The U.V. illumination was created by a normal flash light, which was filtered. Some blue light passed through the filter together with the U.V. light, which is advantageous since it made the propeller blades visible. Complete suppression of the blue light did not improve the quality of the pictures but made orientation on the photographs impossible. Printing in black and white of the red and blue pictures causes some loss of information.

Roughness. To create a fully turbulent boundary layer on the model propeller the leading edge was roughened with 60 μm carborundum. This was done by gluing the carborundum to the foil with very thin varnish over a length of about 1 mm from the leading edge on. The carborundum particles have a very irregular shape, with sharp edges.

Test Conditions

Both propellers were tested at two loadings, corresponding with advance ratios of 0.4 and 0.6, where the advance ratio J is

$$J = \frac{V_A}{nD} \qquad (1)$$

V_A = axial velocity of propeller
n = number of revolutions
D = diameter of propeller

The pressure in the tank p_t was varied and is expressed in the cavitation index based on the rotational tip speed σ_n:
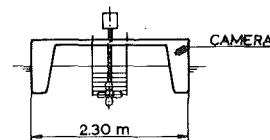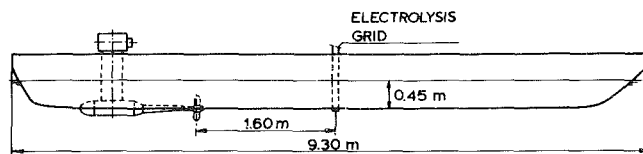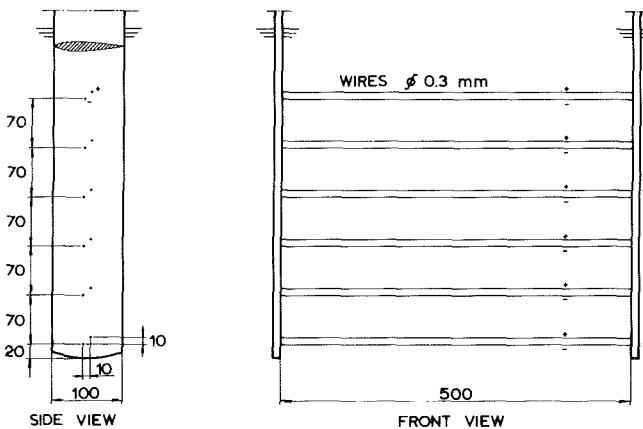

Fig. 2(a)

Fig. 2(b)

Fig. 2 Test equipment and electrolysis grid

$$\sigma_n = \frac{p_t - p_v + \rho g h_s}{\frac{1}{2} n^2 D^2} \qquad (2)$$

where p_t = tank pressure
p_v = vapor pressure
h_s = shaft immersion (always 0.45 m)
ρ = specific mass of water
g = acceleration due to gravity.

The local pressure on the propeller blades p is expressed as

$$C_p = \frac{p - (p_t + \rho g h)}{\frac{1}{2} \rho V^2} \qquad (3)$$

where V is the inflow velocity of the propeller section and h is the immersion of the blade section which depends on the angular blade position; h varies between 0.28 and 0.62 m over the propeller disk.

In order to judge the cavitation danger this pressure coefficient has to be compared with the sectional cavitation index

$$\sigma = \frac{p_t - p_v + \rho g h}{\frac{1}{2} \rho V^2} \qquad (4)$$

Within the limits of attainable pressure and available engine power or maximum carriage speed the propeller revolutions can be varied, thus varying the Reynolds number R_n where

$$R_n = \frac{nD^2}{v} \qquad (5)$$

where v is the kinematic viscosity.

Two values of the Reynolds number were used. The lowest value was about 1×10^6; the highest was about 1.7×10^6. This corresponds with sectional Reynolds numbers at 70 percent of the radius of about 0.84×10^6 and 1.36×10^6, when the sectional Reynolds number is defined as
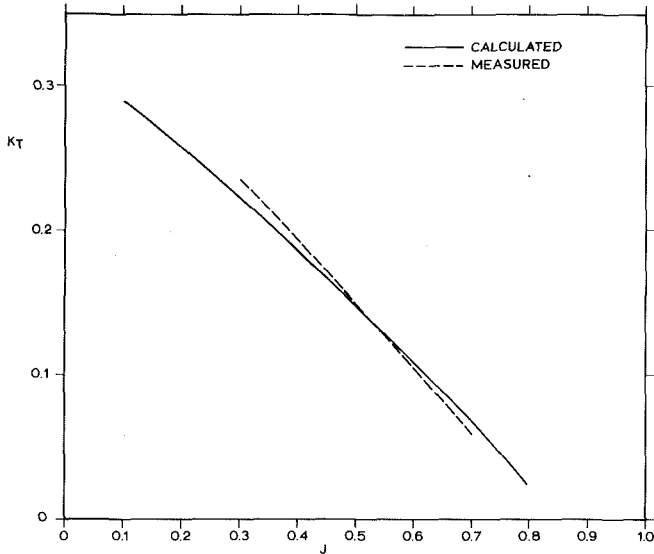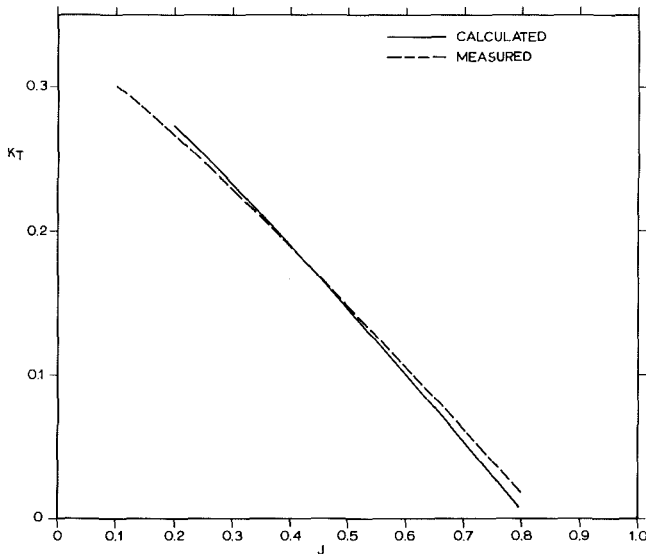
Fig. 3 Thrust coefficients of propeller S

Fig. 4 Thrust coefficient of propeller B

$$Re = \frac{Vc}{v} \qquad (6)$$

in which c is the chord length.

The conditions of the test results are given in dimensionless parameters, from which the test conditions can be derived directly. The temperature of the water in all tests was 10°C.
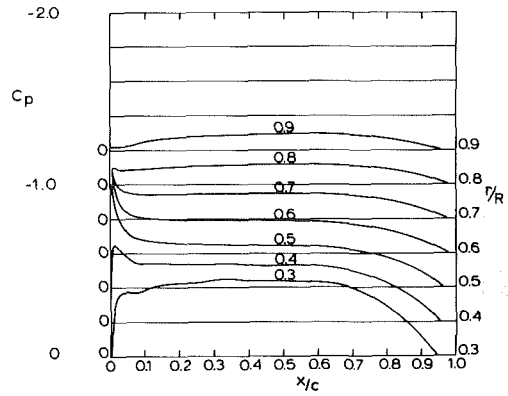
Calculations

For the determination of the inception pressure it is necessary to know the pressure distribution on the propellers. Calculations were made of the distribution of the propeller loading using the lifting surface program as developed by van Gent [5]. The pressure distribution is calculated with a conformal mapping calculation using an effective profile geometry with a camber line derived from the calculated lift distribution and with a geometrical thickness distribution.

A comparison between the calculated and measured thrust coefficients can serve as a check of the potential calculations, because the effect of viscosity on the thrust is small. In Figs. 3 and 4 the calculated thrust coefficients are given and compared with measurements. The agreement between measured and calculated propeller thrust is good. In these calculations an empirical correction, as used by Van Gent [5], was left out.
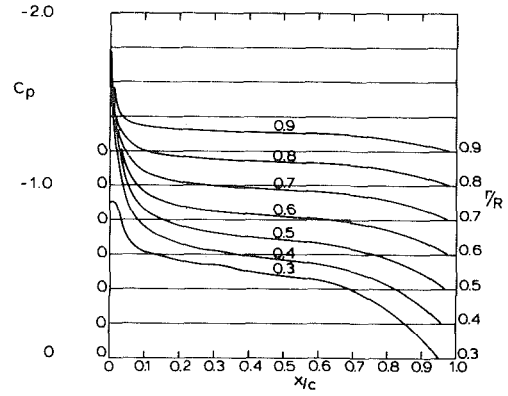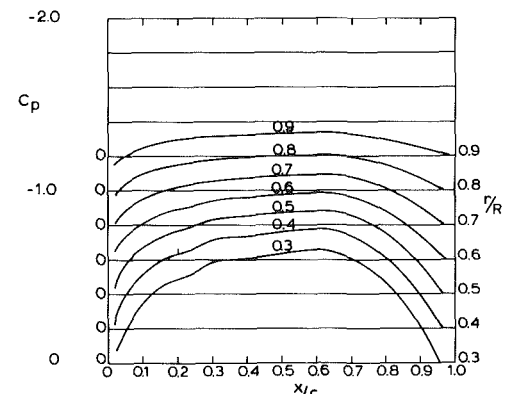

PROPELLER S AT J = 0.4
Fig. 5(a)

PROPELLER S AT J = 0.6
Fig. 5(b)
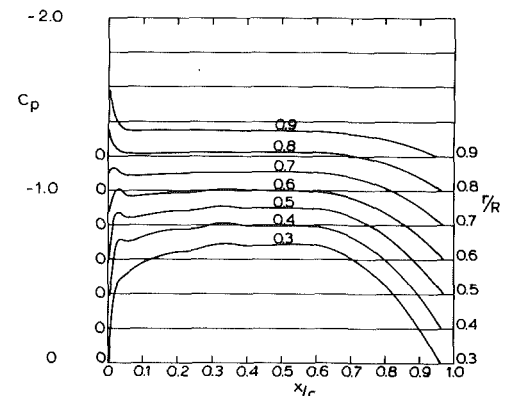
PROPELLER B AT J = 0.4
Fig. 5(c)

PROPELLER B AT J = 0.6
Fig. 5(d)

Fig. 5 Calculated pressure distributions

This empirical correction caused discrepancies between measurements and calculations [4]. The pressure distributions thus calculated are given in Fig. 5. Calculations of the laminar boundary layer using Thwaites' method were made to see if laminar separation would occur at the leading edge. This was only found for propeller S at $J = 0.4$. When no laminar separation was calculated, transition calculations were carried out using the spatial stability charts of Wazzan et al. [6]. These charts were represented by a suitable approximation for use in a computer program. The results were compared with results of boundary layer visualization. This comparison will be discussed in the next section.

Based on these calculations we expect the following conditions on the propeller models:

1 Propeller S at $J = 0.4$: a sharply peaked pressure distribution with laminar boundary layer separation. The type of cavitation will be sheet cavitation.

2 Propeller S at $J = 0.6$: a moderately peaked pressure distribution. The boundary layer remains laminar without separation in the low pressure region. The type of cavitation will be sheet cavitation.

3 Propeller B at $J = 0.6$: a shock-free pressure distribution with mostly laminar boundary layer flow. The type of cavitation will be bubble cavitation.

4 Propeller B at $J = 0.4$: a very flat pressure distribution with a small peak at the leading edge; mostly laminar boundary layer flow. Sheet and bubble cavitation will occur simultaneously.

Boundary Layer Observations

The limiting streamlines on propeller S at $J = 0.4$ are shown in Fig. 6. The separated region near the leading edge is clearly visible and longer in chordwise direction than usual. There is some difference between both smooth blades, which illustrates the sensitivity of the boundary layer for the blade geometry in case of laminar separation. From the calculations, laminar separation was predicted at the leading edge from the hub up to $r/R = 0.82$. The experiments showed a separation region up to $r/R = 0.87$ and 0.73 for blade 4 and 2 respectively. Near the unloaded tip there are some indications on blade 2 that the boundary layer becomes laminar again, as is predicted by the calculations. In this region, however, the radial velocities become important and a two-dimensional boundary layer calculation is no longer sufficient.

The observations of Fig. 6 refer to a Reynolds number of about one million. At a higher Reynolds number of about 1.7 million the laminar separation bubble on blade 2 became shorter in chordwise direction, whereas the radial extent remained nearly unchanged and showed a similar abrupt end. On blade 4 at the higher Reynolds number the separation bubble became too short to be sharply distinguished.

The boundary layer behavior on blade 2 of propeller S at $J = 0.6$ is given in Fig. 7. Laminar separation did not occur which is in agreement with the calculations. From the leading edge until the midchord region the boundary layer is laminar, characterized by the outward direction of the streaks. The change in direction of the streamlines gives the transition region of the boundary layer. This region is somewhat closer to the leading edge for the higher Reynolds number, but turbulent streaks are present at irregular intervals in that case, originating near the leading edge. Those streaks increased in number with increasing Reynolds number and are apparently caused by surface irregularities. This phenomenon can make the transition region disappear and in that case the "smooth" propeller actually is fully roughened.

The boundary layer behavior of propeller B at $J = 0.4$ is shown in Fig. 8. The pressure distribution in this condition is somewhat like that of propeller S at $J = 0.6$, but here the paint
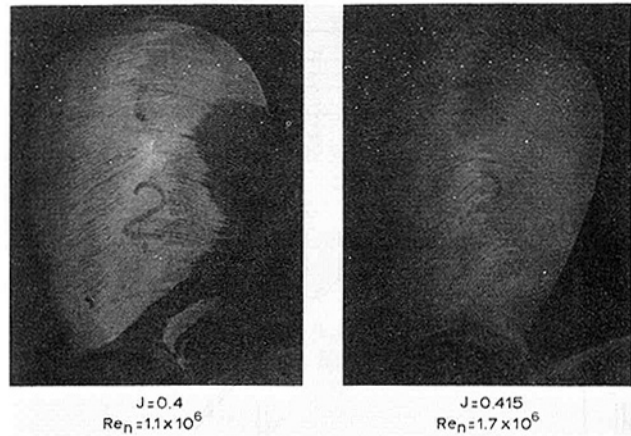

J=0.4
Re$_n$=1.1x10^6

J=0.415
Re$_n$=1.7x10^6

Fig. 6 Boundary layer visualization on propeller S at $J = 0.4$ (Re$_n = 1.1 \times 10^6$)

Re$_n$ = 1.1 x10^6
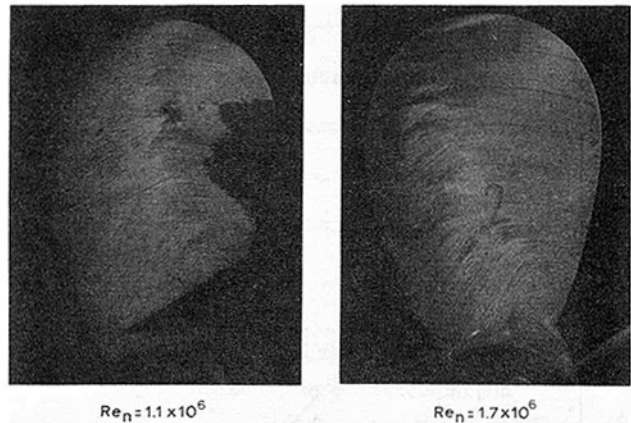
Re$_n$ = 1.7x10^6

Fig. 7 Boundary layer visualization on propeller S at $J = 0.6$
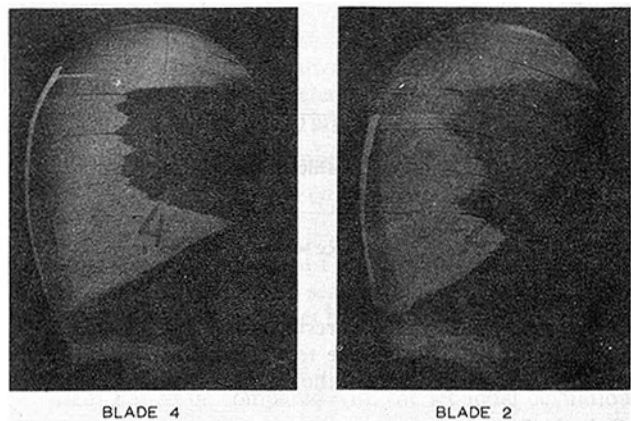

BLADE 4

BLADE 2

Fig. 8 Boundary layer visualization on propeller B at $J = 0.4$

test at a higher Reynolds number did not display turbulent streaks. The adverse pressure gradient in this condition, however, is much smaller than for propeller S, which may result in a more stable boundary layer.

The boundary layer behavior of propeller B at $J = 0.6$ is similar as in Fig. 8. As expected the boundary layer is laminar at the leading edge since there is a favorable pressure gradient up to midchord.

The effect of Reynolds number and of propeller loading on the location of the transition region can be seen from Fig. 8. The effect is moderate and certainly not sufficient to bring the transition region close to the leading edge.

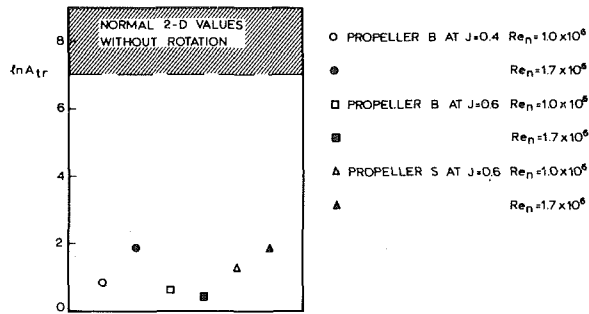Transition calculations were made using the calculated

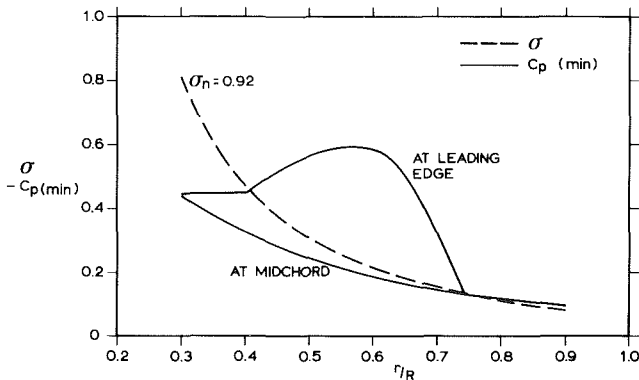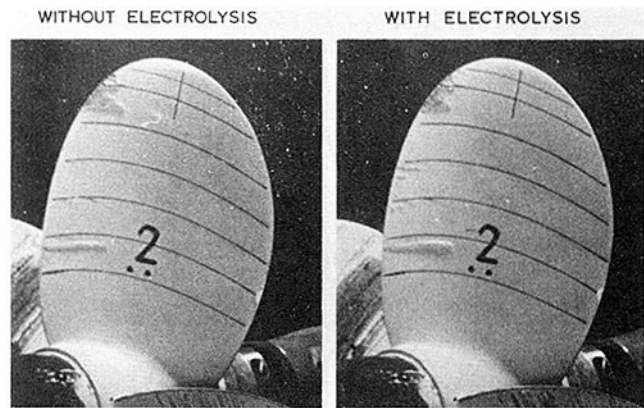Fig. 9 Calculated exponents of amplification rate at observed position of transition ($r/R = 0.7$)

Fig. 10 Radial distribution of calculated minimum pressure coefficients and cavitation indices on propeller S at $J = 0.6$

pressure distributions. The exponent n of the maximum amplification factor e^n in the observed transition region is given in Fig. 9. These exponents are much smaller than the value of 7 to 9 which is normally used as a criterion for transition. Apparently the streamwise instabilities are not the immediate cause of transition. Presumably cross-flow instabilities cause transition on a propeller, as is the case on a rotating disk.

Inception of Sheet Cavitation

Inception of Sheet Cavitation With a Laminar Boundary Layer (Propeller S at $J = 0.6$). The calculated minimum pressure coefficients on propeller S at $J = 0.6$ are given in Fig. 10, together with the radial distribution of the sectional cavitation index σ at a certain tank pressure (expressed as σ_n). When cavitation inception takes place at the vapor pressure, the point where cavitation starts is found from Fig. 10 when $\sigma = -C_p$ (min).

In Fig. 11 propeller S is shown with $\sigma_n = 0.92$. The calculated pressure at the leading edge is far below the vapor pressure (σ is smaller than $-C_p$(min)) and sheet cavitation is calculated to occur from $r/R = 0.40$ to 0.75. At midchord the calculated pressure at $r/R = 0.6$ is close to the vapor pressure, so a fairly large sheet is expected. On the smooth blade, however, no cavitation is visible, except for a few streaks. Electrolysis has no significant effect in this situation, although a few bubbles are visible. The presence of nuclei in the propeller inflow follows from the results in Fig. 16, where a large influence of electrolysis is found in exactly the same condition. So we may conclude that nuclei had no effect. These observations are a clear confirmation of the conclusion of reference [3] that no inception of sheet cavitation occurs when the boundary layer is laminar, and that electrolysis is ineffective in such a case. Application of roughness at the leading edge changes the picture drastically. Sheet cavitation is found in Fig. 11 between $r/R = 0.35$ and 0.9, which is slightly more than calculated. The length of the sheet in
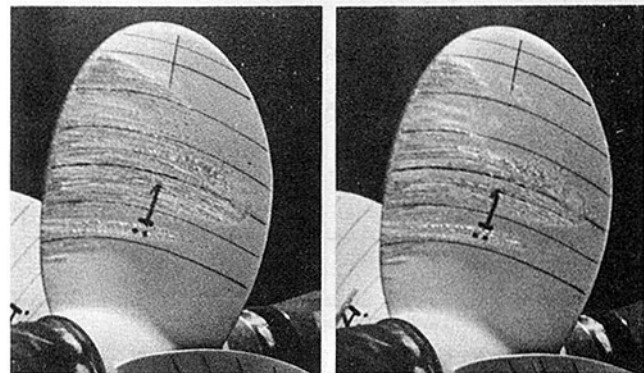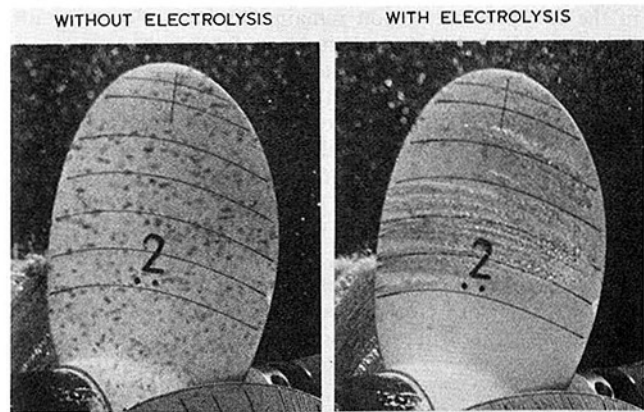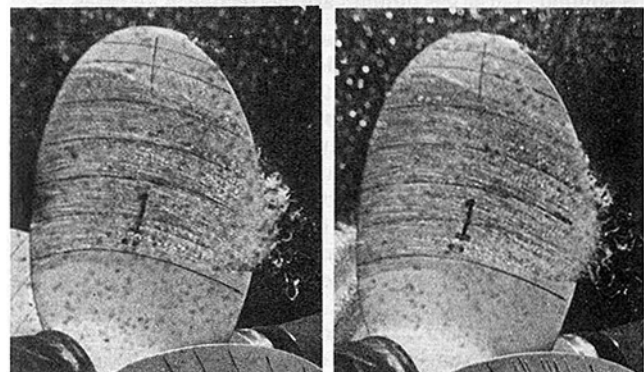

Fig. 11 Cavitation observations on propeller S $J = 0.6$ ($\sigma_n = 0.92$, $Re_n = 1.1 \times 10^6$)

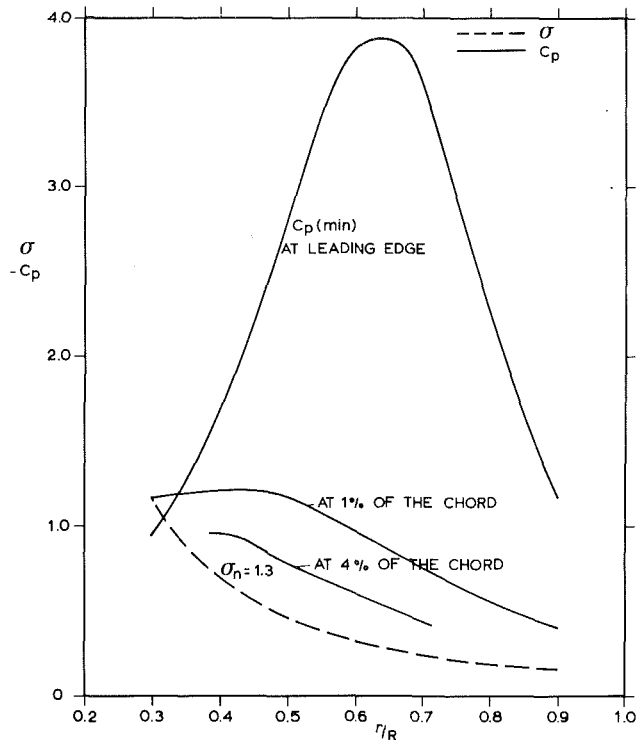Fig. 12 Cavitation observations on propeller S at $J = 0.61$ ($\sigma_n = 0.67$, $Re_n = 1.7 \times 10^6$)

Fig. 13 Radial distribution of calculated minimum pressure coefficients and cavitation indices on propeller S at $J = 0.4$

Fig. 14 Cavitation observations on propeller S at $J = 0.4$ ($\sigma_n = 1.31$, $Re_n = 1.1 \times 10^6$)

chordwise direction is not very regular, which is suspected to be caused by the leading edge roughness.

An increase in Reynolds number shifts the transition region somewhat to the leading edge (Fig. 7), but the boundary layer in the low pressure region remains laminar. However, turbulent streaks were seen to occur more frequently.

Figure 12 gives the cavitation pattern at this higher Reynolds number. The cavitation index is as low as possible. There is an abundant amount of rather large air bubbles in the flow, both with and without electrolysis. These are generated by the electrolysis grid in front of the propeller. Some remarkable things can be seen on the smooth blade of Fig. 12. There is no cavitation at all without electrolysis. The large bubbles, although abundant, do not create inception. But with electrolysis inception does take place. Still the cavitation which occurs with electrolysis is not a sheet, but conists of spots, emanating from the leading edge. The assumption that these cavitating spots are related with the turbulent streaks in the boundary layer is obvious. The nuclei content of the tank itself apparently is too low to create inception, even not in the turbulent spots. Small nuclei do create inception when the boundary layer is turbulent, but not when the boundary layer is laminar. Large gas bubbles are ineffective in all cases.

Inception of Sheet Cavitation With Laminar Separation of the Boundary Layer. (Propeller S at $J = 0.4$). The calculated minimum pressure coefficients on propeller S at $J = 0.4$ are compared with a radial distribution of the cavitation index in Fig. 13. In Fig. 6 it was shown that the increased loading results into a rather long laminar separation bubble in the boundary layer. The cavitation patterns in this condition at $\sigma_n = 1.31$ are given in Fig. 14. In the region of the long separation bubble inception only takes place when electrolysis is applied. Near the tip there is cavitation also without electrolysis.

Inception in a laminar separation bubble is possibly related with the pressure in the reattachment region. This region on blade 2 is located at about 4 percent of the chordlength from the leading edge. In the tip region, however, the boundary layer is already reattached at less than 1 percent of the chord.
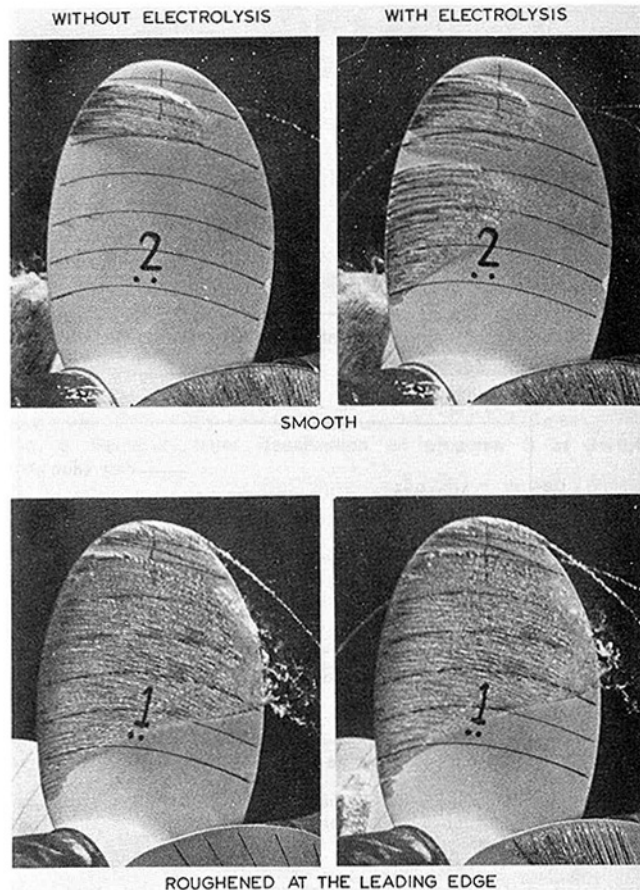
The C_p – curves for both chord positions are given in Fig. 13. At inner radii the C_p-curve at 4 percent of the chord has to be compared with the curve $\sigma_n = 1.3$. Near the tip the C_p-curve at 1 percent of the chord has to be used for this comparison. From this comparison it can be seen that, although the tip is strongly unloaded, the risk of cavitation is not smaller near the tip. That the length of the separation bubble affects the inception pressure is supported by the fact that blade 4, which had the shortest separation bubble (Fig. 6), showed earlier inception than blade 2.

From Fig. 14 it can be seen that electrolysis creates inception when there is a laminar separation bubble in the boundary layer. This was observed only very incidentally in reference [3], probably because the length of the separation bubble was much shorter there and the pressure at reattachment was lower. So a low nuclei content may strongly delay inception of sheet cavitation, but generally this occurs only when the largest nuclei are very small. Between $r/R = 0.7$ and 0.8 no inception takes place on the smooth blade in Fig. 14 irrespective of electrolysis. Apparently this is related with the tendency of the boundary layer in this region to remain laminar.

Roughness eliminates these boundary layer effects and causes inception irrespective of electrolysis. The chordwise extent of the cavity of the roughened blade is significantly larger than on the smooth blade. This may be caused by the presence of the gap in the sheet. On the smooth blade 4 the gap was much smaller and the cavity extent was the same as on the roughened blade 1. It is remarkable that the sheet cavity in Fig. 14 is not a smooth sheet in the region of laminar separation, but consists of spot cavities. Probably the large cavity removes the laminar separation bubble at the leading edge after inception has occurred.
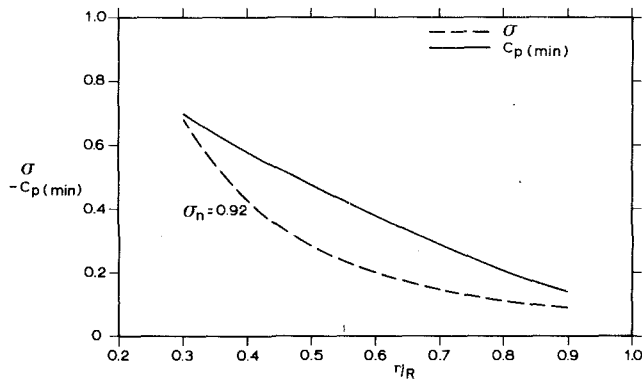
Fig. 15 Radial distribution of calculated minimum pressure coefficients and cavitation indices on propeller B at $J = 0.6$

Inception of Bubble Cavitation

Inception of Bubble Cavitation With a Shock-Free Inflow. (Propeller B at $J = 0.6$). The calculated minimum pressure coefficients, which now occur at midchord, are given in Fig. 15 for propeller B at $J = 0.6$, together with the radial distribution of the cavitation index σ at the tank pressure at which observations are given.

In Fig. 16 the cavitation patterns are shown in this condition ($\sigma_n = 0.92$). The minimum pressure is well below the vapor pressure. Still no cavitation inception takes place on the smooth blade. The largest deviations from the vapor pressure occur at about $r/R = 0.5$ and the maximum diameter of an air bubble which remains stable in this low pressure is 20 μm. It is very plausible that no nuclei larger than 20 μm occurred in the tank water, so the absence of bubble cavitation can be explained by a lack of nuclei.

Inception does take place when electrolysis is applied. The cavities, however, occur closer to the trailing edge than would be expected from the pressure distribution. The reason probably is the effect of cavitation on the pressure distribution.

In reference [3] it was observed that application of roughness at the leading edge sometimes promoted bubble cavitation. From Fig. 16 it is clear that this is not the case in this condition. Only some tip vortex cavitation is caused by the roughness. It can be concluded that the boundary layer on the blade does not affect bubble cavitation, since the boundary layer on the roughened blade is turbulent over the whole blade, while it is laminar until midchord on the smooth blade. Still no difference in cavitation pattern can be seen.

Contrary to what is seen in Fig 16, however, roughness often caused bubble cavitation in the midchord region, even at higher pressures than in Fig. 16. Closer inspection reveals that only when the roughness was applied very thinly, the bubble cavitation was absent. In all other cases the roughness at the leading edge generated nuclei which in turn caused inception of bubble cavitation in the midchord region.

In Fig. 17 the conditions are similar as in Fig. 16, but the Reynolds number was higher. Similar as in Fig. 12 the electrolysis wires are cavitating and generate a large number of bubbles. It is remarkable that these bubbles do not cause bubble cavitation, although the pressure on the blades is far below the vapor pressure. The mechanism causing this is not clear.

Application of electrolysis was ineffective in the condition of Fig. 17. As this higher Reynolds number the tank pressure is also higher. It was systematically found that electrolysis was ineffective at higher tank pressures and carriage velocities, and this is attributed to the fact that the bubbles generated by the electrolysis wires were too small.

In Fig. 17 the roughness at the leading edge does generate nuclei, and bubble cavitation is found also without elec-
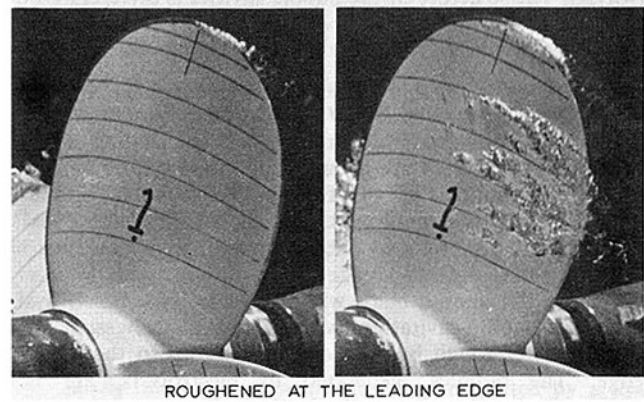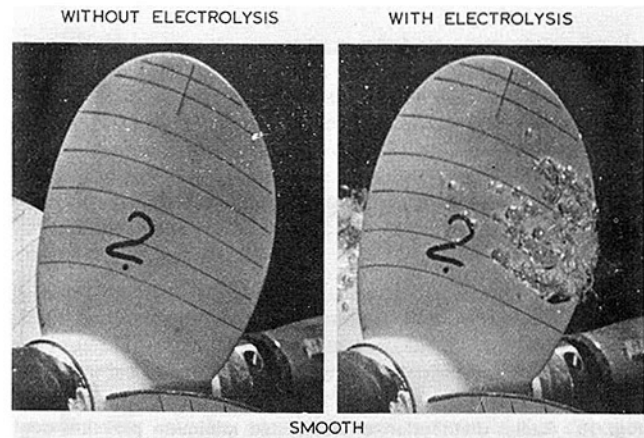

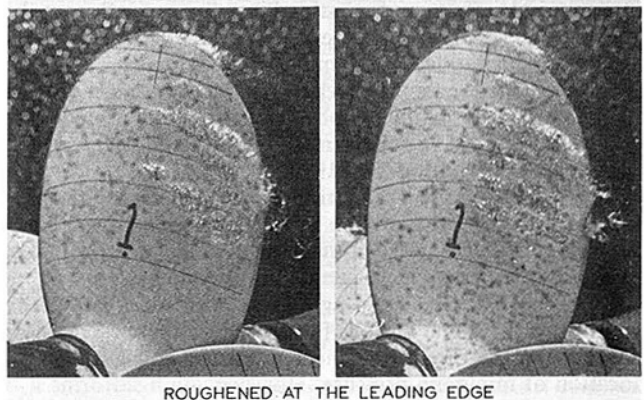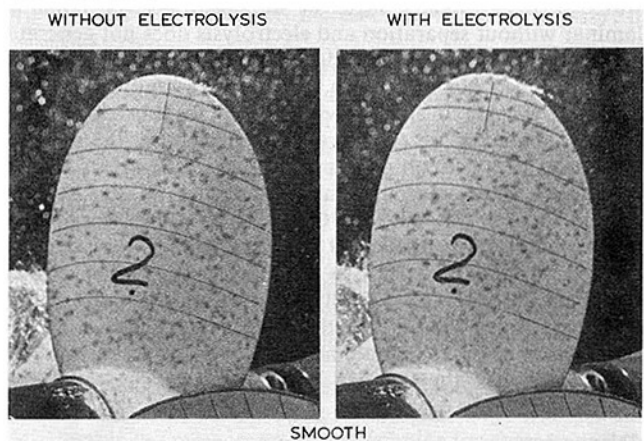Fig. 16 Cavitation observations on propeller B at $J = 0.6$ ($\sigma_n = 0.92$, $Re_n = 1.1 \times 10^6$)

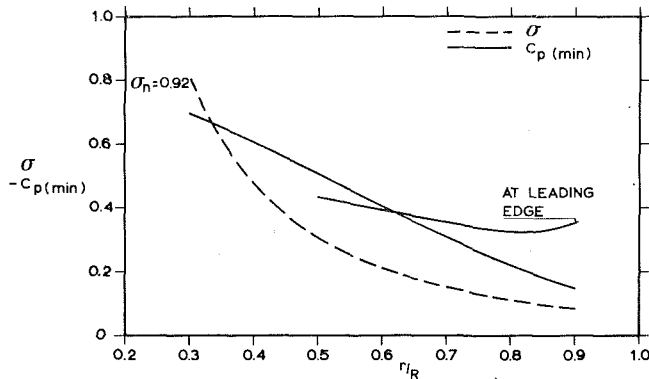Fig. 17 Cavitation observations on propeller B at $J = 0.6$ (σ_n 0.91, $Re_n = 1.7 \times 10^6$)

Fig. 18 Radial distribution of calculated minimum pressure coefficients and cavitation indices on propeller B at J = 0.4

Fig. 19 Cavitation observations on propeller B at J = 0.4 ($\sigma_n = 0.92$, $Re_n = 1.1 \times 10^6$)

trolysis. The structure of the bubble cavities is different from that in Fig. 16, which has to be attributed to the number and size of the nuclei generated by the roughness elements.

Inception of Sheet and Bubble Cavitation in a Flat Pressure Distribution. (Propeller B at $J = 0.4$.) The minimum pressure coefficients both near midchord and near the leading edge of propeller B at $J = 0.4$ are given in Fig. 18, together with the radial distribution of σ at $\sigma_n = 0.92$. A flat pressure distribution with a small peak near the leading edge gives a combination of sheet and bubble cavitation, as is shown in Fig. 19 on the roughened blade. No cavitation at all, however, occurs on the smooth blade without electrolysis. Electrolysis generates bubble cavitation, which again is strongest behind midchord, although bubbles can be seen up to the leading edge. The bubbles, generated by electrolysis, are not uniformly distributed over the blade, only two streaks occur reflecting the layers of bubbles generated by the electrolysis wires. The boundary layer at the leading edge remains laminar without separation and electrolysis does not generate a sheet cavity at the leading edge. The roughness elements on the roughened blade are in a low-pressure region now and cavitate, causing a sheet cavity at the leading edge. The streaky character of the sheet is reflected in the bubble cavitation. Application of electrolysis has little effect on the roughened blade, although the spot cavities at the leading edge in between $r/R = 0.6$ and 0.7 are somewhat larger. When in the condition as in Fig. 19 the Reynolds number was increased from 1.06×10^6 to 1.68×10^6 the observations remained the same. Specifically the sheet at the leading edge remained absent on the smooth blade, which agrees with the observation in Fig. 8 that an increase of the Reynolds number did not remove the laminar boundary layer region at the leading edge.

Discussion

Sheet Cavitation. The observations in Fig. 19 show how strongly scale effects on cavitation inception can influence the cavity pattern, not only near inception, but also with developed cavitation. The laminar boundary layer near the leading edge prevents the sheet cavity; the low nuclei content of the tank water inhibits bubble cavitation; and a blade free of cavitation may be found instead of a blade covered with both types of cavitation (Fig. 19).

The absence of sheet cavitation when the boundary layer is laminar is very persistent. The gap in the sheet cavity on blade 2 of Fig. 14 with electrolysis remained up to the lowest cavitation indices which could be obtained ($\sigma_n = 0.67$ at $Re_n = 1.7 \times 10^6$). This is in agreement with observations on headforms [7, 8] and on foils [9] that inception occurred near the separation or reattachment pressure and not at the location of minimum pressure. However, on headforms it is generally found that a supply of sufficient nuclei causes bubble cavitation, originating at the location of minimum
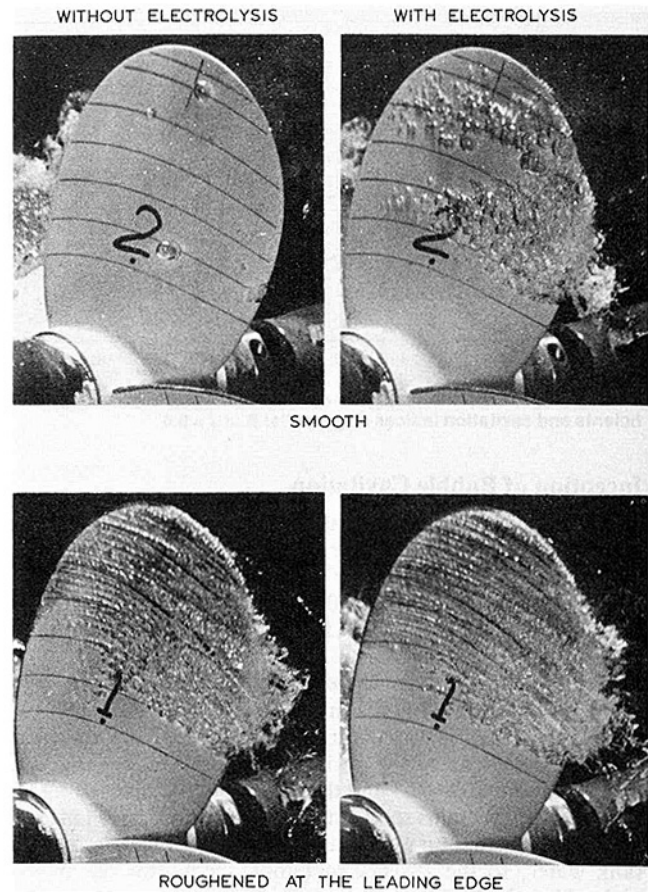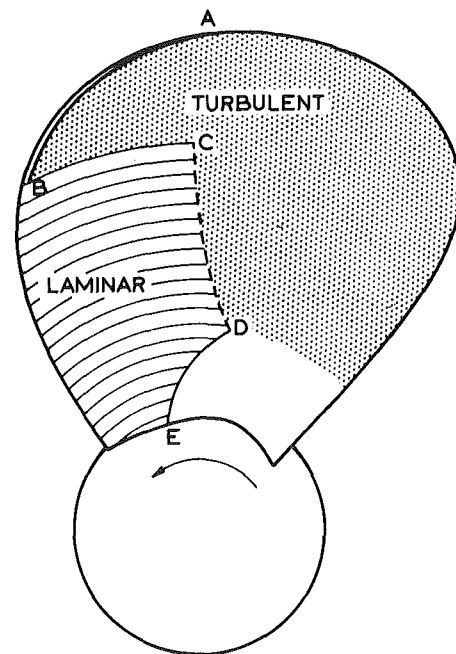

AB   SHORT LAMINAR SEPARATION BUBBLE
BC   CRITICAL RADIUS
CD   TRANSITION REGION
DE   LAMINAR SEPARATION

Fig. 20 Schematic representation of the boundary layer flow on the suction side of a propeller blade

pressure [7, 10]. Possibly the sharp pressure peak which is typical for thin propeller blades, causes "screening" of the bubbles, as calculated by Johnson and Hsieh [11], causing in turn the bubbles of sufficient size not to arrive at the location of the minimum pressure.

The absence of sheet cavitation when the boundary layer is laminar explains why the sheet cavity on model scale often extends less far to the hub than when on full scale.

Generally cavitation tests with model propellers are carried out at the highest obtainable Reynolds number to avoid scale effects on cavitation. However, it requires extremely high Reynolds numbers to bring the transition region to the leading edge (Fig. 8). Before this occurs surface irregularities have already caused turbulent streaks in the laminar boundary layer region, as in Fig. 7, and with increasing Reynolds number those streaks, corresponding with cavitating spots in the cavitating condition, eventually remove the laminar region. In that case the "smooth'" propeller blades are effectively roughened.

Because propeller blades are generally thin, while the propeller loading is concentrated near the tip for reasons of efficiency, laminar separation regularly occurs at outer radii on model scale. The character of the boundary layer on the suction side of the blades is then as sketched in Fig. 20. Sheet cavitation will occur in the cavitating condition from the tip until point B. The location of the "critical" or separation radius BC determines the radial extent of the sheet cavity and this extent is independent of the Reynolds number, but very sensitive to the propeller loading [3]. Only a very low nuclei content can inhibit sheet cavitation when laminar separation occurs, and this is a phenomenon typical for facilities with a very low nuclei content [12, 13].

Application of roughness at the leading edge is effective when the boundary layer is laminar, probably by causing low pressures locally in the boundary layer similar as in the case of laminar separation with reattachment. This is of course, at the risk of causing premature inception, because the roughness elements are located in the minimum pressure region where the danger of premature inception is very large [14]. Some preliminary tests near inception indicate, however, that this effect is restricted to very small cavities on the roughness and for many applications this drawback is much smaller than the scale effect due to laminar boundary layer flow. If the precise inception condition of a roughened propeller has any meaning is doubtful, however, and this should be investigated further. Also the possible effect of roughness on the cavity length (Fig. 14) requires further investigation.

Bubble Cavitation. Although the water in the tank is heavily supersaturated (200–500% in depressurized conditions) the nuclei content is very low and bubble cavitation is inhibited. Generation of additional nuclei is necessary and electrolysis can provide the required nuclei, although only at low tank pressures. So the maximum bubble size of the gas bubbles generated by electrolysis wires has to be investigated further. Specifically the maximum bubble size at higher velocities is unknown. Electrolysis has been investigated mainly at lower velocities (e.g. [15]) with the application of flow visualization in mind.

The observation in Fig. 17, where large bubbles in the fluid did not generate bubble cavitation while small bubbles from the roughness elements did, is not yet understood. It looks like bubble screening takes place, similar as with sheet cavitation, but with the minimum pressure in the midchord region, screening is not expected.

In many cases roughness at the leading edge can replace electrolysis and generate the required nuclei. The amount of nuclei generated by roughness elements, is larger than the amount generated by electrolysis, e.g. in the condition of Fig. 19, resulting in a different structure of the bubble cavitation.

The effect of this structure (e.g. of the maximum cavity size and of the number of bubble cavities) on the production of noise still has to be investigated. When radiated noise has to be measured electrolysis wires are unsuitable because they generate much noise themselves. In that case application of leading edge roughness can be equally effective, although the effect of roughness height, roughness Reynolds number, and saturation rate of the water on the generation of nuclei remains to be investigated.

Experimental Accuracy. During the present investigations differences in cavitation behavior were observed between various blades, especially when laminar separation occurred near the leading edge. The reproduceability of the cavitation pattern on each blade, however, was very good. Possible unsteadiness of the cavitation pattern could be detected because at least three pictures were always taken during one condition. The accuracy of the cavitation index is better than 0.01. The advance ratio J refers to the carriage velocity and has an accuracy of 1 percent. Due to flow disturbances by the catamaran the actual inflow velocity may vary up to 3 percent from the carriage velocity.

Conclusions

The results of the test program up to now can be summarized as follows.

- No cavitation inception of sheet cavitation takes place when the boundary layer is laminar. The creation of additional nuclei by means of electrolysis is ineffective in this case.
- Inception of sheet cavitation when the boundary layer shows laminar separation may be prohibited by a low nuclei content. The inception pressure shows a relationship with the length of the separation bubble. Electrolysis effectively increases the inception pressure in this case.
- Application of roughness at the leading edge causes inception of sheet cavitation, although the inception pressure has to be determined more accurately. Addition of nuclei does not affect the cavitation in this case.
- Inception of bubble cavitation is independent of the propeller boundary layer, but strongly dependent on electrolysis.
- Application of roughness at the leading edge can affect inception of bubble cavitation since apparently nuclei are generated by the roughness elements. The height of the roughness elements relative to the boundary layer thickness is important.
- The hypothesis that screening of bubbles takes place is strengthened by the observations that large bubbles are unable to create inception. This holds for sheet as well as for bubble cavitation.
- With increasing Reynolds number turbulent spots appear in the boundary layer. An increase in the number of these spots will give the impression that the transition region approaches the leading edge. The transition region of the undisturbed flow, however, remains far from the leading edge up to very high Reynolds numbers.

References

1 "Report of the Cavitation Committee Appendix A." *Proceedings of the 15th ITTC*, The Hague, The Netherlands, 1978, pp. 340–347.

2 Kuiper, G., "Cavitation Scale Effects: A Case Study," *International Shipbuilding Progress*, Vol. 25, 1978, pp. 81–90.

3 Kuiper, G., "Scale Effects on Propeller Cavitation Inception—Variation of Roughness and Nuclei," *Twelfth Symp. on Naval Hydrodynamics*, Washington, D.C., 1978.

4 Kuiper, G., "Some Experiments With Distinguished Types of Cavitation on Ship Propellers," *ASME International Symp. on Cavitation Inception*, New York, 1979.

5 Gent, W. van, "On the Use of Lifting Surface Theory for Moderately and Heavily Loaded Ship Propellers," Thesis, *N.S.M.B., Publ. No. 536*, 1977.

6 Wazzan, A. R., Okamura, T. T., and Smith, A. M. O., "Spatial and Temporal Stability Charts for the Falkner Skan Boundary Layer Profiles," Douglas Aircraft Company, Report No. DAC-67086, 1968.

7 Arakeri, V. H., and Acosta, A. J., "Viscous Effects in the Inception of Cavitation on Axisymmetric Bodies," ASME JOURNAL OF FLUIDS ENGINEERING, Vol. 95, 1973.

8 Meulen, J. H. J. van der, "A Holographical Study of the Influence of Boundary Layer and Surface Characteristics on Incipient and Developed Cavitation on Axisymmetric Bodies," *Proceedings of the 12th Symp. on Naval Hydrodynamics*, Washington, D.C., 1978, pp. 433–451.

9 Casey, M. V., "The Inception of Attached Cavitation From Laminar Separation Bubbles on Hydrofoils," *Inst. of Mech. Eng., Conference on Cavitation*, Edinburg, Scotland, 1974.

10 Kodama, Y., Tamiya, S., Take, H., and Kato, H., "The Effect of Nuclei on the Inception of Bubbles and Sheet Cavitation on Axisymmetric Bodies,"

Proceedings of the 12th Symp. on Naval Hydrodynamics, Washington D.C., 1978, pp. 75–86.

11 Johnson, V. E., and Hsieh, T., "The Influence of Trajectories of Gas Nuclei on Cavitation Inception," *Proceedings of the 6th Symp. on Naval Hydrodynamics*, Washington D.C., 1966, p. 7.

12 Albrecht, K., and Bjorheden, O., "Cavitation Testing of Propellers in a Free Surface Tunnel Utilizing Micro Air Bubble Control," ASME JOURNAL OF FLUIDS ENGINEERING, 1975, p. 523.

13 Noordzij, L., "Some Experiments on Cavitation Inception With Propellers in the NSMB Depressurized Towing Tank," *Int. Shipbuilding Progress*, 1976, p. 23.

14 Holl, J. W., "The Estimation of the Effect of Surface Irregularities on the Inception of Cavitation," ASME *Symp. on Cavitation in Fluid Machinery*, G. M. Wood et al., (eds), 1965, p. 3.

15 Tory, A. C., and Haywood, K. H., "The Hydrogen Bubble Technique of Flow Visualization: Factors Affecting Bubble Size and Bouyancy," ASME Fluids Eng. Division, *Fluids Eng. Conference*, Pittsburg, Pa., 1971.

The Onset of Bubble-Ring Cavitation on Hemispherical Headforms

B. R. Parkin

The Pennsylvania State University,
Garfield Thomas Water Tunnel,
Applied Research Laboratory,
State College, Penn. 16801
Mem. ASME

An approximate theory is developed to predict the onset of cavitation on hemispherical headforms for Reynolds numbers at which laminar separation is known to occur. Insofar as it is possible, the theory is based upon first principles. Fairly good agreement is obtained between the cavitation desinence trends recently measured by Holl and Carroll and the present theory. It is also found that the onset cavitation number should be less than the magnitude of the pressure coefficient at the laminar separation point and that the cavitation number increases with free-stream velocity. As long as there is an appreciable concentration of dissolved air in the water, it is also found, in agreement with experiment, that the onset of bubble-ring cavitation is practically independent of air content. Moreover, the observed occurrence of a lowest speed for "bubble-ring" cavitation, which is the only cavitation form considered here, and the range of "cutoff" speeds predicted by the present asymptotic theory show very encouraging agreement. The present theory suggests that this cutoff speed and its accompanying cutoff cavitation number can also depend on the temperature of the water, provided that the initial size attributed to a "typical" spherical free-stream air bubble nucleus also varies with the temperature. At $80°F$ $(26.6°C)$ it is estimated that the typical nucleus from which bubble-ring cavitation originates has a radius of about seven μm. At higher temperatures the nucleus radius decreases from this value while at lower temperatures the initial radius exceeds the value noted.

Introduction

In the following we estimate from first principles the onset of cavitation on an axially symmetric body consisting of a hemispherical nose attached to an after body which is a right circular cylinder of diameter equal to that of the hemisphere. It has been shown [1, 2] that the flow about hemispherical bodies, downstream of the minimum pressure point, will have a laminar separation bubble which is calculated to be present up to Reynolds numbers, based on body diameter, D, of about five and one half million [1, 3]. The free-stream velocity (V_o) is aligned with the body axis. The static pressure at upstream infinity is p_o, and the liquid density is ρ. The flow configuration is illustrated schematically in Fig. 1. The form of cavitation onset under study here is called bubble-ring cavitation [3] and photographs of this form are given in Fig. 2A of reference [3] or Fig. 2 of reference [4].

A concise review of a number of previous investigations which are similar to this one has been given by Holl [5]. Here it seems sufficient to note that all features of the non-cavitating flow, which may have a decisive influence on inception, were not as well known when those earlier studies were carried out as they are today. Therefore, previous theories for cavitation inception on bodies, which are now known to exhibit laminar separation, show at best only qualitative agreement with experiment. Based upon the present more complete knowledge of the physical events
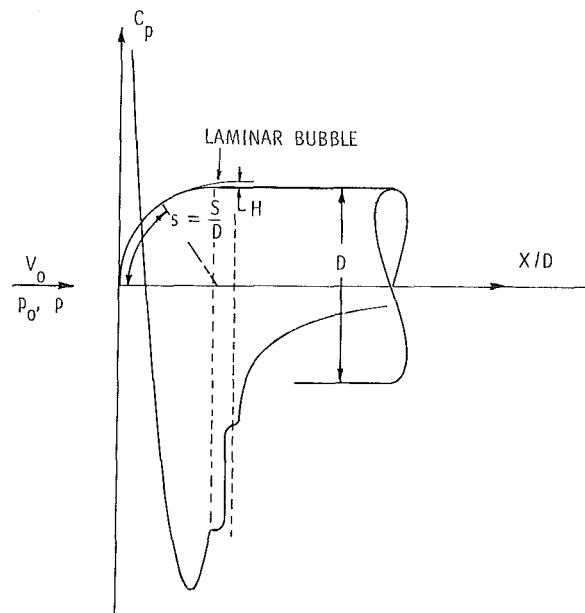
Fig. 1 Schematic diagram of flow about a hemispherical headform when laminar separation is present

which have been observed in the rather special flows of present interest, reference [4] studies those features which seem to be most important with respect to the onset of

cavitation and defines a likely criterion for inception which excludes the role of large pressure fluctuations in the reattachment region of the laminar bubble. It appears that both air diffusion and vaporous growth of cavitation nuclei are important processes contributing to the onset of cavitation observed in the reattachment region. The conditions which are responsible for the initiation of air diffusion into the cavitation bubble from the surrounding water when the microbubble is in the laminar separation zone have been analyzed in reference [6]. From these studies it appears that now we need to consider only those events associated with vaporous bubble growth in order to formulate a theory for the onset of bubble ring cavitation. Once the vaporous microbubble comes to rest in the laminar separation bubble and significant gaseous growth starts, subsequent events leading to the appearance of bubble-ring cavitation in the reattachment region are automatic [4].

Formulation of the Dynamics Problem

Briefly, the criterion from reference [4] for inception centers upon the vaporous growth of a typical free-stream cavitation nucleus of "effective" radius or "size" R_o to a maximum radius, R_m. The value of R_m depends either upon the critical radius for the initiation of sustained air diffusion after the vaporous growth phase is past and the cavitation bubble is fixed at a definite location in the laminar separation bubble, or upon the height of the laminar bubble which limits the greatest radius for vaporous or gaseous growth if bubble-ring cavitation is to be present.

Introducing the dimensionless radius,

$$r = R(t)/R_o,$$

we can write the criterion for the onset of bubble-ring cavitation as

$$(\gamma - \beta)^{-1} \le r_m \le 55.5\, \theta D/(R_o \mathrm{Re}^{0.79}), \tag{1}$$

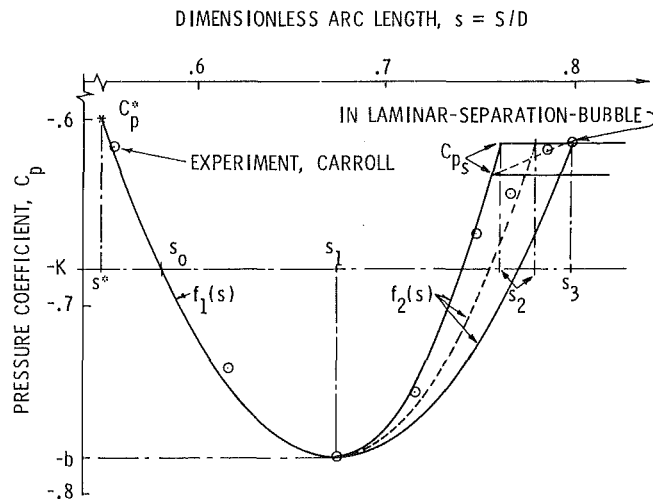where the left-hand side of (1) gives the lower limit of r_m if

Fig. 2 Measured pressure coefficients and parabolic approximations for a 2-in.-dia (0.0508 m) hemispherical headform

gaseous growth is to be possible [6] and the right-hand side is related to experimental data on laminar bubble heights from references [7-9] which are approximated by an analytical expression as shown in [6]. In criterion (1) the various terms are

$$\gamma = p_a/(2\sigma/R_o), \tag{2}$$

$$\beta = (K + C_{p_s})/C_\sigma, \tag{3}$$

and

$$C_\sigma = 4\sigma/(\rho R_o V_o^2). \tag{4}$$

The free parameter θ is the ratio $2R_m/H$, where H is the laminar bubble height. The range of θ is $0.5 \le \theta \le 1.0$. Moreover, Re is the Reynolds number based on D. In (2) p_a is the partial pressure of air in the nucleus of size R_o, and σ is the

_____ Nomenclature _____

b = magnitude of the minimum pressure coefficient on the headform, $b = -C_{p_{\min}}$

C_p^* = measured pressure coefficient at an arbitrary upstream point on the body used for fitting approximating functions

C_p = pressure coefficient = $(p - p_0)/\frac{1}{2}\rho V_o^2$

C_{p_s} = static pressure coefficient in laminar separation bubble, $(p_s = p_o)/\frac{1}{2}\rho V_o^2$

$C_{p_{\min}}$ = minimum static pressure coefficient on headform, $(p_{\min} = p_0)/\frac{1}{2}\rho V_o^2$

C_{p_1} = pressure coefficient at the point s_1 on the body

C_σ = ratio of characteristic surface tension pressure to dynamic pressure, = $4\sigma/(R_o\rho V_o^2)$

D = diameter of the water tunnel model

$f(t)$ = when laboratory time is used

= $[p_0 - p(t)]/\frac{1}{2}\rho V_o^2 = -C_p(t)$

$f_1(s)$ = parabolic approximations to the experimental
$f_2(s)$ pressure distribution on the headform

$f_2(\tau)$ = an approximating function for the pressure distributions on the headform when dimen-

sionless arc length has been transformed to dimensionless bubble time

$F(\tau)$ = dimensionless forcing function experienced by a cavitation bubble, = $-[(K + f(\tau))]/C_\sigma$

$F_a(\tau)$ = dimensionless forcing function for the step-wise-autonomous approximation for cavitation bubble growth

H = maximum height of the laminar separation bubble

K = cavitation number = $(p_o - p_v)/\frac{1}{2}\rho V_0^2$

K_c = "critical" cavitation number
K_{co} = cutoff cavitation number
n = surface tension parameter which governs the slope of the linearly increasing part of the surface tension law $S(r,\sigma)$
p = static pressure at any point in the flow
p_a = partial pressure of air in the free-stream nucleus at the measured dissolved air concentration
p_o = static pressure at upstream infinity
p_v = pressure of the vapor inside the cavitation bubble
p_s = static pressure of the liquid in the separation bubble
$p(t)$ = external static pressure as a function of laboratory time

coefficient of surface tension. In (3) the cavitation number K is given by

$$K = (p_o - p_v) / \frac{1}{2} \rho V_o^2 \qquad (5)$$

and C_{p_s} is the pressure coefficient at laminar separation,

$$C_{p_s} = (p_s - p_o) / \frac{1}{2} \rho V_o^2, \qquad (6)$$

where p_s is the static pressure at laminar separation.

The criterion (1) states two facts. The first is that the vaporous growth phase of a typical nucleus will end when the cavitation bubble reaches its maximum radius. The second is that the radius R_m must be large enough to ensure gaseous growth once the microbubble comes to rest in the laminar separation zone and this maximum diameter cannot exceed the laminar bubble height. If these restrictions are satisfied, bubble-ring cavitation will definitely occur.

The time available for the nucleus to undergo vaporous growth from $r = 1$ to $r = r_m$ is limited by the extent of the region of favorable pressure on the body and by the position of the laminar bubble. The maximum time for vaporous growth, t_m, is measured from the instant that $K + C_p = 0$, where C_p is the pressure coefficient at any point on the body as defined in the Nomenclature above.

At the instant that $t = 0$, it is convenient to assme that

and
$$\left. \begin{array}{l} r(0) = 1 \\[4pt] \dot{r}(0) = 0. \end{array} \right\} \qquad (7)$$

The growth of the cavitation bubble from this initial state to the value r_m takes place in the interval, $0 < t \le t_m$, and the microbubble arrives in the laminar separation zone at the instant $t(r_m) = t_m$.

Therefore, the flow conditions leading to the onset of bubble-ring cavitation depend upon the equation of motion [10] for vaporous growth of a "typical" nucleus in the interval $(0, t_m)$. In dimensionless variables the equation of motion for an isothermal cavitation bubble can be written as

$$r \frac{d^2 r}{d\tau^2} + \frac{3}{2} \left(\frac{dr}{d\tau} \right)^2 = \frac{\gamma}{r^3} - \frac{S(r, n)}{r} - \frac{K + f(\tau)}{C_\sigma}, \qquad (8)$$

where the dimensionless "bubble time", τ, is related to laboratory or "real time", t, by means of

$$\tau = (2\sigma / \rho R_o)^{1/2} t / R_o \qquad (9)$$

The function $S(r, n)$ is the "surface tension law" for an ideal Harvey nucleus [6] which is defined by[1]

$$S(r, n) = \begin{cases} \dfrac{r - 1}{n - 1} , & 1 \le r < n, \\[10pt] 1 , & n \le r. \end{cases} \qquad (10)$$

The quantity n is a free parameter which is defined by the radius, $R = nR_o$, at which the surface energy of the nucleus reaches its full value of σ. Note that at $r = 1$ ($R = R_o$) the surface energy of the nucleus, $S\sigma$, is zero and the nucleus is stable in the sense that it will not dissolve under the action of surface tension. Also, when $n = 1$ the nucleus is a spherical bubble of radius R_o so that equation (10) includes this important case as well as the ideal Harvey nucleus. Returning to equation (8) we observe that the quantity $f(\tau)$ is a dimensionless pressure coefficient defined by

$$p(\tau) = p_o + \frac{1}{2} \rho V_o^2 f(\tau) \qquad (11)$$

and the term

$$-[K + f(\tau)] / C_\sigma = F(\tau) \qquad (12)$$

is a forcing function which causes the vapor bubble to grow from $r = 1$ to $r = r_m$ during the time τ_m.

---

[1]This approximate model for a stable nucleus was first proposed in reference [15]. It is discussed again in references [11], [6], and [4]. Physically it is a device designed to allow for the existence of nuclei which do not dissolve but the value of n is a matter for speculation. In Carroll's experiments [3] the nuclei were probably spherical air bubbles and so $n = 1$ should be used even though such nuclei are not stable.

_____ Nomenclature (cont.) _____

r = dimensionless radius = R/R_o
r_c = critical dimensionless bubble radius
r_m = maximum dimensionless bubble radius
r_o = value of dimensionless radius when $\tau = \tau_o + \tau_a$
r_l = larger critical dimensionless radius
r_s = smaller critical dimensionless radius
R = bubble radius
Re = Reynolds number based on body diameter
R_m = maximum bubble radius
R_o = "radius" of typical nucleus
s = dimensionless arc length along the body surface = S/D
s_0, s_1, s_2, s_3 = particular points on the body
s^* = dimensionless arc length at a point upstream of the minimum pressure point where $C_p = C_p^*$
S = arc length along surface of headform
$S(r,n)$ = surface tension law
t = laboratory or "real" time
t_m = time available for vaporous growth
v = dimensionless bubble-wall velocity
v_o = dimensionless bubble-wall velocity when $\tau = \tau_o + \tau_a$
$v(r_o)$ = dimensionless bubble-wall velocity when $r = r_o$
$v(t)$ = dimensionless bubble-wall velocity as a function of dimensionless time

V_{co} = cutoff velocity
V_o = free-stream velocity
We = Weber number, We $= V_o / \sqrt{\sigma / (\rho D)}$
α = driving parameter, $\alpha = (b - K)/C_\sigma$
α_s = value of bubble driving parameter at the smaller critical radius r_s in which case $r_s = r_c$
β = dimensionless parameter characterizing static pressure in laminar separation zone, $\beta = (K + C_{p_s})/C_\sigma$
γ = dissolved air content parameter $\gamma = p_a / (2\sigma / R_o)$
θ = ratio of maximum vapor bubble diameter to the maximum laminar separation bubble height, $\theta = 2R_m / H$
ρ = liquid density
σ = coefficient of surface tension
τ = dimensionless time, $t\sqrt{2\sigma / \rho R_o^3}$, "bubble time"
τ_a = dimensionless lag time
τ_m = dimensionless time available for vaporous bubble growth
τ_o = duration of favorable environment for growth in which $F_a = \alpha$
μ = dynamic viscosity of liquid
ξ = normalized radius, $\xi = r / \sqrt{\gamma}$
ξ_m = value of ξ when $r = r_m$

Kinematics of Cavitation Bubble Convection

Before we can solve the dynamics problem, consisting of equations (8) and (7) and which is compatible with the criterion (1), it is necessary to provide a rationale which permits up to translate the known pressure distribution, $C_p(s)$, as given in terms of its dimensionless position coordinate, s, along the meridional arc length of the head-form, into the cavitation bubble forcing function $F(\tau)$. We will assume that the boundary layer is simply a vortex sheet which moves with one half of the speed of the inviscid outer flow at the position s at the edge of the boundary layer. Since the nucleus is in the vortex sheet its speed with respect to the body is

$$\frac{ds}{dt} = \frac{1}{2} V_o \sqrt{1 - C_p(s)}. \tag{13}$$

A measured pressure distribution in the neighborhood of the maximum pressure point and also near the laminar separation point is plotted in Fig 2. The experimental values shown are averages of measurements made by J. A. Carroll [3]. These points pertain to experiments in which the water temperature was 78°F (25.56°C) and the free-stream velocity ranged form 20 fps (6.096 m/s) to 60 fps (18.288 m/s). Two parabolic approximations of these data are shown in Fig. 2 as $f_1(s)$ and $f_2(s)$ and they apply in the regions illustrated. Moreover, two values of C_{p_s} are shown by horizontal lines. The higher value, $C_{p_s} = -0.613$, represents the pressure in a fairly short bubble. But since the bubble length varies with Reynolds number, Fig. 2 also shows the value $C_{p_s} = -0.630$ intended to represent the value at laminar separation. This value appears to be independent of free-stream velocity as long as there is a laminar bubble [3]. Also shown in Fig. 2 is the region on the body, below the line $C_p(s) < -K$, where the static pressure is less than the vapor pressure of water. In this region we say that the water is in tension.

We assume that vaporous growth of the cavitation bubble ends at the point s_3 inside or at the start of the laminar bubble and that its subsequent gaseous growth occurs at this fixed point. Then the transit time between s_0 and s_3 is set equal to t_m, the time available for vaporous growth. At $t = t_m$ the bubble radius will be R_m. Therefore, if we use the parabolic approximations f_1 and f_2 instead of $C_p(s)$ in equation (13), we obtain an explicit for t_m [11].

Equations (13) and the functions f_1 and f_2 also provide the basic kinematic relationships caused by the translation of the cavitation bubble along the surface of the body. They can be used to approximate the instantaneous value of static pressure, $p(\tau)$ in the water surrounding the translating bubble and this allows us to evaluate the forcing function $F(\tau)$ as defined by equation (12) in terms of the parabolic approximations f_1 and f_2 [11]. Since we measure τ from that point when the local static pressure first falls to zero, we have $F(0) = 0$. The schematic diagram of Fig. 3 shows the forcing function $F(\tau)$ in the various intervals defined in Fig. 2. As also shown in Fig. 2, we have put $b = -C_p|_{\min}$. Then in Fig. 3 we have expressed $F(\tau)$ at that point which corresponds to $C_p|_{\min}$ as

$$\alpha = (b-K)/C_\sigma. \tag{14}$$

Further details of the kinematic computations are given in reference [11].

Dynamics of Vaporous Growth

The foregoing considerations enable us to proceed with the study of solutions of equation (8) which are subject to the initial conditions (7). Such studies are certainly not new [5] although the present work contains a number of aspects not previously considered. Moreover, in past numerical studies[2]
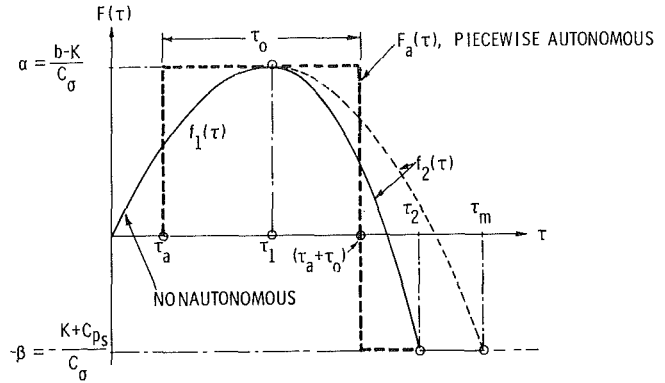
---

[2]Unpublished.

Fig. 3 Schematic diagrams of pressure forcing functions for nonautonomous and piecewise-autonomous cavitation bubble dynamics

of equation (8), with the solution being subject to equation (7) and in which forcing functions similar to $F(\tau)$ were used, the present author found four classes of solutions.

In Class 1, a typical bubble undergoes small-scale oscillations in which the major part of the motion, if not all of it, occurs for values of $r < n$.

In Class 2, a bubble motion of Class-1 type is followed by another periodic motion involving significantly larger amplitudes than the initial oscillation with the maximum radius r_m considerably larger than n.

In Class 3, periodic solutions are found but all values of r_m are large.

In Class 4, the bubble grows without limit.

For reasons discussed above, Class-2 and Class-3 solutions are of interest here. In spite of extensive studies of the stability of nonlinear ordinary differential equations summarized in the literature [12–14], we know of no a priori criteria applicable to equation (8) by which solutions can be classified. Therefore, we shall employ certain additional simplifications in this study in order to find some approximate conditions which will separate the various classes.

The Piecewise-Autonomous Approximation

In order to secure some of the simplicity of autonomous dynamic systems compared to those defined by differential equations depending explicitly on the time, we shall replace $F(\tau)$ as defined above by a sequence of step functions. This further simplifications is illustrated schematically by the heavy dashed lines in Fig. 3. The amplitude of the final step is adjusted so that the value of F is $-\beta$. With these approximations, the pulsed bubble driving function is now

$$F_a(\tau) = \begin{cases} 0 & , \quad 0 \le \tau \le \tau_a, \\ \alpha & , \quad \tau_a < \tau \le \tau_a + \tau_o, \\ -\beta & , \quad \tau_a + \tau_o < \tau \le \tau_m. \end{cases} \tag{15}$$

When using the approximation (15), we apply the initial conditions of equation (7) at $\tau = \tau_a$ instead of at $\tau = 0$. When the start of the solution is delayed in this way we can consider the interval $(0, \tau_a)$ during which $r = 1$, as a rough way of representing Class-2 solutions which contain an initial interval of small amplitude oscillations before oscillations of larger amplitude occur. Class-3 solutions would correspond to $\tau_a = 0$. Negative values of τ_a are not defined.

Matching Conditions. The way in which equation (15) of the piecewise-autonomous system is used to match the parabolic approximation for the forcing function of the non-autonomous system is illustrated in Fig. 3 and details of the procedure are discussed in reference [11]. For present pur-

poses, we only note that it is not intended that $r(\tau)$ for nonautonomous and piecewise-autonomous representations should match at each instant. Only the value of r_m is to be the same for the two representations. In reference [11] it was found that the important matching requirement centers on r_m. In the matching the value of τ_m need not be closely controlled and the matching procedure proposed above is quite satisfactory. Therefore in equation (8) it is reasonable to replace the nonautonomous relationship which follows from equation (12) by the matched stepwise autonomous forcing functions of equation (15). The remaining considerations of the theory employ this simplification.

Limiting Trajectories. We can obtain further guidance about what particular type of solution we might expect for prescribed values of the governing physical parameters α, β, γ, and τ_0 by using an approach suggested previously in reference [15] which is given general consideration in Chapter 2 of reference [14].

It is well known that if one puts $v = dr/d\tau$, the left-hand side of equation (8) can be written as

$$\frac{1}{2r^2} \frac{d}{dr} (r^3 v^2).$$

Therefore, the first integral of the equation of motion (8) can be reduced to a quadrature which is an energy integral. The left-hand side of this equation is the change in kinetic energy. The right-hand side is the work done by the external environment, the air inside the bubble, and the surface tension forces, and we designate this integral by the symbol $W(r)$. As long as we maintain a constant value of α in its interval or a constant value of β in its interval, the formulation adopted here allows for no change in the total energy of the system during these intervals.

As the bubble grows, the logarithmic effect of air content in the energy integral $W(r)$ will be much smaller than the other polynomial terms on the right-hand side of the equation. Therefore, in the first interval where $F_a = \alpha$ the work done will have a general shape of a cubic in r. In a plot of work done against the radius r, one would see a curve which starts from $W(1) = 0$. As r increases $W(r)$ rises to a maximum and subsequently descends to an isolated minimum at some critical radius, $r = r_c$. It can be shown that the minimum of W occurs at a value of r_c greater than n as long as $\tau_0 \rightarrow \infty$, corresponding to step function forcing. Since the kinetic energy is zero for $r = 1$ it will be zero again if $W_{\min} = 0$. The fact that r_c is a minimum of W ensures that the time required for the bubble to grow to r_c is logarithmically infinite when $W_{\min} = 0$. Thus, if α and γ are chosen so as to make $W_{\min} = 0$, appreciable growth will not occur, although Class-1 solutions are certainly not ruled out.

Continuing with step function forcing, we can denote these critical values of α and γ, corresponding to $r = r_c$, by α_c and γ_c. Moreover, the isolated minimum of $W(r)$ at $r = r_c$ corresponds to $\dot{r}(r_c) = \ddot{r}(r_c) = 0$ because the bubble is in static equilibrium. In the phase plane when $v = 0$ and $r = r_c$ the values of α and γ will have assumed their critical values as described above and r_c will coincide with a saddle point. The trajectory through this point will be a separatrix.

Critical values of r, α, and γ follow from the conditions

$$W(r_c) = 0 \rightarrow v(r_c) = 0$$

and

$$\frac{dW}{dr}\bigg|_{r_c} = 0 \rightarrow \frac{dv}{dr}\bigg|_{r_c} = 0.$$

The two equations resulting from these conditions are

$$\frac{2\alpha_c}{3} (r_c^3 - 1) + 2\gamma \ln r_c - r_c^2 + \frac{n^2 + n + 1}{3} = 0 \qquad (16)$$

and

$$\alpha_c r_c^3 - r_c^2 + \gamma = 0. \qquad (17)$$

These equations account for the fact that $r_c \geq n$ as noted previously, and they will certainly apply to spherical bubble nuclei when $n = 1$. The fact that these critical conditions will be associated with relatively small values of the critical radius r_c causes us to designate this saddle point coordinate by r_s and to call it the *smaller critical radius.*

Suppose next that $\alpha > \alpha_c$ and that τ_o has a prescribed finite value and that n and γ are prescribed as before. Then one can inquire as to the values of β and a new value of r_c for which the time required for growth is infinite. As will be shown later, the preceding critical values of r_s and α_c and the new pair of critical values, $\beta_c(\alpha, \gamma)$ and $r_c(\alpha, \gamma)$, put limits on the range of physical parameters within which Class-3 solutions are to be expected. The second pair of critical values are determined from the first integral of the equation of motion in much the same way as indicated above. The condition that the work function $W(r)$ has vanishing slope at $r = r_c$ is the same as that given already by equation (17), for which $r > n$, except that now we must replace α_c with $-\beta_c$. Thus

$$\beta_c = \frac{\gamma}{r_c^3} - \frac{1}{r_c}. \qquad (18)$$

When $r(\tau_a + \tau_o) = r_o \geq n$ the condition that $W(r_c) = 0$ is

$$0 = r_o^3 v_o^2 - \frac{2}{3} \beta_c (r_c^3 - r_o^3) + 2\gamma \ln \frac{r_c}{r_o} - (r_c^2 - r_o^2). \qquad (19)$$

Equation (19) applies when $r_c \geq n$ and $v(r_c) = 0$.

It is interesting to note from equation (18) that, depending upon the value prescribed for the air content, γ, β_c can be negative. In the particular case $\beta_c = 0$, we have $r_c = \sqrt{\gamma}$. If we require that $r_c > n$, then for this case at least, we see that $\gamma > n^2$. This condition will seldom be satisfied and we expect negative values of β_c to be the rule. For example, when $\gamma = 0$, $\beta_c = -1/r_c$. Thus, if a large value of r_c is to be expected, it will be accompanied by a negative β_c of small magnitude. Note that β_c has no explicit dependence on n. Finally we observe that equation (18) states that the forces across the bubble wall are in equilibrium. Therefore we find as expected, that the equation governing the flaccid bubble in reference [6] and equation (18) are identical. We observe in connection with this second set of critical conditions that the affix of the saddle point will be at a larger value of r_c than in the case of r_s above. Accordingly we designate this abscissa in the phase-plane by r_l and call it the *larger critical radius.*

Although the time available for vaporous bubble growth is very short as measured in the laboratory time scale, when we consider the pace of this event in terms of bubble time, τ, the time available is often quite long. As a consequence, our interest will often center on phase-plane trajectories which are fairly close to the separatricies analyzed above. Crude estimates for τ_m, obtained in reference [11] show that the bubble time available for vaporous growth can vary widely. But the results also suggest that in most situations of practical interest, the bubble time available will be very large so that the need to distinguish between this large value and $\tau_m \rightarrow \infty$ may no longer be important.

Classification of Solutions and the Role of Critical Radii. The limiting condition between solution classes 3 and 4 follows from equation (18) which can be expressed in normalized form as

$$\beta\sqrt{\gamma} = -\frac{1}{\xi} \left(1 - \frac{1}{\xi^2}\right), \qquad (20)$$

where $\xi = r_m/\sqrt{\gamma}$. In Fig. 4, $\beta\sqrt{\gamma}$ is plotted against ξ as given by equation (20). Since $r_m \geq n$, ξ will generally be found on that branch of equation (20) which is to the right of the
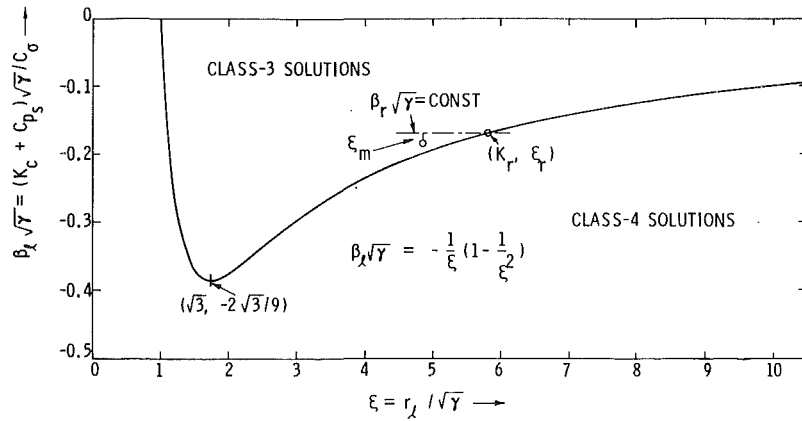
Fig. 4 The critical curve separating Class-3 and Class-4 solutions for vaporous cavitation bubble growth in the matched piecewise-autonomous approximation

minimum and K will be such that $\beta\sqrt{\gamma}$ will be at a point inside the curve.

On the other hand, once γ is selected, the value of the smaller critical radius, r_s, and the corresponding value of the parameter α_c is determined once and for all. Useful reference values of $K = K_r$, $\beta = \beta_r$, and $r = r_r$ are defined when equation (20) for the larger critical radius is solved for ξ_r and when $\beta_r = \beta_s$ corresponding to the cavitation number for the smaller critical radius. Then in Fig. 4 we see that the only permissible values of r_m (or ξ_m) must lie to the left of the intersection at ξ_r between the horizontal line through $\beta = \beta_r$ and the curve of equation (20), provided that $\beta_r < 0$. If $\beta_r \geq 0$ the entire area corresponding to $\beta < 0$ and to the right of the minimum of $\beta\sqrt{\gamma}$ is available for Class-3 solutions. If $\beta_r < 0$, the point $(\xi_m, \beta\sqrt{\gamma})$ must lie within the wedge-shaped region between the horizontal line and the curve if Class-3 solutions are to be found. This restriction also limits the range of r_m to be within the interval

$$n < r_s < r_m < r_r, \qquad (21)$$

where r_s is the smaller critical radius defined by equations (16) and (17). The condition given by the inequality (21) is supplemented by a second inequality,

$$n \leq \frac{1}{\gamma - \beta} < r_m \leq 55.5\theta D/(\mathrm{Re}^{0.79}R_o), \qquad (22)$$

which follows from the criterion (1). If one compares the rough time estimates for reference [11] discussed above with those which are obtained from accurate bubble growth times in the permissible region of Fig. 4 he finds that there will be a range of laboratory situations in which the time available for vaporous growth will be attained only on phase-plane trajectories which are very near a separatrix [11]. In terms of the physical parameters, α, β, and γ associated with such trajectories, the values of these three quantities will be practically indistinguishable from those borne by the nearby separatrix. Therefore, aside from calculations which match the piecewise-autonomous system to the nonautonomous one and the determination of the kinematic results which are needed to define $F(\tau)$, the precise value of τ or τ_m are of little significance in the calculation of incipient cavitation number. This will be particulary true for larger test bodies at moderate free-stream velocities. Therefore useful approximate inception calculations might be based upon the properties of the separatricies only.

Calculations for Cavitation Inception

Review of Basic Formulae. All quantities such as ρ, v, σ, R_o, C_p^*, b, C_{p_s}, D, s^*, s_1, s_2, and s_3 will have been prescribed. The dissolved air content and water temperature will also be given so that Henry's law can be used to find p_a,

the saturation partial pressure of dissolved air in the water. From these data we can calculate the parameters γ and C_a (see equations (2) and (4)). Our aim is to calculate the cavitation number, K, or from equations (14) and (3), the values of α and β, which amounts to the same thing. The maximum radius at the end of vaporous growth, r_m, must lie within the range prescribed by the conditions (21) and (22) above. For the present calculations, we conclude that

$$n < r_m \leq 55.5\theta D/(\mathrm{Re}^{0.79}R_o) \qquad (23)$$

and that the final determination of r_m must await other considerations which follow.

Once r_m is prescribed, we can match the nonautonomous and the piecewise-autonomous systems so that we can replace the nonautonomous equations with those derived for the piecewise-autonomous system.

The Use of Asymptotic Formulae for Inception Calculations. Preceding paragraphs suggest that in the formulation of inception calculations one should recognize two possibilities. These are that for a given Reynolds number, inception can occur at a fairly low or moderate free-stream velocity on a large test body or at a rather high free-stream velocity on a small test body. Because asymptotic formulae are to be used we note that the present calculations will not apply to the second of these possibilities.

The Cavitation Transition State and Cavitation Cutoff Speed. We shall define bubble-ring-cavitation transition to exit at that Reynolds number at which the laminar bubble is about to disappear. For hemisphere headforms the highest Reynolds number at which a laminar bubble might be observed is calculated to be about 5.5×10^6. Since cavitation nuclei have some range of radii R_o and experience some vaporous growth from R_o prior to becoming stabilized in the laminar bubble, it seems likely that bubble-ring cavitation will cease and be replaced by other forms of cavitation at Reynolds numbers which are somewhat less than the value of Reynolds number at which laminar separation disappears in the noncavitating flow. Unfortunately, the author knows of no observations of incipient or desinent bubble-ring cavitation which gives the value of K and other flow parameters which define the "cavitation transition state."

Assuming that values of R_o, θ, and n are known, we can find approximately the cavitation-transition state as defined by the values of K and V_o for bubble-ring inception. The calculations required to determine this pair of values are straightforward and details about them are given in reference [11].

The term "cavitation cutoff" is a shorthand way of describing the smallest values of free-stream velocity and cavitation number at which bubble-ring cavitation can exist.

In the experiments of reference [3] it was found that a bubble-ring cavitation cutoff speed existed at some value of tunnel velocity between 30 and 40 fps (9.144 and 12.192 m/s). This same cutoff phenomenon has been observed independently by research workers in Japan [16]. No systematic experiments were carried out at ARL in order to determine the cutoff values of tunnel speed and desinent cavitation number.

As a first step in the cutoff calculation, we offer an interpretation of the experimental findings which can be expressed in terms of the present theory. One factor may be that since the cutoff speed, V_{co}, is a relatively low speed, the cavitation number at this speed, K_{co}, should be somewhat less than that at the inception numbers at higher speeds. Moreover, since this speed is a threshold value for bubble-ring cavitation, it seems that threshold values of V_{co} and K_{co} should probably be as low as possible. Consequently, the liquid tension will be as large as possible, the largest possible amount of vaporous growth will occur and the lowest threshold cavitation number, K_{co}, will be accompanied by the largest permissible value of r_m, namely,

$$r_m = \frac{55.5\theta D}{\text{Re}^{0.79}R_o} . \tag{24}$$

The idea here is that for Class-2 or Class-3 trajectories the greatest amount of vaporous growth should occur in such a way that the maximum radius is limited by the height of the laminar bubble. Moreover, since we are dealing with the asymptotic theory, the value of r_m will be a larger critical value.

In reference [11] an iterative calculation method is developed for the determination of cutoff speed and cavitation number. We have obtained numerical data from such calculations for the cutoff values, V_{co} and K_{co}, at a water temperature of 80°F (26.67°C). Extensive ranges of R_o (μm) and n have been selected for two air contents in order-to show the general trends forecast by the analysis as clearly as possible. All calculations pertain to $C_{p_s} = -0.630$ and $\theta = 0.5$.

We have extracted those calculated values which lie in the neighborhood of the experimental trends from reference [3] and presented them in the carpet plot of Fig. 5. In this plot the abscissa is simply the cutoff velocity V_{co}. The ordinate is the cutoff cavitation number K_{co} and the change in K_{co} between each ordinate mark is $\Delta K = 0.1$ as shown. Therefore this ordinate has a sliding scale which depends upon the value of n chosen for each calculation of the cutoff condition (V_{co}, K_{co}). For example, suppose the value of n is 6. Then at the ordinate marked 6 in Fig. 5, $K_{co} = 0.5$, and at the ordinate marked 5, we would have $K_{co} = 0.4$ while at the ordinate marked 7, we would have $K_{co} = 0.6$. The ordinate mark of 6 fixes the scale for reading K_{co} values for the curve for $n = 6$ in Fig. 5[3]. It is necessary to choose this kind of a sliding scale becasue it is found from the numerical data that V_{co} is the primary quantity affecting the value of K_{co}. The values of R_o and n affect K_{co} less directly. Figure 5 also shows that if one knows the values of V_{co} and K_{co}, he would be able to determine the nominal properties of a typical nucleus which leads to the observed cutoff in terms of R_o and n. As a result we can at least see from Fig. 5 a limited range of possible nucleus properties which needs to be explored.

Calculations for Prescribed Nucleus and Free-Stream Velocities. It now remains to use the asymptotic theory, in order to estimate the inception cavitation number for bubble-ring cavitation when n and R_o are prescribed and V_o lies anywhere between the upper and lower bounds defined by the cavitation transition and cutoff states.
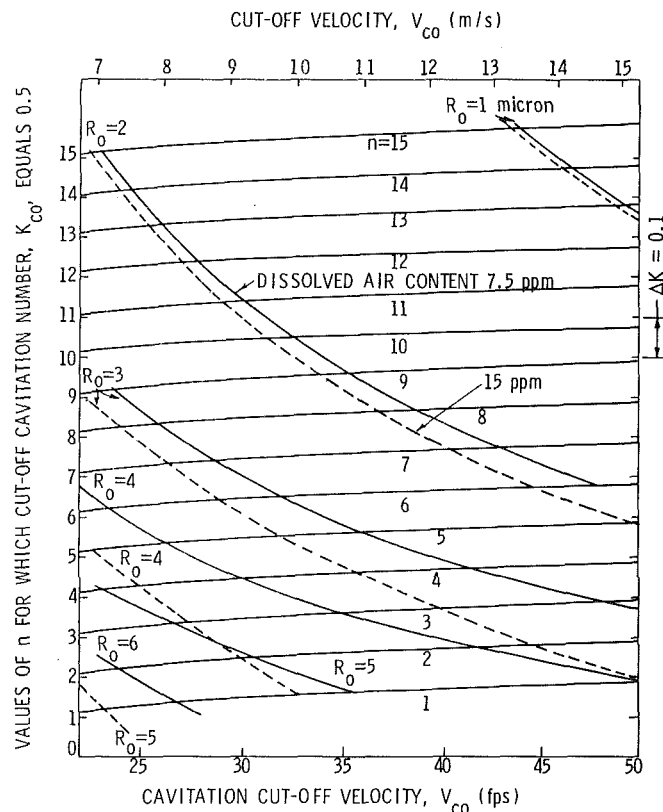

Fig. 5 Cavitation cutoff data for ranges in important physical parameter values; calculations for $C_{ps} = -0.630$ and $\theta = 0.5$

We start with the case in which the cavitation number for the smaller critical value of the cavitation number (as opposed to the onset value) exceeds $-C_{p_s}$. Then the asymptotic value of K for the onset of bubble-ring cavitation is determined from equation (3) and (18). In equation (18) $r_c = r_m$ and r_m is the limiting value given by equation (24). Having specified V_o, n, R_o, γ, and so on, we first calculate r_m from equation (24). Next we use equations (16) and (17) in order to find α_c. Given α_c, K_c can be found from equation (14) because C_o can be calculated at once from the prescribed data of the problem. In this case $K_c \geq -C_{p_s}$. Therefore we can use equation (18) in order to find β. Then the cavitation number for onset follows from equation (3). These calculations, being rather straightforward, permit one to write a rather simple asymptotic formula for bubble-ring onset. The result, in terms of standard dimensionless factors [17], is

$$K = -C_{p_s} - \frac{\text{Re}^{0.79}}{13.875\theta\text{We}^2} \left(1 - \gamma\left(\frac{R_o}{55.5\theta D}\right)^2 \text{Re}^{1.58}\right), \tag{25}$$

where $\text{We} = V_o/\sqrt{\sigma/\rho D}$ is the Weber number based on body diameter. Because R_o is such a small number it is easily seen that equation (25) is essentially independent of air content, γ, for most applicable experimental situations. Thus, we can replace the term in brackets by unity [11]. A comparison of data from reference [3] and calculated values of $\theta = 0.5$ and 1.0 is shown in Fig. 6. The agreement between calculated and observed results is thought to be quite good, although if we were to take $\theta > 1.0$, the agreement could certainly be improved.

One can also carry out inception calculations in which the horizontal line shown in Fig. 4 replaces the asymptotic criterion of equation (18). This calculation can involve Class-2 solutions rather than just Class-3 solutions and it is found that agreement between experiment and theory is very poor [11], as had previously been reported in reference [15].

---

[3] Example: For a dissolved air content of 7.5 ppm and nucleus parameters $n = 5$, $R_o = 3\mu$m Fig. 5 gives $V_{co} = 36.7$ fps and $K_{co} = 9.56$.

The data on bubble-ring cavitation considered thus far are not all of the experimental findings reported by Holl and Carroll [3]. They also discovered a temperature dependence for bubble-ring desinence. Although the present theory appears to exhibit the same trend with temperature it was found [11] that the calculated results shows much less sensitivity to temperature than the experimental trends. In the calculations the only temperature sensitive parameters were the Henry's law constant, the surface tension, the vapor pressure and the kinematic viscosity of water. Evidentally other factors should be considered to complete the theory.

Conclusions

The theoretical findings of this paper have been obtained by means of a simplified "asymptotic theory" which shows very encouraging agreement with the experimental data reported by Holl and Carroll [3]. Evidentally the asymptotic theory introduces small error for many situations of practical interest although there is certainly room for improvement in this simplified analysis.

One finding of the theory is that the caviation number at desinence or inception is less than the magnitude of the pressure coefficient at the lamainar separation point.

As discovered by Holl and Carroll [3], and also reported by Kodama [16], there is a cavitation-cutoff speed which defines a free-stream velocity below which bubble-ring cavitation is not observed although other forms may be present. It is now found both experimentally and theoretically that the cutoff phenomenon exists and that it is sensitive to the temperature of the water.

In addition, the theory suggests that there is also a high-speed limit on bubble-ring cavitation which is associated with the Reynolds number at which the laminar separation bubble starts to disappear. It has been possible to estimate values of the free-stream velocity and cavitation number for this "cavitation-transition" limit. No experimental data are presently available for comparison with the analytical results.

Both theory and experiment show cavitation number versus free-stream velocity trends which are almost independent of dissolved air content as long as there is appreciable dissolved air in the water. It has also been found that the best analytical results are found when the parameter $n = 1$, corresponding to a spherical air bubble nucleus of 7 μm initial radius. However, using the cutoff velocity to match theory and experiment and comparing analytical values for various n, one finds differences in predicted cavitation numbers in the third, and occasionally in the second, decimal place. The chief trend seems to be that as the value of n increases, the nucleus size R_o decreases and the value of incipient cavitation number at a prescribed velocity shows only minor variation.

Acknowledgment

This work was supported by the Naval Sea Systems Command under the cognizance of Code NSEA 63R-31. The author wishes to acknowledge many useful discussions with Drs. J. W. Holl and M. L. Billet during the course of the study. Thanks are also due to Mr. W. R. Hall and Mr. R. A. Kohler for assistance with certain numerical aspects of the work.

References

1 Arakeri, V. H., and Acosta, A. J., "Viscous Effects in the Inception of Cavitation on Axisymmetric Bodies," ASME JOURNAL OF FLUIDS ENGINEERING, Vol. 95, No. 4, Dec. 1973, pp. 519–527.

2 Arakeri, V. H., "A Note on the Transition Observations on an Axisymmetric Body and Some Related Fluctuating Wall Pressure Measurements," ASME JOURNAL OF FLUIDS ENGINEERING, Vol. 97, No. 1, Mar. 1975, pp. 82–86.

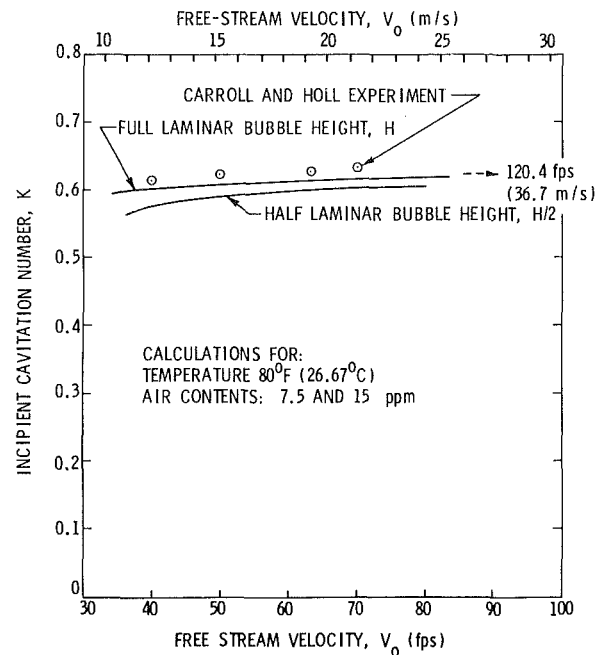Fig. 6 Comparison of experiment and theory for bubble-ring cavitation onset; calculated values of K for maximum vapor bubble radii on one-half laminar bubble height and equal to laminar bubble height are shown

3 Holl, J. W., and Carroll, J. A., "Observations of the Various Types of Limited Cavitation on Axisymmetric Bodies," ASME JOURNAL OF FLUIDS ENGINEERING, Vol. 103, No. 3, Sept. 1981, p. 145.

4 Parkin, B. R., "A Possible Criterion for Cavitation Inception on Hemispherical Headforms," ASME JOURNAL OF FLUIDS ENGINEERING, Vol. 103, No. 4, Dec. 1981, p. 543.

5 Holl, J. W., "Limited Cavitation," in Cavitation State of Knowledge, American Society of Mechanical Engineers, New York, 1969. In particular, see pp. 46–58.

6 Parkin, B. R., "Conditions for Gaseous Microbubble Growth in Laminar Separation Bubbles," ASME JOURNAL OF FLUIDS ENGINEERING, Vol. 103, No. 4, Dec. 1981, p. 577.

7 Arakeri, V. H., "Viscous Effects in Inception and Development of Cavitation on Axi-Symmetric Bodies," Ph.D. Thesis, California Institute of Technology, 1973. (Also released as Report No. 3183.1, Division of Engineering and Applied Science, California Institute of Technology, 1973.)

8 Van der Meulen, J. H. J., "A Holographic Study of Cavitation on Axisymmetric Bodies and the Influence of Polymer Additives," Ph.D. Thesis, Enschede, 1976.

9 Van der Meulen, J. H. J., "A Holographic Study of the Influence of Boundary Layer and Surface Characteristics of Incipient and Developed Cavitation on Axisymmetric Bodies," Proceedings Twelfth Symposium on Naval Hydrodynamics, Office of Publications, National Academy of Sciences, Washington, 1979, 433–451.

10 Plesset, M. S., "Dynamics of Cavitation Bubbles," ASME Journal of Applied Mechanics, Vol. 16, 1949, p. 277.

11 Parkin, B. R., "A Theory for Cavitation Inception in a Flow Having Laminar Separation," Applied Research Laboratory Technical Memorandum File No. 79-198, AD A082 851, The Pennsylvania State University, Nov. 1979.

12 Lefschetz, S., Differential Equations: Geometric Theory, Second Editon, Dover, New York, 1977.

13 Davis, H. T., Introduction to Nonlinear Differential and Integral Equations, U.S. Atomic Energy Commission, U.S. Government Printing Office, Washington, 1960.

14 Nayfeh, A. H., and Mook, D. T., Nonlinear Oscillations, Wiley & Sons, New York, 1979.

15 Parkin, B. R., "Scale Effects in Cavitating Flows," Report No. 21-8, Hydrodynamics Laboratory, California Institute of Technology, Pasadena, Calif., July 31, 1952.

16 Kodama, Y., Private communication on observations of bubble-ring cavitation cutoff from Ship Research Institute of Japan, Dec. 1980.

17 Billet, M. L., Holl, J. W., and Parkin, B. R., "Scale Effects on Cavitating Flows Due to Surface Roughness and Laminar Separation," Proceedings 10th Symposium of the IAHR, Tokyo, Japan, September 29–October 2, 1980. Also to be published in AIAA Journal, 1982.

DISCUSSION

F. G. Hammitt[1]

Dr. Parkin is to be highly commended for this most logical and straightforward analysis of the highly complex problem of bubble-ring cavitation inception on hemispherical head-forms over the range of Reynolds numbers at which laminar separation is known to occur. The overall problem treated is highly complex, involving several stages of bubble behavior, including initial inception from nuclei, vaporous growth, and then gas diffusion effects. It is then necessary to use several approximations and an asymptotic solution in part. In spite of the various approximations, the comparison with experimental measurements is good, so that presumably the approximate solution can be applied with reasonable confidence to other related and similar cavitating flow regimes. The paper involves one of the few relatively comprehensive applications of which I am aware of the general Rayleigh-Plesset spherical bubble dynamics equation for other than simple bubble collapse. The approximations used are such that the required computer time for the analysis is not excessive, and therefore the approximate solution is such as to be of large practical importance.

I would like to urge further solutions of such basically highly complex cavitation flow problems in a similar manner, so that the wealth of experimental measurements available can be further generalized and understood. Again, my congratulations to Dr. Parkin for his considerable persistence in working out in detail this highly complex problem.

Author's Closure

The author thanks Professor Hammitt for his expressions of interest in the present work. He also wishes to second Professor Hammitt's suggestion that investigators make further attempts to estimate cavitation inception from the equations of bubble dynamics combined with those which model the basic fluid mechanics for other flows besides the

---

[1]Professor, Mechanical Engineering Department, University of Michigan, Ann Arbor, Mich. 48109

one studied here. Nevertheless, the author still believes that although some progress has been made in the present study of one special flow, there are still some aspects of this research which could benefit from further study.

One of these is the need to relate the vaporous growth phase more realistically to the initial conditions a typical nucleus might experience and to model more closely the kinematics of the traveling vaporous microbubble in the boundary layer. A second need is to replace the present crude matching approximation used in the bubble growth calculations with a treatment which is more precise. These refinements might then lead to improved agreement between theory and experiment. Of course, additional comprehensive measurements of the kind undertaken by Holl and Carroll [3] but which concentrate on cavitation cut-off and cavitation transition on hemispherical headforms, could be decisive for testing the analytical refinements advocated above.

Finally, it seems useful to suggest possible reasons why the present approximate theory seems to work as well as it does. Perhaps the most important reason is the theory assumes that if the vaporous microbubble becomes fixed in the laminar separation zone on the body, further vaporous growth to its maximum radius occurs under conditions in which the dynamical system is autonomous. It appears, therefore, for this later part of vaporous growth, that the assumptions of the analysis closely match the actual physical situation. Because of this circumstance, the determination of flow paramters asssociated with the separatrix through the saddle point in the phase plans permits one to obtain an estimate for inception conditions which is not too sensitive to the approximations employed during the time that the microbubble travels in the boundary layer and the system is certainly not autonomous. This insensitivity is due to the fact for flow states near the separatrix, the total time available for vaporous growth can undergo large variations with almost no effect on the values of the basic flow parameters which control vapor bubble growth rates and consequently, the cavitation number at inception. If tests are performed on small hemispherical models at high speed, this fortuitous situation might not exist (and it certainly will not hold in different flows in which the dynamical system is never autonomous). Even for the present special flow, we have not established the lower limits of the asymptotic theory in this respect.

Discussion

Optimum Strut-Configuration for Downstream Annular Diffusers With Variable Swirling Inlet Flow[1]

T. Kubota.[2] Regarding the results in Fig. 6, it is shown that the struts are stalled when $\gamma \leqq 10$ deg for two struts and $\gamma \leqq 5$ deg for four struts. To achieve the maximum pressure recovery of a diffuser with struts, the stagger angle should be selected close to the angle of stall limit. Therefore, the discusser would like to ask the authors whether the stall limit is predictable or not, providing that the velocity distribution of swirling inlet flow is prescribed.

Authors' Closure

The interest that Mr. Kubota has shown in our work is appreciated. Before replying to his discussion, we must apologize that there are some simple mistakes in our paper. That is, Fig. 3 should be replaced by Fig. A-1. The values of solidity in the text $l/t = 0.228$ and 0.455 should be replaced by 0.271 and 0.542, respectively. However, the conclusions are not affected by these errors.
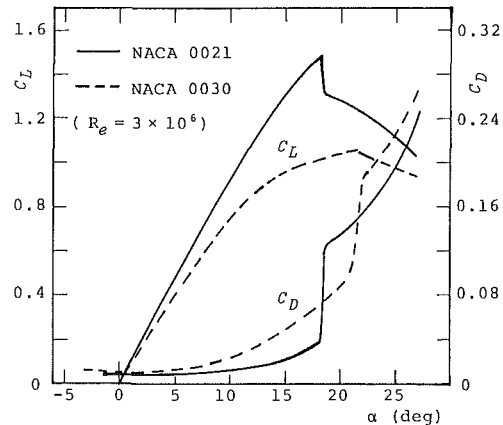
Since the separation of boundary layer on a blade causes the blade stalling, the prediction of stalling of struts should be made at the blade section where the adverse pressure gradient along the blade surface is the most severe. In this sense, estimation of blade loading at the blade section corresponding to the root mean square radius, shown in Table 2, is not appropriate to examine the stall limit. Since the circumferential component of velocity is the largest near the hub wall, as shown in Fig. 5, radius ratio $R/R_0 = 0.5$ is selected as the section to evaluate the stall limit. For various stagger angles of struts corresponding to Fig. 6, the lift coefficient of the blade and the angle of swirl flow downstream of the cascade at that section are estimated using a two-dimensional cascade theory. At the hub section, the solidity is considerably

Table A-1 Lift coefficient C_L of struts and downstream flow angle θ_2 based on two-dimensional performance curves in Fig. A-1 with cascade correction. Swirl flow angle upstream of struts is $\theta_1 = 34$ deg at $R/R_0 = 0.5$.

stagger angle of struts	γ (deg)	4	10	15	20
two C-struts $l/t = 0.411$ $(R/R_0 = 0.5)$	θ_2 (deg)		17.2	20.1	23.2
	C_L		1.29	1.04	0.76
four C-struts $l/t = 0.821$ $(R/R_0 = 0.5)$	θ_2 (deg)	5.7	10.8	15.6	20.6
	C_L	1.16	0.94	0.71	0.50

Fig. A-1   Two-dimensional performance of airfoils [7]

larger than that at the root mean square radius, and as a result cascade correction is required. Weinig's cascade correction is applied to the single airfoil data in Fig. A-1, and it is assumed that the relationship between $\epsilon = C_D/C_L$ and C_L for the cascade is identical to that of single airfoil.

For the case of $\theta_{m1} = 26$ deg in Fig. 6, the inlet flow angle near the hub is 34 deg. The results of calculation are presented in Table A-1, which replaces Table 2. According to the experimental data in Fig. 6, the struts stall at $\gamma = 4$ deg for the case of four struts and at $\gamma = 10$ deg for the case of two struts. The lift coefficients for these stall limits are 1.16 and 1.29, respectively. These critical lift coefficients are a little less than those of single airfoil in two-dimensional flow. The difference is probably due to the cascade effect and the three-dimensional effect or accumulation of blade boundary layer near the hub. For design purposes, if the design lift coefficient is chosen as $C_L = 1.1$ for the sake of safety, the designed stagger angles of struts for the two cases are $\gamma = 5.9$ deg and $\gamma = 13.7$ deg, respectively. As it is observed in Fig. 6, the pressure recovery coefficients C_p at these conditions are almost as high as those at the critical condition of stall.

Initial Region of Subsonic Coaxial Jets of High Mean-Velocity Ratio[1]

M. K. Swaminathan,[2] **G. W. Rankin,**[2] **and K. Sridhar.**[2] The turbulent mixing of coaxial jets has been a topic of continuing interest to many investigators in view of the practical importance. The authors' work deserves credit for

[1] By Y. Senoo, N. Kawaguchi, T. Kojima, and M. Nishi, published in the June, 1981, issue of the ASME JOURNAL OF FLUIDS ENGINEERING, Vol. 103, No. 2, pp. 294–298.

[2] Chief Hydraulic Engineer, Fuji Electric Co. Ltd., Tanabe-Shinden, Kawasaki, 210, Japan.

[1] By N. W. M. Ko and H. Au, published in the June 1981 issue of JOURNAL OF FLUIDS ENGINEERING, Vol. 103, No. 6, pp. 335–338.

[2] Research Fellow, Assistant Professor and Professor, respectively, Department of Mechanical Engineering, University of Windsor, Windsor, Ontario, Canada N9B 3P4.

Copyright © 1982 by ASME

Table 3 Configurations and initial conditions of nozzles

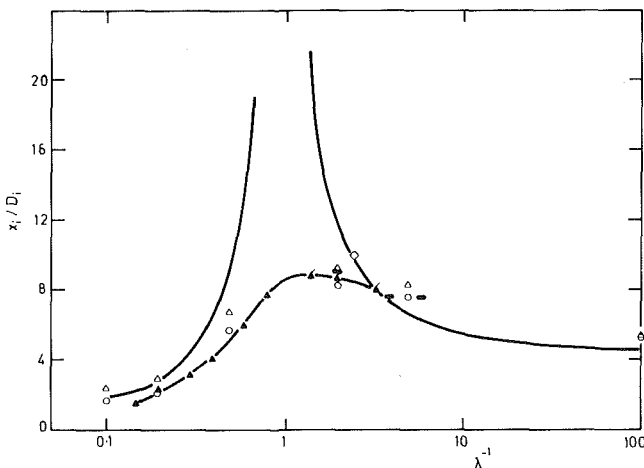|	Ko and Au	Champagne and Wygnanski [11]
D_0 (cm)	4.0	
D_i (cm)	2.0	2.54
Lip thickness (cm)	0.1	
Inner contraction ratio	8:1	144:1
Outer contraction ratio	13:1	100:1
Area ratio	2.73	1.281, 2.94
$\bar{U}_0$ (m/s)	50	60
$\bar{U}_i$ (m/s)	20-40	30
Initial turbulence intensity at inner nozzle	0.4%	0.1%
Initial turbulence intensity at outer nozzle	1.2%	

Fig. 10 Variation of inner core length with mean-velocity ratio. —, Abramovich [15]; —, Forstall and Shapiro [1]; △, 0, Champagne and Wygnanski [11]; ◇, Hammersley [6]; ▲, Kwan [17]; ▴, present data.

and Shapiro [1] concern the closed conduit flow. From the figure, fairly good correlation of the inner core length with the mean-velocity ratio is found. At λ^{-1} less than unity the results of Champagne and Wygnanski [11] at the area ratio of 2.94 seem to be slightly higher than those of the authors while the results at the area ratio of 1.28 seem to agree.

Additional References

15 Abramovich, N., *The Theory of Turbulent Jets*, M.I.T. Press, 1963.

16 Hammersley, R. J., "An Experimental Investigation of the Turbulent Characteristics of Coaxial Jet Flows and Their Role in Aerodynamic Noise Generation," Ph.D. thesis, University of Illinois, 1974.

17 Kwan, A. S. H., "Noise Mechanisms in the Initial Region of Coaxial Jets," Ph.D. thesis, University of Hong Kong, 1975.

Combined Simultaneous Flow Visualization – Hot-Wire Anemometry for the Study of Turbulent Flows [1]

P. Freymuth.[2] This discusser would like to point out that mutual reinforcement of flow visualization techniques and hot-wire techniques has been used previously in the context of investigation of stability and transition. Brown [D1] compared flow visualization and hot-wire results to improve the accuracy of the frequency determination for the organized motion which precedes transition in a boundary layer. Freymuth [D2] correlated hot-wire signals with flow visualization signatures for determining the various regions of transition in a free shear layer. Thus, the utilization of several measurement techniques for improved information flow in experimental fluid mechanics has some precedence. The use of this technique by Professor Falco for the investigation of topics of current interest is encouraging, and, hopefully, it will be used even more frequently in the future.

Additional References

D1 Brown, E. N. M., "Boundary Layer Transition," Rep. AD-4059 13 (TISTP1JW), Notre Dame University, Indiana, May 1963.

D2 Freymuth, P., "On Transition in a Separated Laminar Boundary Layer," *J. Fluid Mech.*, Vol. 25, 1966, pp. 683–704.

A Four Hole Pressure Probe for Fluid Flow Measurements in Three Dimensions[1]

M. W. McBride.[2] The velocity vector measuring probe developed by I. C. Shepherd represents a technique which should find a wind range of application. The four-hole probe has advantages over five-hole probes in that fewer data are required and smaller head volumes are possible. The problems associated with the use of these probes should prove to be equivalent to those experienced with five-hole probes. Comprehensive discussion and examples of Reynolds number and near-wall effects may be found in reference [D1]. The effects of high shear rate and turbulence levels are presented in reference [D2]. Both references measure flows associated with rotating turbomachinery in the relative and absolute frames of reference. Comparisons are made with data acquired by other means. In the cases cited, the four-hole probe would have reduced the data handling and test time required.

Measurements of flow with some axial symmetry could be facilitated by use of the four-hole probe. However, the technique of using six calibration quadrants seems cumbersome and could be replaced by a method which requires only a single calibration quadrant. Coefficients based on three indicated static minus total pressures will be well behaved and may be correlated in either rectangular or spherical-polar coordinates. In the later case, the indicated pitch angle is nearly constant with circumferential angle, and the method requires two sets of calibration curves. These curves are fitted with cubic splines and are well behaved.

The accuracy of the probe and data reduction system measuring unknown flows should be documented by direct comparison with measurements taken by independent methods. The laser doppler velocimeter has been shown to produce accurate velocity component measurements and does not suffer from probe response time limitations. Both four and five-hole probes should be compared to LDV data before judgment of absolute accuracy in time dependent flows is made. This is especially true when turbulence levels of ten percent or higher are present.

In conclusion, the four-hole probe offers a relatively simple method of measuring three dimensional flow fields when limitations of use and accuracy are properly taken into account.

Additional References

D1 Treaster, A. L., Youcum, A. M., "The Calibration and Application of Five-Hole Probes," *Transactions of The Instrument Society of America*, Vol. 18, No. 3, 1979.

D2 Pierzga, M. J., "Experimental Verification of the Streamline Curvature Numerical Analysis Method Applied to the Flow Through an Axial Flow Fan,"

Applied Research Laboratory, The Pennsylvania State University, TM 80-181, May 28, 1980.

Author's Closure

Mr. McBride's comments are appreciated. Most of the points made are accepted, however, the suggestion that the six zone convention be replaced by a single zone convention is not attractive.

The six zone convention was adopted because it yields smooth, well behaved, yet uniformly sensitive relationships between the measured pressure ratios and the parameters sought. Single zone correlations could not cover the same range of probe orientations without possessing singularities, since there is no single pressure difference available as a denominator, which does not go to zero somewhere in the operating range.

An attempt was made to fit the entire correlation surfaces with splined polynomials, however, better accuracy and speed were achieved with a bi-cubic interpolation in the region of the operating point.

| Generation of Oscillating Jets[1]

M. F. Platzer[2] and W. H. Harch.[2] The authors present experimental data that will assist in the design of a jet nozzle which can produce oscillating jet deflections of large amplitude. The nozzle consists of a jet flowing between two cylinders which is periodically subjected to lateral injections of momentum flux. The authors appear to be unaware of a patent by Jacobs and Platzer [1] who suggested that such a nozzle be used on airfoil-jet flap combinations for fast acting lift control. Simmons and Platzer [2] presented frequency response data obtained with such a nozzle and demonstrated its usefulness to produce controlled gusts for wind tunnel dynamic response studies. Further studies using this nozzle were reported by Platzer et al. [3]. However, no systematic investigation was conducted to explore the influence of the various geometric and dynamic parameters on the turning performance. Hence, authors' data provide a valuable base. Further information would be desirable on the precise jet oscillation characteristics. Fluidic nozzles tend to produce a bistable (square wave in time) rather than a sinusoidal jet oscillation. Platzer et al. [4] showed that the type of jet unsteadiness has a substantial effect on its entrainment. Hence a series of conditionally sampled measurements taken on a cross-section traverse downstream of the nozzle would give a better idea of the manner in which this jet is oscillating.

Additional References

1 Jacobs, W. F., and Platzer, M. F., "Airfoil Including Fluidically Controlled Jet Flap," U. S. Patent No. 3,669,386, May 1972.

2 Simmons, J. M., and Platzer, M. F., "Experimental Investigation of Incompressible Flow past Airfoils with Oscillating Jet Flaps," *J. Aircraft*, Vol. 8, No. 8, Aug. 1971, pp. 587–592.

3 Platzer, M. F., Deal, L. J. Johnson, W. S., "Experimental Investigation of Oscillating Jet-Flow Effects," *Proceedings, Symposium on Unsteady Aerodynamics*, Eds., R. B. Kinney and W. R. Sears, Vol. I, July 1975, pp. 393–413.

4 Platzer, M. F., Simmons, J. M., and Bremhorst, K., "Entrainment Characteristics of Unsteady Subsonic Jets," *AIAA-Journal*, Vol. 16, No. 3, Mar. 1978, pp. 282–284.

Authors' Closure

We thank M. F. Platzer and W. H. Harch for drawing our attention to their patent and early work on oscillating jets. Despite close similarities there are notable differences between their nozzle and ours. It seems that in their case the jet deflection is mainly produced by the lateral momentum injection whereas here the Coanda effect is the dominant mechanism as shown by Figs. 7, 9, and 10.

The tendency toward a square wave oscillation of the angle in time has also been observed but only at frequencies below about 10 hz. At higher frequencies the angular oscillations are nearly sinusoidal as shown by Fig. 5. For comparisons between different experiments the physical frequency is certainly not the right parameter and some Strouhal number should be used but it is not clear which one is the most appropriate.

We agree entirely with the last comment concerning the usefulness and interest of detailed measurements of the downstream development of oscillating jets. We have actually already performed such measurements. The results on the rate of spread of flapping jets have just been published [3] and a more detailed account on their structure should be submitted for publication shortly.

| Drag Reducing Polymer in Helicoidal Flow[1]

P. Dunn.[2] The noteworthy contributions of this paper are: (1) identification of a novel flow configuration in which the effect of polymer additives possibly could be dissociated from those related intrinsically to the three-dimensional nature of turbulent flow, (2) measurement of a polymer effect in a "screw-cylinder" configuration, and (3) demonstration that certain chemicals reduce the polymer effect in this flow arrangement. Dr. Kuo and the late Professor Kovasznay are to be complimented for this unique approach that adds to the understanding of drag reduction by polymers.

As noted in the paper's discussion, the present experiment differs from the "ideal," three-dimensional, laminar-flow experiment in two main respects: (1) the magnitude of the circumferential velocity in most cases is an order of magnitude greater than those of the other two-velocity components, and (2) approximately one-half of the data gathered was in the turbulent flow regime. Because of these constraints, it cannot be determined if there is a significant effect by polymer additives in "truly" three-dimensional laminar flows. The observed polymer effect in the present experiment most likely was the result of the enhanced shearing and stretching of the solution in the circumferential direction. Future experiments should be guided by the present one and focus on obtaining more data with a similar configuration, but at lower Taylor numbers (less than 100).

It also is interesting to note that noticable changes in the coefficients α and A of the curve fit of the test data for the water-only case occur when the flow enters the turbulent regime (between $n = 1000$ and 1500 rpm or correspondingly between $T = 345$ and 518). Similar changes in α and A, however, are not evident for the polymer case. This suggests that the effect may evidence itself in a more continuous fashion as the flow progresses from laminar to transition to turbulent flow. To examine this, it may be beneficial to recast both sets of data in dimensional form, e. g., torque coefficient versus Taylor number, as described in reference [1].

Authors' Closure

Dr. Dunn has rightly pointed out the direction of performing future experiments at lower Taylor number. Lower Taylor number tests will be valuable in two respects: (1) verification of the effect of polymer additives in a screw-

---

cylinder system in laminar flow and (2) development of a quantitative relationship of polymer effect and strain rate.

The results in this study as well as those mentioned in Ref. 5 indicate that the polymer effects will not be observable until the polymer solution has reached a certain strain rate (or time scale). Thus, in order to produce observable polymer effect, the polymer solution strain rate has to be high enough which depends on the polymer molecular weight and concentration. To measure the polymer effect in a similar screw-cylinder configuration at lower Taylor number, the design of a new apparatus can be guided by specifying the desired Taylor number range and the expected strain rate range. For example, according to Fig. 4, the polymer effect can be measured perhaps at a rotational speed as low as 300 rpm. Using $R\omega/\delta$ as the scale for the strain rate, at $n = 300$ rpm, $R\omega/\delta$ is about 400 s^{-1}. Suppose a new apparatus is to be designed to run the experiment at a Taylor number range of 20 and above, the required R and δ can be determined by solving

$$T = 20$$

and

$$\frac{R\omega}{\delta} = 400$$

simultaneously for a desired rotational speed ω. For instance, if choosing $\omega = 31.42$ rad/sec (300rpm) for water at 20°C, the design values of R and δ would be R = 0.538cm and δ = 0.042cm. The average gap width of the new apparatus is less than half of the gap width (0.0915cm) shown in Fig. 3. In general, narrowing the gap width is most effective in reducing the Taylor number.

Authors' Correction

In Fig. 1, the thread peak-to-valley depth should be 0.075cm and the screw diameter should be 1.195cm.

| Cavitation Inception in Spool Valves[1]

A. Lichtarowicz[2]

The authors should be congratulated on their interesting paper describing methods of detecting cavitation inception in spool valves. As pointed out in the paper, it is very dificult to establish the exact point of cavitation inception in an actual piece of engineering hardware.

The comparison of the ratio of cavitating to noncavitating energy spectra, as used by the authors, seems to be a very useful method of detecting cavitation inception, though perhaps it is a little cumbersome.

The writer, from his experiences, fully endorses the statement made that in laboratory models the use stethoscope gives a very reliable indication of the inception point which agrees with the data obtained with much more sophisticated electronic equipment.

Another useful method used by the writer [reference A] is to place a small "hydrophone" made from a piezo-electric crystal in the vicinity of the emerging jet, but not in its path. The change in the output as observed on an oscilloscope screen proved to be very reliable method of detecting the cavitation inception, especially as cavitation initially occurred in bursts.

Figure 1 shows results extracted from Pearce [B]. They relate to the cavitation inception for a sharp edge orifice plate (similar to that used for flow measurement). The orifice diameter was 2.5 mm and the test fluid was aviation kerosene. Each point was obtained by holding the downstream pressure
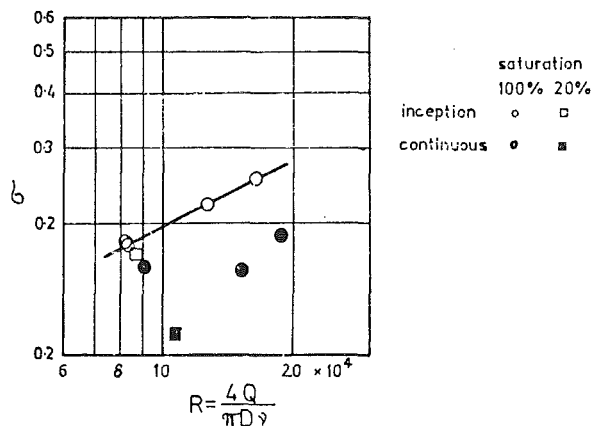
Fig. 1 Cavitation index-Reynolds number variation for shape edge orifice plate

constant and increasing the upstream pressure till the cavitation was well established. The results are similar to the author's Fig. 22. Two additional points were obtained with reduced air content in the test liquid. These points seem to confirm the author's statement that the air content changes do not affect the cavitation inception, at least for the range of air contents tested.

Finally the writer would like to sound a word of warning. Both the authors' Fig. 22 and Fig. 1 in the discussion relate the cavitation number with Reynolds number. In both cases the variation Reynolds number was obtained mainly by flow variation and by size variation, but fluid properties varied only by a factor of about 2. To ensure that these graphs can be generalized, further testing with different liquids is required.

Author's Closure

The authors thank Dr. Lichtarowicz for his interesting discussion of the paper. Two of the issues he raised have already been replied to in the closure to Dr. Cunningham in the December 1981 issue. It should be noted, however, that the results presented by Dr. Lichtarowicz in his Fig. 1 corroborate our conclusion that the small residence time for the oil in each valve inhibited significant growth of air bubbles by gaseous diffusion. He is also correct in his assessment that low-intensity cavitation near inception is of no importance in oil hydraulic systems.

The authors agree with Dr. Lichtarowicz that the comparison of the ratio of cavitating to non-cavitating energy spectra, though a useful method of detecting cavitation inception, may be cumbersome if the proper data acquisition system is not available. In this study the ratio could be obtained quickly with the digital signal analyzer. Although the authors mainly used spectra for detection of cavitation, on occasion tests were conducted by comparing single pressure transducer signals in the time domain. A better statistical representation results, however, by taking an adequate number (say 50) ensemble averages, the results of which can be displayed with nearly equal usefulness in (1) the time domain, (2) the frequency domain, or (3) by a probability density plot.

Dr. Lichtarowicz has made a valid point in warning that the results presented in Fig. 22 and his Fig. 1 were obtained mainly in variation in size and flow, and not by a large change in fluid properties. Plans are being made, however, to conduct tests with the model valve using water, thereby increasing the Reynolds number range by more than one order of magnitude. Apparently, the cavitation index plotted in his Fig. 1 is not based on the definition given by equation (6), but rather the definition for σ provided in Lichtarowicz and Pearce [11].

Internal Fluid Flow: The Fluid Dynamics of Flow on Pipes and Ducts, by A. J. Ward-Smith, Oxford University Press, 1980, 566 pages, $98.00 and **Fundamentals of Pipe Flow,** by Robert P. Benedict, John Wiley & Sons, Inc., 1980, 531 pages, $39.95.

Reviewed by Warren M. Hagist

These two books cover essentially the same subject matter (flow of Newtonian fluids in pipes) in approximately the same number of pages. Both were written for the practicing engineer but both, according to the authors, could be used as texts at the senior and graduate levels.

The book by Ward-Smith, after a 21 page introduction, is divided into three parts. The introduction familiarizes the reader with some of the general concepts of fluid mechanics: physical properties; dimensionless groups; and general features of laminar, transitional, and turbulent flows. Part I, entitled "Mathematical Foundations," presents in Section A the fundamental equations of fluid dynamics and thermodynamics in both differential and integral form. Section B is a most complete discussion of one-dimensional gasdynamics. Part II, entitled "The Fluid Dynamics of the Component Parts of System," comprises 60 percent of the book. It is a series of sections, each one being a detailed discussion of the flow in a particular kind of component of a piping system. These sections are very thorough and contain not only curves from which the engineer may pick numerical values but much theoretical development. Part III, entitled "Factors Relating to Over-all Systems Performance," discusses pipe networks and the interactions between the system operating curve and the pump characteristic. The book concludes with an excellent 21 page list of references.

The book by Benedict is divided into four parts. Part I, "Flow of Ideal Fluids in Pipes," presents the fundamental equations of compressible and incompressible inviscid flows. The equations are presented in both differential and integral form with examples of exact and numerical solutions. Part II, "Real Fluid Concepts," has three chapters. The first gives a brief treatment of boundary layers using integral methods. The second is an extensive discussion of the velocity distribution for turbulent flow in smooth and rough pipes. The third is devoted to the friction factor and the various plots that go with it. Part III, entitled "Flow of Real Fluids in Pipes," make up 50 percent of the book. This part is divided

into five chapters which discuss, in turn: the flow of liquids; the flow of gases; the flow of liquid-vapor mixtures; the loss through piping components; and the flow through networks. The book concludes with Part IV entitled "Thermodynamic Measurements in Pipes." Here there are chapters on temperature, pressure, and flow measurement and a concluding chapter which treats special techniques such as skin friction measurements. In this book there is a list of references at the end of each chapter.

There are some significant differences between the two books (price being the one that is first noticed). Benedict's book is well-stocked with numerical examples worked out in considerable detail. Ward-Smith's book has none. Benedict has a chapter on the flow of liquid-vapor mixtures in which he discusses the two-phase flashing flow of water and steam. Ward-Smith's book is restricted to single phase flows. Ward-Smith's discussions of flow through components are more detailed that Benedict's. As an example, Ward-Smith has a twelve page section devoted to flows through branches and junctions, while Benedict discusses this topic on four pages, most of which are occupied with numerical examples. Another example: Ward-Smith's section on pipe bends extends for 58 pages and is probably the best that has been written on the subject. Benedict devotes eight pages, with three numerical examples, to the subject. If you need a number quickly, go to Benedict. If you have some time and want to improve your understanding of flow through bends, go to Ward-Smith. Ward-Smith has a very useful (to this reviewer anyway) section on losses through gauzes and baffles. Benedict does not discuss this at all.

Benedict includes a few examples using the Hazen-Williams formula. Ward-Smith does not do this, and in his preface he says, "This approach is inconsistent with the principles of dimensional analysis and should now be quitely laid to rest." Hurray for Ward-Smith! How frustrating it is, after extrolling the virtues of Reynolds number and other dimensionless parameters, to have the professor in the next course say, "Yes, but for real problems we have this handy nomograph . . . . .".

Neither of the two books discusses unsteady flows. Both books are well-written and have been well-prepared by the printers. The many plots are clear and easy to read, but some are smaller than one would like. As is usually the case when two books like these appear, one should really own both of them.